UPO

Università del Piemonte Orientale

Department of Health Sciences

Ph.D. Program in Medical Sciences and Biotechnology
XXXIV cycle

Magnetic nanoparticles as nanocarriers and immune modulators for cancer targeted therapy

Supervisor: Prof. Maria Prat

Co-Supervisor: Prof. Antonia Follenzi

Coordinator: Prof. Marisa Gariglio

PhD candidate: Annarita D'Urso

SSD: BIO/17

Ad una persona speciale,
mia cugina Lucia!

TABLE OF CONTENTS

ABSTRACT

Superparamagnetic iron oxide nanoparticles (SPIONs) and in general magnetic nanoparticles (MNPs) have attracted great interest in the cancer therapy as nanocarriers. SPIONs can be multifunctionalized and manipulated by an external gradient magnetic field (GMF) and an alternating magnetic field (AMF), mediating targeting of different classes of biologically active molecules (chemotherapeutics, antibodies, nucleic acids) and hyperthermia, respectively. SPIONs can also be used not only to target cancer cells, but also the tumor microenvironment (TME), by modulating the activities of the infiltrating host 's cells residing there to restore an anti-tumor response. Indeed, tumor-associated macrophages (TAMs) are the major cell population in the TME and play a prominent role in favoring tumor progression, displaying an M2 phenotype. Macrophages are highly plastic cells, which can acquire different phenotypes according to the microenvironmental stimuli they receive, and can be polarized towards two extreme phenotypes, the classically-activated M1 pro-inflammatory one and the alternatively-activated M2 anti-inflammatory and pro-tumor one. TAMs display an irregular unfolded protein response (UPR) in their endoplasmic reticulum (ER) to endure the surrounding environment stress and ensure the pro-tumor activity. Recent studies have suggested that the protein kinase R (PKR)-like endoplasmic reticulum kinase (PERK) arm of the UPR is uniquely upregulated in TAMs to contribute to the metabolic adaptation necessary to support tumor growth; while other studies have shown that the arm inositol-Requiring Protein 1 (IRE-1) induces the macrophage polarization towards pro-inflammatory phenotype (M1) by activating the XBP1 protein. In this contest, the re-education of TAMs from the M2 immunosuppressive to the M1 tumoricidal phenotype by modulating UPR with nanotechnology represents an alternative and effective anti-cancer strategy.

Herein we showed that: i) magnetic nanoparticles (MNPs) provided by Laboratory of Microbiology of the Facultad de Ciencias, Universidad de Granada and shown to be fully cytocompatible (MTT assay, ROS production, ER-stress induction), with their intrinsic properties polarize primary macrophages isolated from peritoneal exudate (PEMs) toward the pro-inflammatory M1 phenotype (CD 86^+; CD 80^+); ii) PEMs can be polarized towards the M1 phenotype and the M2 phenotype (CD 206^+) by culturing them in the presence of LPS/IFN-γ and IL-4, respectively; iii) siRNA/PERK coupling to MNPs required the coating of MNPs with polydopamine (PDA); iv) PDA-MNPs/siPERK were internalized by PEMs and could inhibit the expression of PERK, as well as of other proteins of its pathway (ATF4, CHOP) and affect the activity of other components of the UPR response (XBP1s, ATF6) (q-RT-PCR and immunoblotting experiments); v) TAMs obtained by PEMs polarized toward M2 phenotype with IL-4, and treated with the ER-stressor tunicamycin to activate the UPR response could be to re-educated toward the M1 phenotype by treatment with PDA-MNPs/siPERK (expression of gene markers and activation of signaling pathways of the two phenotypes evaluated by q-RT-PCR and by immunoblotting, respectively); vi) finally, the phenotypic switch of TAMs-like macrophages to M1 phenotype after 3 days incubation with PDA-MNPs/siPERK was confirmed by cytofluorimetric analysis for CD206 and CD86, the specific markers of the M2 and of the M1 phenotype, respectively.

Taken together, the results of this study indicate that TAMs-like macrophages can switch from the M2 phenotype supporting tumor growth to the M1 inflammatory anti-tumor phenotype by the inhibition of ER-stress sensor PERK. These studies would be the basis for possible future *in vivo* translational applications for cancer therapies.

SOMMARIO

Le nanoparticelle di ossido di ferro superparamagnetiche (SPIONs), e in generale le nanoparticelle magnetiche (MNPs), hanno suscitato un grande interesse nella terapia del cancro come nanovettori. Gli SPIONs possono essere multifunzionalizzati ed essere manipolati esternamente da un campo magnetico a gradiente (GMF) e da un campo magnetico alternato (AMF), mediando rispettivamente il targeting di diverse classi di molecole biologicamente attive (chemioterapici, anticorpi, acidi nucleici) e l'ipertermia. Le SPIONs possono essere utilizzate non solo per attaccare le cellule tumorali, ma anche per indebolire il microambiente tumorale (TME) modulando le attività delle cellule infiltranti il TME così da ripristinare una risposta antitumorale. La principale popolazione cellulare del TME sono i macrofagi associati al tumore (TAMs), che svolgono un ruolo fondamentale nella progressione del tumore, e mostrano un fenotipo M2. I macrofagi, infatti, sono cellule caratterizzate da un'elevata plasticità, che tendono ad acquisire differenti fenotipi a seconda degli stimoli micro-ambientali che ricevono. In particolare, essi possono essere polarizzate verso due fenotipi estremi, quello pro-infiammatorio M1 attivato classicamente e quello antinfiammatorio e pro-tumorale M2 attivato alternativamente. I TAMs mostrano una risposta proteica irregolare (UPR) nel loro reticolo endoplasmatico (ER) in modo da contrastare lo stress dell'ambiente circostante e garantire l'attività pro-tumorale. Infatti, studi recenti suggeriscono che il braccio *protein kinase R (PKR)-like endoplasmic reticulum kinase* (PERK) della risposta UPR tende ad essere sovra-regolato nei TAMs così da contribuire all'adattamento metabolico necessario per sostenere la crescita del tumore; mentre da altri studi emerge che il braccio dell'UPR *inositol-Requiring Protein 1* (IRE-1) attivando il fattore di trascrizione XBP1 tende a favorire la polarizzazione dei macrofagi verso un fenotipo infiammatorio (M1). In questo contesto, la rieducazione dei TAMs dal fenotipo immunosoppressivo M2 al fenotipo tumoricida M1 modulando l'attività dell'UPR mediante l'uso della nanotecnologia rappresenta una strategia anticancro alternativa ed efficace.

Qui abbiamo mostrato che: i) le MNPs, fornite dal Laboratorio di Microbiologia della Facultad de Ciencias, 'Universidad de Granada, e dimostrate citocompatibili (saggio MTT, produzione ROS e induzione di ER-stress), con le loro proprietà intrinseche polarizzano i macrofagi primari isolati dall'essudato peritoneale (PEMs) verso il fenotipo pro-infiammatorio M1 (CD 86$^+$; CD 80$^+$); ii) i PEMs possono essere polarizzati verso il fenotipo M1 e il fenotipo M2 (CD 206$^+$) coltivandoli rispettivamente in presenza di LPS/IFN-γ e IL-4; iii) l'accoppiamento del siRNA/PERK alle MNPs richiede che queste ultime siano rivestite di polidopamina (PDA); iv) PDA-MNPs/siPERK vengono internalizzate dai PEMs e inibiscono l'espressione di PERK, così come di altre proteine della sua via di segnalazione (ATF4, CHOP) influenzando anche l'attività di altri componenti della risposta UPR (XBP1s, ATF6) (q-RT-PCR e immunoblotting); v) i TAMs, ottenuti da PEMs polarizzati verso il fenotipo M2 con IL-4 e trattati con l'induttore di ER-stress tunicamicina per attivare la risposta UPR, possono essere rieducati al fenotipo M1 mediante trattamento con PDA-MNPs/siPERK (espressione di geni markers insieme con l'attivazione delle vie di segnalazione dei due fenotipi valutate rispettivamente mediante q-RT-PCR e immunoblotting); vi) infine, lo *switch* fenotipico di macrofagi simili a TAMs al fenotipo M1 dopo 3 giorni di incubazione con PDA-MNPs/siPERK è stato confermato dall'analisi citofluorimetrica per CD206 e CD86, i marcatori specifici rispettivamente del fenotipo M2 e M1.

Nel loro insieme, i risultati di questo studio indicano che macrofagi simili a TAMs possono passare dal fenotipo M2 che sostiene la crescita del tumore al fenotipo M1 con attività antitumorale e pro-infiammatoria mediante l'inibizione del sensore di ER-stress PERK. Questi studi potrebbero porre la base per future applicazioni traslazionali per le terapie del cancro.

ACRONYMS

Ap, apatite
AMF, alternating magnetic field
ATF4, Activating Transcription Factor 4
ATF6α, Activating Transcription Factor 6α
BIP, binding Ig protein
CHOP,C/EBP homologous protein
DA, dopamine
DOXO, Doxorubicin
eif2-α, Eukaryotic translation initiation factor 2-α
EPR, enhanced permeation and retention
ER, endoplasmic reticulum
ERAD, ER-associated degradation
FITC, Fluorescein-5-isothiocyanate
GMF, gradient magnetic field
H_2O-DEPC, diethylpyrocarbonate - treated water
IFN-γ, Interferon-γ
IL-4, Interleukin-4
IRE1α, inositol requiring protein 1α
LPS, liposaccharide
MAPK1/2, mitogen-activated protein kinase 1/2
m-CSF, macrophage-colony stimulating factor
MDR, multi-drug resistance
MNP, magnetic nanoparticle
NP, nanoparticle
PDA, polydopamine
PE, phycoerythrin
PE-Cy7, phycoerythrin-Cyanine7
PEMs, peritoneal macrophages
PERK, protein kinase R (PKR)-like ER kinase
ROS, Reactive Oxygen Species
SPIONs, superparamagnetic iron oxide nanoparticles
TAMs, tumor associated macrophages
TME, tumor microenvironment
TRITC, Tetramethylrhodamine
UPR, unfolded protein response

CHAPTER I

Introduction and Scientific background

1.1. Cancer

1.1.a Cancer: The Modern Disease per Excellence

Cancer is a complex and heterogeneous disease in which various etiological factors, such as hereditary, environmental factors and lifestyle are involved (Hanahan and Weinberg, 2011).

Scientists have identified more than 250 different types of cancers and evidenced that molecular mechanisms at the basis of the pathogenesis and pathophysiology of these diseases are related with genetic and epigenetic changes and also to inflammation (Takeshima and Ushijima, 2019). In fact, tumorigenesis is caused by different genetic mutations, which inactivate so-called tumor suppressor genes and/or activate oncogenes promoting the progression of cancer. These genetic alterations can be frameshift mutations, missense mutations or nonsense mutations and their main gene targets are genes normally involved in the control of cell proliferation, genes that regulate programmed cell death (apoptosis) and/or genes involved in DNA repair (Hassanpour and Dehghani, 2017).

This genomic instability causes the dysregulation of various cell processes, such as uncontrolled cell growth, insensitivity to antigrowth factors, evasion of apoptosis, sustained angiogenesis and cell invasiveness, resulting in spreading to other organs (metastasis) (Bielenberg et al., 2015), chronic inflammation (Zhao et al., 2021) and, moreover, evasion from the patient's immune system (Chow et al., 2012). All these features are considered hallmarks of the oncologic diseases. Although genetic mutations have been the focus of cancer research for many years, it has been recognized that epigenetic changes, referring to heritable changes in gene expression occurring without alteration in the DNA sequence, contribute to the pathogenesis of cancer by altering gene expression. Furthermore, it is well-known that both genetics and epigenetics cooperate at all stages of cancer development (Hanahan, 2022).

Interestingly, chronic inflammation is also involved in cancer pathogenesis; in particular, inflammatory mediators act in an autocrine and/or paracrine manner on both malignant and non-malignant cells contributing peculiar properties to the so called tumor microenvironment (Labani-Motlagh et al., 2020). During the past decades several achievements have been made in in treating cancers, nevertheless nowadays cancer is still a serious health problem, since it is an important cause of morbidity and mortality worldwide (Siegel et al., 2020). In fact, the World Health Organization (WHO) has reported that 9.6 million people worldwide died from cancer in 2020, which still makes it the second leading cause of death in the world (Ahmad et al., 2022; Kocarnik et al., 2022). Hence, even after the epidemiology of COVID-19, cancer is still referred to as the "Pathology of the Century" or to "the quintessential product of modernity"; for this reason, the drug discovery in oncology is a constantly evolving field.

1.1.b Cancer Treatments

Currently, the main approaches used to treat tumors are still surgery, radiotherapy and chemotherapy even if innovative treatments, such as hyperthermia, phototherapy are under active development. Nevertheless, cancer research is trying to develop new therapeutic approaches, which aim to the personalized medicine or the correction of genetic aberrations responsible for neoplastic transformation using the genomic editing with the CRISPR/Cas9 technology (Falzone et al., 2018). Surgery is the "gold standard" in cancer treatment because it is associated with high levels of success in terms of remission and cure, as it attempts to excise 100% of the malignant cells. However, this is highly dependent on the type of cancer, location, and stage of the cancer development. Surgery is very common in the treatment of breast cancer (partial or full mastectomies), ovarian cancer, some

intestinal cancers, and lung cancers (pneumonectomy, lobectomy). In any case, this approach may be associated with other co-morbidities, psychological problems and poor quality of life for patients. Molecular radiotherapy is a well- known therapeutic approach used in clinical practice since many decades, based on the use of radioactive compounds (radiopharmaceuticals), which with their ionizing radiation cause DNA damage in malignant cells. Generally, radiopharmaceuticals are administered by ingestion or injection and their action is expressed toward the target cells recognized by specific carrier or depends on the radioisotope properties.

Radiotherapy is often given as an adjuvant to chemotherapy to treat approximately 60% of all cancers, or after surgery to eliminate any remaining malignant cells (Urruticoechea et al., 2010). Chemotherapy is the standard cancer therapy, which can be carried out alone or in combination with radiotherapy and surgery. In last case before surgery the chemotherapy is used to shrink the tumor size or after it to prevent metastasis diffusion. The classical/conventional chemotherapy includes drugs with high cytotoxic activity and they can be classified according to their mechanism of action in alkylating agents, antimetabolites, antibiotics, natural products and microtubule inhibitors. Due to their lack of specify for tumor cells, these drugs can also interact with healthy tissues causing severe side effects. In particular, the non-selective action of anticancer drugs results in substantial toxicity to many normal rapidly dividing cells (e.g. bone marrow cells, hair follicles and epithelial cells in general) (Malam et al., 2009; Sanna et al., 2014). Therefore, these chemotherapeutic agents are administered at the maximum tolerated dose (MTD), which may not eradicate completely tumors and at the same time causes a severe morbidity of the patient. Besides to the immediate side effects, traditional chemotherapeutics can also damage permanent cells such as cardiac cells, kidneys and brain causing a chronic toxicity. Moreover, chemotherapy is associated with the frequent complication called multi-drug resistance (MDR) that is developed upon the treatment of the cancer, so that tumor cells can evade the therapy. In the evolution of cancer therapies, a major impulse has arrived from the advances in the field of molecular biology and immunology, which resulted in the development of new cancer drugs, which started the era of precision medicine applied to cancer. These are monoclonal antibodies and small molecules, which target specific mutations responsible for the oncogenic behavior of tumor cells, such as tyrosine kinase inhibitors (Zeng et al, 2021; Unnisa et al., 2022). Finally starting from the 2010 immune checkpoint inhibitors, monoclonal antibodies which act by enhancing immune system response by blocking suppressive signals through the PD-1/PD-L1 and CTLA-4 pathways are been used (Le Saux et al., 2021) (Fig. 1.1).
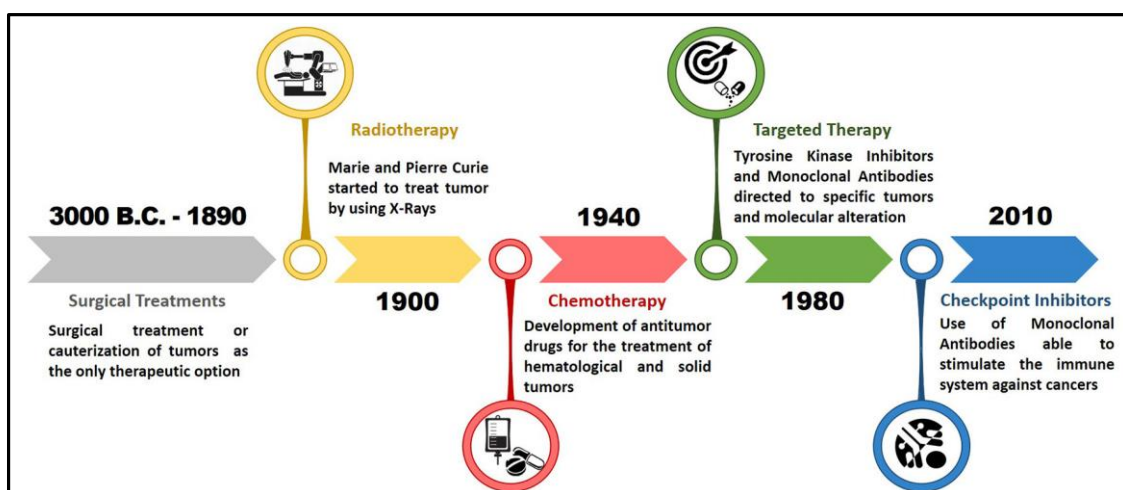
Figure 1.1. Timeline of epochal turning point in modern oncology. After the development of radiotherapy in the early 1900, the modern oncology began with the discovery of the first chemotherapeutic drugs around 1940. Then a breakthrough occurred with the development of targeted therapy in 1980, which determined an improvement in the effectiveness of cancer treatments, and finally, the latest advance took place in 2010 with the introduction of immune checkpoints inhibitors for the treatment of advanced and metastatic tumors (from Falzone et al., 2018).

1.1.c Drug classes in the cancer therapy

Nowadays, treatments based on single chemotherapeutic drugs generally face lack effectiveness in cancer therapy, whereas new therapeutic approaches (see Fig. 1.2) or the combination of more therapeutic methods involving different mechanisms of action are needed to achieve higher effectiveness (Van der Meel et al., 2019).

Figure 1.2. Anticancer drug classes from standard chemotherapeutics to small molecules. Here reported a typical chemotherapeutic, nucleic acids, small molecules, such as tyrosine kinase inhibitors, and monoclonal a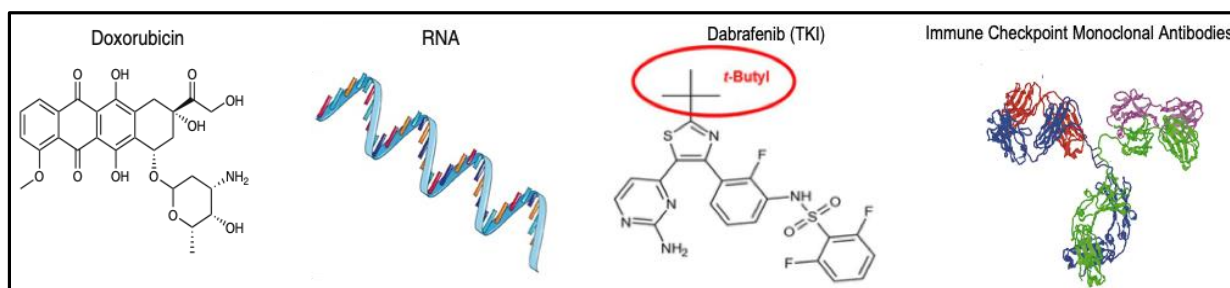ntibodies. While Doxorubicin is an effective traditional chemotherapeutic drug with important side effects, the other three types of molecules represent novel approaches in the so called personalized medicine. These molecules can also be administered in combination and loaded on nanoparticles (nanomedicine) (modified from Van der Meel et al., 2019).

Doxorubicin: a traditional chemotherapeutic drug

Doxorubicin belongs to the anthracycline family, a big group of anti-proliferative antibiotics; it was first extracted from Streptomyces peucetius var. caesius in the 1970'. The anthracycline Doxorubicin (DOXO) is one of the most effective chemotherapeutics used for treatment of solid tumors, such as hepatoma, sarcomas, osteosarcomas, lymphomas and adenocarcinomas of the stomach and of the breast. DOXO acts on target cells with different mechanisms (Xiao et al., 2019). Its interaction with cells begins with passive diffusion through the cell membrane; within the cells, it generates reactive oxygen species (ROS), causing free radical formation and oxidative stress. It can enter the mitochondria, causing DNA damage and energetic stress, by activating the caspase cascade, leading to cell death by apoptosis and triggering autophagy as a consequence of cell energy depletion. Finally, it can translocate into the nucleus, where it intercalates between double-stranded DNA helices and inhibits the enzymes topoisomerases I and II, provoking lethal changes in chromatin structure and the generation of free radicals which, when combined with iron ions, induce oxidative damage to cellular membranes, DNA, and proteins (Aubel-Sadron et al., 1984). However, DOXO treatments can induce severe cardiotoxicity due to DOXO accumulation in cardiac tissue (Elliott, 2006), which then imposes a narrow therapeutic dose, thus limiting DOXO effectiveness (Thorn et al., 2012). DOXO efficiency is also compromised by the generation of resistance in cancer cells and by the reduction of drug activity due to physicochemical or physiological conditions in the tumor microenvironment, e.g., hypoxia, acidity, defective vasculature, and the presence of lymphatic vessels.

Small interfering RNAs (siRNAs) in cancer therapy

Recently, much attention has been paid to therapeutic approaches based on gene functionality, such as the potential application of RNA interference (RNAi) for cancer treatment (Tatiparti et al., 2017). RNAi is a natural defense mechanism against the invasion of exogenous genes, and it was discovered in the nematode Caenorhabditis elegans in 1998 (Fire et al., 1998). RNAi is an endogenous post-transcriptional regulation process that consists of small regulatory RNAs including microRNAs

(miRNAs) and small interfering RNAs (siRNAs) which are able to silence target messenger RNAs (mRNAs) in a sequence-specific way. RNAi mechanism is triggered initially by the enzyme Dicer which cleaves double-stranded RNAs (dsRNAs) into short double-stranded siRNAs of 21–25 nt. A siRNA molecule is composed by a siRNA passenger strand, which is then unwound, and by a siRNA guide strand. This latter is loaded into the RNA-induced silencing (RISC) complex, leading to cleavage of the target mRNAs by Argonaute 2 (Ago2) when the guide strand sequence is paired with an mRNA complementary sequence causing the downregulation of this target protein (Fig.1.3).
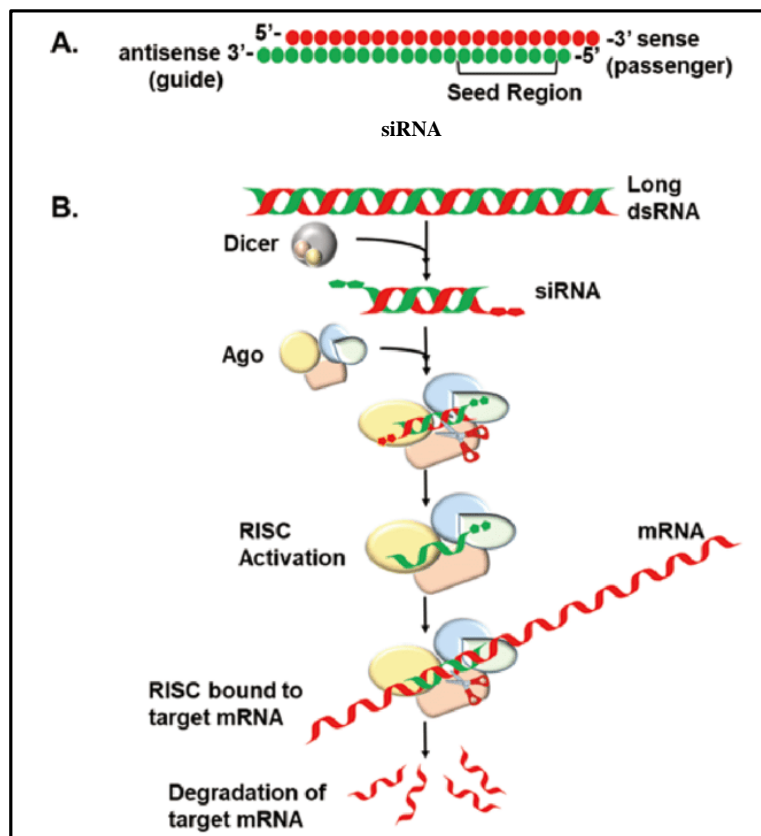

Figure 1.3. (**A**) **Structure and (B) siRNA pathway.** Long double-stranded RNA (dsRNA) is processed by Dicer to form a small interfering RNA (siRNA), which associates with RNA-induced silencing protein complex (RISC) and mediates target sequence specificity for subsequent mRNA cleavage (from Tatiparti et al., 2017).

Once that siRNA activity was demonstrated also in mammalian cells, this important mechanism has been exploited for novel therapeutic approaches for different diseases including cancer, by designing oligonucleotide molecules specific for the mRNA and its corresponding protein to be downregulated (Hu et al., 2020; Fakhr et al., 2016). The first siRNA-based drug, ONPATTRO™, targeting liver transthyretin amyloidosis, was approved by the U.S. Food and Drug Administration (FDA) in the 2018 and many siRNA drugs have then been proposed in different clinical trials (Ledford et al., 2018). The application of siRNA technology in therapy still faces multiple obstacles regarding efficient delivery and effectiveness; in fact, siRNAs are a class of double-stranded RNAs with high hydrophilicity and numerous negative charges. These features make them membrane impermeable and highly unstable in biological systems besides conferring them immunogenicity (Rutz and Scheffold, 2004). Therefore, the use of siRNA technology as novel therapeutic approach for different diseases requires that siRNA molecules are subjected to chemical modification or co-formulated with lipids, polymers, or nanoparticles to shield the negative charges in order to facilitate their transport across cell membranes and also, to protect them from enzymatic degradation. In this scenario,

nanomedicine has a crucial role allowing to overcome all these challenges (Mahmoodi Chalbatani et al., 2019).

1.2. Nanomedicine in cancer therapy

1.2.a What is the nanomedicine?

Nanomedicine can be defined as the medical applications of nanotechnology (Ouyang et al., 2022). To date, the International Organization for Standardization (ISO) defines all nanomaterials as materials with dimensions in the nanoscale (1–200 nm), whose behavior can be described with neither classical physics nor quantum mechanics (Soetaert et al., 2020). In fact, at dimensions substantially greater than 100 nm, classical physics adequately describes most material properties; whereas quantum mechanical properties dominate at dimensions smaller than 1 nm (Rahman et al., 2022). Nanomaterials are characterized by a high surface area- to-volume ratio with properties that are significantly influenced by both classical and quantum effects. Consequently, these materials have unique chemical, physical, and biological properties unlike their bulk (large dimensions) or atomic/molecular counterparts. These unique properties can be exploited for novel applications ranging from the materials science to biomedicine, including oncology (Pelaz et al., 2017). In this scenario, nanomedicine which comprises chemistry, physics and biology, offers many advantages providing smart nanoplatforms, which are able to move within biological membranes by carrying and delivering the drug into specific tissues and cells (Van der Meel et al., 2019). Nanomaterials with a diameter range from 10 up to 200 nm are generally considered suitable for cancer therapy; in fact, thanks to their nanometric size they can escape the capture from cells of the reticuloendothelial system (RES) and thus they can circulate within the blood stream for longer periods of time. In contrast, smaller particles can easily leak from the normal vasculature (less than 1–2 nm) to damage normal cells and can be easily filtered by kidneys (less than 10 nm in diameter) (Venturoli and Rippe, 2005), while particles larger than 200 nm are cleared from circulation by phagocytes. Moreover, thanks to their surface characteristics these nanomaterials can be functionalized with a large number of cancer drugs, such as traditional chemotherapeutics, but also monoclonal antibodies (Sarup et al., 1991; Iafisco et al., 2013; Le Saux et al., 2021), small molecules (Zeng et al. 2021; Unnisa et al., 2022) and nucleic acids (Zhou et al., 2020) or diagnostic agents resulting in a theranostic effect.

Thus, nanomaterial based platforms are very efficient drug delivery systems, which, by increasing the half-life of chemotherapeutics, can reduce the amount of administered drugs and, at the same time, can reduce their systemic toxicity (Wolfram and Ferrari, 2019) Furthermore, they can allow minimally invasive therapies minimizing side effects (Ouyang et al., 2022). Although there are several difficulties for such nanoformulations to advance in the clinical development and to satisfy all stages of regulatory processes, the application of nanotechnology in cancer therapy represents an evolution of the "magic bullet" concept and can reasonably constitute a suitable platform to develop a next generation of programmable and personalized nanomedicine to be used in clinical practice (Sanna and Sechi, 2020).

1.2.b Nanoparticles

Nanoparticles (NPs) are key actors of the nanomedicine, and currently, a large variety of nanoparticle types exist both for therapeutic and diagnostic applications. These synthetic structures can be generally divided into two categories: organic, such as liposomes, polymeric micelles or inorganic NPs (iron oxide NPs, calcium phosphate NPs) (Jurj et al., 2017).
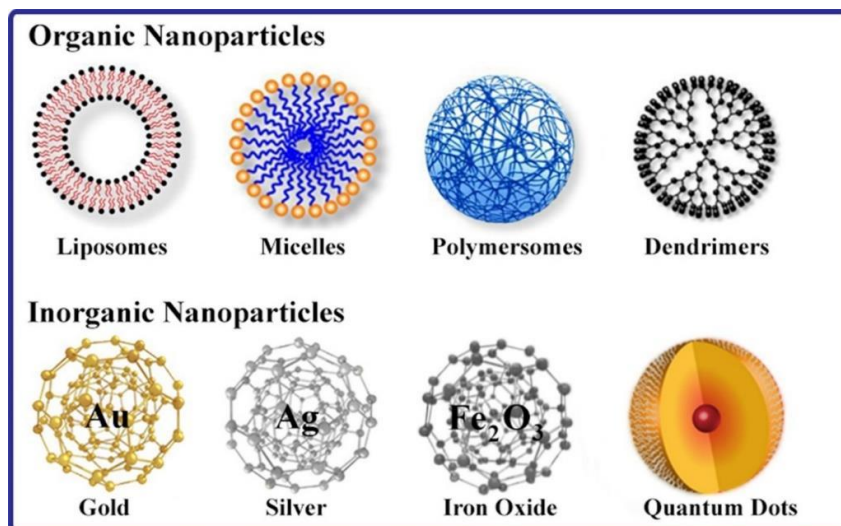
Figure 1.4. Scheme showing the different types of nanoparticles used in drug delivery for the treatment of the various types of cancers (from Itani et al., 2019)

First nano-scale particles approved as drug-carriers for clinical application were organic NPs, such as liposomes, which consist of an outer lipid layer and a core entrapping hydrophobic and hydrophilic drugs (Itani et al., 2019). In fact, organic NPs have been more successful compared to inorganic NPs in their translation into the clinic, since they are characterized by high biocompatibility reducing long-term side effects. They are mainly being developed for applications like vaccination, long-lasting depot delivery systems, hemostasis, and topical agents for systemic delivery through the skin (Izci et al., 2021). Translation of inorganic NPs into the clinic has been more limited, despite major successes on a preclinical level due to their lower biocompatibility and lack of knowledge and consensus pertaining to their safety and long-term deposition in different organs such as the liver and spleen (Sousa De Almeida et al., 2021). Nevertheless, inorganic NPs also have many advantages, such as a high surface area to volume ratio, a wide and easily modified surface conjugation chemistry and easy preparation. Herein I will briefly report on two types of inorganic nanoparticles: nanocrystalline apatite (Ap), on which I have published two papers reported in appendix and superparamagnetic iron oxide nanoparticles (SPIONs), which have been topic of my PhD thesis project, but also of another published work I have contributed during this PhD period.

Crystalline apatite nanoparticles (Ap NPs)

Apatite (Ap) NPs, which consist of calcium phosphate and closely mimic bone apatite nanocrystals both from chemical and structural points of view (Gómez-Morales et al.,2013) are particularly suited for therapeutic and diagnostic applications, especially in bone pathologies. They present the following advantageous properties: high biocompatibility, good biodegradability, high loading capacity with the ability to bind moieties through both surface calcium and phosphate groups by isothermal adsorption. Moreover, because of their good stability at physiological pH with partial solubility at acidic pH they behave as smart complexes sensitive to local stimuli, e.g., binding drugs at physiological pH and releasing them at acidic pH (Haque et al., 2020), as the one found in inflamed or tumor tissues (Iafisco et al., 2013; Gómez-Morales et al., 2021). Ap NPs have already been shown to be valuable nanocarriers for different types of molecules, including nucleic acids, proteins, antibiotics, chemotherapeutics, fluorophores, and luminescent moieties (Munir et al., 2021). Indeed, more recently they have been doped with lantanides such as Tb^{3+} to prepare luminescent apatite-based nanomaterials for drug release and bioimaging applications (Gómez-Morales et al., 2021). Moreover, Tb^{3+}-doped citrate-coated Ap were functionalized with the non-steroidal anti-inflammatory drug

sodium diclofenac (Cano Plá et al., 2022). The maximum adsorbed amounts at 37 °C were higher than at 25 °C, and particularly when using the Tb^{3+}-doped particles. Diclofenac-release efficiencies were higher at pH 5.2, a condition simulating a local inflammation. The luminescence properties of diclofenac-loaded Tb^{3+}-doped particles were affected by pH, being the relative luminescence intensity higher at pH 5.2 and the luminescence lifetime higher at pH 7.4, but not influenced either by the temperature or by the diclofenac-loaded amount. Both undoped and Tb^{3+}-doped nanoparticles were cytocompatible. In addition, diclofenac release increased COX-2 expression and decreased PGE_2 production in an in vitro inflammation model. These findings evidence the potential of these nanoparticles for osteo-localized delivery of anti-inflammatory drugs and the possibility to localize the inflammation, characterized by a decrease in pH, by changes in luminescence.

Superparamagnetic iron oxide nanoparticles (SPIONs)

Besides the general properties of NPs, superparamagnetic iron oxide nanoparticles (SPIONs) have generated important prospects in nanomedicine, because of their fascinating physicochemical and magnetic properties (Mulens-Arias et al., 2020). Magnetic iron oxides, e.g. magnetite (Fe_3O_4) and maghemite (γ-Fe_2O_3) are the most common SPIONs used for biomedical applications. They have an inverse spinel crystalline structure with sub-lattices containing Fe having tetrahedral and octahedral coordination with oxygen, respectively (Soetaert et al., 2020). Magnetism arises from quantum mechanical interactions among orbital and spin motions of electrons in atoms; in the case of iron oxide nanoparticles there are the unpaired 3d electrons in Fe^{3+} and Fe^{2+} cations, from which the magnetic moments of the NPs derive. In particular, they inherently possess a nonzero net magnetic moment in the absence of a magnetic field. In these conditions, SPIONs display only weak reciprocal attractive magnetic interactions that keep them well dispersed, avoiding aggregation due to the magnetic dipole particle interaction (Tong et al., 2019). Due to their nanosizes SPIONs behave as a single magnetic domain, so when an external field is applied they rapidly rotate to align their magnetic moments promoting a net magnetization, which allows to control movement of these nanocarriers by external stimuli (Oltolina et al., 2020). Thanks to their supermagnetism effects, iron oxide nanoparticles can be also hyperthermic agents. Hyperthermia is a cancer therapy having the objective to raise the local tumor temperature (42 - 46°C) either to kill cancer cells, which are more sensitive to heat than normal healthy cells or to sensitize them to other treatments (Torres et al., 2019). When SPIONs are subjected to an efficient alternating magnetic field (AMF), they can develop magnetic energy, which is then translated into heat. This behavior is governed by Neel and Brown's relaxation. Heat is a pleiotropic damaging agent, so hyperthermia can inhibit or abrogate DNA damage repair, initiate apoptosis or other programmed cell death, or cause severe disruption of cell membranes leading to cell lysis (ZibaHedayatnasab et al., 2017; Zhu et al., 2017). SPIONs can be also used for diagnostic purposes, for example as targeted so as to allow diagnosis of cancer diseases in their early stages (Dadfar et al., 2019). As for all NPs, SPIONs can be functionalized with several chemotherapeutics and radiotherapeutics allowing drug delivery approaches exploiting both the passive and active targeting. Increasing applications of SPIONs have also been found in the areas of gene delivery and delivery of peptides and antibodies to their site of action. Therefore, SPIONs are multifunctional platforms, thus allowing multimodal therapy (Defu et al., 2020). As opposed to other magnetic nanoparticles (MNPs), such as nickel, cobalt, SPIONs are characterized by low toxicity in humans due to their involvement in iron metabolism. Indeed, FDA-approved applications of iron oxide nanoparticles not only include the cancer therapy, but also the iron deficiency anemia. Recent preclinical and clinical evidence showed that iron oxide NPs have the potential to activate anti-tumor immune processes. The mechanism(s) of this anti-tumor immune stimulation are unknown and complex; however, early indications suggest that phagocyte ingestion of iron oxide nanoparticles may stimulate 'pro-inflammatory' cell phenotypes, similarly to infection by pathogens that reverse cancer-induced immune suppression (Soetaert et al., 2020). For all these features SPIONs is opening up broad horizons in the current cancer research. In the same way, it is possible to exploit physical-

chemical aspects, as magnetic properties of some chemical elements (iron, nickel, cobalt) to engineer smart nanosystems (Fig.1.5).
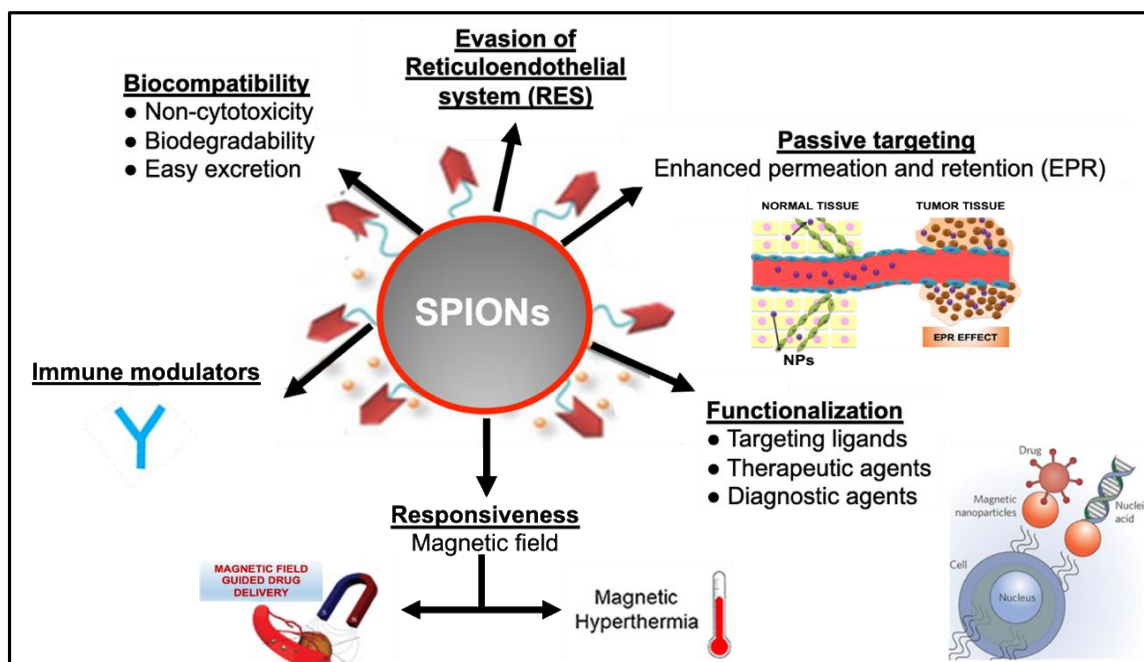

Figure 1.5. SPIONs as nanoparticle platform for multimodal tumor therapy. SPIONs can be functionalized with various cargos such as cytotoxic agents for chemotherapy, diagnostic agent, nuclei acid for gene therapy and/or immune modulators for immunotherapy. The application of gradient magnetic field can guide them to tumor site., while in alternating magnetic fields magnetic hyperthermia can be induced to increase treatment efficacy.

In this perspective, it is important to combine all the desired properties into one single nanosystem, thus appropriate modifications of the surface of NPs are often required in order to endow the nanoplatform with specific features, such as biocompatibility, various functionalization, colloidal stability. In recent years, the innovative discovery of a versatile biomaterial for surface modification, such as polydopamine (PDA), has attracted great attentions for the surface functionalization of nanoparticles (Wang et al., 2018).

Nanoparticles coated by polydopamine (PDA)

PDA was first reported in the pioneering work by Lee et al. in 2007, where these researchers identified that the adhesive versatility of proteins secreted by mussels is due to a derivative of dopamine (DA) called polydopamine (PDA). They carried out the polymerization of this catecholamine by means of stirring dopamine hydrochloride in a Tris-HCl buffer saline solution under alkali condition. Then, they showed that DA was able to polymerize and attach to almost all material surfaces (Fig.1.6), including metals, ceramics, semiconductors, and synthetic polymers via both covalent and noncovalent bonds. Numerous researchers have thus been pursuing the fabrication of multifunctional PDA-modified nanoparticles for different biomedical applications during the past decade; nevertheless, the specific synthetic mechanism of PDA polymerization still remains unclear (Jin et al., 2020). Intriguingly, the surface functionalization of nanoparticle with PDA offers many advantages: primarily, the chemical synthesis of PDA is simple and mild with no need for organic solvent owing to its unique adhesion property. In addition, via altering the essential parameters such as pH, temperature, concentration of DA, oxidants and reaction time, the PDA coating is highly

controllable in term of particle size, film thickness and so on. Secondly, the drug loading ability of the nanoparticles can be significantly improved by PDA coating because of its richness of catechol/quinone moieties, which offers the potential to anchor functional molecules onto the nanoparticles by physical (π-π stacking or hydrogen bond) or chemical bonding (Michael addition or Schiff base reactions). Lastly, the intriguing properties of PDA coating provide the nanoparticles with increased hydrophilicity, excellent biocompatibility, appropriate biodegradability, strong photothermal conversion capacity and Reactive Oxygen Species (ROS) scavenging properties. As a result, PDA modification enhances multifunctionality of NPs including targeting, imaging, photodynamic therapy (PDT) and also the tissue regeneration ability. Therefore, PDA-modified nanocarriers have aroused great interests in cancer therapy, antibacterial application, theranostic, tissue repair and so on (Gu et al., 2015).
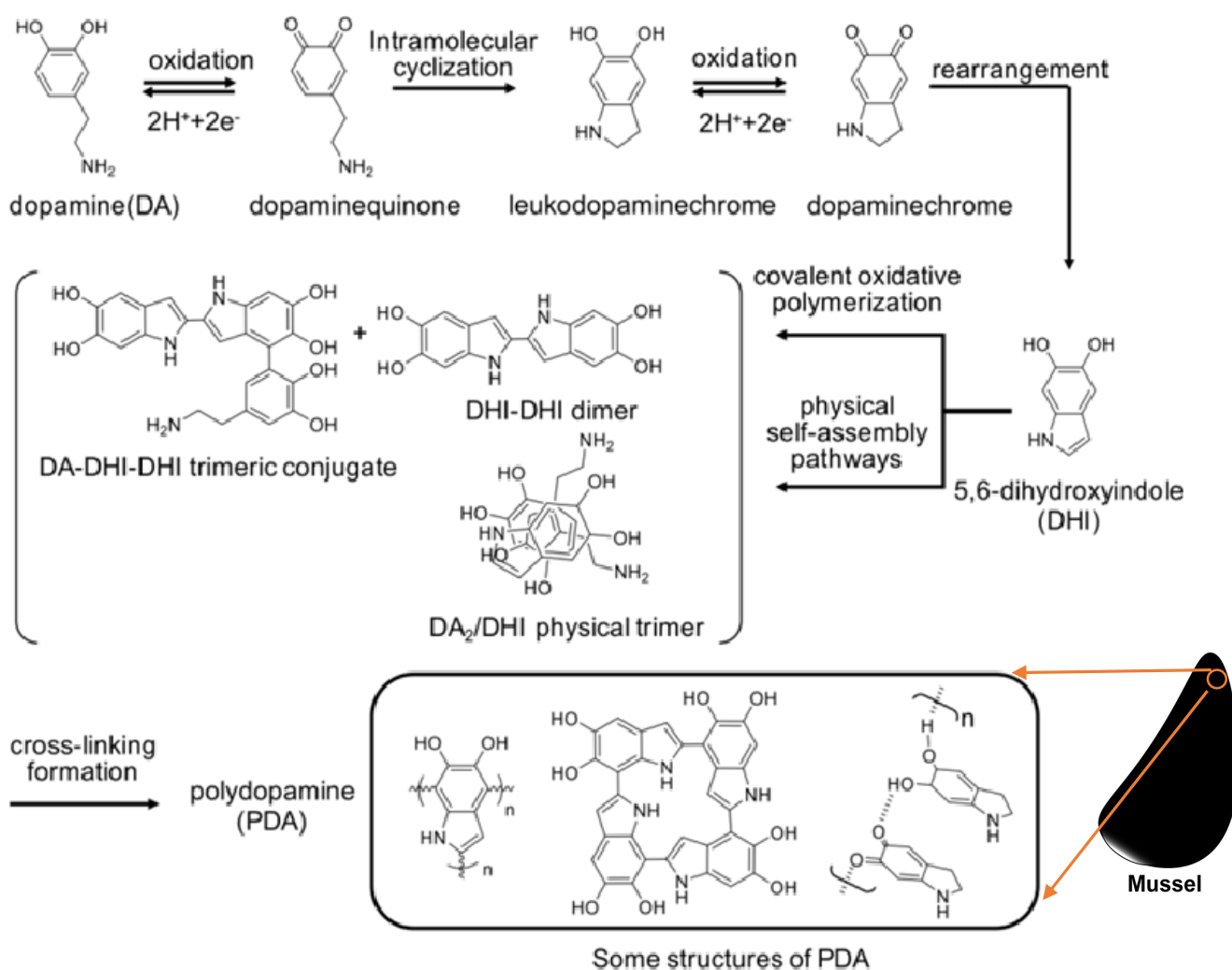

Figure 1.6. Various proposed reaction mechanisms and structures for PDA (Kohri et al., 2016).

1.2.c Mechanisms of Targeting

To successfully achieve targeted delivery of drugs to tumor site, an effective cancer therapy requires a consistent knowledge of the role of various physiological barriers and their patho-physiological state, along with the understanding the targeting strategies (Yao et al., 2020)., which can be broadly divided into two categories, passive and active targeting (Fig.1.7).

Passive targeting

In passive targeting mechanisms, the drugs are delivered to the target site exploiting the different anatomic-physiological properties of tumor, inflamed and normal tissues. In fact, the high proliferation of cancer cells induces neovascularization with the formation of leaky, and poorly differentiated blood vessels with enhanced vascular permeability to ensure sufficient supply of nutrients and oxygen to tumor tissues for rapid proliferation. This phenomenon is well-known as enhanced permeation and retention (EPR) effect, which was first reported by Matsumura and Maeda (Maeda et al., 2013). Hence, the passive targeted delivery refers to NPs circulating in the bloodstream that enter via passive diffusion the interstitial fluid through an abnormal vascular wall characterized by pores large up to about 400 nm and their accumulation in neoplastic tissues. In addition to the EPR effect, other biological effects can promote the passive targeted delivery of drugs to tumor cells. For example, the poor lymphatic drainage associated with cancer supports the retention of NPs in tumor site increasing the possibility that nanocarriers release their contents to tumor cells. The tumor microenvironment also affects the passive mechanisms of targeting carried on by nanomedicines. An evident example is the glycolysis, the main source of energy for cancer cell proliferation, which yields an acidic environment and reduces the pH of the tumor microenvironment allowing the activation of pH-sensitive NPs and consequently the release of drugs within the vicinity of cancer cells (Lim et al., 2018). However, there are some limitations of the passive targeting. Interestingly, the EPR effect is a very heterogeneous phenomenon, varying dramatically from tumor to tumor and from patient to patient (Jain and Stylianopoulos, 2010). Moreover, the abnormal structure of tumor blood vessels can cause an uneven distribution of NPs, which often accumulate at the edge of the tumor, resulting in limited anticancer activity of nanocarriers.

Active targeting

Starting from the Paul Ehrlich's concept of "magic bullet" proposed in the early 20th century (Schwartz, 2004), the targeted drug delivery in cancer research has emerged as an effective strategy to enhance selectivity of the anticancer agents for tumor cells allowing to overcome problems of conventional therapies (Sanna and Sechi, 2020). Next to the passive targeting mechanisms based on the use of patho-physiological properties of the tumor site, different active targeting strategies were developed, which are still under intensive investigation for their optimization. The first category of active strategies is the use of ligand-loaded nanosystems. In this strategy, the surface of NPs contains ligands or antibodies that recognize specific biomarkers, which are overexpressed on the surface of cancer cells. Accordingly, these interactions allow to NPs to discriminate tumor cells from healthy cells and to successfully release the carried therapeutic drugs to tumors. Biomarkers on targeted cells can be tumor -specific antigens or receptors for growth factors, such as transferrin receptor, folate receptor, and the epidermal growth factor receptor (EGFR), the hepatocyte growth factor receptor (HGFR) glycoproteins, which promote the internalization of NPs. The second category comprise stimulus-response systems. These use specific stimulus signals to promote the directional delivery of NPs to tumors and to boost the anticancer activities of NP-carried drugs. The signals can be tumor intrinsic, such as an increased glutamine level (Iyer et., 2020) and hypoxia (Zhou et al., 2021), or tumor extrinsic, such as a light source (Shakeri-Zadeh et al., 2021), a magnetic field (Oltolina et al, 2020), or ultrasound (Paproski et al.,2016).

The third method involves biological systems for targeted delivery, as NPs loaded in cell membranes (Zhen et al.,2019), extracellular vesicle, or even in live cells. In this latest case, research mainly focuses on immune cells, for example a series of studies have demonstrated that macrophages can be exploited as cell carriers to actively transport NPs into tumor cells (Li et al., 2019). All these active targeting strategies play a significant role in overcoming drug resistance.
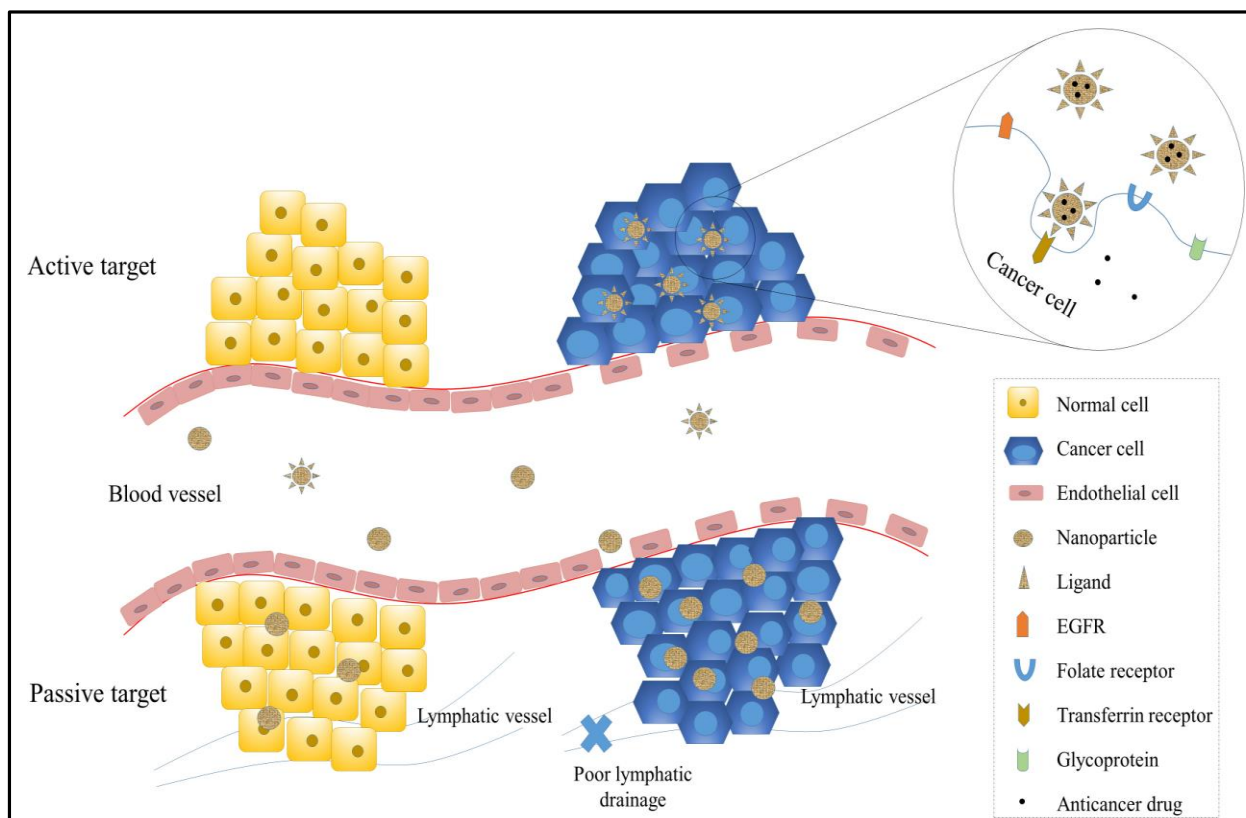

Figure 1.7. Passive and active targeting of NPs to cancer cells. Targeting of NPs enhance therapeutic efficiency and reduce systemic toxicity. Passive targeting of NPs is mainly achieved by the enhanced permeability and retention (EPR) effect, which exploits the increased vascular permeability and weakened lymphatic drainage of cancer cells and enable NPs to target cancer cells. Active targeting is achieved by the interaction between ligands and receptors. The receptors on cancer cells include, for example, transferrin receptors, folate receptors, glycoprotein (such as lectin), and epidermal growth factor receptor (EGFR) (from Yao et al., 2020).

Indeed, multi-drug resistance is problem frequently encountered in traditional chemotherapeutic treatments of cancer, resulting in a failure of the cancer therapy and thus poor prognosis. One of more common mechanisms of tumor drug resistance is the presence of efflux transporters, such as the family of the ABC transporters, which reduce intercellular drug concentration by pumping the drug out of the cell. Many studies have demonstrated that some chemotherapeutics-loaded NPs can bypass the exposure of anti-tumor drugs to efflux transporters, since NPs largely enter the cell through endocytosis instead of diffusion and release the drug at a perinuclear site within the cell, away from cell membranes and efflux pumps (Murakami et al., 2011). Combination therapy is another strategy to treat drug-resistant cancers. To this end, the assembling of multiple therapeutic agents within a single drug nanocarrier can fight drug resistance and improve the therapeutic effect of cancer therapy.

1.3. Nanomedicine and cancer immunotherapy

Nanomedicine in cancer therapy does not only enhance the conventional chemotherapies, but it has also become a hotspot for immunotherapy. Cancer immunotherapy is a promising therapeutic strategy, which has attracted extensive attention in the last decades, because it aims to awaken the patients' innate or adaptive immune systems to combat tumors. In fact, it is well-known that cancer cells are able to silence the host's immune system in order to escape the body's immune surveillance and to induce tumor progression. For this reason, several approaches were developed to stimulate the host's antitumor immune response removing the cancer immunosuppression (Le Saux et al., 2021). Despite excellent therapeutic outcome in some hematological and solid cancers, the regular clinical use of cancer immunotherapies reveals major limitations, such as off target effects, autoimmunity and nonspecific inflammation. Nevertheless, the application of nanotechnology can overcome some of the challenges that currently limit cancer immunotherapy (Irvine and Dane, 2020). In particular, nanomedicine with its targeting mechanisms enhances the efficacy of immunotherapies allowing to deliver immunotherapeutic drugs in target sites of the human body ensuring the high specificity. In addition, nanoparticles, being multiplatform, are able to deliver to tumor cells different molecules facilitating both the combination therapy and theranostic effects. Strikingly, nanoparticles can also serve as immune modulators by mimicking or enhancing immune cell functions (Gandhapudi et al., 2019). This nanoparticle-mediated immune modulation can be employed along with immunotherapies as part of multifaceted, combinatorial treatment strategies. Given the advances in nanotechnology and the clinical success of cancer immunotherapy, the convergence of these two disciplines is surely generating substantial momentum for improving cancer treatment (Bockamp et al., 2020).

1.3.a Tumor Microenvironment (TME): The Main Player that Shapes the Immune Response

At the beginning, targets of cancer immunotherapies were cancer cells themselves or cancer stem cells without focusing on tumor microenvironment (TME), which is one of the major obstacles limiting the therapeutic effectiveness. TME is a complex tissue environment (Fig.1.8), which plays a critical role in protecting the tumor cells from body repair mechanism and promoting tumor progression, invasion and metastasis (Kashfi et al., 2021). Cancer cells in the TME are a minority, while the noncancer components account for the majority. These are tumor-associated macrophages (TAMs), stromal cells, tumor-associated fibroblasts (CAFs), bone marrow-derived inhibitory cells (MDSCs), extracellular matrix, blood and lymphatic vessel, and other infiltrating immune cells (Cassim and Pouyssegur, 2020). All the above non-tumorigenic cells mentioned are co-opted in the TME and educated to promote the tumor growth by secreting soluble factors including chemokines and cytokines as well as growth factors. For this reason, cancer research is significantly focusing on the understanding of TME in order to give new therapeutic strategies to enhance the antitumor immunity and avoid the drug resistance of conventional therapies. Currently, several strategies were proposed to manipulate and enhance anti-tumor responses in TME, including the following: (1) The use of immune checkpoint inhibitors; (2) Targeting regulatory cells in TME, such as TAMs and MDSCs; (3) Modifying the chemokine and the cytokine profile of TME, because they heavily influence the cellular composition of tumors; (4) Modulating toll-like receptors (TLRs), since TLR agonists can trigger rapidly both the innate and the adaptive immunity; (5) The use of virus-like particles (VLPs) as immune modulator of TME (Jin et al., 2020).
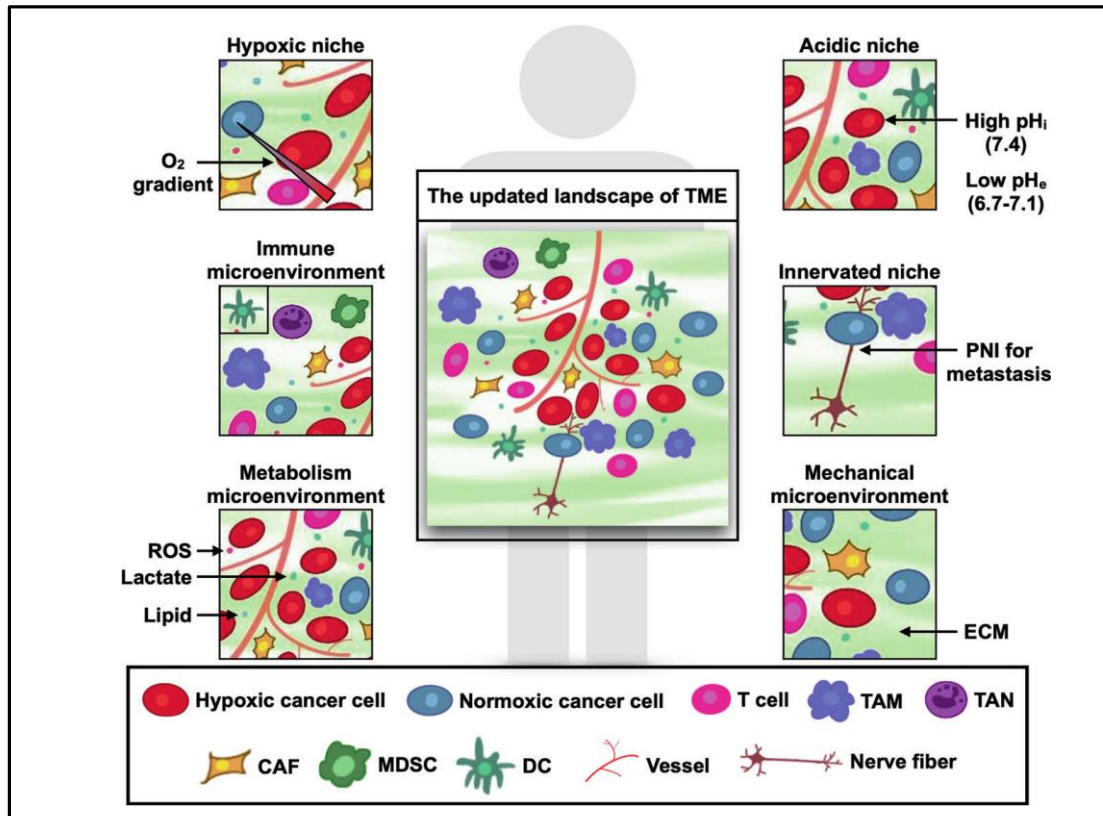
Figure 1.8. The updated landscape of tumor microenvironment (TME). TME comprises cancer cells, stromal cells, blood vessels, nerve fibers, extracellular matrix and associated acellular components. TME is home for cancer cells and serves as a bridge connecting cancer with the whole organism. TME can be classified into six specialized microenvironments, namely, hypoxic niche, immune microenvironment, metabolism microenvironment, acidic niche, innervated niche, and mechanical microenvironment (from Jin et al., 2020).

Although the precise composition of the TME varies in an organ-dependent manner and it also depends on the nature of tumor, the most numerous cells in TME are always TAMs, so they are attractive targets for cancer immunotherapy (Lin et al., 2021).

1.3.b Tumor-associated macrophages (TAMs)

TAMs are vital elements of the TME (Ke Li et al., 2020), since they are the main tumor infiltrating immune cells, which account about 50% of tumor mass and they are present in all stages of tumor development, where they provide a beneficial effect on the tumor progression, angiogenesis, invasiveness and immunosuppression; moreover, they are also involved in chemoresistance (Ruffell et al., 2015). As a matter of fact, high levels of TAMs are often associated with a poor clinical prognosis in different types of cancer (Lin et al., 2021). For this reason, TAMs have attracted more and more attention in cancer immunotherapy over the years. At the beginning, the targeted elimination of TAMs has represented an interesting strategy for new anticancer drug development, but the TAMs depletion has brought no clinical benefits causing a quick tumor growth once the therapy was finished (Kowal et al., 2019; van Dalen et al., 2019). On the contrary, the re-education of TAMs in the tumor microenvironment is becoming a promising immunotherapeutic approach to trigger antitumor immune response and eliminate tumor immune escape (Kowal et al., 2019; Xu et al., 2020).

Macrophages as perfect cells for reprogramming

Macrophages are key effectors in innate immunity; they were discovered at the end of 19th century by Ilya Mechnikov and at these times they were designated as simple scavengers of cellular debris and other cellular wastes (Poltavets et al., 2020). Today, it is well established that macrophages play an indispensable role in a variety of physiologic and pathologic processes, including organ development, host defense, acute and chronic inflammation, and tissue homeostasis and remodeling (Wang et al., 2018). In contrast with many other cell types, macrophages cannot be traced to a single origin and they have been identified in all tissues. Some macrophages reside in tissues and they are known as tissue -resident macrophages, such as Kupffer cells in liver, pulmonary macrophages or peritoneal macrophages (Cassado et al., 2015). They originate from progenitor cells generated in the yolk sac, they have a long lifespan, and they are essential components to maintain tissue homeostasis (Gomez et al., 2015). Others are monocyte-derived macrophages that originate from bone marrow hematopoietic stem cells and differentiate into macrophages after they are recruited to inflammatory tissues (Ding et al., 2022). Plasticity of macrophages, i.e. the fact that these cells can acquire different phenotypes according to the microenvironmental stimuli they receive, is a hallmark and their phenotypic changes are often referred to as "polarization" (Kowai et al., 2019). Because of its complexity, the polarization of macrophage phenotype remains controversial. To simplify, the functional spectrum of macrophages (Fig.1.9) can be divided in two extreme poles: classically-activated macrophages (M1) and alternatively-activated macrophages (M2) (Lin et al., 2021). M1 macrophages, which can be activated by exogenous inducers, such as lipopolysaccaride (LPS), interferon gamma (INF-γ) as well as other factors, participate in antigen presentation and they can have tumoricidal activity. They contribute to the inflammatory immune response by producing type I pro-inflammatory cytokines, such as Il-1β, tumor necrosis factor-α (TNF-α), etc; killer molecules, such as nitric oxide (NO), reactive oxygen species (ROS); chemokines (CCL2, CXCL-10) and they express on their surface high levels of the major histocompatibility complex class II (MHCII) and other co-stimulatory molecules, such as CD80 and CD86. These type I membrane proteins work in tandem and they are considered specific markers of the M1 phenotype (Rhee et al., 2016). On the contrary, M2 macrophages, which arise in response to interleukin-4 (IL-4), promote anti-inflammatory responses producing type II cytokines, such as IL-10, TGF-β; pro-angiogenic and matrix remodeling factors, such as vascular endothelial growth factor (VEGF), matrix metal protease (MMPs). There are three subtypes of M2 macrophages: M2a, M2b, M2c according to the stimuli received; they are involved in the tissue repair and they have pro-tumorigenic functions. M2 macrophages can be recognized by their markers: 1) high levels of arginase I (ArgI) that mediates the collagen production; 2) the activation of peroxisome proliferator-activated receptor gamma (PPARγ) with its metabolic downstream effects; 3) the presence of specific surface proteins, such as CD206. CD206 is also known as mannose receptor C type 1 (MRC1), which is the receptor for various pathogens including viruses, fungi, and bacteria (Gionfriddo et al., 2020; Nielsen et al., 2020). The polarization of macrophages is a complex process regulated by multiple interactions and a variety of signaling pathways, such as NF-kB, STAT3 and MAPK1/2 (Sun et al., 2016). It is well established that the p65 subunit is the primary mediator of NF-kB transcriptional activity for proinflammatory genes inducing the M1 macrophage polarization (Biswas and Lewis, 2010), while the activation of STAT3 is linked to the transcription of M2-specific genes (Zi Yin et al., 2018). In addition, it has been widely shown that the activation of MAPK, in particular kinase 1/2, has a crucial role in the differentiation into M2 macrophages (Neamatallah et al., 2019). Hence, macrophages can continually oscillate between these two phenotypes to respond and accommodate to different physiological conditions. It is well-known that the imbalance of macrophage polarization can lead to a variety of diseases, such as atherosclerosis, tumors and asthma (Lin et al., 2021). Under the influence of cancer cell-derived signals in TME, TAMs mainly exhibit an M2-like phenotype, which promote the formation of blood and lymphatic vessels, enhance tumor cell proliferation and migration, and immunosuppression (Sun et al., 2016). Therefore, the repolarization or reprogramming of TAMs from

M2 to M1 phenotype may represent a breakthrough for cancer immunotherapy (Kumari and Choi, 2022). Nevertheless, it is important to highlight that the M1/M2 classification of macrophages proposed in the early 21st century is a simplified approach, so it should be used with caution in *in vivo* studies, especially in the context of cancer, where the landscape is much more complex (Poltavets et al., 2020).
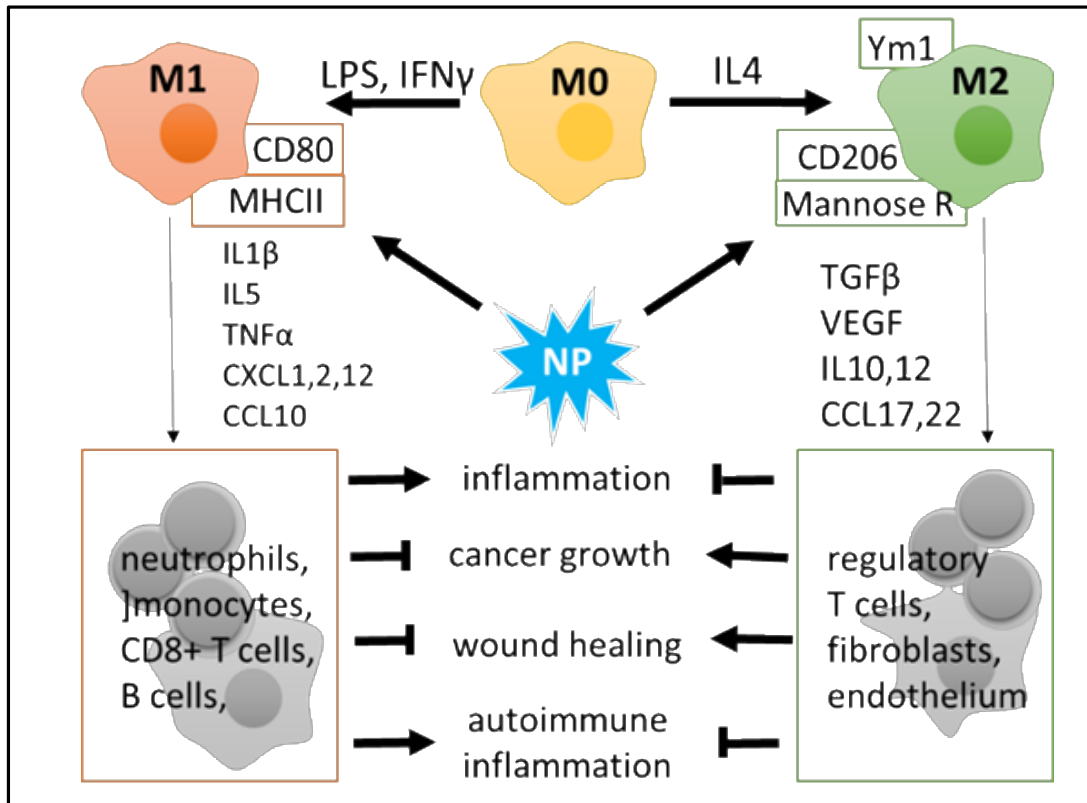

Figure 1.9. Macrophage polarization: (M1) classical, pro-inflammatory phenotype and (M2) alternative, anti-inflammatory phenotype. M1 polarization can be triggered by lipopolysaccharides (LPS) and/or interferon gamma (INF-γ). M1 macrophages express high levels of CD80 and MHCII and produce pro-inflammatory cytokines to stimulate the innate and adaptive immune activity of monocytes, neutrophils, T-and B-lymphocytes. M2 cells are characterized by surface markers Ym1, CD206, and mannose receptor, as well as by cytokines that have a potential for immunosuppression and tissue regeneration. Tumor-associated macrophages develop an M2 phenotype and promote the immune escape of tumor cells (from Dukhinova et al., 2019).

The Use of Iron Oxide Nanoparticles to Reprogram Macrophage

Macrophages are highly active phagocytes and they are the first cells to encounter external substances, including nanoparticles. Thus, these nanocarriers could affect the polarization states of macrophages depending on their physicochemical properties (Dukhinova et al., 2019). Indeed, many studies have shown that iron oxide nanoparticles have strong effects on macrophage polarization favoring the M1 phenotype (Ke Li et al., 2020). These biological effects of SPIONs are probably the result of intrinsic features of their iron oxide core, which affects several signaling pathways linked to the iron metabolism and the production of reactive oxygen species altering the intracellular redox balance (Reichel et al., 2019). The precise molecular mechanisms governing the interactions of macrophages with SPIONs are still unclear, but at the same time their impact on macrophage reprogramming has enhanced the interest in studying them not only as nanocarriers, but also as immunomodulator agent in cancer therapy (Mulens-Arias et al., 2021a; Nascimento et al., 2021).

1.3.c ER Stress Responses: An Emerging Modulator for Innate Immunity

The environmental stress imposed to TAMs in TME is translated in an increase of intracellular energetic demands, such as high need of new proteins provoking a stress in the endoplasmic reticulum (ER). Indeed, it is widely reported that TAMs display an irregular unfolded protein response (UPR) in their ER, an adaptive signaling pathway aiming at restoring ER homeostasis. Therefore, the modulation of UPR in TAMs can be seen as a promising strategy to re-educate them toward M1 phenotype in the tumor microenvironment (Conza and Ho, 2020; Siwecka et al., 2019).

ER Stress and the Unfolded Protein Response

The endoplasmic reticulum (ER) is a multifunctional organelle, which contributes to the maintenance of cellular calcium homeostasis, lipid synthesis and, moreover, it is the primary site for synthesis, folding and post-translational processing of proteins (Sicari et al., 2020). ER constantly monitor the quality of proteins in order to ensure that only properly folded proteins are exported to other compartments; thus, the accumulation of unfolded or misfolded proteins in the ER lumen rapidly results in a stress condition known as ER stress, which consequently activates the Unfolded protein response (UPR) process (Obacz et al., 2017). The UPR is a cytoprotective mechanism to alleviate stress of ER and restore cellular homeostasis. The activation of UPR combines several intracellular signaling pathways (Fig.1.10) to slow down ongoing protein synthesis and to increase the folding capacity of the ER. If the adaptive UPR is successful, the cellular protein synthesis resumes, and the cellular homeostasis is restored. By contrast when ER-stress persists, UPR induces oxidative stress and activates cell death pathways (Schmitz et al., 2018). The UPR signaling cascade is primarily initiated by three sensors that are inserted into the ER membrane: protein kinase R (PKR)-like ER kinase (PERK), inositol-requiring protein 1α (IRE1α) and ATF6α (also called cyclic AMP-dependent transcription factor 6α) (Sicari et al., 2019). PERK and IRE1α share similar luminal domains and possess cytosolic ser/thr kinase domains. In non-stressed cells, the major ER chaperone binding-immunoglobulin protein (BIP), also called 78 kDa glucose-regulated protein (GRP78), binds to the ER luminal domains of PERK and IRE1α and keeps them in a monomeric inactive state. Increased binding of BIP/GRP78 to misfolded proteins in ER relieves both PERK and IRE1α and facilitates their activation by dimerization (or oligomerization) followed by trans(auto)phosphorylation. Phosphorylated IRE1α activates its RNAase domain to catalyze the excision of 26 nucleotides of XBP1 mRNA, thereby generating a spliced XBP1 mRNA. This transcript is translated into the active XBP1 protein, a multifunctional transcriptional regulator, which modulates the expression of genes involved in glycosylation, protein folding, lipid synthesis and ER-associated degradation (ERAD) (Conza and Ho, 2020). In the meantime, active PERK phosphorylates the eukaryotic translation initiation factor 2 (eIF2) subunit α to attenuate the global protein synthesis and at the same time it also activates the ATF4 transcription factor. ATF4 mediates many adaptive responses, such as autophagy or the amino acid metabolism, but it also induces the CCAAT/enhancer binding protein (C/EBP) homologous protein (CHOP, encoded by DDIT3). CHOP can redirect the UPR response toward cell death (Sheshadri et al., 2021). Finally, ATF6α is a transcription factor that is processed into its mature form by Golgi-associated proteases upon relief from BIP/GRP78 interactions. The released cytoplasmic domain contains the basic-region leucine zipper (bZIP) transactivation domain, which regulate the transcription of different genes involved in the ERAD and in the protein folding, known as UPR genes. These three branches of the UPR often act in concert but can also be activated sequentially; in any case they work in a coordinate way to compensate ER stress (Chang et al., 2018). Hence, it is apparent that the ER stress and the UPR play an important role in physiology and in the development of numerous diseases including cancer. In this regard, recent findings have shown that the activity of PERK in TAMs plays a pivotal role promoting their immunosuppressive effects (Raines et al., 2022). On the contrary, other studies have reported that the over-activation of IRE-1 is involved in the macrophage polarization during inflammatory diseases (Batista et al., 2020).

Therefore, it is becoming increasingly clear that the modulation of UPR in macrophages may offer therapeutic potential both in cancer and autoimmune diseases.
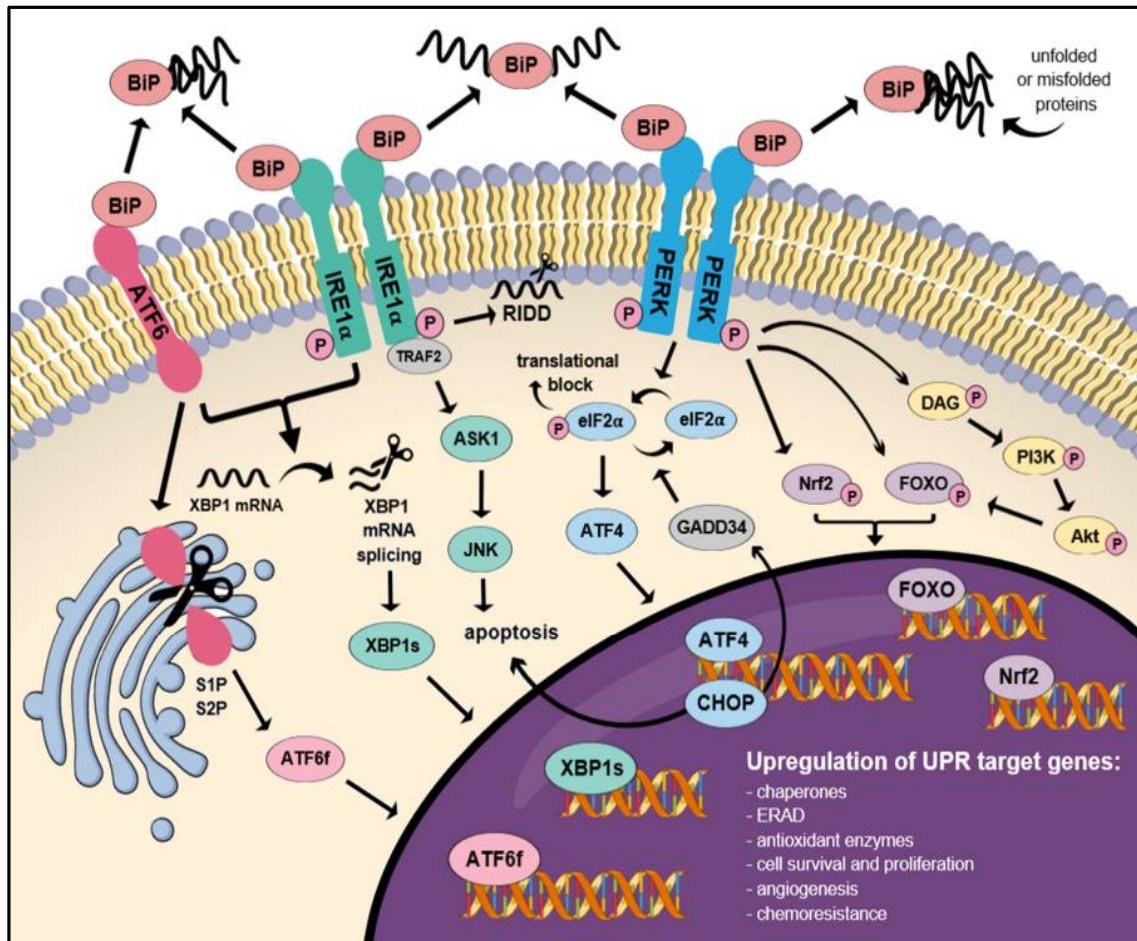

Figure 1.10. Three major branches of the Unfolded Protein Response (UPR) signaling pathway and their interconnections. Activation of the UPR arms—IRE1, PERK, and ATF6 activate the downstream signaling cascade driven by transcription factors XBP1s, ATF4, and ATF6f, respectively. The integration of these outputs trigger a large number of biological effects, which can contribute to the development of various disease (from Siwecka et al., 2019).

Aim of the thesis

To cure cancer new therapeutic strategies are required. Nanoparticles (NPs), in particular magnetic NPs (MNPs), which are stimulus-sensitive (in this case to an external gradient magnetic field) are efficient multifunctional platforms for drug delivery, able to target tumor cells and the tumor microenvironment (TME), making real the old concept of the magic bullet proposed by P. Ehrlich.

The re-education of the tumor-associated macrophages (TAMs), which have a prominent role in the development and progression of cancer in the TME could represent a new potential approach for cancer therapy. In this regard, TAMs were shown to display an irregular unfolded protein response (UPR) in their endoplasmic reticulum (ER) to endure the environmental stress and ensure pro-cancer activity. Recent studies have suggested that two UPR signal activators, PERK and IRE-1, contribute to the metabolic adaptation of TAMs in opposite ways. In particular, protein IRE1α-mediated X-box-binding protein (XBP1) signaling promotes a M1 phenotype and it is involved in the pathogenesis of inflammatory diseases, while the PERK arm of the UPR is a critical metabolic hub for the immunosuppressive function of TAMs (M2 phenotype). Therefore, the modulation of UPR response represents an attractive strategy to re-educate TAMs in TME.

Based on these evidences, we propose to re-educate in an *in vitro* model pro-tumorigenic M2-like macrophages into an anti-tumor M1-like phenotype by modulating UPR with magnetic nanocarriers, which with their intrinsic properties also affect the macrophage polarization toward M1 phenotype. Hence, the main goals of this PhD thesis are:

i) to develop and test MNPs functionalized with small interfering RNAs (siRNA) to down-regulate the PERK expression in macrophages derived from murine peritoneal exudate (PEMs);

ii) to induce the macrophage polarization in PEMs towards either the M1 or the M2 phenotype by administering pro- and anti-inflammatory stimuli, respectively. The macrophages obtained after the treatments will characterized analyzing specific surface markers along with gene expression profile of polarized macrophage phenotypes;

iii) to evaluate whether PERK silencing induced by siRNA-loaded nanoparticles can re-educate TAMs-like macrophages from the M2 to the M1 phenotype.

Therefore, the overall goal is to examine the ability to induce *in vitro* PEMs polarization and to modulate their polarization by siRNA-loaded magnetic nanocarriers. These studies would be the basis for possible future *in vivo* translational applications for cancer therapies.

CHAPTER II

Materials and Methods

2.1 Cell culture

Cell line

RAW264.7 cells are monocyte/macrophage-like cells, established from a tumor induced in BALB/c mice with the Abelson murine leukemia virus and they were purchased from ATCC. Cells were maintained in Dulbecco's Modified Eagle Medium (DMEM) supplemented with 10% fetal calf serum (FCS), 100 U/mL penicillin, and 100 µg/mL streptomycin (here referred as complete medium) at 37°C and in a humidified 5% CO_2 atmosphere. Cells were sub-cultured twice a week, when they were at 80–90% confluence.
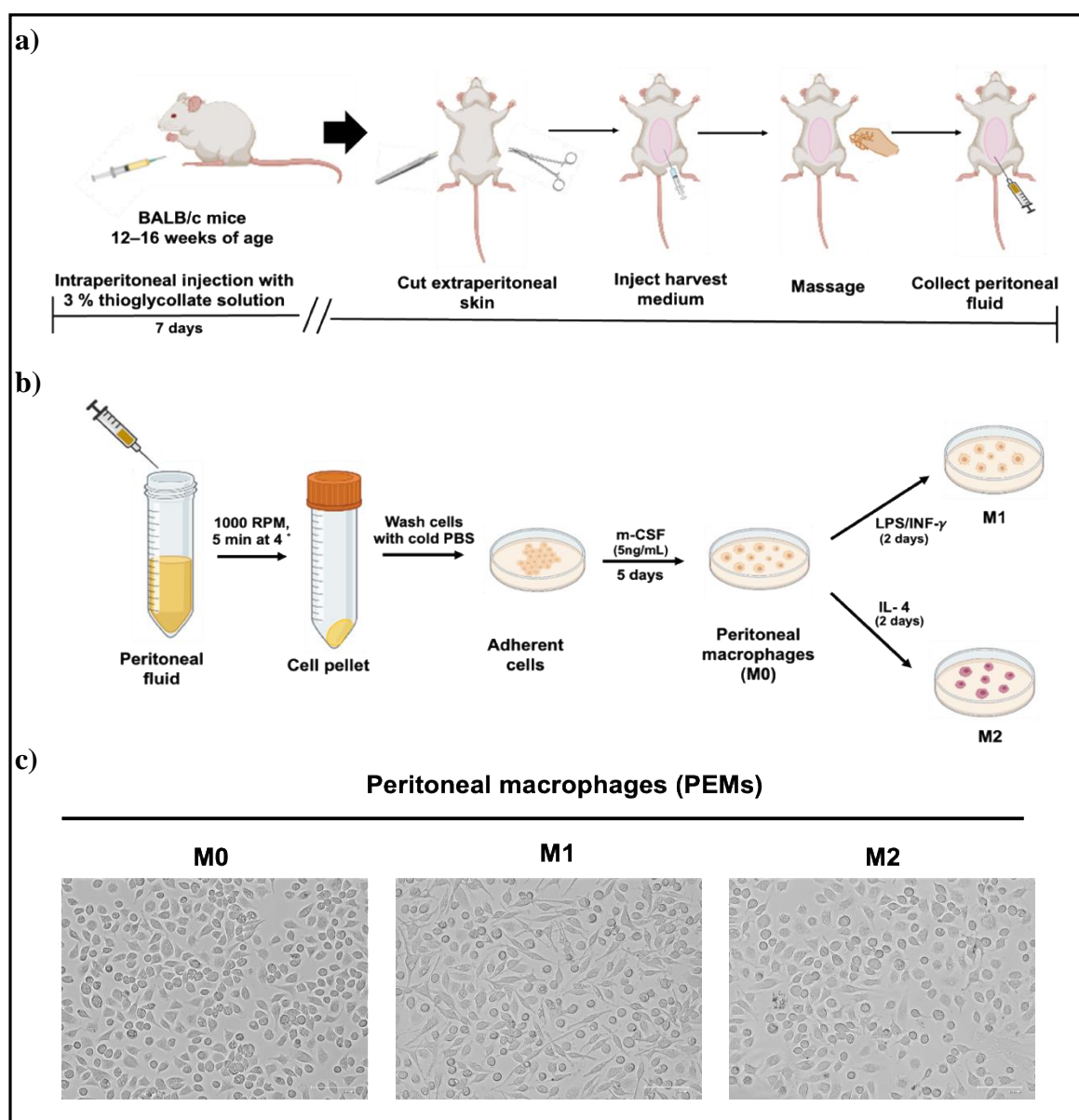
Isolation of peritoneal macrophages

Figure 2.1. Isolation (a) and polarization (b,c) of peritoneal macrophages (PEMs).

Primary macrophages were isolated from male and female BALB/c mice, 12–16 weeks of age. One mL of 3 % thioglycollate solution was injected into the peritoneal cavity of the mouse and after 6 days, macrophages derived from murine peritoneal exudate were isolated according to the method described by Rios et al. (2017). Briefly, mice were killed, and 10 ml of complete medium with few heparin drops was injected into the abdomen. The fluid was withdrawn, centrifuged (1000 rpm for 5 min at 4°C), and the cell pellet was resuspended in 10 ml of complete medium; cells were then washed twice by centrifugation in the same conditions. The pellet was resuspended in complete medium, and cells were plated in 6-well plates (2×10^6 cells/well). After 16h culture at 37 °C, non-adherent cells were removed, adherent cells were washed with phosphate buffered saline (PBS), pH 7.2, and new medium was added. These cells, called from now on PEMs, were maintained in culture in the presence of macrophage-Colony Stimulating Factor (rm m-CSF, Cat. 12340042, ImmunoTools GmbH, Friesoythe, Germany) for some days until use (Fig. 2.1a,b). All procedures were carried out in sterile conditions and in accordance with the Animal Care and Use Committee of UPO, the European Community Directive for Care and Italian Laws on animal experimentation (Law by Decree 116/92).

2.2. Synthesis of Magnetic Nanoparticles

Purely inorganic magnetite nanoparticles (MNPs) were prepared in the Laboratory of Microbiology of the Facultad de Ciencias at the Universidad de Granada under the supervision of Prof. Concepción Jiménez López using the experimental protocol of Valverde-Tercedor et al. (2015). Briefly, the synthesis of MNPs was carried out at 25 °C and 1 atm total pressure from a solution containing 3.5 mM $NaHCO_3$, 3.5 mM Na_2CO_3, 2.78 mM $Fe(ClO_4)_2$, and 5.56 mM $FeCl_3$ at a pH value of 9. All solutions were prepared from oxygen-free Milli-Q water deoxygenated and all steps were performed inside an anaerobic chamber filled with an atmosphere of N_2 with 4% of H_2 to prevent magnetite oxidation. After an incubation of 30 days inside the anaerobic chamber at 25 °C, the resulting magnetite nanoparticles were washed three times with deoxygenated Milli-Q water (50 mL) and stored until use at room temperature.

2.3. Nanoparticles functionalization with the polydopamine (PDA-MNPs)

PDA-MNPs were prepared via dopamine (Sigma-Aldrich, St. Louis, MO, USA) solution oxidation according to the method described by Mu et al. (2018). First, 1 mg of MNPs were resuspended into 0.5 mL Tris-buffered saline solution (TBS), pH 8.5 containing 1 mg/mL dopamine (DA). After stirring for 3 h at room temperature, with the color of the suspension turning to dark brown, the DA molecules were oxidized and self-polymerized on the surface of MNPs (Fig.2.2a). The PDA-loaded MNPs were then recovered by magnetic decantation, washed three times with TBS, resuspended in TBS and stored at 4 °C until use. All solutions were prepared with diethylpyrocarbonate-treated water (H_2O-DEPC). The amount of adsorbed DA was calculated from the difference between the concentrations of the DA in solutions before and after the adsorption on MNPs (the so-called supernatant) and was measured by UV−vis spectroscopy at a wavelength of 550 nm (Nieto et al., 2018), using as reference a standard curve of known concentrations of DA solutions. More than three replicas were performed for experiment.

2.4. Stability of the PDA adsorbed on MNPs

The stability of the PDA adsorbed on MNPs was monitored at different time points (1, 3, 5, 7 days) on suspensions maintained at 37 °C. Supernatants were collected after the magnetic decantation of PDA-MNPs and their absorbances were analyzed by the UV-Vis spectroscopy at a wavelength of 550 nm, and then they were compared to the absorbance of a reference solution of PDA. Each sample was analyzed in triplicates and the experiment was repeated three times.
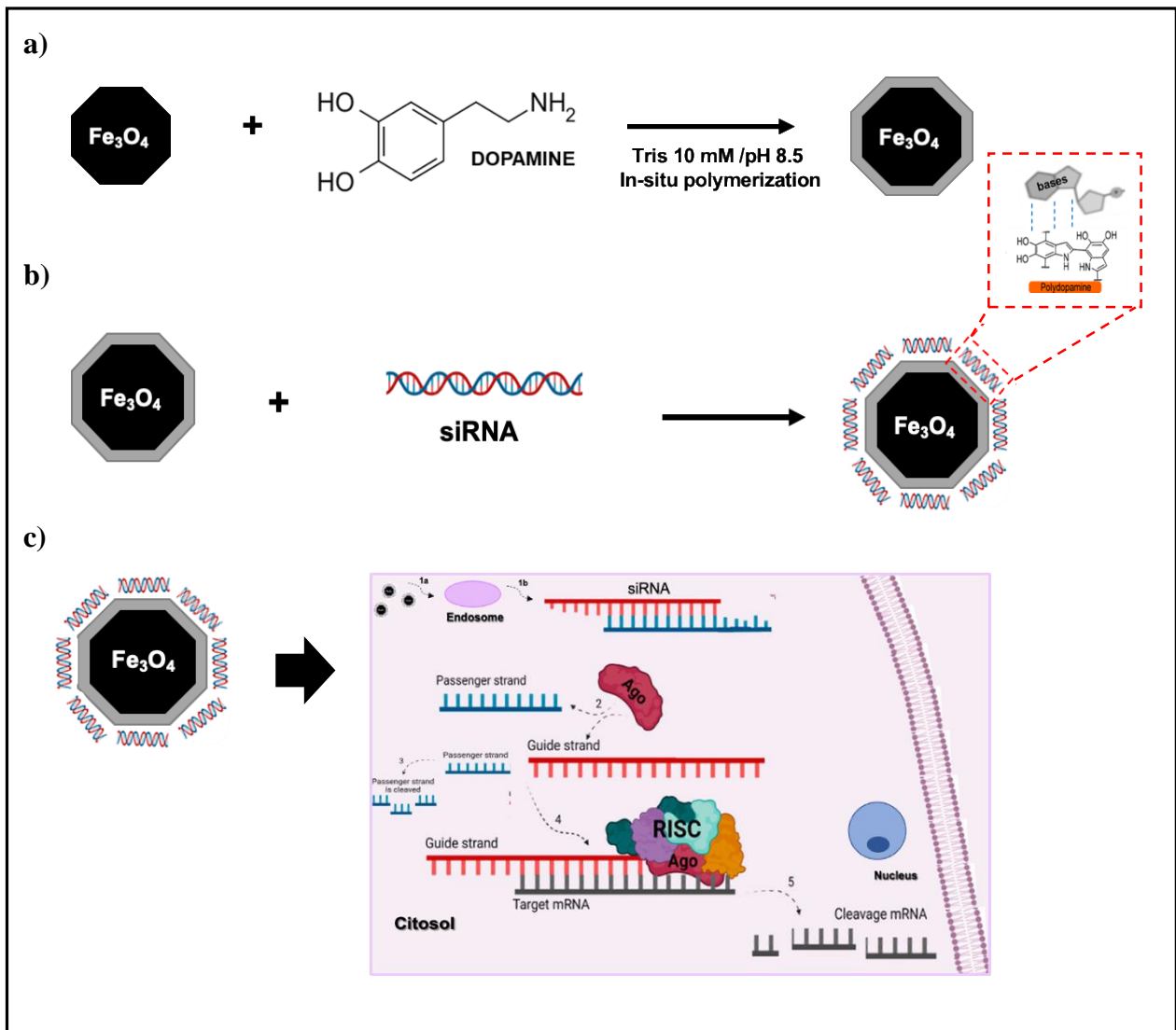
Figure 2.2. Scheme of the preparation of siRNA coupling to MNPs and its delivery to cells by these functionalized MNPs.

2.5. Cytocompatibility

<u>MTT assay</u>

RAW 264.7 and PEMs (1×10^4 and 2×10^4 cells/microwell of 96-well plates, respectively) were seeded for 24 hours and incubated for 72 h with different concentrations of nanoparticles, ranging from 0.1 to 100 μg/mL, which were added in 100 μL of fresh medium. In another series of experiments, cells were incubated with 100 μg/mL of PDA-MNPs for 24, 48,72h. At the end of the incubation time, cell viability was evaluated by MTT (Sigma-Aldrich) colorimetric assay. Briefly, 20 μL of MTT solution (5 mg/mL in a PBS solution) were added to each well. The plate was then incubated at 37 °C for 2-3 hours. After the removal of the solution, 125 μl of isopropanol-0.2 N HCl were added to dissolve formazan crystals. One hundred μl were then removed carefully and the optical density was measured in a multi-well reader (2030 Multilabel Reader Victor TM X4, PerkinElmer) at 570 nm. The experiments were carried on in triplicates at least three times.

Detection of Reactive Oxygen Species (ROS) Production

To measure the potential oxidative stress in living cells, as a consequence of the presence of the PDA-MNPs, the CellROX Green Reagent (Thermo Fisher Scientific, Waltham, MA, USA) was used following the protocol recommended by the manufacturer. Briefly, cells (approximately 60×10^3 RAW264.7/well and 4×10^5 PEMs/well) were seeded on glass coverslips in 24-well plates. After cells were incubated with 100 µg/mL of PDA-MNPs for different times (from 4h to 24h), cells were washed with PBS and CellROX Green Reagent was added to a final concentration of 5 µM in 300 µL of DMEM medium without serum and the plate was incubated in the dark at 37 °C for 30 min. The combination of bacterial lipopolysaccharides (LPS; Sigma-Aldrich) plus *interferon gamma* (*IFN-γ; Immunotools*) was used as a positive control. At the end of the incubation, the coverslips were washed with PBS, pH 7.2, fixed with 4% paraformaldehyde (PAF, Thermo Fisher Scientific) in PBS, washed again, and permeabilized with 0.1% Triton-X100 (Sigma-Aldrich) for 10 min. Finally, the coverslips were stained and mounted on specimen slides (Biosigma, Cona, Italy). The cytoskeletal actin was stained with Tetramethylrhodamine (TRITC)-phalloidine (1/200, Sigma-Aldrich excitation at 543 nm; emission at 560–620 nm), and the cell nuclei were stained with DAPI (catalog # 62248, Thermo Fisher Scientific, 1/50)**.** The CellROX Green Reagent is only fluorescent in the oxidized state because of ROS production. Therefore, the emission of green fluorescence (at 485/520 nm) is stable and is produced after DNA binding, and thus, its signal is mainly located in the nucleus. Fluorescence was detected at fluorescence microscope (Spectral Confocal Leica TCS SP2 AOBS) and images were taken at 200x magnification. The ImageJ software was used for the analysis.

Detection of ER stress and the activation of Unfolded protein response (UPR)

The stress of endoplasmic reticulum (ER) caused into cells by PDA-MNPs was detected indirectly by measuring the levels of specific UPR factors. Briefly, cells (approximately 3×10^5 RAW 264.7/well and 2×10^6 PEMs/well) were seeded in 6-well plates and after 24h they were incubated with 100 µg/mL of PDA-MNPs for different times (from 4h to 24h). Tunicamycin (2µg/mL, T7765_Sigma-Aldrich) was used as a positive control. The transcriptional expression of UPR proteins (Bip, XBP1s, ATF4, ATF6) was evaluated by q-RT-PCR, as described beyond.

2.6. Interactions of PDA-MNPs with Cells in the Absence/Presence of a GMF

Prussian Blue Staining

Cells (approximately 60×10^3 RAW 264.7/well and 4×10^5 PEMs/well) were seeded on glass coverslips in 24-well plates, and after 24 h, 100 µg/mL PDA-MNPs were added. After incubating at 37 °C for different times (from 0.5 to 30 min) in the absence (-GMF) and presence (+GMF) of a gradient magnetic field, the coverslips were washed with fresh PBS, pH 7.2, and fixed with PAF (2% in PBS). Then, the Prussian blue solution (1:1 of 2% potassium ferrocyanide and 2% HCl, both in H_2O) was added to the coverslips. In these conditions, any ferric ion (+3) present in the samples combines with the ferrocyanide and results in the formation of bright blue pigments called Prussian blue or ferric ferrocyanide. After two other washes with fresh PBS, Nuclear Fast Red (Sigma-Aldrich) was added to stain cell nuclei. Finally, the coverslips were washed with H_2O and mounted on slides by using one drop of Eukitt quick-hardening mounting medium for each sample. The interaction of the stained PDA-MNPs with cells was analyzed by optical microscopy at 100×. Experiments were performed in triplicates at least 3 times.

Iron Quantification by Potassium Thiocyanate

RAW264.7 and PEMs were seeded in 6-well plates and, after 24 h incubation at 37 °C 100-µg/mL PDA-MNPs suspensions in complete DMEM medium were added for different times (0.5, 5, 30 min) in the presence and absence of a GMF (Mag0201, Nanoeast, Nanjing, China). At the end of the treatments the supernatants were removed, cells were washed with fresh PBS, trypsinized, transferred to 0.5 mL Eppendorf tubes, and centrifuged at 1000 rpm for 5 min. Then, the cell pellets were dissolved in 37% HCl, mixed with 10% H_2O_2, and incubated for 20 min at room temperature. Samples were then reacted with 1 mL 1% potassium thiocyanate in Milli-Q water, and their absorbance was measured at 490 nm. The concentration of ferric ions in the samples was calculated referring to the absorbance obtained from a standard curve calculated from known amounts of PDA-MNPs following the same protocol (Oltolina et al., 2020). The endogenous iron of the cells was subtracted from the treated samples normalized by the untreated control cells. Experiments were performed in triplicates at least 3 times.

Internalization of PDA-MNPs in PEMs

Cells (8×10^5 PEMs/well) seeded in 12-well plate in complete medium were incubated after 24 h with 20 µg/mL of PDA-MNPs for 30 min in presence/absence of a gradient magnetic field and then incubated for further 24 h. Cells were then harvested after trypsinization, centrifuged, fixed in 2% PAF in PBS with FBS (20%) and NaN_3 (0.02%), and then flow cytometry analysis was performed to assess the physical parameters (side-scatter and forward scatter) of cells. Data were analyzed by FlowJo™ v10 Software (Bioscience).

2.7. Loading of siRNA on MNPs

Small interfering RNA (siRNA; 10µM) was incubated with different amounts of MNPs and PDA-MNPs (5, 20, 50 µg in a final volume of 50 µL under ultrasonic stirring for 30 min at 4 °C. Non-targeting siRNA-MOCK (sc-37007; *Santa Cruz* Biotechnology, Heidelberg, Germany) was used for these experiments. Nanoparticles/siRNA were then separated from their supernatants by magnetic decantation, nanocomplexes were resuspended in 50 µl of DEPC-water and 10 µl of each sample was run into a 3% w/v agarose gel electrophoresis in tris-acetate-EDTA running buffer (TAE 1X) at 120V for 20 min. Also the supernatants were analyzed with this method. siRNA bands were visualized by staining with SYBR. Images were captured under UV illumination and the densitometric analysis was done using ImageJ software.

In another series of experiments the fluorescent Alexa 488/siMOCK (sc-3890, Santa Cruz Biotechnology) was added to 100 µg/mL PDA-MNPs at a ratio of 50nM, and the mixture was sonicated for 30 min at 4 °C. The amount of absorbed fluorescent siMOCK on PDA-MNPs was calculated using a reference calibration curve obtained from the fluorescence intensity of standard solutions of siMOCK with concentrations ranging from 12 to 70 nM measured by multiwell reader fluorescence spectrophotometry (excitation 490 nm and emission 530 nm; 2030 Multilabel Reader Victor TM X4, PerkinElmer).

2.8. Interaction of siRNA-functionalized PDA-MNPs with cells: cell uptake and gene silencing

Next experiments were performed to evaluate the cellular uptake of the PDA-MNPs/siRNA, as well as its effects in silencing PERK and in the reprogramming of PEMs from the M2 phenotype to the M1 phenotype.

In all cases cells were treated with the PDA-MNPs/siRNA (Fig.2.2b). Briefly, PEMs (2×10^6 cells/well and 4×10^5 PEMs/well) were seeded in a 6 well plate and 24 well plate, respectively, with complete DMEM for 24 h. Then, they were incubated at 37 °C with PDA-MNPs/siRNA for 30 min under the magnetic field (Mag0201, Nanoeast) and then under normal conditions for 24 or 48 h. Alexa488/siMOCK and siPERK (Cat. sc-36214, *Santa Cruz* Biotechnology) were used. siPERK duplex was purchased as a solution of three specific siRNA. In general, 20 µg of nanoparticles and 100 pmol of siRNA were diluted in 50 µL of Opti-MEM Reduced Serum Medium separately and then mixed together. The mixtures were sonicated at 4°C for 30 min and then added to the cells. PEMs were also transiently transfected with 100 pmol siRNA using the Lipofectamine 2000 transfection reagent (Invitrogen Life Technologies, Monza, Italy) at 2:1 (lipid/siRNA) ratio following the manufacturer's instructions for siRNA transfection. The transfection mixture was added to cells in Opti-MEM Reduced Serum Medium (Thermo Fisher Scientific) and incubated at 37℃ for 6 h before the medium was replaced with complete DMEM. Lipofectamine 2000 and PDA-MNPs (20 µg), as well as tunicamycin (see beyond) were internal controls. The results of the treatments with PDA-MNPs/siRNA were analyzed in immunofluorescence and flow cytometry for cellular-uptake, q-RT-PCR for gene expression and immunoblotting for protein expression.

Cell uptake

PEMs were incubated with Alexa488/siMOCK either coupled to PDA-MNPs or administered through Lipofectamine 2000 on glass coverslip in 24 well plates for fluorescence and directly in 6 well plates for flow cytometry analysis. In case of PDA-MNPs cells were subjected to a gradient magnetic field for 30 min. All the samples, including the controls of PDA-MNPs and Lipofectamine 2000 alone, were incubated for 24h, before being analyzed for the uptaken fluorescence and, after being detached by trypsin, by flow cytometry, which was analyzed with the Attune flow cytometer (Invitrogen Life Technologies). For each group, the fluorescence (Ex/Em: 480/520 nm) of Alexa 488/siMOCK per 1×10^5 cells was acquired. The untreated cells were used as the control. Data were analyzed by FlowJo™ v10 Software (Bioscience).

Gene silencing by siPERK

PEMs seeded in a 6 well plate were incubated with siPERK either coupled to PDA-MNPs (Fig.2.2b,c) or administered through Lipofectamine 2000 and the selective inhibitor of PERK GSK2606414 (GSK-414; Sigma-Aldrich) and then +/- tunicamycin for 8 h. Cells were harvested after 24 h and 48 h to analyze both the transcriptional and translational regulation of PERK gene and other genes of UPR by q-RT-PCR and immunoblot analysis, respectively. Tables 1 and 2 report the list of the primers and the antibodies used.

2.9 Polarization of PEMs

Peritoneal macrophages were incubated for 5 days with 5 ng/mL recombinant murine macrophage colony-stimulating factor (m-CSF) as described by Hamidzadeh et al. (2020). Next, the cells were cultured for 48 h in complete DMEM supplemented with 20 ng/ml IL-4 (Cat.12340042, Immunotools) to polarize them towards the M2 phenotype, or with 100 ng/ml LPS (Sigma-Aldrich) and 5 ng/ml IFN-γ (Cat.12343112, Immunotools) to polarize them towards the M1 phenotype (Feito et al., 2019) (Fig.2.1 b, c). The expression of genes associated with the M1 phenotype (iNOS, TNF-α, COX-2) and with the phenotype M2 (Arg-1, TGF-β and PPAR-γ) was used as proof that the treatments with the cytokines induced the two phenotypes. The possibility that PDA-MNPs by themselves could polarize PEMs towards an M1 phenotype was also assessed, in line with what reported in the literature (Reichel et al., 2019). The properties induced by the treatments with the

LPS/IFN-γ were also tested by examining the expression of cell surface markers, i.e. CD80 and CD86 both in flow cytometry and immunofluorescence.

2.10 Reprogramming of PEMs

PEMs, which were pretreated with IL-4 to induce an M2 phenotype, were then added with PDA-MNPs/siPERK, LIPO/siPERK and the GSK-414 drug to reprogram cells to the M1 phenotype and incubated for 24 or 48h. Eight h before the end of the incubation tunicamycin (2 μg/mL) was added. Reprogramming was assessed by analyzing the level of expression of genes associated the M2 phenotype (ATF4, CHOP, Arg-1, TGF-β and PPAR-γ) and the M1 phenotype (iNOS, TNF-α, COX-2)(Jablonski et al., 2015). Moreover, the level of phosphorylation of molecules involved in pathways leading to the two phenotypes (eiF2α, STAT, MAPK 1/2, NF-κBp65) was analyzed in extracts from cells treated for 48 h by immunoblotting. Also in these series of experiments the immunophenotype of the cells was assessed for the expression of the M1 CD86 marker and the M2 CD206 marker.

2.11 Quantitative Real-time PCR

The mRNA levels of genes were analyzed by quantitative real-time PCR (q-RT-PCR). Total RNA was extracted with Trizol (Invitrogen Life Technologies). The RNA concentration and quality were determined by NanoDrop 2000C spectrophotometer (Thermo Fisher Scientific, Wilmington, DE, USA). After RNA purification and treatment with DNAse I (Thermo Scientific) 1 μg was retrotranscribed in cDNA with the RevertAidTM H Minus First Strand cDNA Synthesis Kit (K6022_Thermo Fisher Scientific) using oligo(dT) primers. Gene assays were performed in triplicate for each treatment in a 12 μL reaction volume containing 1 μL of RT products, 6 μL Sso-Fast EVA Green SMX (Bio-Rad, Hercules, CA, USA), 500 nM each forward and reverse primers. The sequences of primers are listed in Table 1. Automated CFX96 real-time thermocycler (Bio- Rad) was used and the reaction conditions were 95 °C for 1 min, followed by 45 cycles at 98 °C for 5 s and anneal/extend step for 5 s at 60 °C, with data collection. At the end of these cycles, a melting curve (65 °C to 95 °C, with plate read every 0.5 °C) was performed to assess the specificity of the amplification product by single peak melting temperature verification. Results were analyzed with Bio-Rad CFX Manager and the gene expressions were calculated by the ΔΔCt method and β-actin served as an internal control.

Table 1. Primer sequences for quantitative real-time PCR.

Gene	Primer sequence	Product Length bp
PERK	CCAGGCATTGTGAGGTATTT	98
	TCTGTGCTTTCGTCTTTGAG	
ATF4 F	GTTTAGAGCTAGGCAGTGAAG	93
	CCTTTACACATGGAGGGATTAG	
XBP1s	AGTCCGCAGCAGGTG	93
	GGTCCAACTTGTCCAGAATG	
Bip	GAGAGAGGGAGAGAAGAACA	99
	GCCACCACTTCAAAGACA	
Chop	ACACGCACATCCCAAAG	108
	ACCACTCTGTTTCCGTTTC	
ATF 6	GATGGTGACAACCAGAAAGA	109
	TGGAGGTGGAGGCATATAA	
Arg-I	ATCCCACCTAGGAGACAAAG	116
	GGGACCTGGAATCTGTCTAT	
TGF-β	CTCCCGTGGCTTCTAGTGC	133
	GCCTTAGTTTGGACAGGATCTG	
PPAR γ	GTGACTCTGCTCAAGTATGG	114
	GAACTCCCTGGTCATGAATC	
iNOS	GTTCTCAGCCCAACAATACAAG	127
	GTGGACGGGTCGATGTCAC	
TNF-α	AGCCCCCAGTCTGTATCCTT	212
	CTCCCTTTGCAGAACTCAGG	
Cox-2	GGGTGTGAAGGGAAATAAGG	125
	AGTGCTGGGCAAAGAATG	
β-actina	GATGACCCAGATCATGTTTGA	161
	GGAGAGCATAGCCCTCGTAG	

2.12 Immunoblotting

The protein levels were determined by the western blotting assay. After the different treatments, cells were washed twice in cold PBS and lysed in iced with RIPA Lysis Buffer (20 mM Tris-HCl pH 7.5, 150 mM NaCl, 50 mM HEPES, 0.1% SDS, 1 mM Ethylene glycol-bis(2-aminoethylether)-N,N,N′ (EGTA), 1% NP-40, 1% sodium deoxycholate, 2.5 mM sodium pyrophosphate, and 10% glycerol) supplemented with protease inhibitors cocktail (Sigma-Aldrich). Cell lysates were centrifuged at 13,000 rpm at 4 °C for 15 min. Clarified cell extracts (30 μg of protein) were denatured by heating for 5 min at 95 °C in reducing Laemmli buffer; proteins were separated in SDS-PAGE and transferred onto polyvinylidene difluoride (PVDF) filters. Filters were blocked with 5% non-fat dry milk for 2 h, rinsed in water, and probed with different antibodies in TBS, pH 8.0, 5% BSA, overnight at 4°C. The list of primary antibodies used is reported in Table 2. After extensive washing, immunocomplexes were detected with appropriate horseradish peroxidase-conjugated secondary anti-IgG antibodies (diluted 1/5000, Sigma-Aldrich), followed by enhanced chemiluminescence (ECL kit; Biorad), and were analyzed in a Versadoc instrument (Bio-Rad Laboratories S.r.l, Segrate, Milan, Italy). Bands were subjected to densitometric analysis using ImageJ software.

Table 2. Primary antibodies used for immunoblotting.

Antigen	Species	Dilutions	Expected Band	Source
PERK	Rabbit polyclonal	1/500	140 kDa	Cell Signaling Technology
eif2-α	Mouse monoclonal	1/500	38 kDa	Cell Signaling Technology
Phospho eif2-α	Rabbit polyclonal	1/500	38 kDa	Cell Signaling Technology
STAT3	Mouse monoclonal	1/500	80 kDa	Cell Signaling Technology
Phospho STAT3	Rabbit polyclonal	1/500	80 kDa	Cell Signaling Technology
NF-kb p65	Rabbit polyclonal	1/500	65 kDa	Santa Cruz Technology
Phospho NF-kbp65	Mouse monoclonal	1/500	65 kDa	Santa Cruz Technology
MAPKK1/2	Rabbit polyclonal	1/500	42-44kDa	Millipore
Phospho MAPKK1/2	Rabbit polyclonal	1/500	42-44kDa	Millipore
α-Tubulin	Mouse monoclonal	1/500	55-60 kDa	Millipore
Vinculin	Mouse monoclonal	1/500	120 kDa	Santa Cruz Technology

2.13 Flow cytometry

PEMs were seeded in 12-well plates and underwent the different treatments described. After detachment and centrifugation, cells were incubated in 100 µl of staining buffer (PBS, 20% FBS and 0.1% sodium azide) with 20 µl of inactivated normal mouse serum for 30 min at 4 °C to block the Fc receptors on the macrophage plasma membrane, before adding the primary antibody, and to prevent non-specific binding. Cells were incubated for further 30 min in the dark with a single and/or a combination of the antibodies conjugated with single fluorophores (phycoerythrin, Fluorescein-5-isothiocyanate, phycoerythrin-Cyanine7, PE, FITC, PE-Cy7) listed in Table 3. Then, cells were washed with 1 mL of FACS buffer (PBS, 20% FBS and 0.1% sodium azide) and centrifuged at 1500 rpm for 5 min. The cell pellets were resuspended in 300 µl of FACS buffer and were analyzed on the Attune flow cytometer (Invitrogen Life Technologies). The conditions for data acquisition and analysis were established using the unlabeled cells as negative control. Each experiment was carried out three times and single representative experiments are displayed. For statistical significance, at least 100,000 cells were analyzed in each sample and the mean of the fluorescence emitted by these single cells was used.

Table 3. Primary antibodies used for flow cytometry.

Antigen	Species	Dilutions	Source
F4/80-FITC	Mouse monoclonal	1/100	eBioscience
CD206-PE-Cy7	Mouse monoclonal	1/3600	eBioscience
CD86-PE	Mouse monoclonal	1/100	eBioscience
CD80-PE	Mouse monoclonal	1/100	eBioscience
CD11b-FITC	Mouse monoclonal	1/100	eBioscience
CD11b-PE	Mouse monoclonal	1/100	eBioscience
CD11b-PE-Cy7	Mouse monoclonal	1/100	eBioscience
CD45-APC-eFluor 780	Mouse monoclonal	1/100	eBioscience

2.14 Immunofluorescence microscopy

PEMs were seeded on glass coverslips (12 mm diameter) in 24-well plates, and, after the different treatments, they were fixed with 4% PAF for 20 min at 25 °C. The cells were washed three times with PBS, permeabilized with TBS-5% BSA-0.1% Triton-X100-5% FCS for 1h and then they were incubated in the dark for 2h with primary antibodies reported in Table 4. After three washes with TBS-5% BSA-0.1% Triton-X100, samples were incubated with Alexa Fluor 488-labelled secondary antibodies (1:500, Sigma) and PE-labelled streptavidin (1:500, Sigma-Aldrich), while the cell nuclei were stained with DAPI (1/50, Thermo Fisher Scientific). Finally, coverslips were washed twice in PBS Triton X-100 and mounted with mowiol_4-88 (Sigma-Aldrich). Fluorescence was detected at the fluorescence microscope (Leica DM 2500), in particular the fluorescence of Alexa Fluor 488 was excited at 488 nm and the emitted fluorescence was measured at 491–586 nm. PE fluorescence was excited a 488 nm and measured at 575–675 nm. DAPI fluorescence was excited at 405 nm and measured at 420–480 nm. Images were taken at 200x magnification and analyzed by the ImageJ software.

Table 4. Primary antibodies used for immunofluorescence.

Antigen	Species	Dilutions	Source
F4/80-BIOTIN	Mouse monoclonal	1/400	eBioscience
CD206-Alexa488	Rabbit polyclonal	1/50	eBioscience
CD86-Alexa488	Rat	1/50	eBioscience
CD80-Alexa488	Rat	1/50	eBioscience

2.15 Statistical Analysis

Data are expressed as mean ± standard error of at least 3 triplicates. Statistical analyses were performed using a two-way ANOVA, with a Bonferroni's multiple comparisons test for grouped analyses using GraphPad Prism version 7 for Mac, GraphPad Software (GraphPad Prism, San Diego, CA, USA). Statistical differences between the treatments were considered significant when p values were $p < 0.05$ (*), $p < 0.01$ (**), $p < 0.001$ (***), and $p < 0.0001$ (****).

CHAPTER III

Results and discussion

3.1. Synthesis of magnetic nanoparticles (MNPs)

MNPs were synthetized, characterized, and provided by the group Laboratory of Microbiology of the Facultad de Ciencias at the Universidad de Granada with which we have a collaboration. These MNPs, shown in Fig. 3.1a, were obtained by a co-precipitation method mixing aqueous solutions of $FeCl_2$ and $FeCl_3$ with the addition of NaOH and $NaHCO_3$. MNPs consist of a core of iron oxide, which confers them the typical magnetic features that could be exploited to drive them when a magnetic field is applied (Shubayev et al., 2009). In detail, MNPs are composed by magnetite crystals (Fe_3O_4) with sizes ranging from 10 to 30 nm and their morphology is poorly defined. In addition, they have a small magnetic moment per particle and their isoelectric point (iep), determined from the ζ-potential calculations, is 7.0 (García Rubia et al., 2018).

3.2. Coupling of Polydopamine on iron oxide nanoparticles (MNPs)

MNPs were coated with polydopamine (PDA), a polymer produced by self-oxidation of dopamine under alkaline condition, and thus becoming black-brown, which has adhesive properties similar to proteins of mussels (A. Jin et al., 2020). As shown in Fig. 3.1a, upon incubation with dopamine MNPs acquired a black color, which is due to the adsorption of PDA at their surfaces. By contrast, the colloidal suspension of MNPs at the same concentration, but in the absence of PDA remains significantly clearer. The concentrations of PDA were quantified by UV-Vis spectroscopy ($\lambda = 550$ nm); in particular, after 3 washes with DEPC-H_2O the amount of PDA absorbed on MNPs was 1.2 mg/mg of MNPs, which represents about 80% of the originally incubated soluble dopamine (Fig. 3.1b). Moreover, the coating of PDA on iron oxide nanoparticles surfaces was found not to affect the magnetic properties of MNPs and to increase only slightly nanoparticle size (Ge et al., 2016).

3.3. Stability of the PDA-MNPs

The stability of PDA-MNPs was tested at different times (from 1 to 7 days), by evaluating the amount of PDA released from the MNPs in the soluble fraction at 37 °C. MNPs were separated from the latter by magnetic decantation. Around 98% of the PDA remained stable at the surface for all this period, revealing the high stability of the PDA-MNPs. Moreover, the same amount of the PDA (98% of the amount detected at day 7) was still detectable after 5 months at 4°C, showing the strong interaction of the polymer with the MNPs.

3.4. Cytocompatibility of PDA-MNPs on macrophages

The cytocompatibility of any kind of NP is the first parameter to be ascertained before their eventual biomedical application and macrophages are the first cells involved in the uptake of foreign substances, such as nanoparticles can be. Thus, the cytocompatibility of PDA-MNPs on these cells was tested in MTT assays. In a first series of experiments, RAW 264.7 cells were incubated with increasing concentrations of PDA-MNPs and MNPs (up to 100 μg/mL) and PDA at comparable concentrations for 72h. Results (Fig. 3.2a) did not show a significant reduction in viability compared to untreated cells in all assessed concentrations, except at 100 μg/mL, where viability was reduced to about 80%, which, anyway, is a value above the cut off of 70% indicated by ISO 10993-5:2009. PDA by itself was highly cytocompatible, so the coupling of PDA on MNPs still improved the cytocompatibility of nanocarriers as also reported other works (Ge et al., 2016b; Siciliano et al., 2022). MTT assays were also performed on cells incubated for 24 and 48 h with the highest PDA-

MNPs concentration used in all these experiments (100 μg/mL) and similar results were observed (Fig. 3.2b); in fact, >80% of the cells survived confirming the biocompatibility of these nanoparticles on this macrophage-like cell line. Given that primary cells are more sensitive than immortalized cell lines, we also evaluated the viability of macrophages isolated from murine peritoneal exudate (PEMs; see beyond and Fig. 3.11 for their characterization) after 3 day incubation with PDA-MNPs, MNPs at different concentrations and PDA at comparable concentrations. Also in this case no significant toxicity was observed in any condition; only when cells were incubated with the two highest PDA-MNPs concentration of 10 and 100 μg/mL cell viability was decreased, but it was always around 90 and 80% (Fig. 3.2c) It can thus be concluded that PDA-MNPs are endowed of a good cytocompatibility on macrophages.

Different types of nanoparticles including those containing graphene have been reported to induce the cytotoxicity by increasing the cellular oxidative stress through the generation of reactive oxygen species (ROS) (Oltolina et al., 2020).Therefore, we also analyzed the cytocompatibility of PDA-MNPs by assessing the level of ROS possibly induced in the two macrophage models. RAW 264.7 cells were incubated with the highest dose of PDA-MNPs (100 μg/mL) for different periods of time and ROS production was evaluated as a virtual green color (CellROX® Green Reagent) under confocal microscopy. Indeed, a significant production of ROS was detected in cells incubated with PDA-MNPs for 4 and 8h (Fig. 3.3a); this cell response was however extinguished afterwards, suggesting that cells can control the oxidative stress. In the positive control cells stimulated with LPS/INF-γ for 24h produced a noticeable amount of ROS. Since the oxidative stress is closely connected with the protein-folding homeostasis in the Endoplasmic Reticulum (ER)(Khan et al., 2020), we examined also whether PDA-MNPs could affect pathways linked to ER stress, collectively called the unfolded protein response (UPR). In cells treated as above (100 μg/mL of PDA-MNPs for the four different time points) the ability of PDA-MNPs to induce the UPR response was analyzed by quantitative real-time PCR (q-RT-PCR) for the ER chaperone BiP and XBP1s, ATF4, ATF6 (Fig. 3.3b). These proteins are downstream effectors of the ER-stress sensors IRE-1, PERK and ATF6, respectively (Sicari et al., 2020). As positive control, we used tunicamycin (TM), a well-known ER-stressor (Zhong et al., 2017). With the exception of XBP1s, the other three genes are only barely affected by the incubation of cells with PDA-MNPs. In the cases of BiP and ATF4 the genes appear to undergo downregulation with time after being activated at shorter times. Only in the case of XBP1s a late and quantitatively significant activation was observed. This finding is in line with the report that XBP1s plays a crucial role in macrophages during inflammatory diseases (Raines et al., 2022).

When the same experiments were performed on PEMs, it was found that ROS production was high, but only after 4 h of incubation of the cells with PDA-MNPs and thus was completely extinguished afterword (Fig. 3.4a). The UPR response displayed a patter somehow different from the one observed for RAW 264.7 cells. The major difference is a higher ER response (Fig. 3.4b). In the cases of BiP and XBP1s, ATF6 the response is strong at 8 h (BiP and ATF6) or at 16 h (XBP1s), but then it is down regulated at 24 h, showing that cells can control the ER stress. Only in the case of ATF4 gene upregulation is maximal at 24h. Thus, with the exception of one of the four ER stress marker, both cell types can control and downregulate the ER-stress, which was fully dismissed. Taken together, these results indicate that PDA-MNPs, being xenobiotic agents, affect both the cellular redox balance and the normal functioning of the ER, but they do not alter the cellular homeostasis for a prolonged time causing cell damage, thus PDA-MNPs are highly cytocompatible.

3.5 Interaction of PDA-MNPs with cells

After confirming the full cytocompatibility of PDA-MNPs, we tested their ability to interact with macrophages in the presence/absence of a magnet. In fact, it is well known that the apposition of a GMF enhances the interaction of the magnetic nanoparticles with cells (Oltolina et al., 2020). Both

RAW 264.7 and PEMs macrophages plated on coverslips were incubated for different times with 100 µg/mL PDA-MNPs in the presence or absence of a magnet, were fixed, washed, and stained with Prussian blue in order to detect iron oxide nanoparticles. As shown in Figs. 3.5a and 3.6a, when a magnetic field was applied both to RAW 264.7 and to PEMs, PDA-MNPs were already clearly visible after 30 seconds of incubation, the earliest time point analyzed. By contrast, PDA-MNPs were detectable only after 5 min incubation in the absence of a magnetic field in the two macrophage models. However, when increasing the time incubation to 30 min PDA-MNPs were more detectable both in the absence and presence of a GMF, even if there was always a significant difference between samples treated with the magnet and untreated samples. Similar results were also confirmed by the quantification of iron internalized in the cells detectable through Potassium Thiocyanate (Figs. 3.5b and 3.6b). In fact, in the absence of a GMF, the amount of iron associated with macrophages is very low after 0.5 min of incubation with PDA-MNPs. Nevertheless, this concentration increased in a time-dependent way reaching after 30 min a value of 50 µg/mL for RAW 264.7 and 30 for PEMs. When the same experiment was performed in the presence of a GMF, the iron concentration associated to the cells was 60 for RAW 264.7 and 45 for PEMs. At any time point, the application of a GMF enhanced the interactions between the nanoparticles and the cells, and this effect was time-dependent. At the latest time of 30 min the difference between sample treated with GMF or not was less evident probably because of the sedimentation of nanoparticles on the cell surface. The internalization of the PDA-MNPs into PEMs was also evaluated by a series of experiments in flow cytometry. After cells were incubated 24h with a low amount of PDA-MNPs (20ug/mL), the analysis of the physical parameters was performed in order to reveal variation in the cell parameters in terms of increased size and granularity. Results showed that the cell interaction with PDA-MNPs affected the granularity of cells (side scatter), but no their sizes (forward scatter). In fact, the histograms (Fig.3.7a) report that the cellular complexity in term of the granularity increased 80% compared to the untreated samples. Given that the apposition of a GMF enhances the interaction of PDA-MNPs with cells, the same experiment was performed in the presence of a GMF. Likewise, the cellular sizes did not change, but the granularity further increased of about 16%. (Fig.3.7b) Therefore, we considered the increase of the cellular complexity as an indirect measure of the cellular uptake of nanoparticles confirming the internalization of PDA-MNPs into PEMs.

3.6 Loading of siRNA onto MNPs requires the presence of PDA on MNPs

PDA has numerous surface functional groups, which can facilitate the functionalization of PDA-MNPs with biomolecules, such as nucleic acids Thus, these magnetic nanocarriers were used to deliver to cells oligonucleotides, such as small interfering RNA (siRNA) (A. Jin et al., 2020).

siRNA (10 µM) was thus incubated with 5, 20, 50 µg of MNPs and PDA-MNPs under ultrasonic stirring for 30 min and then, nanocomplexes were analyzed in agarose gel electrophoresis.
The siRNA associated to nanoparticles could not be visualized, because these nanocomplexes did not migrate under the electric field in the agarose gel, unlike the naked siRNA used as control (Fig. 3.8a). Moreover, the ratio MNPs/iRNA, which was in favour of MNPs, did not allow to visualize the siRNA, because of the interference of the MNPs (Jin et al., 2019).
Thus, the capability of NPs to bind siRNA molecules was evaluated by an indirect method, by visualizing on agarose gel the amount of unbound siRNA left in the sample after magnetic decantation of the nanoparticles. The amount of siRNA in the soluble fractions obtained after incubation with PDA-MNPs was clearly decreased in a dose dependent way, as confirmed also by the densitometric analysis of the bands (Fig. 3.8b). These data clearly show that siRNA can be loaded on PDA-MNPs. In contrast, in the case of siRNA incubated with naked MNPs, the same original amounts of siRNA were present in the soluble fractions after magnetic decantation of the nanoparticles. It can thus be concluded that PDA coating is necessary to bind to siRNA molecules on MNPs. Probably, siRNA molecules bind to the surface of PDA-MNPs by $\pi-\pi$ stacking interactions between the aromatic

groups of the PDA and the nucleobases of siRNA (Mu et al., 2018). To quantify the adsorption efficiency of PDA-MNPs/siRNA, we measured the fluorescence intensity of a FITC-labeled siRNA (50 nM) after coupling with PDA-MNPs (100µg/mL). In this case, the FITC-siRNA concentration associated with PDA-MNPs after ultrasonic stirring for 30 min was about 70% of the amount present in the original solution.

3.7 Cellular uptake of siRNA-PDA-MNPs

The efficiency of the siRNA-coated nanocomplexes to deliver siRNA to target cells was first examined in HeLa cells, a well-recognized *in vitro* model with high sensitivity for RNA interference (Tatiparti et al., 2017). In particular, the use of these cells, which were incubated with different amounts PDA-MNPs coated with siRNA specific for the housekeeping Cortactin, were used to confirm that the functionalized PDA-MNPs/siRNA could induce the knock-down of a target protein, which was detected by western blot (data not shown). To visualize the uptake of the siRNA-PDA-MNPs by PEMs, PDA-MNPs functionalized with a FITC-labelled siRNA (Alexa488/siMOCK) were used and cells plated on coverslips and incubated with the nanocarriers for 24h were analyzed by fluorescence microscopy. Cells in which fluorescent-siRNA was transfected through lipofectamine were used as positive control (Fig. 3.9a). When cells were incubated with siRNA/PDA-MNPs the green fluorescent signal was slightly detectable, but if a GMF was applied to cells for 30 min before the 24 h incubation a significant number of green spots were detectable within the cytoplasm. Thus, the application of a magnet enhances the cellular uptake of PDA-MNPs. As expected, no green fluorescent signals were detectable when cells were incubated with equal amount of PDA-MNPs.

Flow cytometry analysis were performed to quantify the cellular uptake of PDA-MNPs in PEMs both in the absence and presence of GMF. In the absence of the GMF siRNA/PDA-MNPs was up-taken only by 17% of the cells (Fig. 3.9b); however, in the presence of a GMF more than 30% of the cells displayed a green fluorescence signal. By comparison, more than 92% of the PEMs stained positively if they were transfected through lipofectamine. All together these results indicate that PDA-MNPs could be promising candidates to delivery siRNA molecules to cells, especially when they are exposed to an external magnetic field.

3.8. PERK gene silencing in PEMs

To alter the unfolded protein response (UPR) in the endoplasmic reticulum (ER) of PEMs, the downregulation of PERK, one of three ER transmembrane sensors (Di Conza and Ho.,2020), was induced through the RNA interference (RNAi) mechanism. Thus, PEMs were transfected for 24h or 48h with lipocomplexes (LIPO/siPERK) as control, or were incubated for 24h or 48h with siPERK molecules coupled to PDA-MNPs. Lipofectamine 2000 and PDA-MNPs at the same concentrations were used as internal controls. The times were chosen on the basis of the experiments read-out, i.e. 24h if the effects were evaluated as gene expression by q-RT-PCR and 48h if the effects were evaluated as protein expression by immunoblotting.

Upon incubation of PEMs with PDA-MNPs/siPERK or LIPO/siPERK for 48h the expression of PERK protein is silenced in the case of LIPO/siPERK and down-regulated in the case of PDA-MNPs/siPERK in respect to cells incubated with their control complexes without siPERK and to untreated cells (Fig. 3.10a). Then, since the active PERK phosphorylates the downstream mediator eif2-α (Eukaryotic translation initiation factor 2), we assessed the activation (i.e. the phosphorylation) of this protein. Indeed, we found that the silencing of PERK reduced significantly the phosphorylation of eif2-α in respect to the untreated cells and control cells treated with nanocomplexes and Lipofectamine without siPERK. In this series of experiments we also treated cells with tunicamycin (TM), a well-known ER-stressor. Indeed, we found that tunicamycin abrogated the expression of the

PERK protein, but significantly increased the phosphorylation of eif2-α. Overall, these results confirm the ability of the nanocarriers to induce the silencing of a target gene into cells.

The downregulation of the PERK gene in PEMs was then evaluated by q-RT-PCR analyzing the expression levels of PERK downstream targets ATF4 and CHOP. In this case PEMs incubated with siPERK containing complexes and GSK-414, which is a selective inhibitor of PERK, were then treated in the last 8h with tunicamycin, which increased the expression of these two target genes, which were down-regulated if cells were incubated with siPERK associated with PDA-NPs and LIPO (Fig. 3.10b).

Under ER-stress the UPR signal activators act in a coordinated way to detect misfolded proteins in ER and to re-establish the cellular homeostasis. Therefore, the activities of IRE-1 and ATF6, other ER-stress sensors along with PERK (Chang et al., 2018), were examined after the knockdown of the PERK. After 24h from PERK inhibition with PDA-MNPs/siPERK and LIPO/siPERK, the expression of ATF6 and the spliced form of XBP1, a downstream effector of IRE-1 (Sicari et al., 2020), was analyzed by q-RT-PCR. GSK-414 was used as further internal control in these experiments. Results (Fig. 3.10b) indicate that in all cases the PERK inhibition increased the activity of other ER-stress sensors compared to untreated cells, but not at the same way of the positive control, which was represented by tunicamycin. In particular, it was observed a significantly increase of the splicing of XBP1 when cells were treated with lipo-complexes or GSK-414, less in the case of nanoparticles. As already discussed, it is worth highlighting that XBP1s is involved in promoting the M1 phenotype, which is associated with inflammatory diseases.

3.9. Characterization and *in vitro* differentiation of PEMs

The primary macrophages derived from murine peritoneal exudate (PEMs) were used for most of the experiments, since they represent better than the RAW 264.7 cell line the properties of the *in vivo* macrophages, also in view of the possibility to extend these studies *in vivo*. PEMs were isolated as described in the materials and methods section; in particular they were recovered from BALB/c mice, which received the local administration of thioglycolate to increase the yield of the peritoneal cells from 2-3 to 9-12 million for mouse without altering the physiological characteristics of the cells (Zhao et al ., 2017). The size and granularity of the adherent cells recovered after 16h culture were analyzed by flow-cytometry: these peritoneal cells were dispersed among a minimum of two populations highlighting their heterogeneity (Fig. 3.11a). Indeed, the peritoneal cavity is a common source not only of macrophages, but also of different immune cell types, such as B- and T-cells, dendritic cells (DCs) and natural killer (NK)(Cassado et al.,2015). Therefore, PEMs for the expression of the surface markers CD45(Altin and Sloan., 1998), CD11b and F4/80 by flow cytometry to confirm their macrophage identity. About 47% of population were hematopoietic cells, being CD45-positive, whose 70% also expressed CD11b with high levels of F4/80[+] (Fig. 3.11b). Both CD11b and F4/80[+] are macrophage markers, but while CD11b receptors are also expressed on the surface of other leukocytes, the glycoprotein F4/80+ is exclusively expressed on macrophages (Cassado et al.,2015) . Overall, these data clearly show that about 60% of recovered cells are macrophages. It is well-known that these cells can acquire distinct functional phenotypes in response to their local microenvironment.

This dynamic process of macrophage functional change is defined as macrophage polarization characterized by two extreme poles referred as classically activated macrophages (M1) and alternatively activated macrophages (M2) (Kasfi et al., 2021). In particular, M1 macrophages are responsible for ongoing immune surveillance against pathogenicity; while M2 macrophages assume a predominantly anti-inflammatory role, attenuating the host immune response. Interestingly, the phenotype of polarized M1 and M2 macrophages can be also achieved in *in vitro* experiments using specific cytokines and growth factors (Hörhold et al., 2020; Poltavets et al., 2020). Thus, we also

investigated whether primary peritoneal macrophages (PEMs) could be induced to differentiate *in vitro* towards either the M1 or the M2 phenotypes. PEMs were isolated on the basis of their adherence properties and cultured for 5 days with the macrophage colony-stimulating factor (m-CSF) to promote their survival and the proliferation of mature monocytes/macrophages (Otero et al.,2009; Hamidzadeh et al., 2020). Cells were then stimulated for 48 h with IFN-γ and LPS to differentiate M1 or treated with IL-4 to induce the M2 state. To evaluate whether the M1/M2 polarization in PEMs occurred, we analyzed the expression of CD86 and CD206 that are specific markers for M1 and M2 phenotypes, respectively. Fig. 3.12a shows that nearly 30% of the $F4/80^+$ cells expressed also the mannose receptor CD206 on their surface, whose levels reached a value of 60% when PEMs were stimulated with IL-4. In contrast, the expression of CD206 decreased from 48% in untreated cells to about 13% after LPS/ IFN-γ treatment. In the mirror experiments, the basal expression of CD86 protein, which was low in untreated macrophage population (2%), was significantly increased (48%) following the stimulation with LPS/IFN-γ, treatment able to switch PEMs into a pro-inflammatory state. The data obtained in flow cytometry were confirmed in immunofluorescence experiments with FITC-labeled CD86 and CD206 antibodies visualized at the confocal microscopy. Indeed, CD86 staining was detected when macrophages were incubated with LPS plus IFN-γ (Fig. 3.12b), while CD206 expression was significantly increased in PEMs cells treated with IL-4 compared to untreated macrophages (Fig. 3.12c).

To better characterize the two phenotypes acquired *in vitro* by PEMs upon cytokine treatments, cells were stimulated as above and the expression of genes specifically associated to the two phenotypes were evaluated by q-RT-PCR analysis. Based on the literature we choose to analyze the expression of some cytokines (TNF-α, COX-2, TGF- β), enzymes (iNOS, Arg-1) and the nuclear receptor PPAR-γ (Jablonski et al., 2015). As shown in Fig. 3.12d the relative mRNA levels of TNF-α, COX-2 and iNOS were significantly higher in macrophages treated with LPS/INF-γ (M1 phenotype), while the expression of TGF- β, Arg-1 and PPAR-γ was increased in macrophages treated with IL-4 (M2 phenotype). All together, these findings indicate that PEMs can be induced to differentiate into M1 and M2 macrophages following stimulation with specific biomolecules.

3.10 PDA/MNPs promote M1 polarization of PEMs

Since the iron exposure of cells is correlated to an inflammatory macrophage phenotype (Mulens-Arias et al., 2020, 2021a), we investigated the effects of PDA-MNPs on the macrophage polarization of PEMs. Thus, peritoneal macrophages derived from BALB/c mice, after 5 days cultivation in the presence of m-CSF, were incubated for different times with 100 μg/mL PDA-MNPs, and then the expression of the genes associated with the pro-inflammatory phenotype, such as iNOS, TNF-α, and COX-2, was analyzed by q-RT-PCR, using macrophages treated LPS/IFN-γ for 8h as positive control. The three genes considered were all upregulated; in particular, iNOS mainly after 8h treatment with nanoparticles, while TNF-α and COX-2 even after 4 and 16h treatment (Fig. 3.13a). All the genes were downregulated after 24 h treatment, switching back to nearly basal levels. Thus, the inflammatory response induced in PEMs is temporary and cells can control it (Fig. 3.4b). These data were confirmed in another series of experiments evaluated by flow cytometry. Upon incubation with m-CSF the original cell population obtained from the peritoneal exudate expressed the F4/80 marker, and after further incubation with PDA-MNPs (100 μg/mL) for three days PEMs increased the expression of the M1 phenotype markers CD86 and CD80 (from 9 and 34% to 59 and 67% respectively) (Fig. 3.13b). These values were even higher than the ones observed in samples stimulated with LPS/INF-γ. Finally, also immunofluorescence experiments confirmed the ability of PDA-MNPs to promote the M1 macrophage phenotype in PEMs. Indeed, the expression of CD86 (Fig.3.13c) and CD80 (Fig. 3.13d), visualized as green signals, was increased after 3 days incubation with nanoparticles. From all these experiments it is thus clear that PDA-MNPs can induce M1 macrophage polarization.

3.11. Reprogramming TAMs-like macrophages toward the M1 phenotype

Macrophages present in the tumor microenvironment (TME) are called tumor-associated macrophages (TAMs) and have a crucial role in the development and progression of cancer, with an immunosuppressive role (Lin et al., 2021). Indeed, it is well established that TAMs have a M2-like phenotype and display an irregular UPR response in their ER in order to endure the environment stress, to which they are subjected. We thus planned a series of experiments to examine the ability of PEMs induced to M2 phenotype to switch from the M2 to the M1 phenotype upon incubation with the PDA-MNPs/siPERK nanocomplexes. LIPO/siPERK along with GSK-414 inhibitor were used as positive controls. First, PEMs were polarized toward M2 phenotype with IL-4 as previously described, and then they were treated for 8h with ER-stressor tunicamycin in order to induce TAMs-like macrophages with an M2 phenotype. Herein, PEMs will be named as M0, M1, M2, and M2/TM if untreated, treated with LPS/IFN-γ, treated with IL-4 and treated with IL-4 and tunicamycin (TAMs-like macrophage), respectively. In agreement with recent studies which reported that the PERK arm of the UPR is uniquely upregulated in TAMs (Raines et al., 2022; Sheshadri et al., 2021), we validated this observation in our model where the expression of PERK, as well as that of the downstream genes ATF4 and CHOP, were increased in PEMs treated with IL-4 and TM (M2/TM; Fig. 3.14a). When these cells were incubated for 24 or 48h with LIPO/siPERK, PDA-MNPs/siPERK and PERK inhibitor GSK-414, a significant inhibition of the expression of PERK, ATF4 and CHOP by q-RT-PCR was evident (Fig. 3.14a). The treatment with LIPO/siPERK, PDA-MNPs/siPERK and GSK-414 inhibited also the phosphorylation of eiF2α, as detected in immunoblotting (Fig. 3.14b). Thus, PEMs cells treated with IL-4 and TM represent a promising *in vitro* model to investigate the macrophage reprogramming from M2 to M1 phenotype. To evaluate the ability of PDA-MNPs/siPERK to re-educate TAMs-like macrophages from the M2 to the M1 phenotype, the expression of gene markers of two phenotypes were examined by q-RT-PCR after cells were incubated for 24h with nanocomplexes, as well as with LIPO/siPERK and GSK-414. Notably, we found that in TAMs-like macrophages the downregulation of PERK enhanced the expression of M1 markers iNOS and TNF-α, while it decreased the expression of the gene markers of the M2 macrophage phenotype Arg-1, TGF-β and PPAR-γ (Fig. 3.14c).

The transcriptional reprogramming of macrophages is complex, and it is regulated by different signaling molecular pathways including the NF-κB, MAPKs and STAT3 (Sun et al., 2016). It is well-known that the activation of NF-κB p65 is a hallmark of M1 macrophage activation regulating the expression of an array of inflammatory genes; in addition, its activation is associated with the overactivation of IRE-1, the ER-stress sensor, which collaborates with PERK (Jiang et al., 2021). The activation of the STAT3, instead, drives the transcription of many genes associated with M2 macrophage phenotype, typical of TAMs (Riera-Borrull et al., 2017). Likewise, the ERK 1-2 signaling activation facilitates the macrophage differentiation toward an M2 phenotype promoting angiogenesis, cancer cell migration, and invasion (Gao et al., 2018) . Therefore, we investigated how the inhibition of PERK in TAMs-like macrophages affected these molecular mechanisms. After PEMs were polarized toward M2 phenotype and incubated for 48h with siRNA-lipo-complexes and nanocomplexes, the phosphorylation levels of NF-κBp65, ERK1/2 and STAT3 were analyzed by immunoblotting. GSK-414 was used as a further control. Western blot results (Fig. 3.14d) along with the densitometric analysis of relative bands (Fig. 3.14e) showed that in all cases, the knockdown of the PERK protein into TAMs-like macrophages activated NF-kBp65 suggesting that the switch from the M2 to the M1 phenotype took place. Moreover, the phosphorylation of STAT3 and ERK1/2 was inhibited following the downregulation of PERK in macrophages confirming their polarization toward the M1 phenotype. To confirm that PDA-MNPs/siPERK and lipo-complexes induced the re-polarization of TAM-like macrophages, we examined by flow cytometry the expression of CD86 and CD206, specific markers of the M1 and the M2 phenotypes, respectively. It is evident from histograms in Fig. 3.14f that the expression of the CD86 on the surface of macrophages was

significantly increased after the inhibition of PERK, in particular in the case of PDA-MNPs/siRNA. By contrast, the expression of CD206 decreased of about 30% in the case of PDA-MNPs/siPERK. Taken together, the results of this study indicate that TAMs-like macrophages can switch to the M1-inflammatory phenotype by the inhibition of ER-stress sensor PERK.
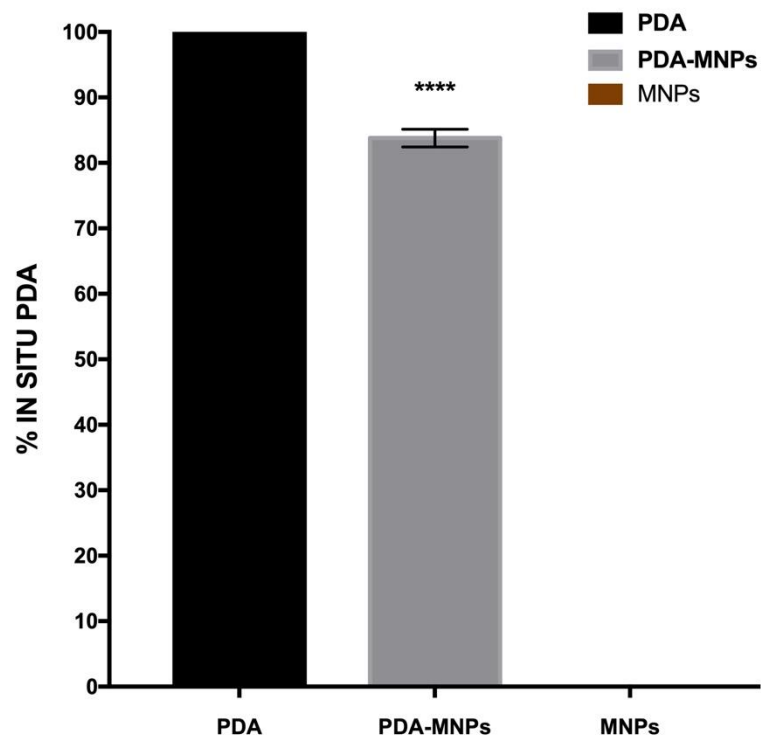
Figures

(a)
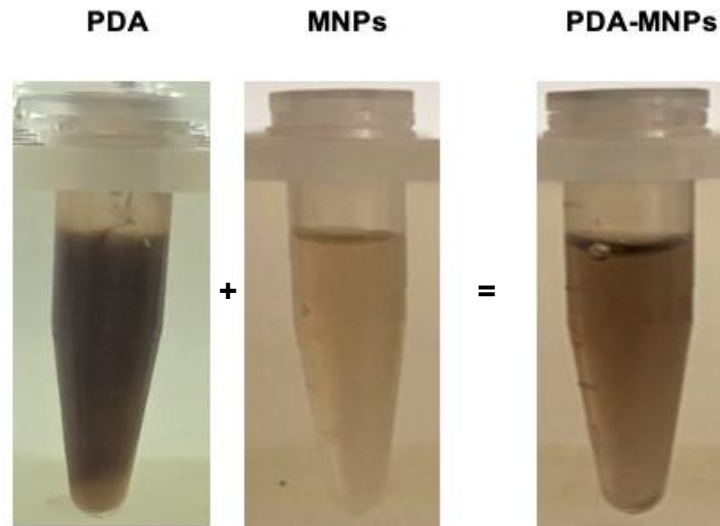
(b)

Fig. 3.1. Adsorption of PDA on MNPs. (a) Representative images of dopamine after polymerization reaction (PDA) and MNPs before and after coupling (PDA-MNPs). **(b)** Values of PDA (polymerized *in situ*) measured at 550nm. Percentage of ratio between PDA and PDA-MNPs or MNPs alone are shown. The results were obtained in three independent experiments made in triplicates. Differences between groups assessed by 2-way ANOVA with Bonferroni's multiple comparison post-test (**** $p < 0.0001$).

(a)

(b)

(c)
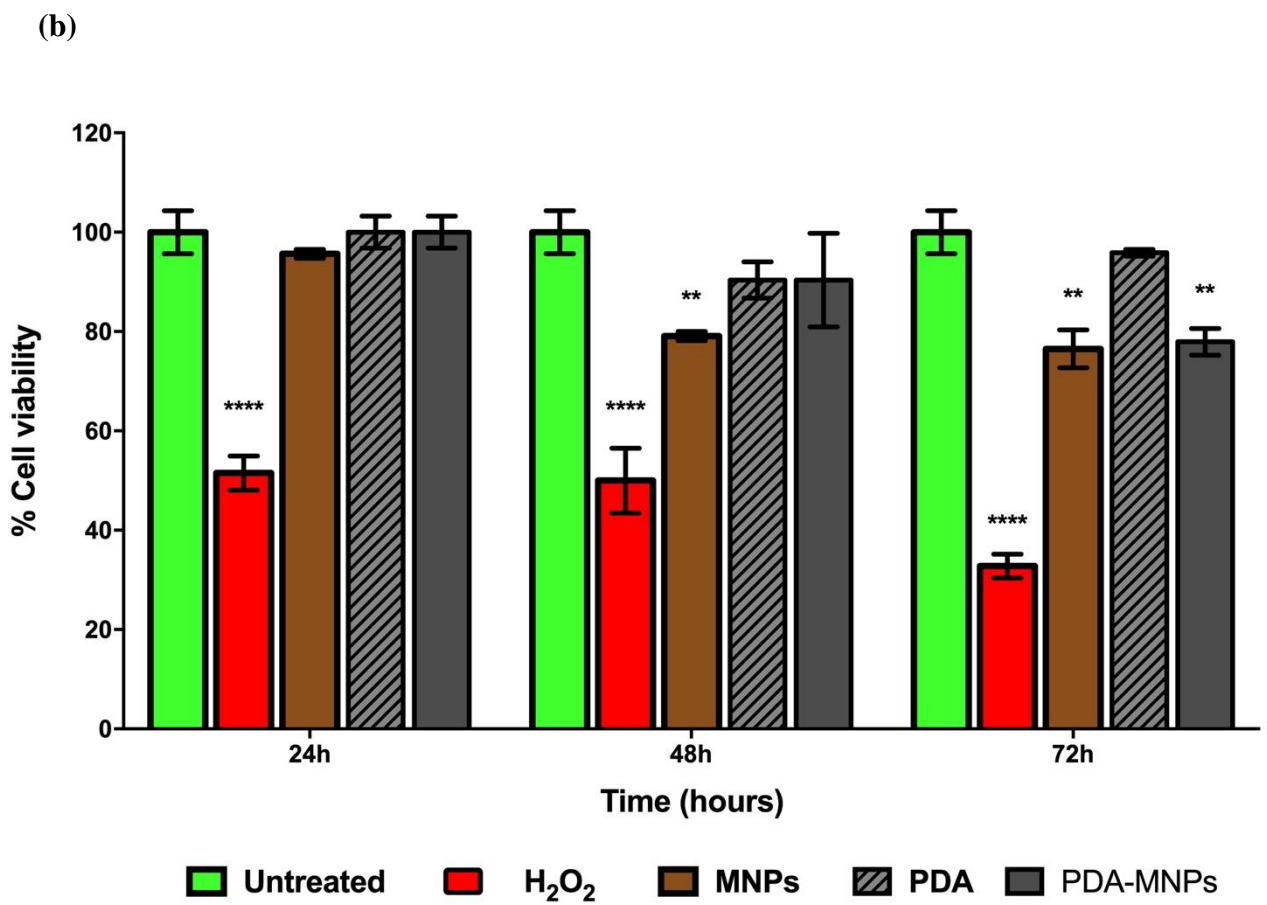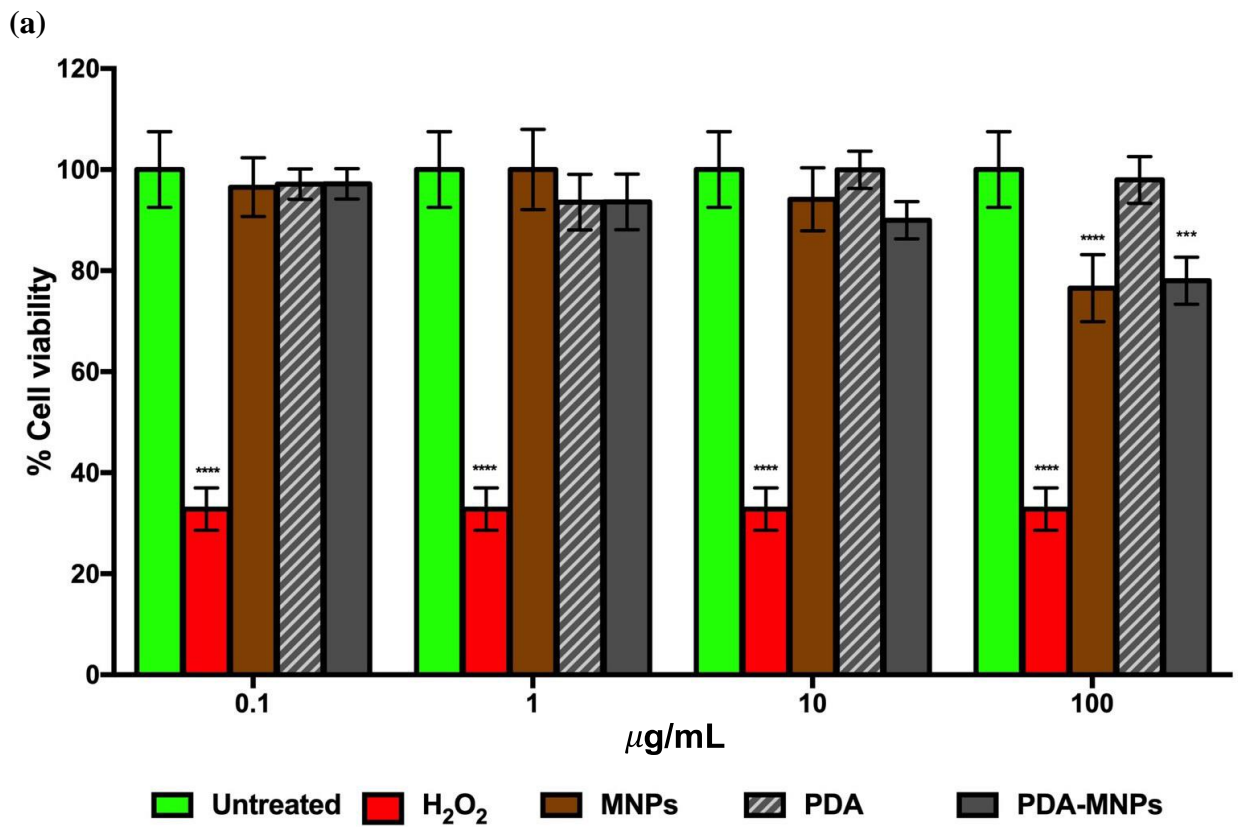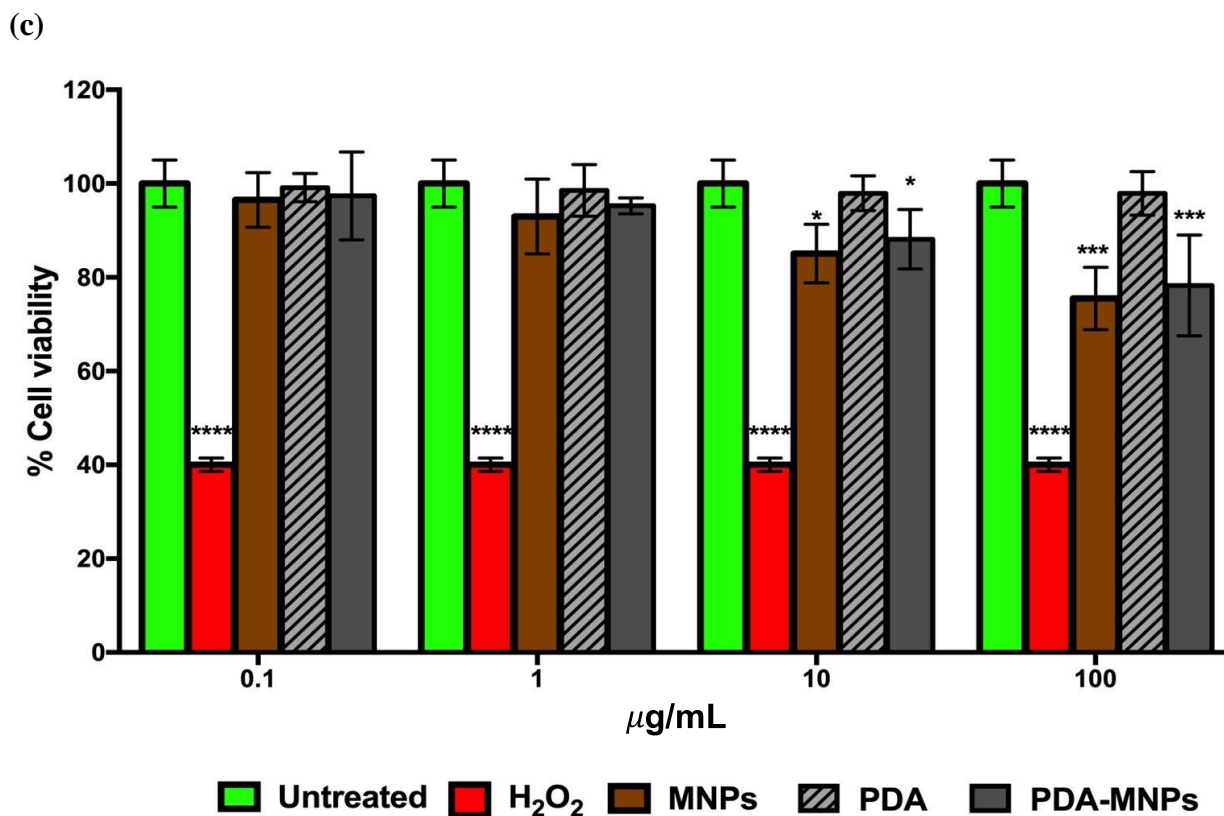
Fig. 3.2. Cytocompatibility of PDA-MNPs on RAW 264.7 cells (a, b) and PEMs (c). Cells were incubated with PDA-MNPs at different concentrations **(a,c)** for 72 h. RAW 264.7 cells were incubated for different periods of time with MNPs at 100 µg/mL concentration (**b).** Cell viability was assessed with MTT assays at each time point. Untreated cells were taken as reference value (100%), while the exposure to H_2O_2 at 1 µM represented the positive control. Data are expressed as means ± SD of at least four independent experiments performed in triplicate. Statistical analyses were carried out using One-way ANOVA, with Bonferroni comparison post-test vs the untreated controls (* $p \leq 0,05$; ** $p \leq 0,01$; *** $p \leq 0,001$; **** $p < 0.0001$).
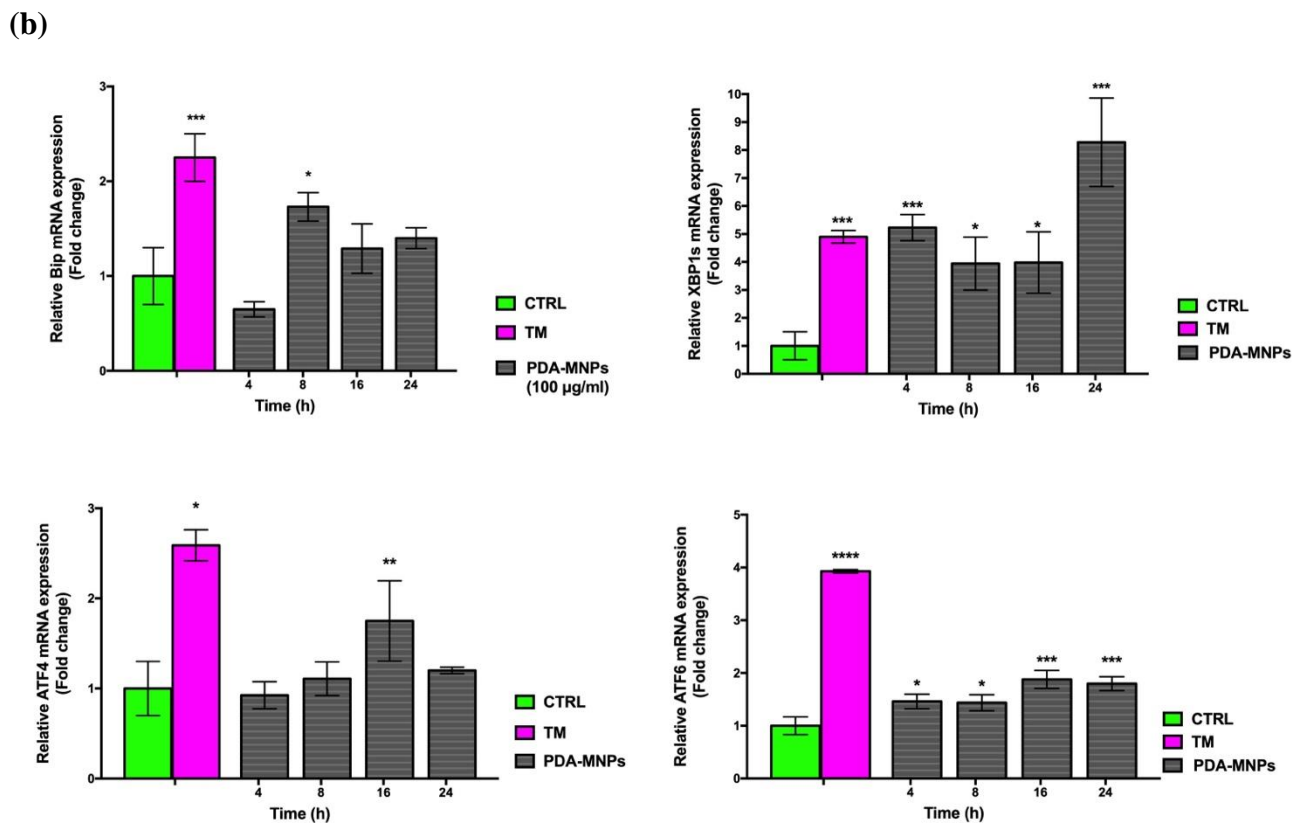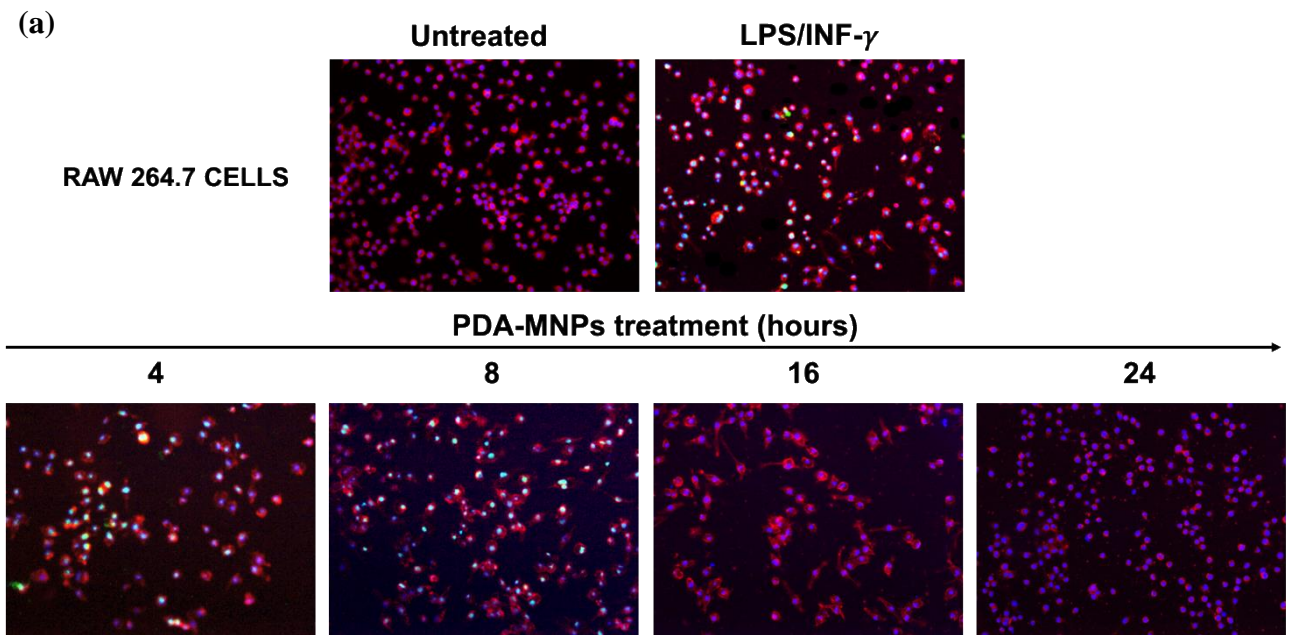
Fig. 3.3. ROS and ER-stress levels in RAW264.7 cells after exposure to PDA-MNPs. (a) Immunofluorescence images showing reactive oxygen species (ROS) production in cells incubated with PDA-MNPs (100 µg/mL) for different time points (from 4 to 24 h). Fixed and permeabilized cells were stained for actin with TRITC-phalloidin (red) and for nuclei with DAPI (blue), while the ROS production was visualized in green. LPS/INF-γ 24 h treated cells were used as positive control. Magnification, 200x. (b) Histograms showing the expression of ER-stress markers (Bip, XBP1s, ATF4 and ATF6) assessed by q-RT-PCR on cells incubated with PDA-MNPs (100 µg/mL), in the same conditions as above. ER-stress was mostly observed in cells treated with tunicamycin 2µg/mL for 8 h, used as positive control. Gene expression is shown as fold-change relative to untreated cells. Data are expressed as mean ± SD of three independent experiments (*p ≤ 0,05; **p ≤ 0,01; ***p ≤ 0,001; **** p < 0.0001).

Fig. 3.4. ROS and ER-stress levels in PEMs (peritoneal macrophages) after exposure to PDA-MNPs. **(a)** Immunofluorescence images showing reactive oxygen species (ROS) production in cells incubated with PDA-MNPs (100 μg/mL) for different time points (from 4 to 24 h). Fixed and permeabilized cells were stained for actin with TRITC-phalloidin (red) and for nuclei with DAPI (blue), while the ROS production was visualized in green. LPS/INF-γ 24 hours treated cells were used as positive control. Magnification, 200x. **(b)** Histograms showing the expression of ER-stress markers (Bip, XBP1s, ATF4 and ATF6) assessed by q-RT-PCR on cells incubated with PDA-MNPs (100 μg/mL), in the same conditions as above. ER-stress was mostly observed in cells treated with tunicamycin 2μg/mL for 8 h, used as positive control. Gene expression is shown as fold-change relative to untreated cells. Data are expressed as mean ± SD of three independent experiments (*p ≤ 0,05; **p ≤ 0,01; ***p ≤ 0,001; **** p < 0.0001).
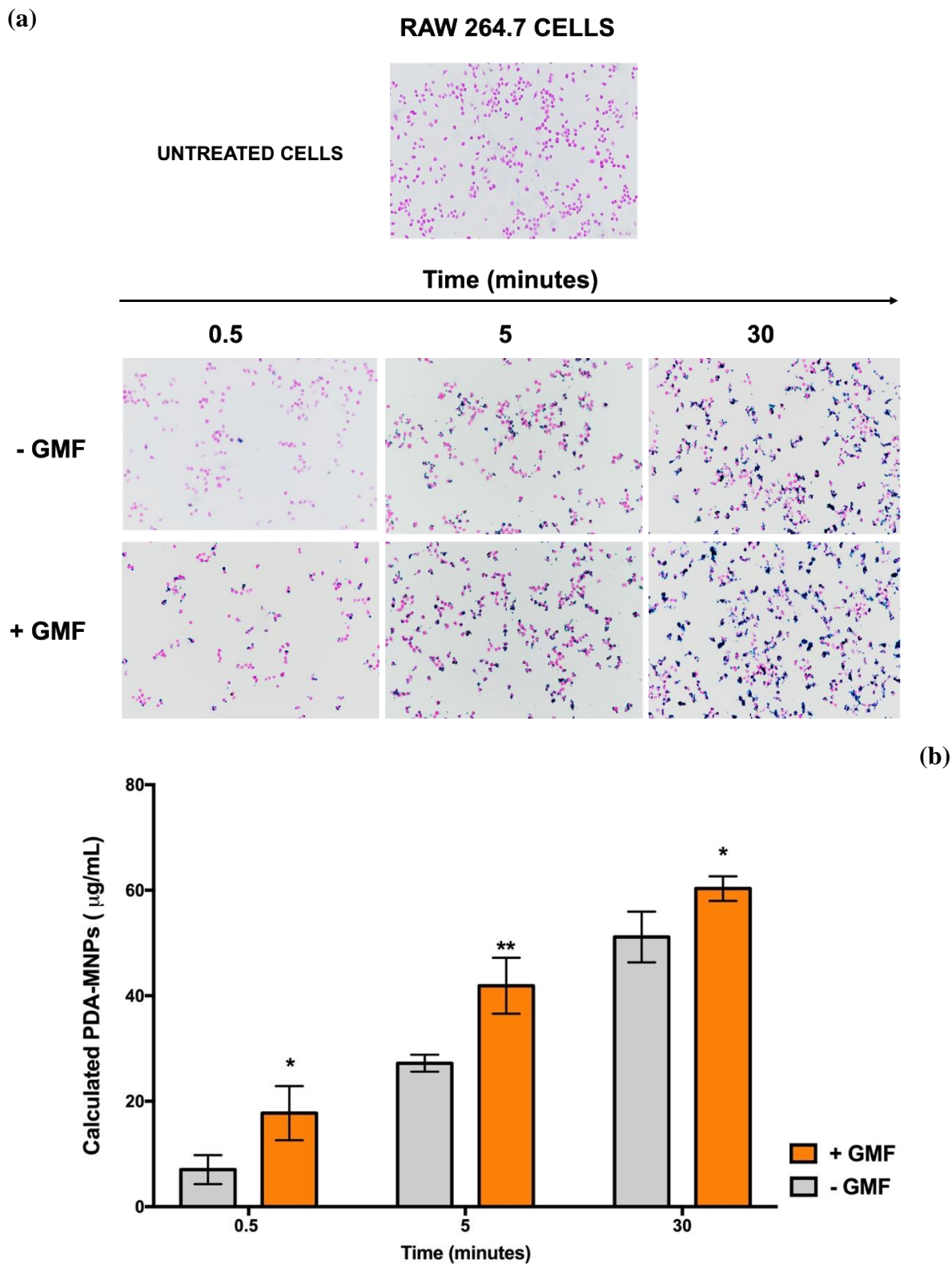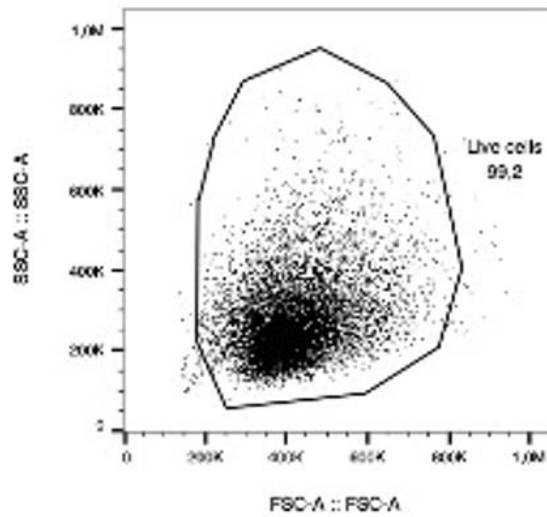
Fig. 3.5. Interaction of PDA-MNPs with RAW 264.7 cells in presence/absence of a gradient magnetic field (GMF). (a) Images showing cells treated with PDA-MNPs and stained Prussian blue staining and nuclear fast red counterstaining. Magnification 200x. **(b)** Amount of iron associated with cells as quantified with potassium thiocyanate: Cells were incubated with PDA-MNPs for different time-points (from 0.5 to 30 min) in absence (-GMF) or presence (+GMF) of a gradient magnetic field. Untreated cells were used as negative control. Results are expressed as mean μg/mL ± SD and were obtained from three independent experiments performed in triplicates. Data were analyzed by 2-way ANOVA with Bonferroni's multiple comparison post-test. (* $p < 0.05$; ** $p < 0.01$).
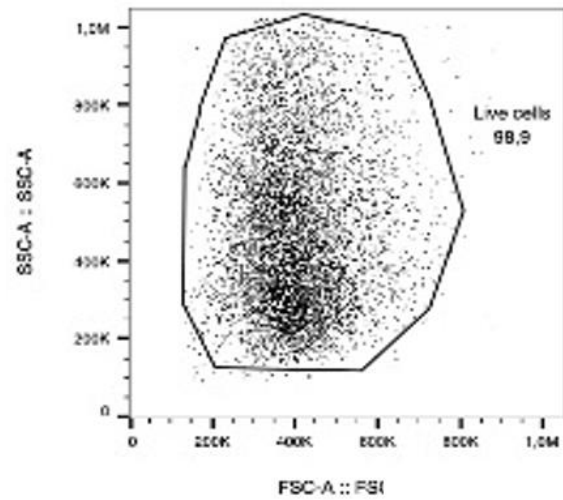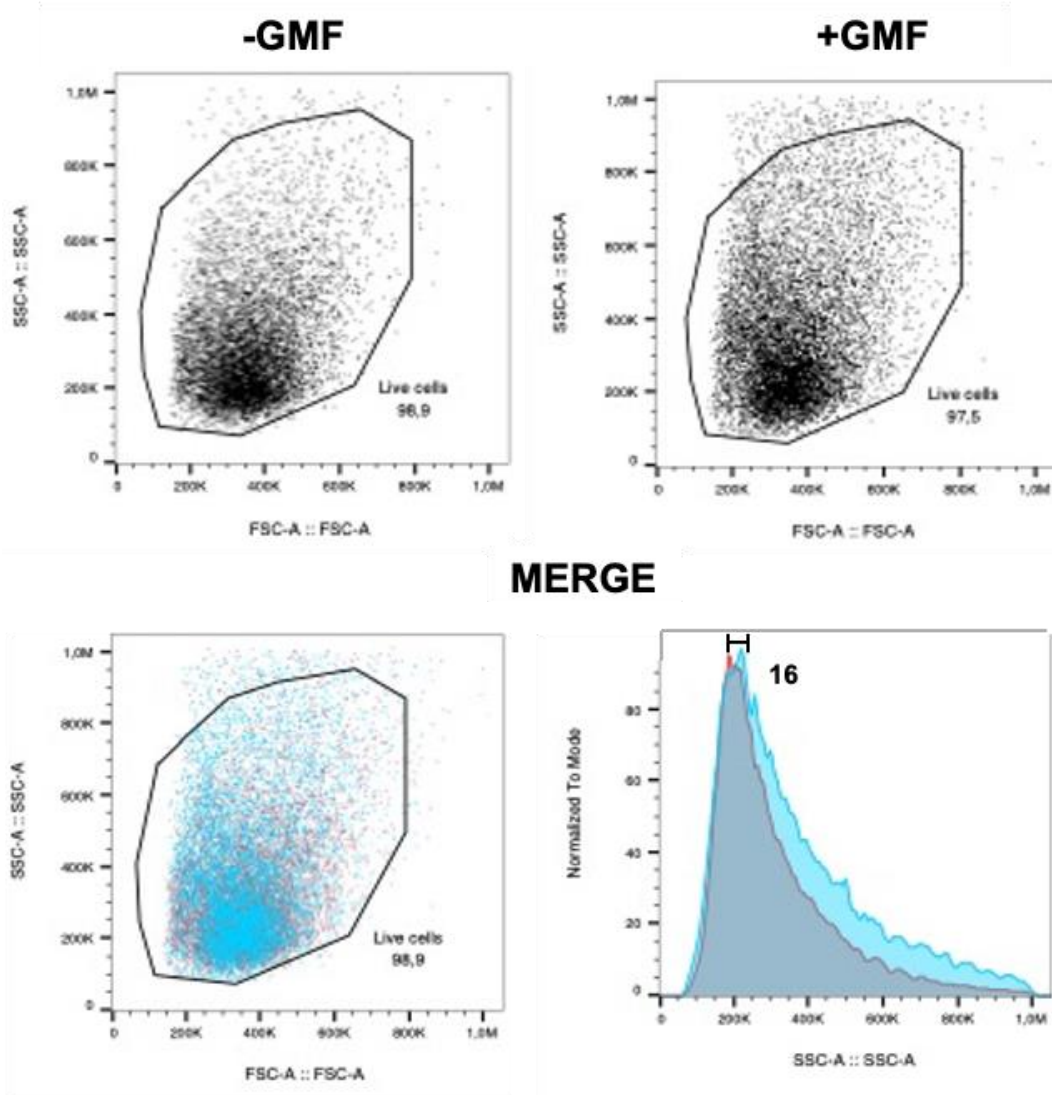
(a)

PERITONEAL MACROPHAGES (PEMs)
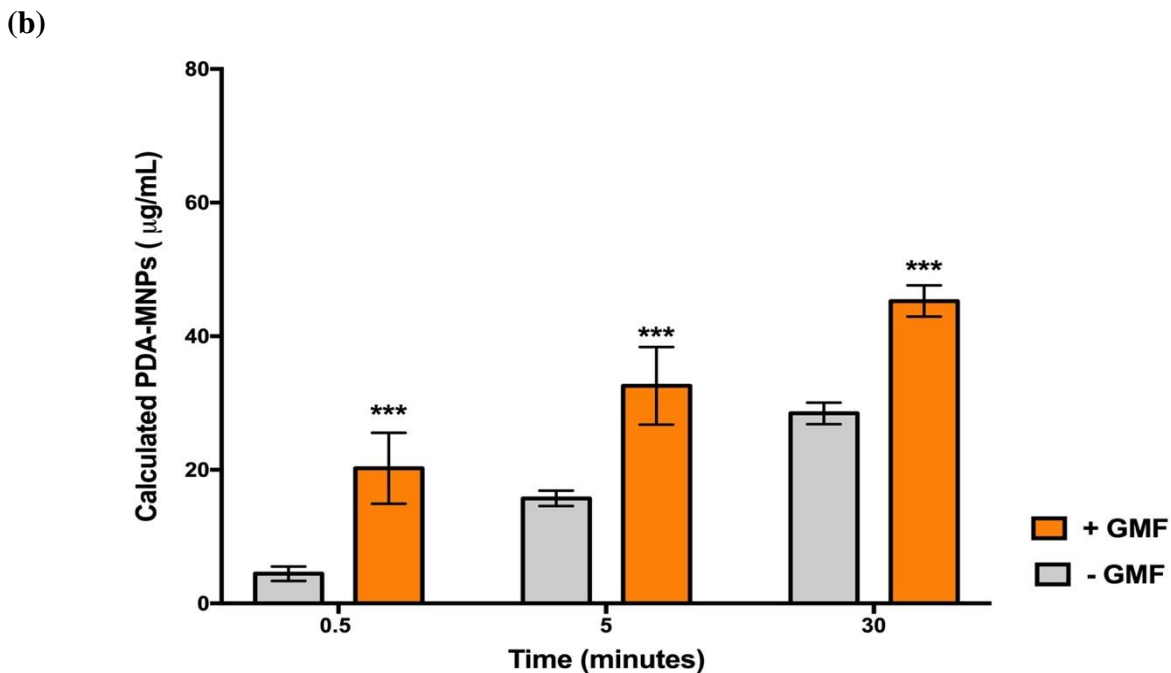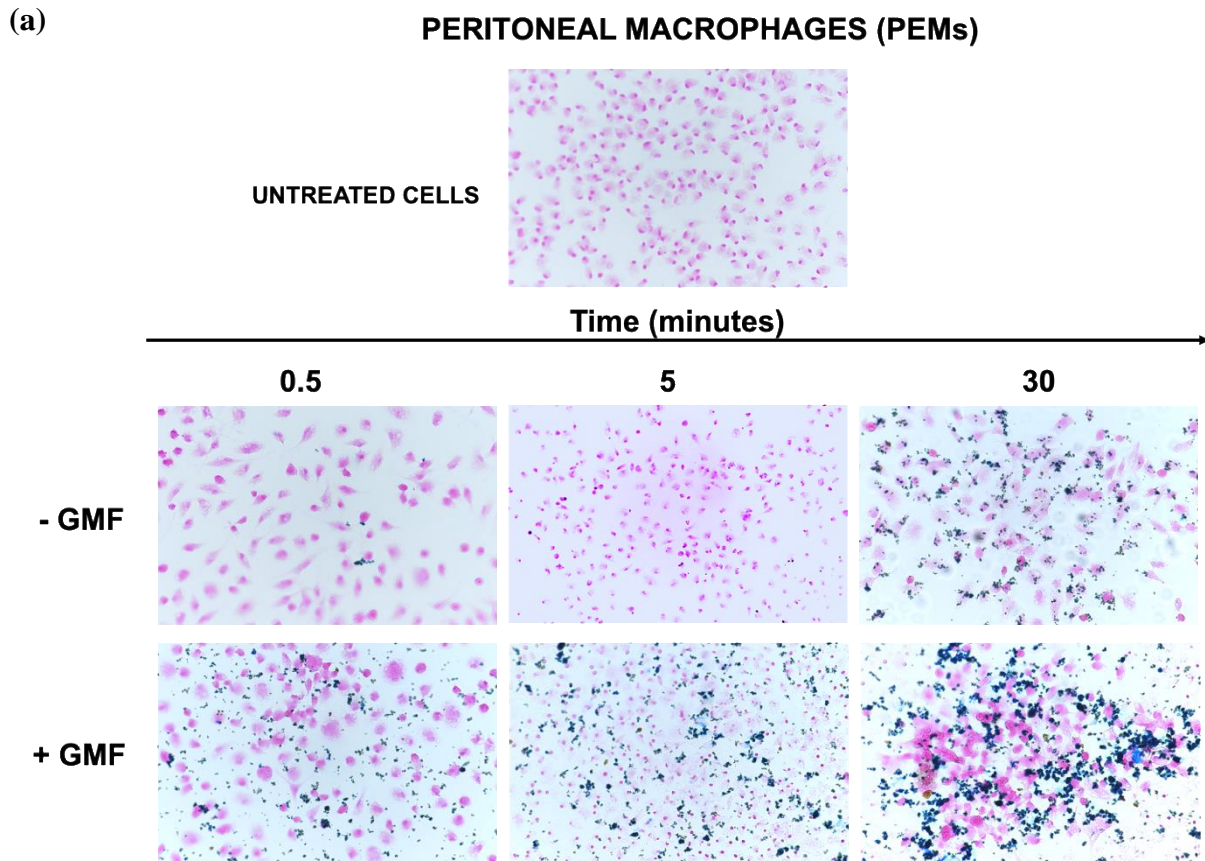
Fig. 3.6. Interaction of PDA-MNPs with PEMs in presence/absence of a gradient magnetic field (GMF). **(a)** Images showing PEMs treated with PDA-MNPs and stained Prussian blue staining and nuclear fast red counterstaining. Magnification 200x. **(b)** Amount of iron associated with cells as quantified with potassium thiocyanate: Cells were incubated with PDA-MNPs for different time-points (from 0.5 to 30 min) in absence (-GMF) or presence (+GMF) of a gradient magnetic field. Untreated cells were used as negative control. Results are expressed as mean µg/mL ± SD and were obtained from three independent experiments performed in triplicates. Data were analyzed by 2-way ANOVA with Bonferroni's multiple comparison post-test. (*** $p <$ 0.001)

PRIMARY MURINE MACROPHAGES (PEMs)

(b)
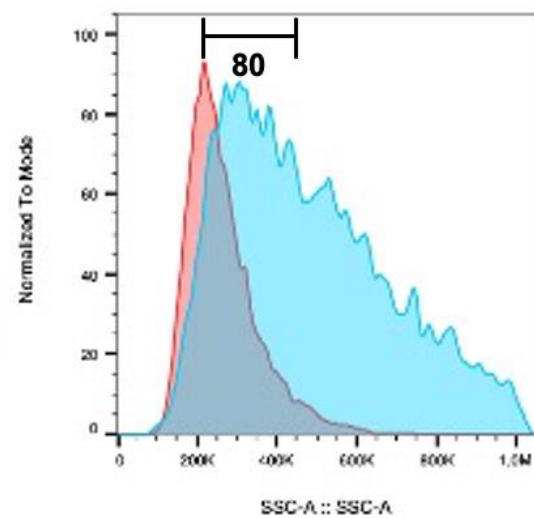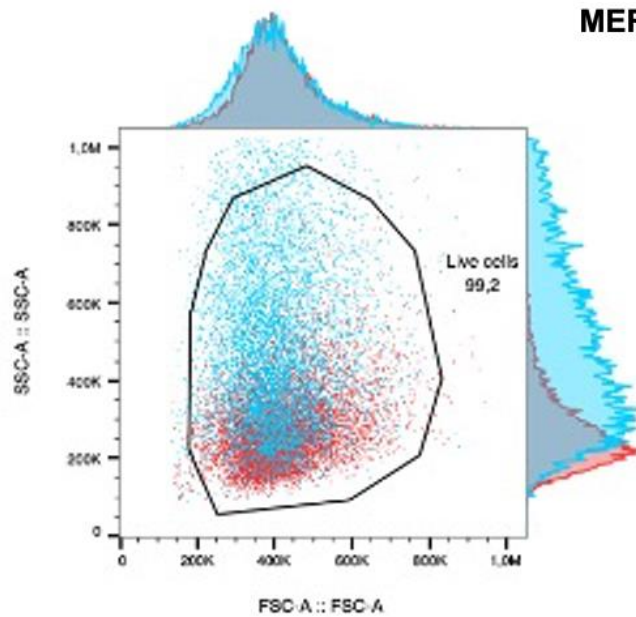
Fig. 3.7. Interaction of PDA-MNPs with PEMs in presence/absence of a gradient magnetic field (GMF). **(a)** Representative images showing the granularity and size of untreated control cells (left) or cells treated with PDA-MNPs 20µg for 24h (righ). Merge panels are shown below. **(b)** The apposition of a GMF increases the granularity of cells treated with PDA-MNPs (right), in respect to the lack of exposure to GMF (left). Merge panels are shown below and were used for calculations.
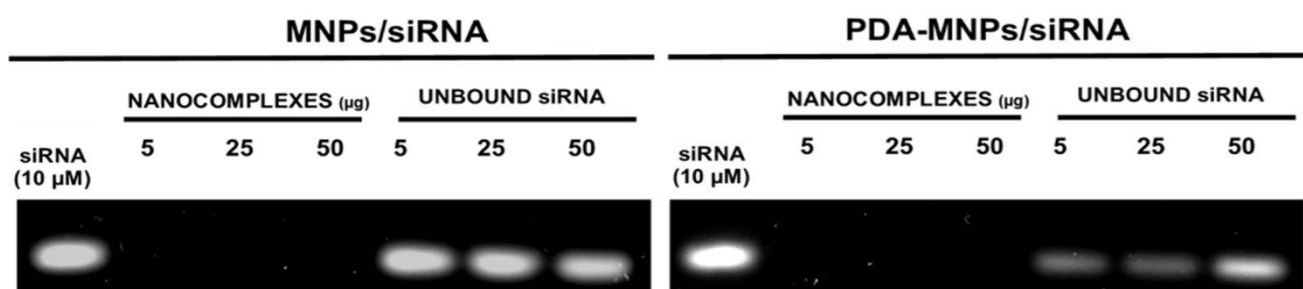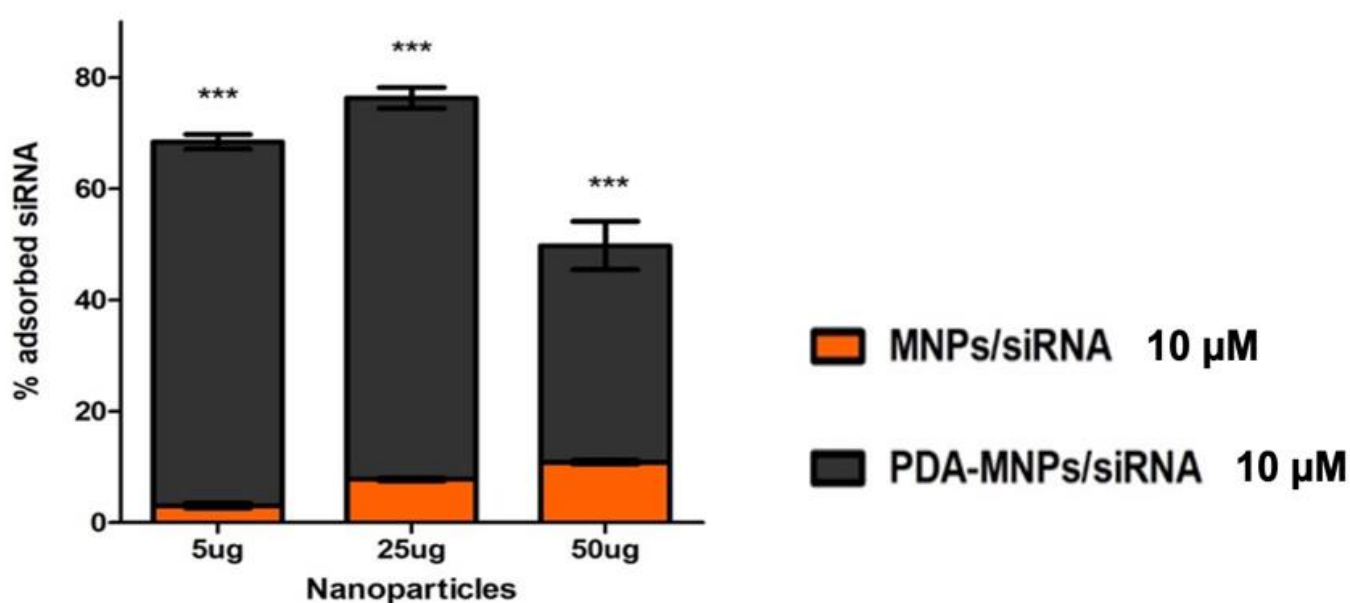
Fig. 3.8. Loading of siRNA onto MNPs requires the presence of PDA on MNPs. (a) Images show the amount of siRNA unbound after incubation with MNPs (left) and with PDA-MNPs (right), as examined by agarose gel electrophoresis. This assay does not allow the visualization of siRNA bound to either MNPs or PDA-MNPs, although present. Different ratios of nanoparticles with 10 μM siRNA were used in this typical experiment. **(b)** Quantification of percentage of siRNA bound to MNPs or PDA-MNPs, obtained by subtracting from the total siRNA the amount of unbound siRNA after magnetic decantation (densitometric analysis). Results are expressed as % absorption $\pm$ SD and were obtained from three independent experiments performed in triplicates. Data were analyzed by 2-way ANOVA with Bonferroni's multiple comparison post-test. (*** $p < 0.001$).
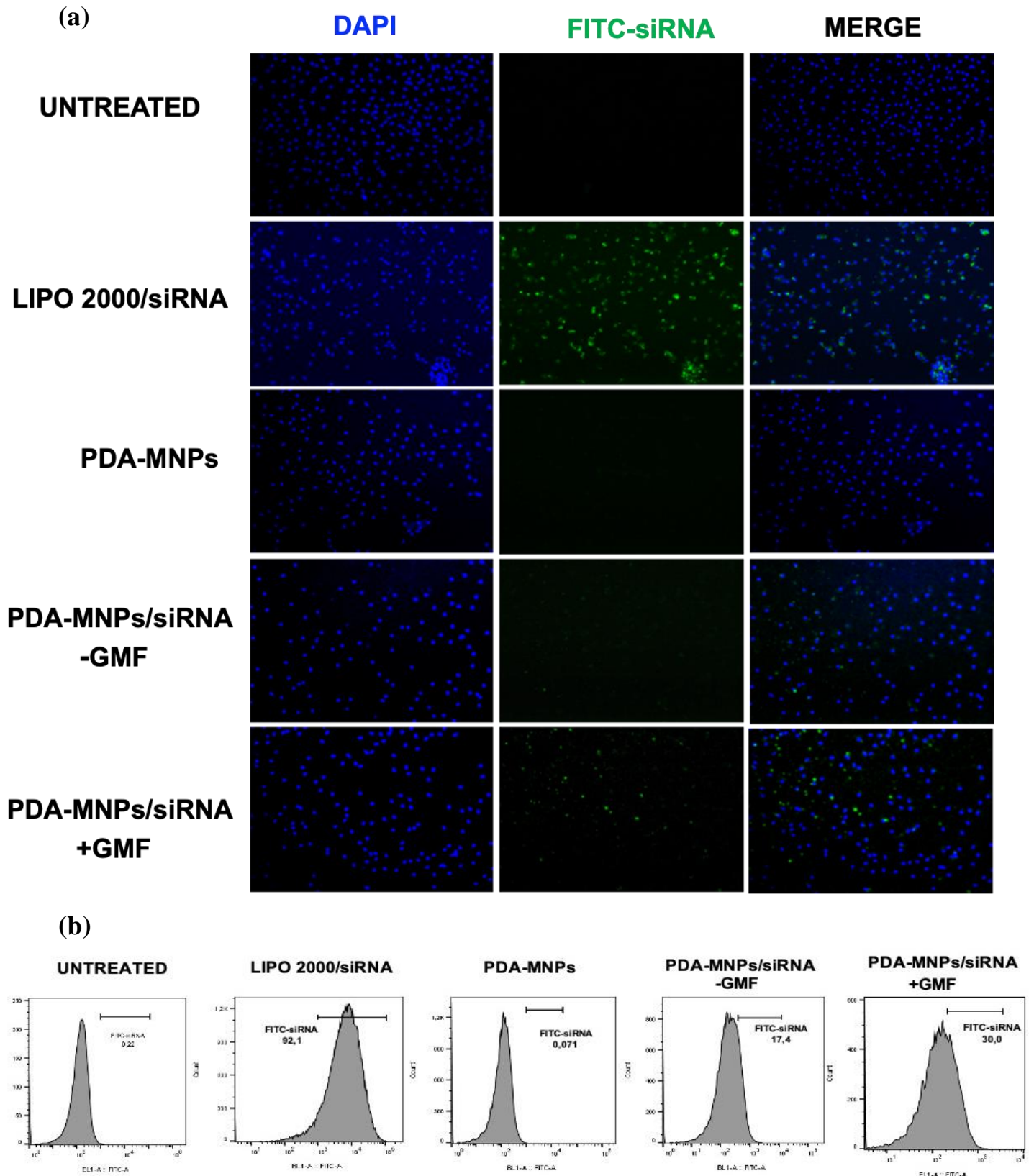
Fig. 3.9. Typical experiments showing cellular uptake of PDA-MNPs/siRNA. (a) Fluorescence microscopy to measure the delivery of siRNAs loaded on nanoparticles into PEMs in presence/absence of GMF. Cells were incubated with FITC-labeled siRNAs complexes (20 µg) for 24h. Images were acquired after fixation, permeabilization, and staining for nuclei with DAPI (blue). siRNA transfection with Lipofectamine 2000 (LIPO) and PDA-MNPs alone represented the controls. **(b)** Cell uptake efficiency in PEMs, measured by flow cytometry. Values of FITC-siRNAs are indicated for each treatment.

(a)
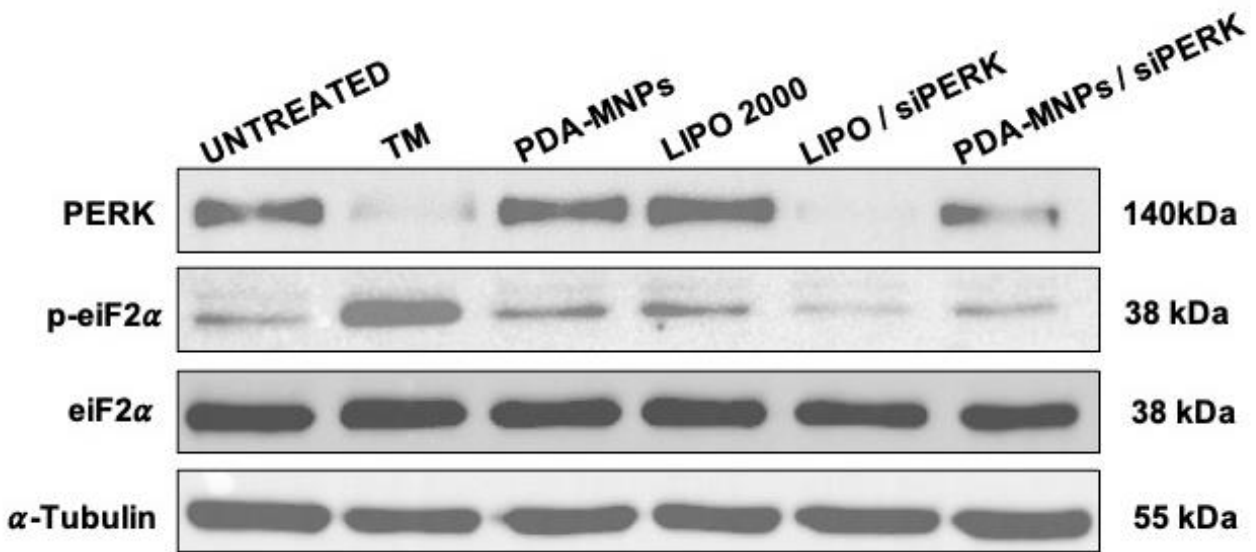
(b)
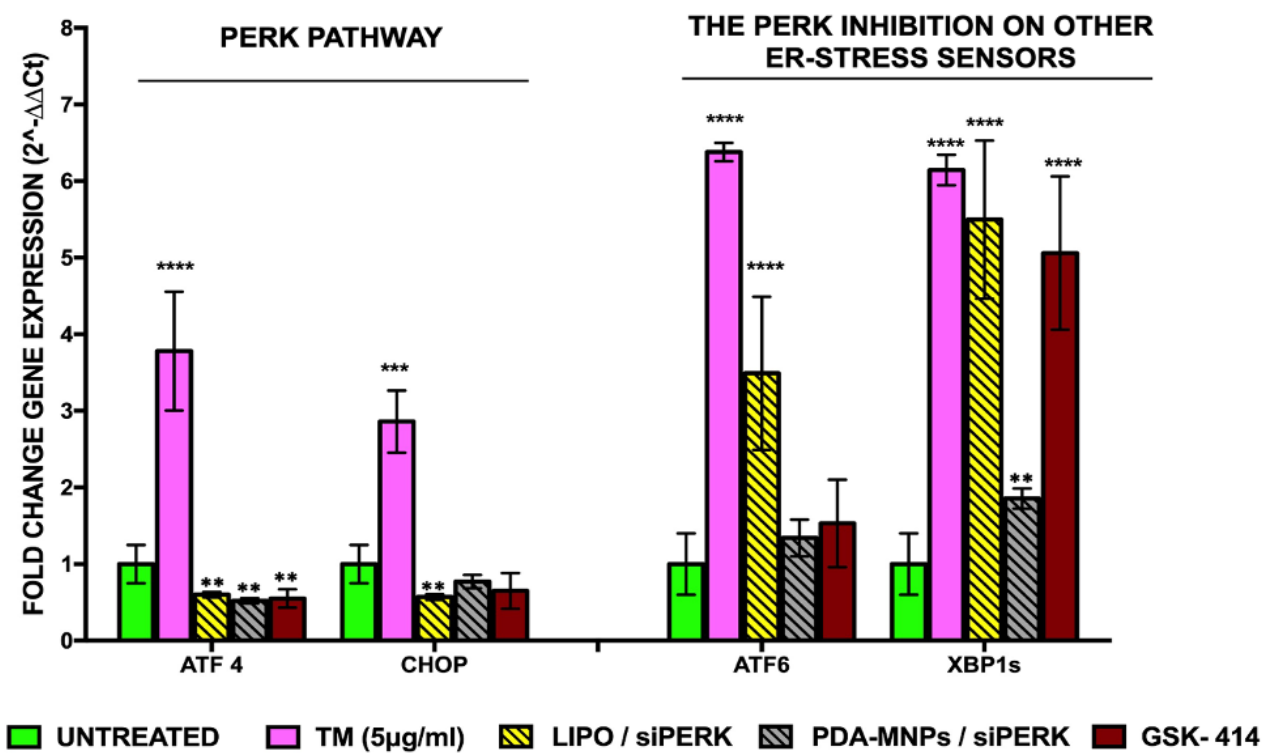
(a)

Fig. 3.10. Gene silencing by siRNA delivered by nanoparticles in PEMs. (a) WB analysis of the silencing of PERK and its downstream effector phospho-eiF2-α in PEMs treated with PDA-MNPs/siPERK for 48h. Tunicamycin (TM, 2µg/mL) was used as positive inducer control for ER stress. The protein expression of α-Tubulin was used as internal control. **(b)** Histograms showing mRNA levels of phospho-eiF2-α downstream effectors and ER-stress sensors detected by q-RT-PCR following the silencing of PERK in PEMs cells with PDA-MNPs/siPERK. GSK-414 (5µM) and LIPO/siPERK were used as positive controls for gene silencing. Gene expression was expressed as fold-change relative to untreated cells. Data are expressed as the mean ± SD of three independent experiments (*p ≤ 0,05; **p ≤ 0,01; ***p ≤ 0,001; **** p < 0.0001).

PRIMARY MACROPHAGES FROM MICE PERITONEAL EXUDATE (PEMs)
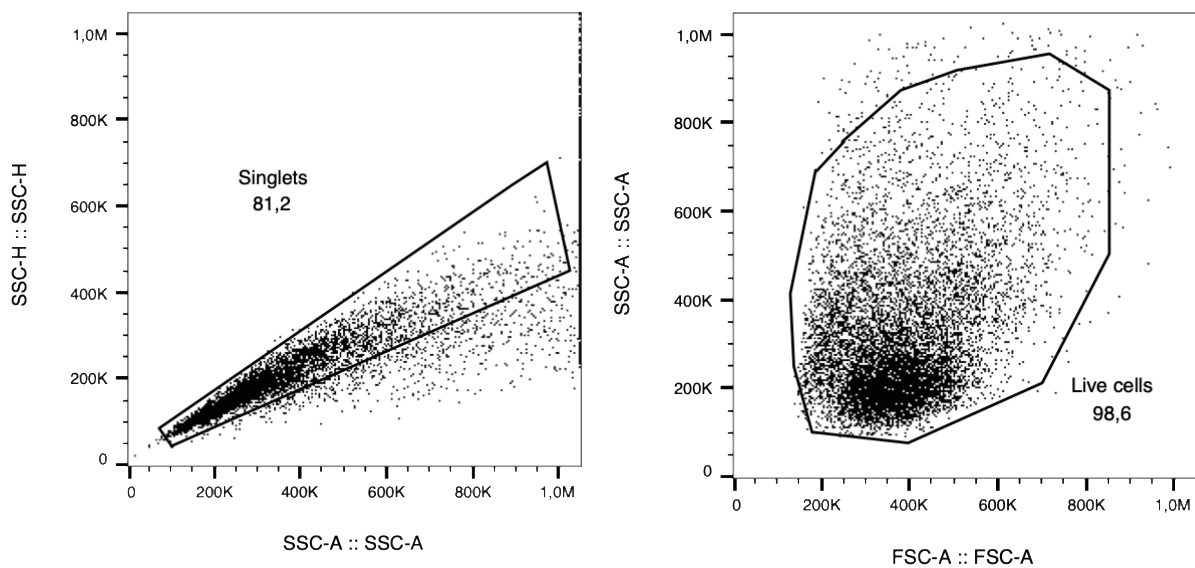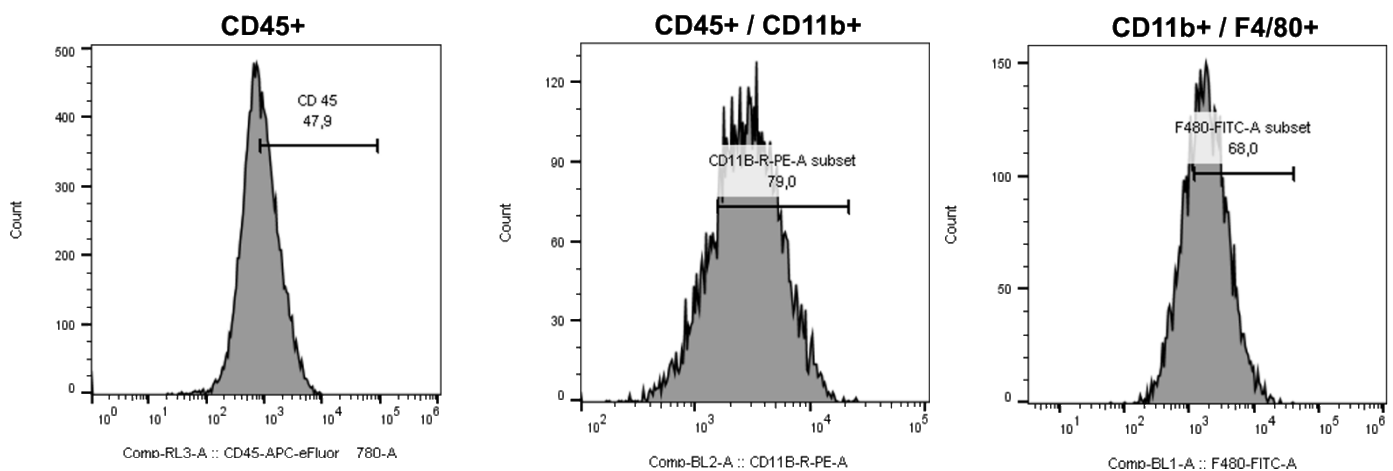

(b)

PEMs

Fig. 3.11. Characterization of primary macrophages from mice peritoneal exudate (PEMs) by flow cytometry analysis. (a) Representative flow cytometry images of the size (left) and granularity (right) of PEMs. FSC: forward scatter (size); SSC: side scatter (granularity). **(b)** The population of PEMs were characterized using a combination of labeled antibodies for CD45 (leucocyte common antigen, 47,9 % positive). The CD45 positive population was further characterized by CD11b (macrophage and dendritic cells, 79% positive). CD11b subset was further characterized by F4/80 (macrophages, 60% positive) Results are representative of three independent experiments.
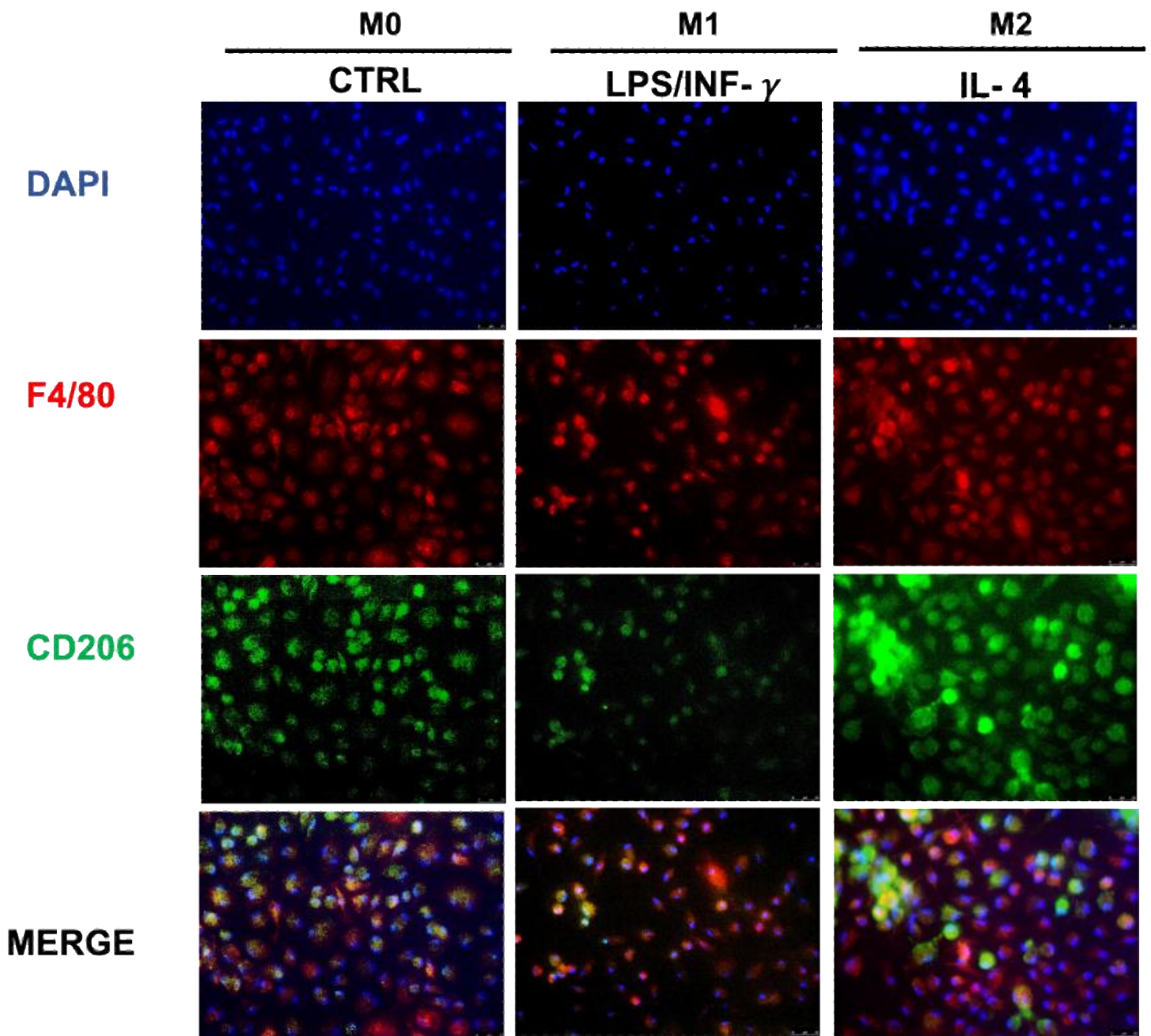
a)

	M0	M1	M2
	F480+	F480+/CD86+	F480+/CD206+

CTRL

IL- 4 (20 ng / ml)

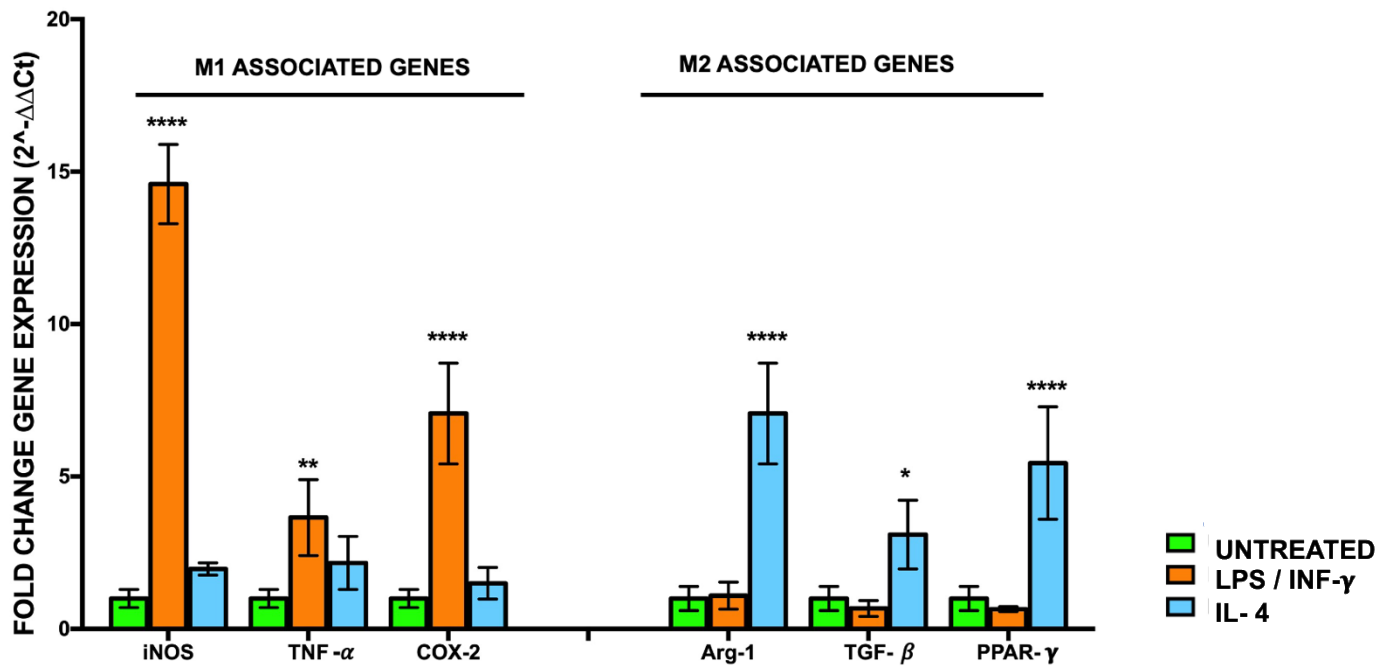LPS /INF-γ (100 ng/ml) (100 U/ml)
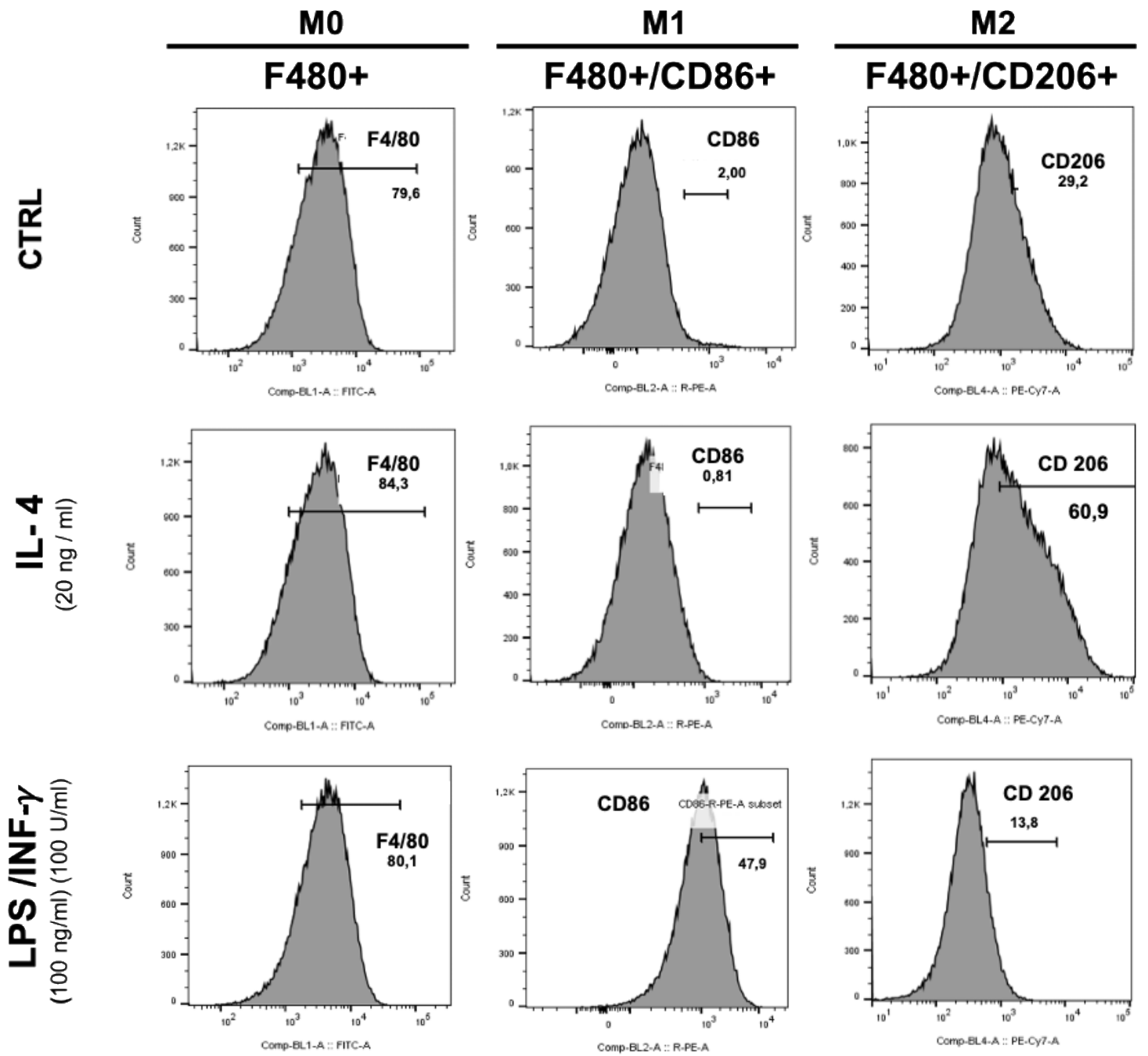
(b)
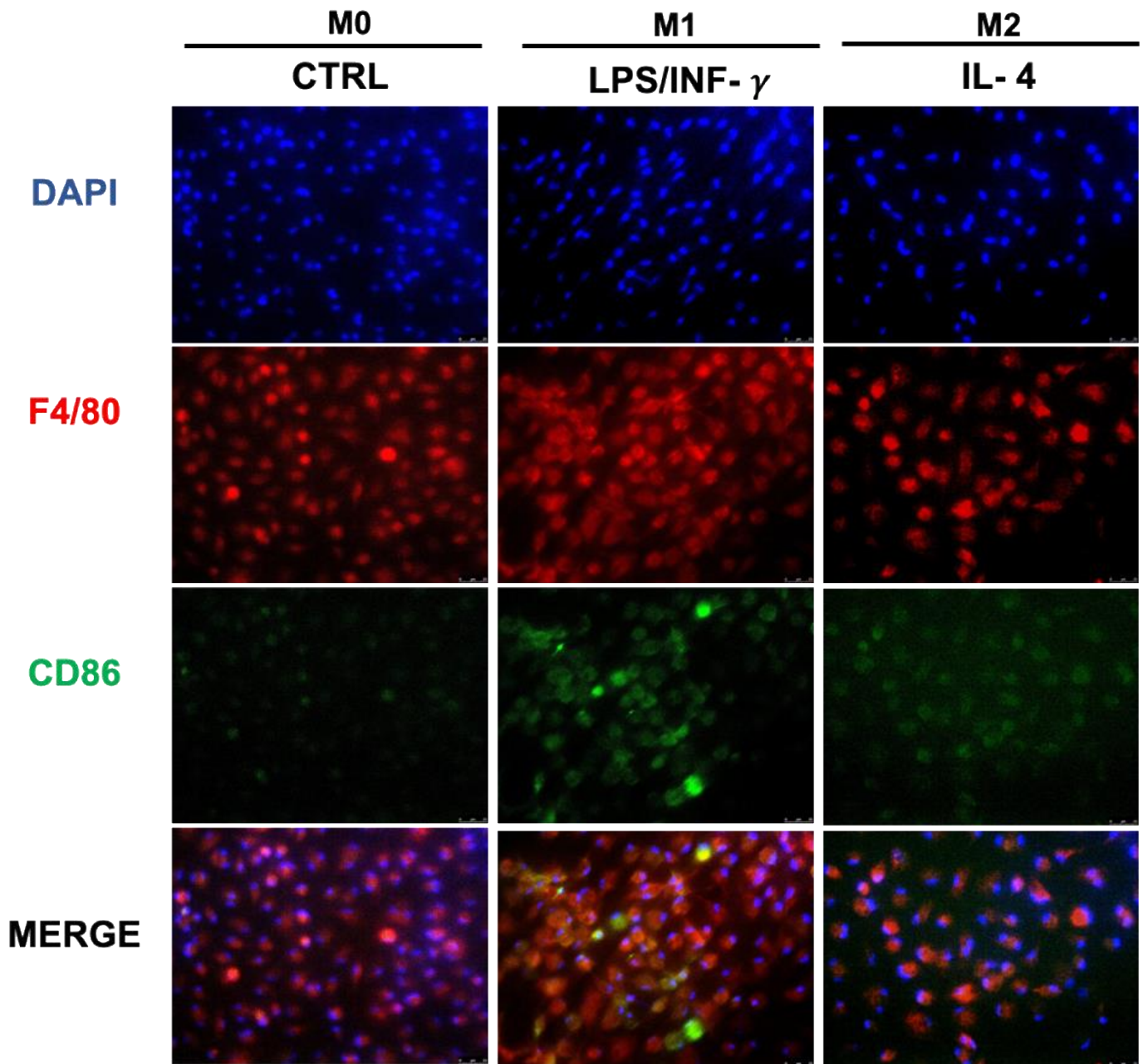
(c)

(d)

Fig. 3.12. PEMs can be polarized *in vitro* towards the M1 or M2 phenotypes. PEMs were isolated and cultured for 5 days with the macrophage colony-stimulating factor (M-CSF) and then stimulated for 48 h either with LPS/IFN-γ or with IL-4 to induce the M1and M2 phenotype, respectively. **(a)** Histograms show the FACS analyses of the expression of F4/80 (FITC), CD 86 (PE) and CD 206 (PE/Cy7), markers of macrophage in M0, M1, and M2, respectively. **(b, c)** Immunofluorescence images of differentiated PEMs into M1 and M2 phenotypes. Cells were fixed, permeabilized and stained with FITC-streptavidin F4/80 antibody for the macrophage identification (red) and DAPI (blue) for nuclei. The separate expression of CD86 **(b)** and CD206 **(c)** was visualized by the green signal at 200x magnification. **(d)** Relative expression of specific genes for M1 and M2 phenotypes was determined by q-RT-PCR. Gene expression was expressed as fold-change relative to untreated M0 cells. Data are expressed as the fold change expression ± SD of three independent experiments (*p ≤ 0,05; **p ≤ 0,01; **** p < 0.0001).
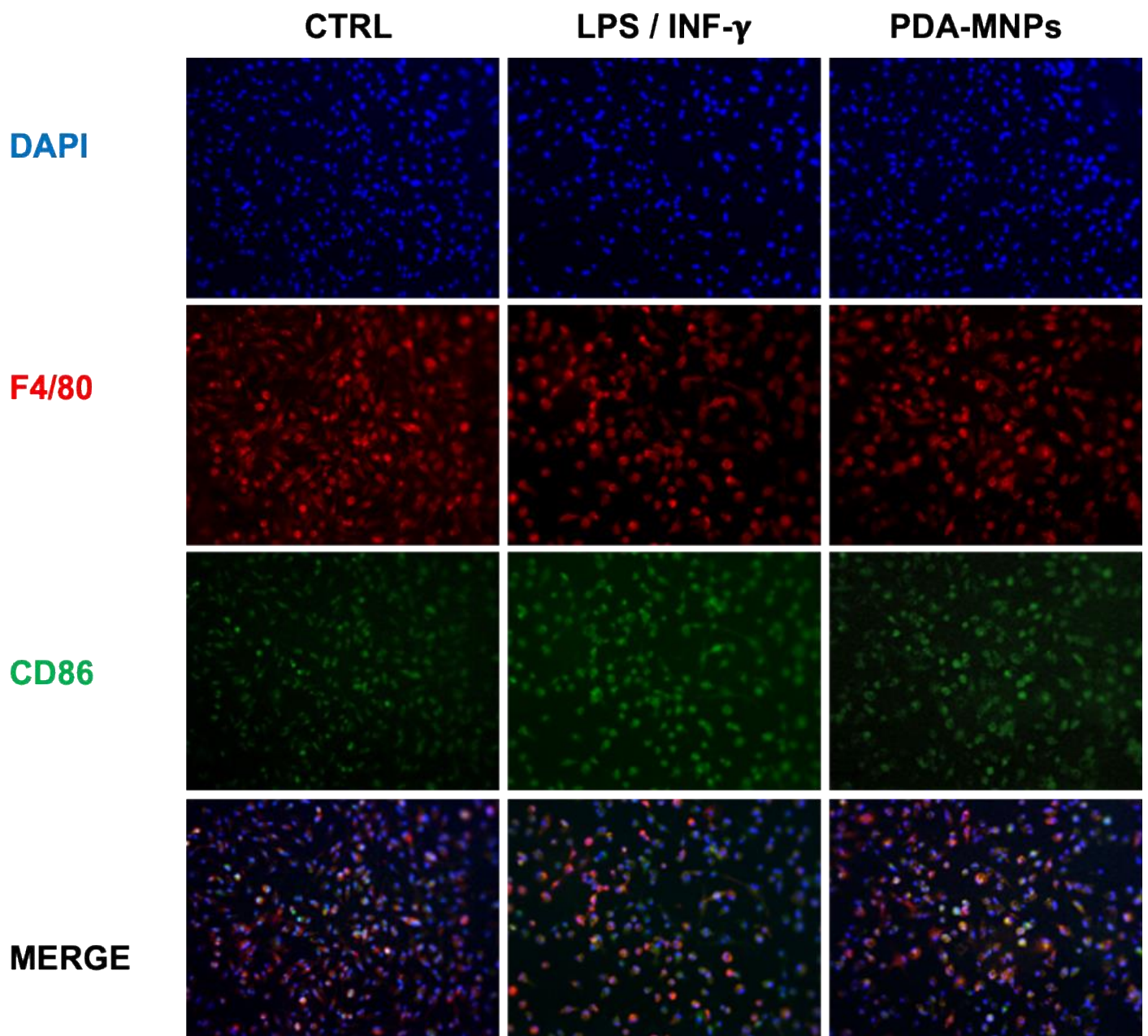
.

(a)

(b)

(c)

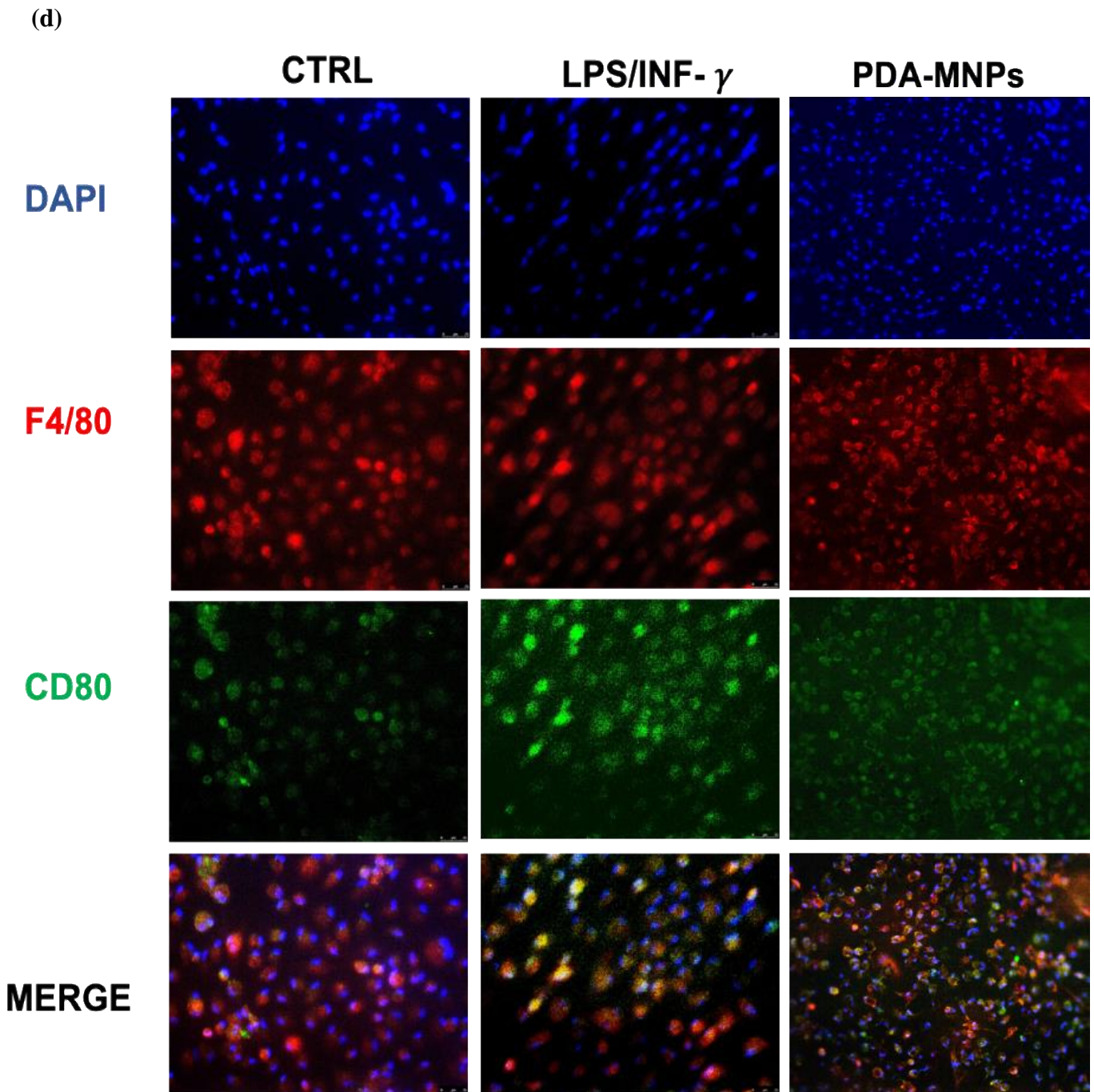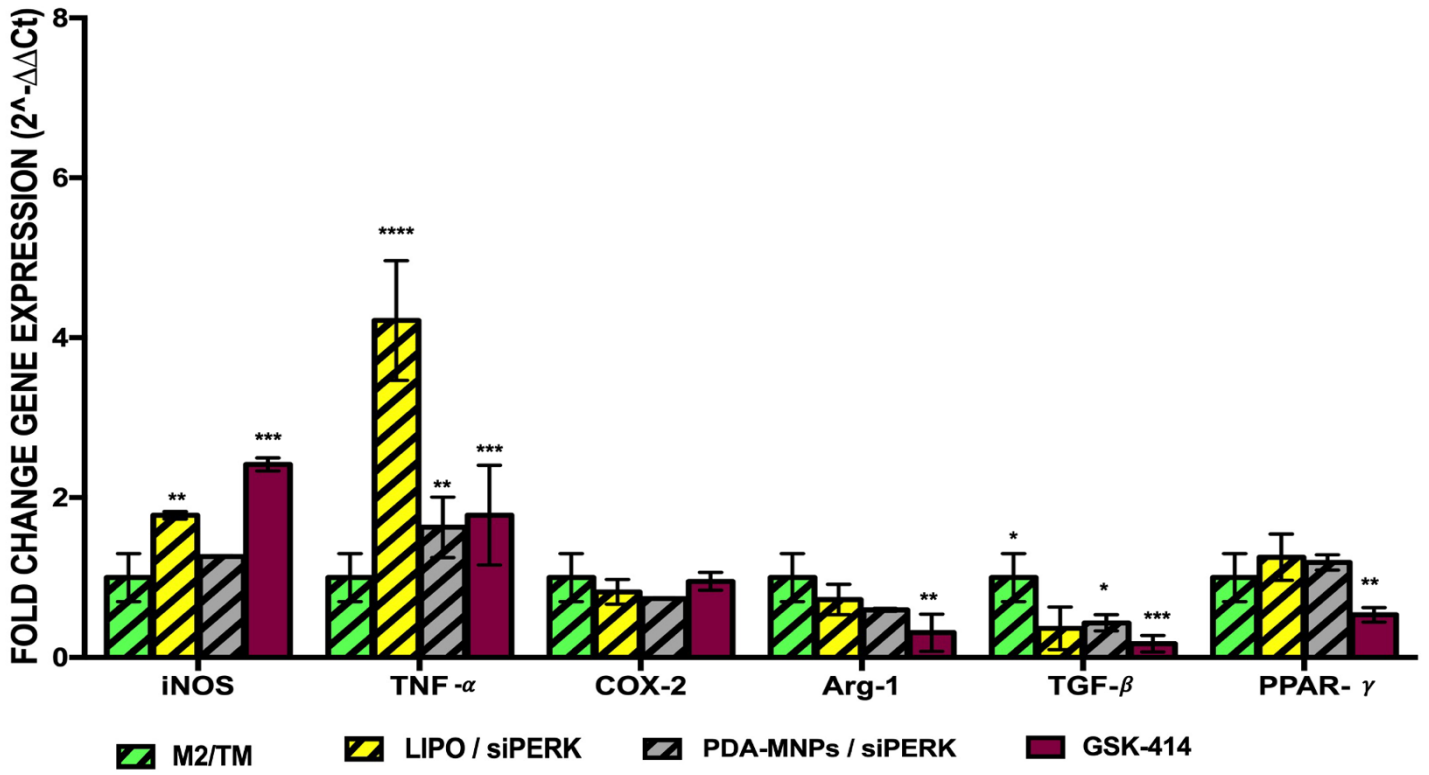|	CTRL	LPS / INF-γ	PDA-MNPs
DAPI			
F4/80			
CD86			
MERGE			

(d)
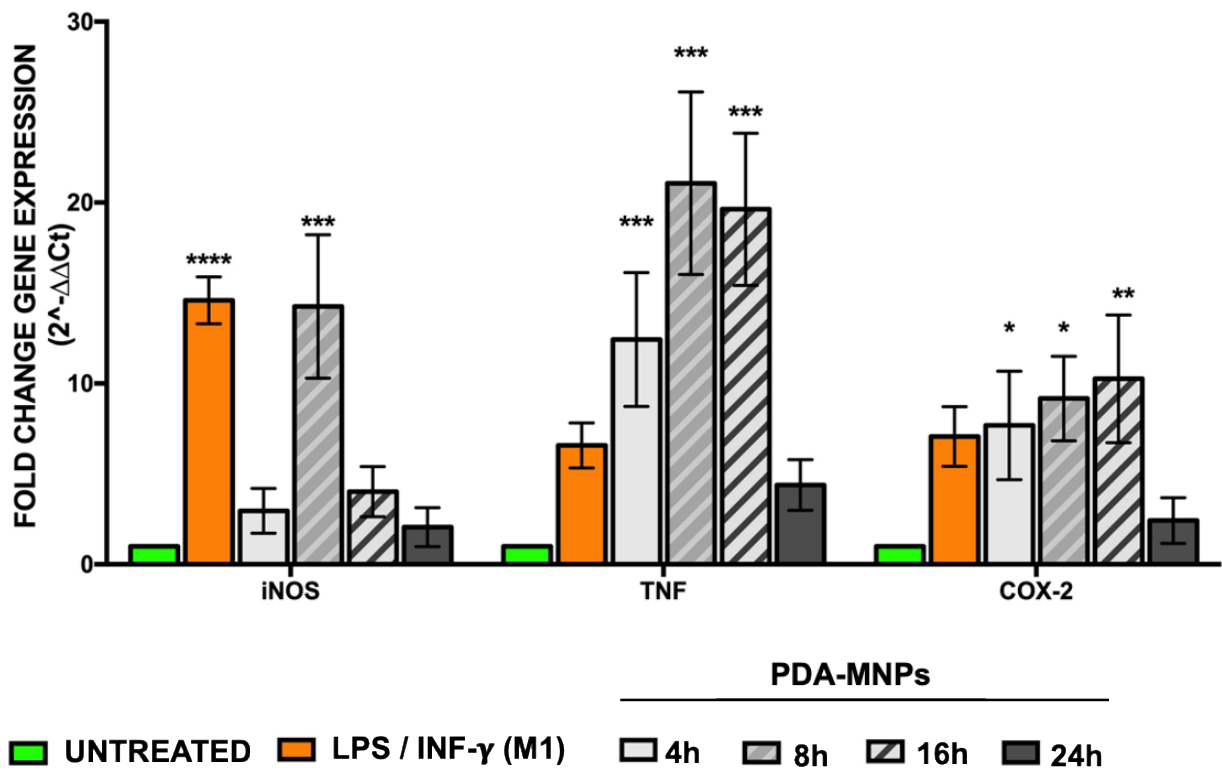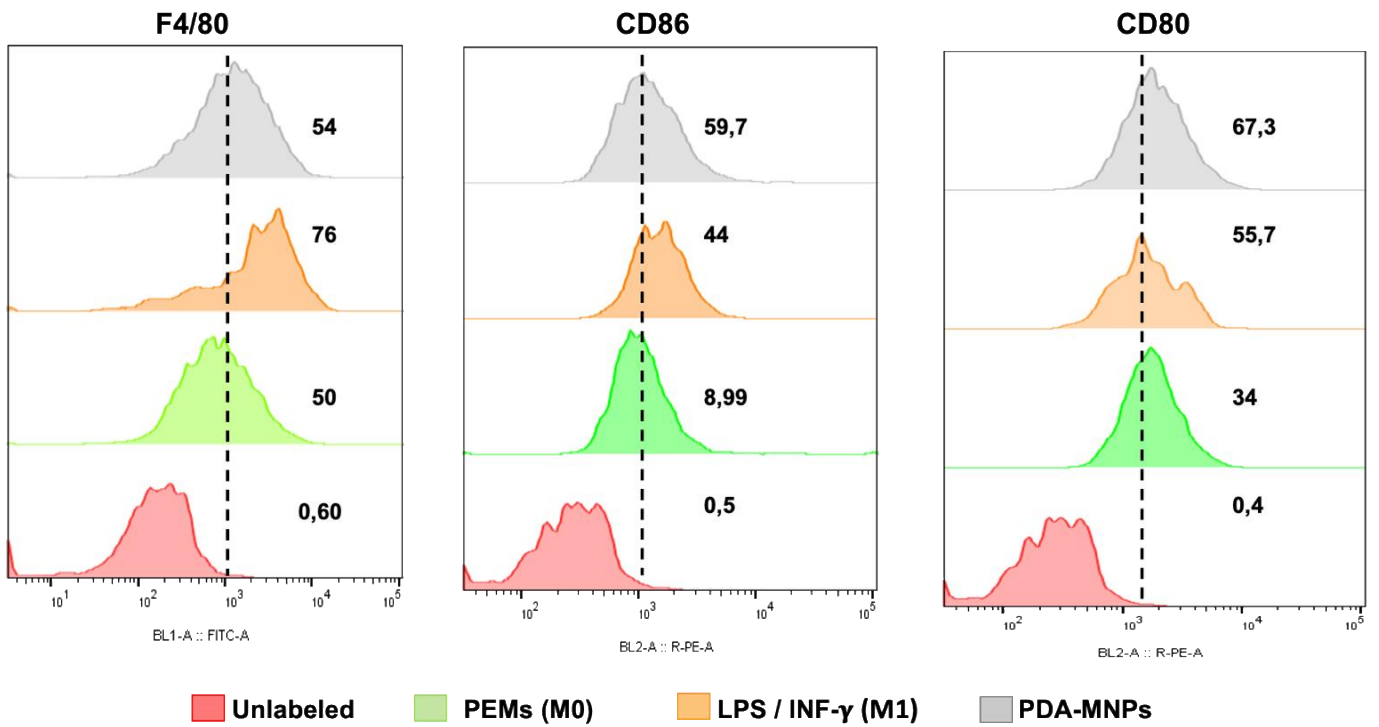
Fig. 3.13. The effects of PDA-MNPs on the macrophage polarization of PEMs. (a) Relative expression of specific genes for M1 phenotype was determined by q-RT-PCR after incubation of cells with PDA-MNPs (100 µg/mL) for different time points. M0 cells (green) and LPS/ IFN-γ induced-PEMs (M1) (orange) were used as controls, and gene expression was expressed as fold-change relative to M0 cells. Experiments were performed in triplicates; data represent fold change ± SD of three experiments. **(b,c,d)** PEMs were incubated with PDA-MNPs (100 µg/mL) for 3 days and the percentage values of CD86 and CD80 expression were assessed by **(b)** flow cytometry and **(c,d)** visualised at fluorescence microscopy. Macrophages are visualized in red (FITC-Streptavidin-F4/80), nuclei in blue (DAPI), while the expression of CD86/CD80 are visualized as the green dots. Magnification 200x. Unlabeled M0 were used to set-up the measures in flow cytometry experiments. Statistical analyses were performed using One-Way Anova followed by Bonferroni 's post-test (*p ≤ 0,05; ***p ≤ 0,001; **** p < 0.0001).

(a)

(b)

(c)

(d)

M2/TM

	CTRL	LIPO / siPERK	PDA-MNPs / siPERK	GSK- 414	
120 kDa					Vinculin
80 kDa					p-STAT3
80 kDa					STAT3
65 kDa					p- NF-KBp65
65 kDa					NF-KBp65
44/42 kDa					p- MAPK 1/2
44/42 kDa					MAPK 1/2

(e)

CTRL (M2/TM)   LIPO / siPERK   PDA-MNPs/siPERK   GSK-414

(f)

CD86   **CD206**

28,6

21,9

36,7

18

0,3

BL2-A :: CD86-R-PE-A

30,4

13,3

32,2

42,9

0,7

BL4-A :: CD206-PE-Cv7-A

■ Unlabeled (M2)   ■ IL-4 (M2)   ■ LIPO-siPERK   ■ PDA-MNPs-siPERK   ■ GSK-414
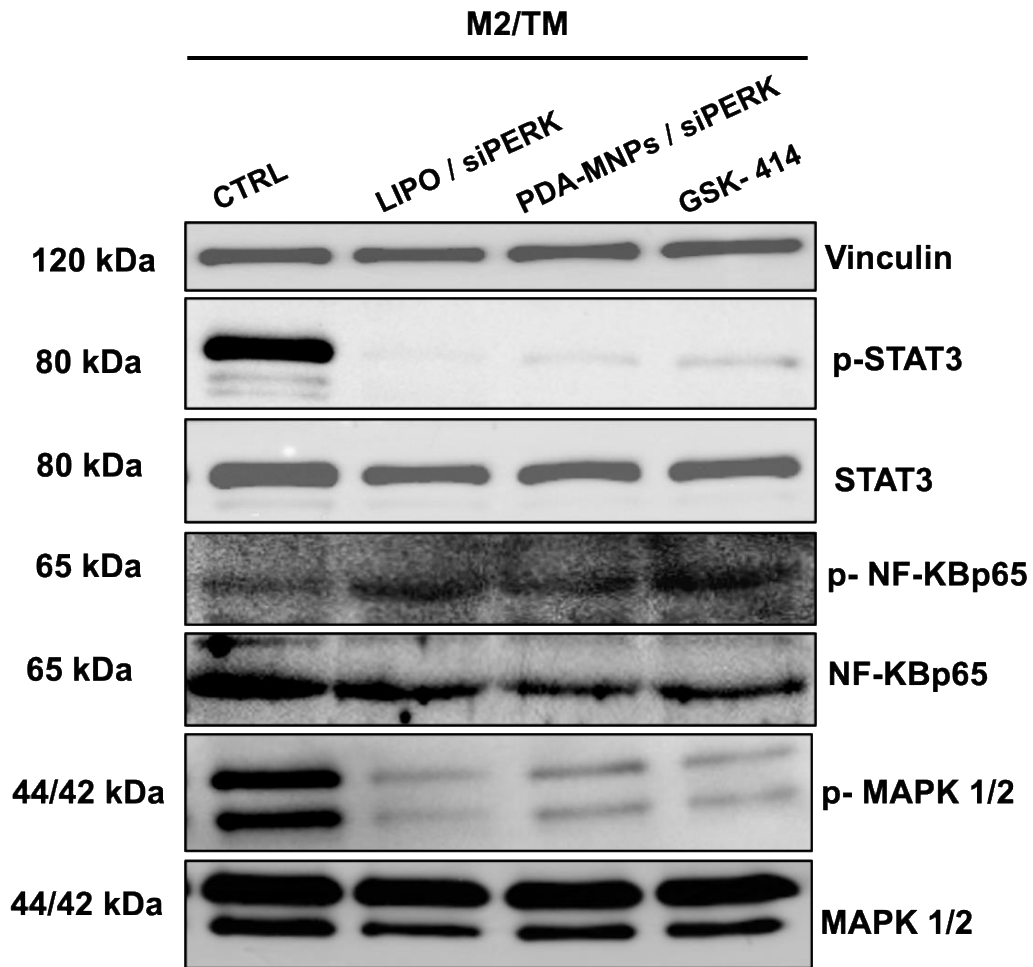
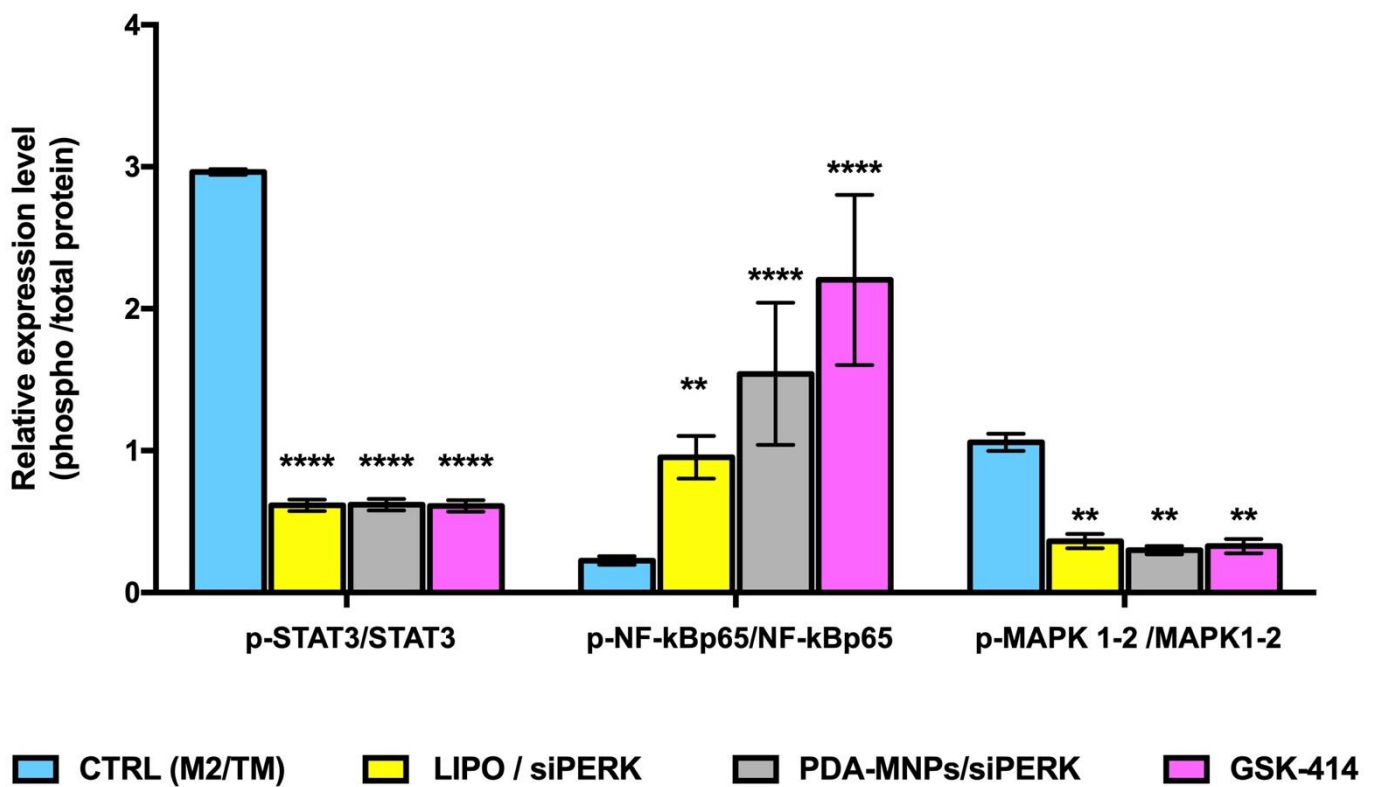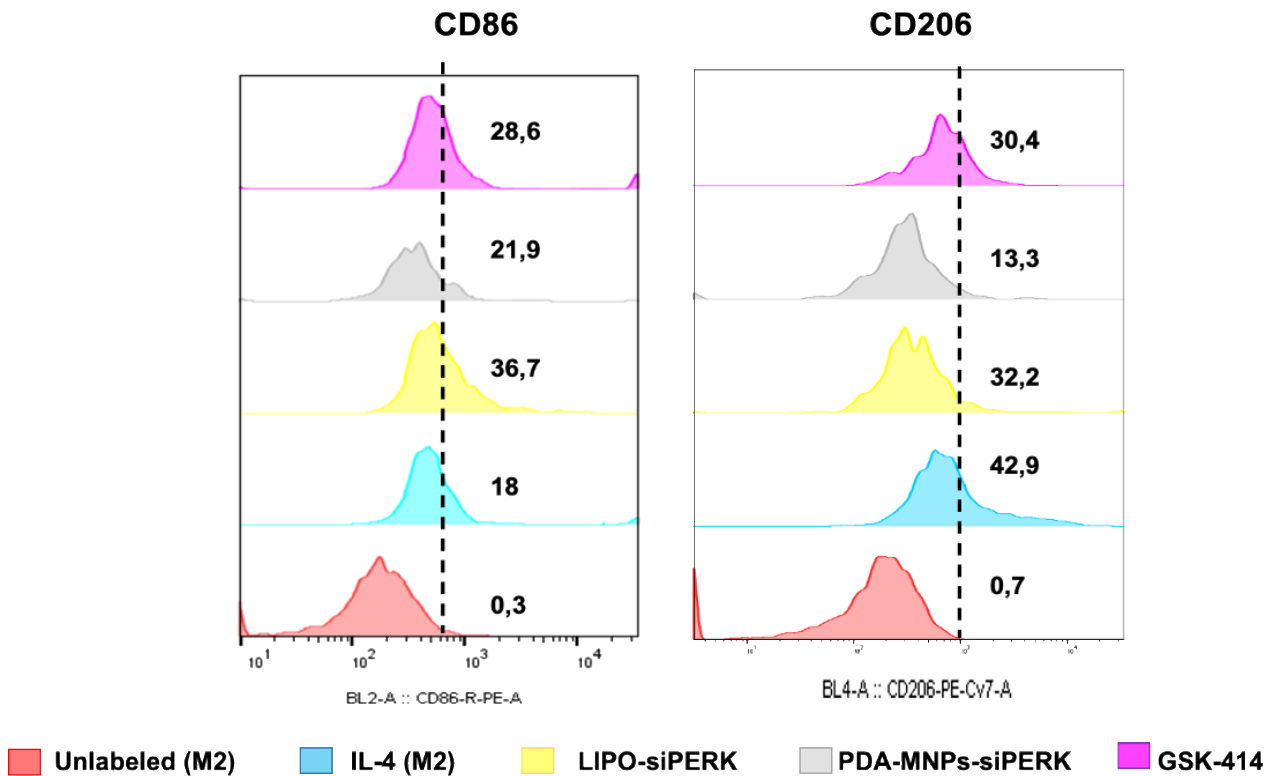**Fig. 3.14. Reprogramming of TAMs from M2 to M1 phenotype.** PEMs were polarized to M2 phenotype with IL-4, treated with ER-stress sensor tunicamycin (2μg/mL) and incubated with LIPO/siPERK, PDA-MNPs/siPERK and GSK-414 (5 μM). **(a)** After 24h incubation the mRNA levels of PERK, ATF4, CHOP were assessed by q-RT-PCR. **(b)** After 48h the expression and the state of phosphorylation of Eif2-α was analyzed by immunoblot assay. **(c)** The relative expression of the genes specific for M1 or M2 phenotypes was determined by q-RT-PCR after M2 macrophages were incubated for 24h with LIPO/siPERK, PDA-MNPs/siPERK and GSK-414 for PERK silencing. **(d)** WB representing the expression and state of activation in M2/TM (TAMs-like) of NF-kB p65, STAT3 and MAPK1/2, 48h after silencing PERK mRNA. Vinculin was used as internal control and densitometric analysis are shown **(e)**. **(f)** Histograms showing the expression of CD86 and CD206 determined by flow cytometry analysis after M2/TM were incubated for 3 days with LIPO/siPERK, PDA-MNPs/siPERK and GSK-414. Results for qRT-PCR are expressed as fold change ± SD respect to the untreated M2/TM, obtained in three independent experiments made in triplicates and analyzed by 2-way ANOVA with Bonferroni's multiple comparison test (*p ≤ 0,05; **p ≤ 0,01;*** p ≤ 0,001; **** p < 0.0001).

CHAPTER IV

General conclusions and future perspective

The application of nanotechnology in medicine and in particular in cancer therapy is already a reality (Cheng et al., 2021). The major advantage of NPs is that they are efficient multifunctional platforms for drug delivery, generally able to target tumor cells, thus allowing to decrease the dose of the chemotherapeutics and by consequence of the associated unwanted side effects. This strategy can be extended also to TME, where TAMs, which are the major cell population there, play a key role in the tumor progression, displaying an M2 phenotype. We have reproduced an *in vitro* system simulating the TAMs-M2 macrophages –which play a negative immunosuppressive activity– and the M1 macrophages –which play a positive anti-tumor pro-inflammatory role– using PEMs and stimulating them by cytokines, in particular with IL-4 and LPS/IFNγ (Feito et al., 2019). The two macrophage populations, which represent the two extreme polarized phenotypes of the macrophages, differ for cell surface markers and gene profile and can thus be easily identified (Kasfi et al., 2021).

Our aim was to reprogram pro-tumor M2 macrophages to anti-tumor M1 macrophages. This was done by using MNPs functionalized with siRNA/PERK, small interfering RNAs which can modulate the expression of the UPR in the endoplasmic reticulum (ER) of TAMs-M2 cells.

MNPs were chosen as nanocarriers for their specific property of being sensitive to external gradient magnetic field and thus for the possibility to be re-directed on a wanted site by the application of a magnet for eventual *in vivo* studies; moreover, we found that also in *in vitro* studies they enhance their uptake by the cells in the presence of a magnet, in agreement with what already reported (Oltolina et al., 2020). In addition, we focused our attention on these magnetic nanocarriers, because they also stimulate the macrophage polarization favoring the pro-inflammatory and immunostimulatory M1 phenotype due to their intrinsic features (Mulens-Arias et al., 2021).

We found that the coupling of siRNA to MNPs required previous coating of MNPs with PDA, to provide functional groups for siRNA binding (Mu et al. 2018).

PERK was chosen as target gene to be silenced since the PERK arm of the UPR is a critical metabolic hub for the immunosuppressive function of TAMs-M2 macrophages (Raines et al. 2022).

We showed that upon the administration of PDA-MNPs/siPERK the expression of PERK, as well as of other proteins of its pathway (ATF4, CHOP) and of the URP response (XBP1s, ATF6) were inhibited in TAMs-M2 cells. Moreover, upon 3 days incubation with PDA-MNPs/siPERK TAMs-like macrophages switched to the M1 phenotype, as confirmed by cytofluorimetric analysis for CD206 and CD86, the specific markers of the two phenotypes.

These are preliminary *in vitro* studies and thus have their limit, but they are proof of concept for the strategy to target TME for a positive anti-tumor response and put the basis for possible future *in vivo* translational applications for cancer therapies. Before *in vivo* experiments, *in vitro* experiments with organoids reconstituting the characteristics of the TME could be envisaged (Hong et al., 2021). The possibility to administer the silencing moiety (Jin et al., 2019) through lentiviral vectors coupled to MNPs (Borroni et al., 2017) should also be taken into consideration as an improvement of the strategy, since in this case the shRNA would be encapsulated in the highly stable lentiviral vector and also protected from possible degradation.

References

Ahmad FB, Cisewski JA, Anderson RN. Provisional Mortality Data - United States, 2021. MMWR Morb Mortal Wkly Rep. 2022;71:597-600.

Altin JG, Sloan EK. The role of CD45 and CD45-associated molecules in T cell activation. *Immunol Cell Biol.* 1997;75:430-45.

Aubel-Sadron G, Londos-Gagliardi D. Daunorubicin and doxorubicin, anthracycline antibiotics, a physicochemical and biological review. *Biochimie.* 1984;66:333-52.

Bahrami B, Hojjat-Farsangi M, Mohammadi H, Anvari E, Ghalamfarsa G, Yousefi M, Jadidi-Niaragh F. Nanoparticles and targeted drug delivery in cancer therapy. *Immunol Lett.* 2017;190:64-83.

Batista A, Rodvold JJ, Xian S, Searles SC, Lew A, Iwawaki T, Almanza G, Waller TC, Lin J, Jepsen K, Carter H, Zanetti M. IRE1α regulates macrophage polarization, PD-L1 expression, and tumor survival. *PLoS Biology* 2020, *18:*e3000687.

Bielenberg DR, Zetter BR. The Contribution of Angiogenesis to the Process of Metastasis. *Cancer J.* 2015;21:267-73.

Biswas, S.K.; Lewis, C.E. NF-ΚB as a Central Regulator of Macrophage Function in Tumors. *Journal of Leukocyte Biology* 2010, 88, 877–884.

Bockamp E, Rosigkeit S, Siegl D, Schuppan D. Nano-Enhanced Cancer Immunotherapy: Immunology Encounters Nanotechnology. *Cells* 2020, *9,* 2102.

Borroni E, Miola M, Ferraris S, Ricci G, Žužek Rožman K, Kostevšek N, Catizone A, Rimondini L, Prat M, Verné E, Follenzi A. Tumor targeting by lentiviral vectors combined with magnetic nanoparticles in mice. *Acta Biomater.* 2017;59:303-316.

Cano Plá SM, D'Urso A, Fernández-Sánchez JF, Colangelo D, Choquesillo-Lazarte D, Ferracini R, Bosetti M, Prat M, Gómez-Morales J. Biomimetic Citrate-Coated Luminescent Apatite Nanoplatforms for Diclofenac Delivery in Inflammatory Environments. *Nanomaterials.* 2022;12:562.

Cassado Ados A, D'Império Lima MR, Bortoluci KR. Revisiting mouse peritoneal macrophages: heterogeneity, development, and function. *Front Immunol.* 2015;6:225.

Cassim S, Pouyssegur J. Tumor Microenvironment: A Metabolic Player That Shapes the Immune Response. *International Journal of Molecular Sciences* 2019;21:157.

Chang TK, Lawrence DA, Lu M, Tan J, Harnoss JM, Marsters SA, Liu P, Sandoval W, Martin SE, Ashkenazi A. Coordination between Two Branches of the Unfolded Protein Response Determines Apoptotic Cell Fate. *Molecular Cell* 2018;71:629-636.e5.

Cheng Z, Li M, Dey R, Chen Y. Nanomaterials for cancer therapy: current progress and perspectives. *J Hematol Oncol.* 2021;14:85.

Chenthamara D, Subramaniam S, Ramakrishnan SG, Krishnaswamy S, Essa MM, Lin FH, Qoronfleh MW. Therapeutic Efficacy of Nanoparticles and Routes of Administration. *Biomaterials Research* 2019;23:20.

Chow MT, Möller A, Smyth MJ. Inflammation and Immune Surveillance in Cancer. *Seminars in Cancer Biology* 2012;22:23–32.

Cole AJ, Yang VC, David AE. Cancer theranostics: the rise of targeted magnetic nanoparticles. *Trends Biotechnol*. 2011;29:323-32.

Dadfar SM, Roemhild K, Drude NI, von Stillfried S, Knüchel R, Kiessling F, Lammers T. Iron Oxide Nanoparticles: Diagnostic, Therapeutic and Theranostic Applications. *Advanced Drug Delivery Reviews* 2019;138:302–325.

Di Conza G, Ho PC. ER Stress Responses: An Emerging Modulator for Innate Immunity. *Cells*. 2020;9:695.

Ding X, Sun X, Cai H, Wu L, Liu Y, Zhao Y, Zhou D, Yu G, Zhou X. Engineering Macrophages *via* Nanotechnology and Genetic Manipulation for Cancer Therapy. Front Oncol. 2022 Jan 6;11:786913.

Dukhinova MS, Prilepskii AY, Shtil AA, Vinogradov VV. Metal Oxide Nanoparticles in Therapeutic Regulation of Macrophage Functions. *Nanomaterials (Basel)*. 2019;9:1631.

Elliott P. Pathogenesis of cardiotoxicity induced by anthracyclines. *Semin Oncol*. 2006;33:S2-7.

Fakhr E, Zare F, Teimoori-Toolabi L. Precise and Efficient SiRNA Design: A Key Point in Competent Gene Silencing. *Cancer Gene Therapy* 2016; 23:73–82.

Falzone L, Salomone S, Libra M. Evolution of Cancer Pharmacological Treatments at the Turn of the Third Millennium. *Front Pharmacol*. 2018;9:1300.

Feito MJ, Diez-Orejas R, Cicuéndez M, Casarrubios L, Rojo JM, Portolés MT. Characterization of M1 and M2 Polarization Phenotypes in Peritoneal Macrophages after Treatment with Graphene Oxide Nanosheets. *Colloids and Surfaces B: Biointerfaces* 2019;176: 96–105.

Fire A, Xu S, Montgomery MK, Kostas SA, Driver SE, Mello CC. Potent and specific genetic interference by double-stranded RNA in Caenorhabditis elegans. *Nature*. 1998;391:806-11.

Gandhapudi SK, Ward M, Bush JPC, Bedu-Addo F, Conn G, Woodward JG. Antigen Priming with Enantiospecific Cationic Lipid Nanoparticles Induces Potent Antitumor CTL Responses through Novel Induction of a Type I IFN Response. *J Immunol*. 2019;202:3524-3536.

Gao L, Zhang W, Zhong WQ, Liu ZJ, Li HM, Yu ZL, Zhao YF. Tumor associated macrophages induce epithelial to mesenchymal transition via the EGFR/ERK1/2 pathway in head and neck squamous cell carcinoma. *Oncology Reports* 2018;40:2558–2572.

García Rubia G, Peigneux A, Jabalera Y, Puerma J, Oltolina F, Elert K, Colangelo D, Gómez Morales J, Prat M, Jimenez-Lopez C. pH-Dependent Adsorption Release of Doxorubicin on MamC-Biomimetic Magnetite Nanoparticles. *Langmuir*. 2018;34:13713–13724.

Garg AD, Kaczmarek A, Krysko O, Vandenabeele P, Krysko DV, Agostinis P. ER stress-induced inflammation: does it aid or impede disease progression? *Trends in Molecular Medicine* 2012;18:589–598.

Ge R, Li X, Lin M, Wang D, Li S, Liu S, Tang Q, Liu Y, Jiang J, Liu L, Sun H, Zhang H, Yang B. Fe3O4@polydopamine Composite Theranostic Superparticles Employing Preassembled Fe3O4 Nanoparticles as the Core. *ACS Appl Mater Interfaces*. 2016;8:22942-52.

Genard G, Lucas S, Michiels C. Reprogramming of Tumor-Associated Macrophages with Anticancer Therapies: Radiotherapy versus Chemo- and Immunotherapies. *Front Immunol*. 2017;8:828.

Gionfriddo G, Plastina P, Augimeri G, Catalano S, Giordano C, Barone I, Morelli C, Giordano F, Gelsomino L, Sisci D, Witkamp R, Andò S, van Norren K, Bonofiglio D. Modulating Tumor-Associated Macrophage Polarization by Synthetic and Natural PPARγ Ligands as a Potential Target in Breast Cancer. *Cells*. 2020;9:174.

Gómez-Morales J, Fernández-Penas R, Romero-Castillo I, Verdugo-Escamilla C, ChoquesilloLazarte D, D'Urso A, Prat M, Fernández-Sánchez JF. Crystallization, Luminescence and Cytocompatibility of Hexagonal Calcium Doped Terbium Phosphate Hydrate Nanoparticles. *Nanomaterials (Basel)*. 2021;11:322.

Gómez-Morales J, Iafisco M. Progress on the Preparation of Nanocrystalline Apatites and Surface Characterization: Overview of Fundamental and Applied Aspects. *Prog. Cryst. Growth Charact. Mater.* 2013; 59:1-46.

Gu, X., Zhang, Y., Sun, H., Song, X., Fu, C., and Dong, P. (2015). Mussel-inspired polydopamine coated iron oxide nanoparticles for biomedical application. Journal of Nanomaterials 2015; 2015 Article ID 154592.

Hamidzadeh K, Belew AT, El-Sayed NM, Mosser DM. The transition of M-CSF-derived human macrophages to a growth-promoting phenotype. *Blood Adv*. 2020;4:5460-5472.

Hanahan D, Weinberg RA. Hallmarks of cancer: the next generation. *Cell*. 2011;144:646-74.

Hanahan D. Hallmarks of Cancer: New Dimensions. *Cancer Discovery*. 2022;12:31–46.

Haque ST, Islam RA, Gan SH, Chowdhury EH. Characterization and Evaluation of Bone-Derived Nanoparticles as a Novel pH-Responsive Carrier for Delivery of Doxorubicin into Breast Cancer Cells. *Int J Mol Sci*. 2020;21:6721.

Hassanpour SH, Dehghani M. Review of Cancer from Perspective of Molecular. *Journal of Cancer Research and Practice* 2017;4:127–129.

Hedayatnasab Z, Abnisa F, Daud WMAW. Review on magnetic nanoparticles for magnetic nanofluid hyperthermia application. *Mater. Des.* 2017;123:174–196.

Hong HK, Yun NH, Jeong YL, Park J, Doh J, Lee WY, Cho YB. Establishment of patient-derived organotypic tumor spheroid models for tumor microenvironment modeling. *Cancer Med*. 2021;10:5589-5598.

Hörhold F, Eisel D, Oswald M, Kolte A, Röll D, Osen W, Eichmüller SB, König R. Reprogramming of macrophages employing gene regulatory and metabolic network models. *PLoS Computational Biology* 2020;16:e1007657.

Hu B, Zhong L, Weng Y, Peng L, Huang Y, Zhao Y, Liang XJ. Therapeutic siRNA: state of the art. *Signal Transduction and Targeted Therapy* 2020;5:101.

Iafisco M, Delgado-Lopez JM, Varoni EM, Tampieri A, Rimondini L, Gomez-Morales J, Prat M. Cell surface receptor targeted biomimetic apatite nanocrystals for cancer therapy. Small. 2013;9:3834-44.

International Standard Organization. ISO 10993-5 Biological Evaluation of Medical Devices Part 5: Tests for In Vitro Cytotoxicity; International Standard Organization: Geneve, Switzerland, 2009.

Irvine DJ, Dane EL. Enhancing cancer immunotherapy with nanomedicine. *Nature Reviews Immunology* 2020;20:321-334.

Itani R, Al Faraj A. siRNA Conjugated Nanoparticles-A Next Generation Strategy to Treat Lung Cancer. *Int J Mol Sci*. 2019;20:6088.

Iyer R, Nguyen T, Padanilam D, Xu C, Saha D, Nguyen KT, Hong Y. Glutathione-responsive biodegradable polyurethane nanoparticles for lung cancer treatment. *J Control Release*. 2020;321:363-371.

Izci M, Maksoudian C, Manshian BB, Soenen SJ. The Use of Alternative Strategies for Enhanced Nanoparticle Delivery to Solid Tumors. *Chem Rev*. 2021;121:1746-1803.

Jablonski KA, Amici SA, Webb LM, Ruiz-Rosado Jde D, Popovich PG, Partida-Sanchez S, Guerau-de-Arellano M. Novel Markers to Delineate Murine M1 and M2 Macrophages. *PLoS One*. 2015;10:e0145342.

Jain RK, Stylianopoulos T. Delivering nanomedicine to solid tumors. *Nat Rev Clin Oncol*. 2010;11:653-64.

Jiang M, Li X, Zhang J, Lu Y, Shi Y, et al. Dual Inhibition of Endoplasmic Reticulum Stress and Oxidation Stress Manipulates the Polarization of Macrophages under Hypoxia to Sensitize Immunotherapy. *ACS Nano* 2021;15:14522–14534.

Jin A, Wang Y, Lin K, Jiang L. Nanoparticles modified by polydopamine: Working as "drug" carriers. Bioact Mater. 2020;5:522-541.

Jin L, Wang Q, Chen J, Wang Z, Xin H, Zhang D. Efficient Delivery of Therapeutic siRNA by Fe_3O_4 Magnetic Nanoparticles into Oral Cancer Cells. *Pharmaceutics.* 2019; 11:615.

Jin MZ, Jin WL. The Updated Landscape of Tumor Microenvironment and Drug Repurposing. *Signal Transduction and Targeted Therapy.* 2020;5:166.

Jin R, Liu L, Zhu W, et al. Iron oxide nanoparticles promote macrophage autophagy and inflammatory response through activation of toll-like Receptor-4 signaling. Biomaterials. 2019;203:23-30.

Jonathan M. Kocarnik, P. corresponding author 1 K.C.B. 1 F.E.D. Cancer Incidence, Mortality, Years of Life Lost, Years Lived With Disability, and Disability-Adjusted Life Years for 29 Cancer Groups From 2010 to 2019: A Systematic Analysis for the Global Burden of Disease Study 2019. JAMA Oncol. 2022;8:420-444.

Jurj, A, Braicu, C, Pop, L.A, Tomuleasa, C, Gherman, C.D, Berindan-Neagoe, I. The New Era of Nanotechnology, an Alternative to Change Cancer Treatment. *Drug Design, Development and Therapy* 2017;11:2871–2890.

Kashfi K, Kannikal J, Nath N. Macrophage Reprogramming and Cancer Therapeutics: Role of iNOS-Derived NO. *Cells*. 2021;10:3194.

Khan AA, Allemailem KS, Almatroudi A, Almatroodi SA, Mahzari A, Alsahli MA, Rahmani AH. Endoplasmic Reticulum Stress Provocation by Different Nanoparticles: An Innovative Approach to Manage the Cancer and Other Common Diseases. *Molecules* 2020;25:5336.

Kowal J, Kornete M, Joyce JA Re-Education of Macrophages as a Therapeutic Strategy in Cancer. *Immunotherapy* 2019;11:677–689.

Kumar, Vijay. "Macrophages: the potent immunoregulatory innate immune cells." *Macrophage Act.-Biol. Dis* (2019).

Kumari, N, Choi, S. H. Tumor-associated macrophages in cancer: recent advancements in cancer nanoimmunotherapies. *J. Exp. Clin.Cancer Res.* 2022; *41*:1–39.

Labani-Motlagh A, Ashja-Mahdavi M, Loskog A.The Tumor Microenvironment: A Milieu Hindering and Obstructing Antitumor Immune Responses. *Frontiers in Immunology* 2020; 11:940.

Le Saux O, Lounici Y, Wajda P, Barrin S, Caux C, Dubois B, Ray-Coquard I. Neoadjuvant immune checkpoint inhibitors in cancer, current state of the art. *Crit Rev Oncol Hematol.* 2021;157:103172.

Ledford H. Gene-silencing technology gets first drug approval after 20-year wait. *Nature*. 2018;560:291-292.

Li CX, Zhang Y, Dong X, Zhang L, Liu MD, Li B, Zhang MK, Feng J, Zhang XZ. Artificially Reprogrammed Macrophages as Tumor-Tropic Immunosuppression-Resistant Biologics to Realize Therapeutics Production and Immune Activation. *Advanced Materials* 2019;31: e1807211.

Li K, Lu L, Xue C, Liu J, He Y, Zhou J, Xia Z, Dai L, Luo Z, Mao Y, Cai K. Polarization of tumor-associated macrophage phenotype via porous hollow iron nanoparticles for tumor immunotherapy in vivo. *Nanoscale*. 2020;12:130-144.

Lim EK, Chung BH, Chung SJ. Recent Advances in pH-Sensitive Polymeric Nanoparticles for Smart Drug Delivery in Cancer Therapy. *Curr Drug Targets*. 2018;19:300-317.

Lin X, Fang Y, Jin X, Zhang M, Shi K. Modulating Repolarization of Tumor-Associated Macrophages with Targeted Therapeutic Nanoparticles as a Potential Strategy for Cancer Therapy. *ACS Appl Bio Mater*. 2021;4:5871-5896.

Liu M, Zeng G, Wang K, Wan Q, Tao L, Zhang X, Wei Y. Recent developments in polydopamine: an emerging soft matter for surface modification and biomedical applications. *Nanoscale*. 2016;8:16819-16840.

Mahmoodi Chalbatani, G Dana, H Gharagouzloo, E Grijalvo, S Eritja, R, Logsdon, C.D, Memari, F, Miri, S.R, Rad, M.R, Marmari, V. Small Interfering RNAs (SiRNAs) in Cancer Therapy: A Nano-Based Approach. *Int J Nanomedicine* 2019;14:3111–3128.

Malam Y, Loizidou M, Seifalian AM. Liposomes and nanoparticles: nanosized vehicles for drug delivery in cancer. *Trends Pharmacol Sci*. 2009;30:592-9.

Mu X, Li J, Yan S, Zhang H, Zhang W, Zhang F, Jiang J. siRNA Delivery with Stem Cell Membrane-Coated Magnetic Nanoparticles for Imaging-Guided Photothermal Therapy and Gene Therapy. *ACS Biomater Sci Eng*. 2018;4:3895-3905.

Mulens-Arias, V, Rojas, J. M, Barber, D. F. The Use of Iron Oxide Nanoparticles to Reprogram Macrophage Responses and the Immunological Tumor Microenvironment. *Frontiers in Immunology* 2021; 12: 2229.

Mulens-Arias, V, Rojas, J.M, Barber, D.F. The Intrinsic Biological Identities of Iron Oxide Nanoparticles and Their Coatings: Unexplored Territory for Combinatorial Therapies. *Nanomaterials (Basel)* 2020;10:837.

Munir MU, Salman S, Javed I, Bukhari SNA, Ahmad N, Shad NA, Aziz F. Nano-Hydroxyapatite as a Delivery System: Overview and Advancements. *Artif Cells Nanomed. Biotechnol.* 2021;49:717–727.

Murakami M, Cabral H, Matsumoto Y, Wu S, Kano MR, Yamori T, Nishiyama N, Kataoka K. Improving drug potency and efficacy by nanocarrier-mediated subcellular targeting. *Sci Transl Med*. 2011;3:64.

Nascimento, C. S, Alves, É. A. R., de Melo, C. P., Corrêa-Oliveira, R., Calzavara-Silva, C. E. Immunotherapy for cancer: Effects of iron oxide nanoparticles on polarization of tumor-associated macrophages. *Nanomedicine 2021;16*: 2633–2650.

Neamatallah T. Mitogen-Activated Protein Kinase Pathway: A Critical Regulator in Tumor-Associated Macrophage Polarization. *Journal of Microscopy and Ultrastructure* 2019;7:53.

Nielsen MC, Hvidbjerg Gantzel R, Clària J, Trebicka J, Møller HJ, Grønbæk H. Macrophage Activation Markers, CD163 and CD206, in Acute-on-Chronic Liver Failure. *Cells*. 2020;9:1175.

Nieto, C, Vega, M.A, Marcelo, G, Martín Del Valle, E.M. Polydopamine Nanoparticles Kill Cancer Cells. *RSC Advances* 2018;8:36201–36208.

Obacz, J, Avril, T, Rubio-Patiño, C, Bossowski, J.P, Igbaria, A, Ricci, J.E, Chevet, E. Regulation of Tumor–Stroma Interactions by the Unfolded Protein Response. *FEBS Journal* 2019; 286:279–296.

Oltolina, F, Peigneux, A, Colangelo, D, Clemente, N, D'urso, A, Valente, G, Iglesias, G.R, Jiménez-Lopez, C, Prat, M. Biomimetic Magnetite Nanoparticles as Targeted Drug Nanocarriers and Mediators of Hyperthermia in an Experimental Cancer Model. *Cancers (Basel)* 2020;12:1–25.

Otero K, Turnbull IR, Poliani PL, et al. Macrophage colony-stimulating factor induces the proliferation and survival of macrophages via a pathway involving DAP12 and beta-catenin. *Nat Immunol*. 2009;10:734-743.

Ouyang J, Xie A, Zhou J, Liu R, Wang L, Liu H, Kong N, Tao W. Minimally invasive nanomedicine: nanotechnology in photo-/ultrasound-/radiation-/magnetism-mediated therapy and imaging. *Chem Soc Rev*. 2022 May 26. doi: 10.1039/d1cs01148k.

Paproski RJ, Forbrich A, Huynh E, Chen J, Lewis JD, Zheng G, Zemp RJ. Porphyrin Nanodroplets: Sub-micrometer Ultrasound and Photoacoustic Contrast Imaging Agents. *Small*. 2016;12:371-80.

Pelaz B, Alexiou C, Alvarez-Puebla RA, Alves F, Andrews AM, et al. Diverse Applications of Nanomedicine. *ACS Nano* 2017;11:2313–2381.

Poltavets AS, Vishnyakova PA, Elchaninov AV, Sukhikh GT, Fatkhudinov TK. Macrophage Modification Strategies for Efficient Cell Therapy. Macrophage Modification Strategies for Efficient Cell Therapy. *Cells* 2020;9:1535.

Rahman M, Islam F, Afsana Mim S, Khan S, Islam R, Haque A, Mitra S, Emran T. bin; Rauf A, Multifunctional Therapeutic Approach of Nanomedicines against Inflammation in Cancer and Aging. *Journal of Nanomaterials* 2022; Vol.2022, pp.1–19. Article ID 4217529.

Raines LN, Zhao H, Wang Y, Chen HY, Gallart-Ayala H, et al. PERK Is a Critical Metabolic Hub for Immunosuppressive Function in Macrophages. *Nature Immunology* 2022;23:431–445.

Reichel D, Tripathi M, Perez JM.Biological Effects of Nanoparticles on Macrophage Polarization in the Tumor Microenvironment. *Nanotheranostics* 2019;3:66–88.

Rhee I. Diverse Macrophages Polarization in Tumor Microenvironment. *Archives of Pharmacal Research* 2016;39:1588–1596.

Riera-Borrull M, Cuevas VD, Alonso B, Vega MA, Joven J, Izquierdo E, Corbí ÁL. Palmitate Conditions Macrophages for Enhanced Responses toward Inflammatory Stimuli via JNK Activation. *The Journal of Immunology* 2017;199:3858–3869.

Rios FJ, Touyz RM, Montezano AC. Isolation and Differentiation of Murine Macrophages. In *Methods in Molecular Biology*; Humana Press Inc., 2017; Vol. 1527, pp. 297–309.

Ruffell B, Coussens LM. Macrophages and therapeutic resistance in cancer. *Cancer Cell*. 2015;27:462-72.

Rutz S, Scheffold A. Towards in Vivo Application of RNA Interference - New Toys, Old Problems. *Arthritis Research and Therapy* 2004;6:78–85.

Sanna V, Pala N, Sechi M. Targeted therapy using nanotechnology: focus on cancer. *Int J Nanomedicine*. 2014;9:467-83.

Sanna V, Sechi M. Therapeutic Potential of Targeted Nanoparticles and Perspective on Nanotherapies. *ACS Medicinal Chemistry Letters* 2020;11:1069–1073.

Sarup JC, Johnson RM, King KL, Fendly BM, Lipari MT, Napier MA, Ullrich A, Shepard HM. Characterization of an anti-p185HER2 monoclonal antibody that stimulates receptor function and inhibits tumor cell growth. *Growth Regul.* 1991;1:72-82.

Schirrmacher V. From Chemotherapy to Biological Therapy: A Review of Novel Concepts to Reduce the Side Effects of Systemic Cancer Treatment (Review). *International Journal of Oncology* 2019;54:407–419.

Schmitz ML, Shaban MS, Albert BV, Gökçen A, Kracht M. The Crosstalk of Endoplasmic Reticulum (ER) Stress Pathways with NF-KB: Complex Mechanisms Relevant for Cancer, Inflammation and Infection. *Biomedicines* 2018;6:58.

Schwartz RS. Paul Ehrlich's magic bullets. *N Engl J Med*. 2004;350:1079-8.

Shakeri-Zadeh A, Zareyi H, Sheervalilou R, Laurent S, Ghaznavi H, Samadian H. Gold nanoparticle-mediated bubbles in cancer nanotechnology. *J Control Release*. 2021;330:49-60.

Sheshadri N, Poria DK, Sharan S, Hu Y, Yan C, Koparde V N, Balamurugan K, Sterneck E. PERK Signaling through C/EBPδ Contributes to ER Stress-Induced Expression of Immunomodulatory and Tumor Promoting Chemokines by Cancer Cells. *Cell Death and Disease* 2021;12:1038.

Shubayev VI, Pisanic TR 2nd, Jin S.Magnetic Nanoparticles for Theragnostics. *Advanced Drug Delivery Reviews* 2009;61:467–477.

Sicari D, Delaunay-Moisan A, Combettes L, Chevet E, Igbaria A. A Guide to Assessing Endoplasmic Reticulum Homeostasis and Stress in Mammalian Systems. *FEBS Journal* 2020;287:27-42.

Siciliano, G, Monteduro, A. G, Turco, A, Primiceri, E, Rizzato, S, Depalo, N, Curri, M. L, Maruccio, G. Polydopamine-Coated Magnetic Iron Oxide Nanoparticles: From Design to Applications. *Nanomaterials* 2022; 12:1145.

Siegel RL, Miller KD, Jemal A. Cancer Statistics, 2020. *CA: A Cancer Journal for Clinicians* 2020;70:7–30.

Siwecka N, Rozpędek W, Pytel D, Wawrzynkiewicz A, Dziki A, Dziki Ł, Diehl JA, J, Majsterek I. Dual Role of Endoplasmic Reticulum Stress-Mediated Unfolded Protein Response Signaling Pathway in Carcinogenesis. *International Journal of Molecular Sciences* 2019;20:4354.

Soetaert F, Korangath P, Serantes D, Fiering S, Ivkov R. Cancer Therapy with Iron Oxide Nanoparticles: Agents of Thermal and Immune Therapies. *Advanced Drug Delivery Reviews* 2020;163-164:65–83.

Sousa De Almeida M, Susnik E, Drasler B, Taladriz-Blanco P, Petri-Fink A, Rothen-Rutishauser B. Understanding Nanoparticle Endocytosis to Improve Targeting Strategies in Nanomedicine. *Chem Soc Rev*. 2021;50:5397-5434

Sun J, Song B, Zhang L, Shao Q, Liu Y, Yuan D, Zhang Y, Qu X. Fucoidan Inhibits CCL22 Production through NF-KB Pathway in M2 Macrophages: A Potential Therapeutic Strategy for Cancer. *Scientific Reports* 2016;6:35855.

Takeshima H, Ushijima T. Accumulation of Genetic and Epigenetic Alterations in Normal Cells and Cancer Risk. *npj Precision Oncology* 2019;6:3:7.

Tatiparti K, Sau S, Kashaw SK, Iyer AK. SiRNA Delivery Strategies: A Comprehensive Review of Recent Developments. *Nanomaterials* 2017;7:77.

Tong S, Zhu H, Bao G. Magnetic Iron Oxide Nanoparticles for Disease Detection and Therapy. *Materials Today* 2019;31:86–99.

Torres TE, Lima E Jr, Calatayud MP, Sanz B, Ibarra A, Fernández-Pacheco R, Mayoral A, Marquina C, Ibarra MR, Goya GF. The relevance of Brownian relaxation as power absorption mechanism in Magnetic Hyperthermia. *Sci Rep.* 2019;9:3992.

Unnisa A, Chettupalli AK, Hussain T, Kamal MA. Recent Advances in Epidermal Growth Factor Receptor Inhibitors (EGFRIs) and their role in the Treatment of Cancer: A Review. *Anticancer Agents Med Chem.* 2022 Apr 8. doi: 10.2174/1871520622666220408090541

Urruticoechea A, Alemany R, Balart J, Villanueva A, Viñals F, Capellá G. Recent advances in cancer therapy: an overview. *Curr Pharm Des.* 2010;16:3-10.

Valverde-Tercedor C, Montalbán-López M, Perez-Gonzalez T, Sanchez-Quesada MS, Prozorov, T, Pineda-Molina E, Fernandez-Vivas MA, Rodriguez-Navarro AB, Trubitsyn D, Bazylinski DA, Jimenez-Lopez C. Size control of in vitro synthesized magnetite crystals by the MamC protein of Magnetococcus marinus strain MC-1. *Appl. Microbiol. Biotechnol.* 2015;99:5109–5121.

van Dalen FJ, van Stevendaal MHME, Fennemann FL, Verdoes M, Ilina O. Molecular Repolarisation of Tumour-Associated Macrophages. *Molecules* 2018;24:9.

van der Meel R, Sulheim E, Shi Y, Kiessling F, Mulder WJM, Lammers T. Smart Cancer Nanomedicine. *Nature Nanotechnology* 2019;14:1007–1017.

Venturoli D, Rippe B. Ficoll and dextran vs. globular proteins as probes for testing glomerular permselectivity: effects of molecular size, shape, charge, and deformability. *Am J Physiol Renal Physiol.* 2005;288:F605-13.

Wang LX, Zhang SX, Wu HJ, Rong, XL, Guo J. M2b Macrophage Polarization and Its Roles in Diseases. *Journal of Leukocyte Biology* 2019;106:345–358.

Wang Z, Duan Y, Duan Y. Application of polydopamine in tumor targeted drug delivery system and its drug release behavior. *J Control Release.* 2018;290:56-74.

Wolfram J, Ferrari M. Clinical Cancer Nanomedicine. *Nano Today*. 2019;25:85-98.

Xiao B, Hong L, Cai,X, Mei S, Zhang P, Shao L. The True Colors of Autophagy in Doxorubicin-Induced Cardiotoxicity (Review). *Oncology Letters* 2019;18:2165–2172.

Xu X, Gong X, Wang Y, Li J, Wang H, Wang J, Sha X, Li Y, Zhang Z. Reprogramming Tumor Associated Macrophages toward M1 Phenotypes with Nanomedicine for Anticancer Immunotherapy. *Advanced Therapeutics* 2020;3:1900181.

Yao Y, Zhou Y, Liu L, Xu Y, Chen Q, Wang Y, Wu S, Deng Y, Zhang J, Shao A. Nanoparticle-Based Drug Delivery in Cancer Therapy and Its Role in Overcoming Drug Resistance. *Frontiers in Molecular Biosciences* 2020;7:193.

Yin Z, Ma T, Lin Y, Lu X, Zhang C, Chen S, Jian Z. IL-6/STAT3 Pathway Intermediates M1/M2 Macrophage Polarization during the Development of Hepatocellular Carcinoma. *Journal of Cellular Biochemistry* 2018;119:9419–9432.

Yosef N, Vadakkan TJ, Park JH, Poché RA, Thomas JL, Dickinson ME. The phenotypic and functional properties of mouse yolk-sac-derived embryonic macrophages. *Dev Biol.* 2018;442:138-154.

Zeng R, Luo L, Sun X, Bao Z, Du W, Dai R, Tang W, Gao B, Xiang Y. EGFR/BRAF/MEK co-inhibition for EGFR-mutated lung adenocarcinoma patients with an acquired BRAF^{V600E} mutation: a case report and review of literature. *Cancer Drug Resist.* 2021;4:1019-1027.

Zhao H, Wu L, Yan G, Chen Y, Zhou M, Wu Y, Li Y. Inflammation and Tumor Progression: Signaling Pathways and Targeted Intervention. *Signal Transduction and Targeted Therapy* 2021;6:263.

Zhao YL; Tian PX; Han F, Zheng J, Xia XX, Xue WJ, Ding XM, Ding CG. Comparison of the Characteristics of Macrophages Derived from Murine Spleen, Peritoneal Cavity, and Bone Marrow. *Journal of Zhejiang University: Science B* 2017;18:1055–1063.

Zhen X, Cheng P, Pu K. Recent Advances in Cell Membrane-Camouflaged Nanoparticles for Cancer Phototherapy. *Small.* 2019;15:e1804105.

Zhi D, Yang T, Yang J, Fu S, Zhang S. Targeting strategies for superparamagnetic iron oxide nanoparticles in cancer therapy. *Acta Biomater.* 2020;102:13-34.

Zhong JT, Yu J, Wang HJ, Shi Y, Zhao TS, He BX, Qiao B, Feng Z.W. Effects of Endoplasmic Reticulum Stress on the Autophagy, Apoptosis, and Chemotherapy Resistance of Human Breast Cancer Cells by Regulating the PI3K/AKT/MTOR Signaling Pathway. *Tumor Biology* 2017;39: 1010428317697562.

Zhou H, Guo M, Li J, Qin F, Wang Y, Liu T, Liu J, Sabet ZF, Wang Y, Liu Y, Huo Q, Chen C. Hypoxia-Triggered Self-Assembly of Ultrasmall Iron Oxide Nanoparticles to Amplify the Imaging Signal of a Tumor. *J Am Chem Soc.* 2021;143:1846-1853.

Zhou S, Chen W, Cole J, Zhu G. Delivery of Nucleic Acid Therapeutics for Cancer Immunotherapy. *Medicine in Drug Discovery* 2020, *6*, 100023.

Zhou Z, Mao H, Yang L. Magnetic nanoparticles for precision oncology: theranostic magnetic iron oxide nanoparticles for image-guided and targeted cancer therapy. *Nanomedicine (Lond).* 2017;12:73-87.

Appendix

Student declaration

I declare that the PhD thesis titled "Magnetic nanoparticles as nanocarriers and immune modulators for cancer targeted therapy" represent my own work and that it has not been submitted in any previous application for a degree.

The work done in my PhD program is not exclusive of this thesis, but I also contributed to the following publications:

- Oltolina, F.; Peigneux, A.; Colangelo, D.; Clemente, N.; D'urso, A.; Valente, G.; Iglesias, G.R.; Jiménez-Lopez, C.; Prat, M. Biomimetic Magnetite Nanoparticles as Targeted Drug Nanocarriers and Mediators of Hyperthermia in an Experimental Cancer Model. *Cancers (Basel)* 2020, *12*, 1–25.

- Gómez-Morales, J.; Fernández-Penas, R.; Romero-Castillo, I.; Verdugo-Escamilla, C.; Choquesillo-Lazarte, D.; D'urso, A.; Prat, M.; Fernández-Sánchez, J.F. Crystallization, Luminescence and Cytocompatibility of Hexagonal Calcium Doped Terbium Phosphate Hydrate Nanoparticles. *Nanomaterials* 2021, *11*, 1–19.

- Cano Plá SM, D'Urso A, Fernández-Sánchez JF, Colangelo D, Choquesillo-Lazarte D, Ferracini R, Bosetti M, Prat M, Gómez-Morales J. Biomimetic Citrate-Coated Luminescent Apatite Nanoplatforms for Diclofenac Delivery in Inflammatory Environments. Nanomaterials (Basel). 2022 Feb 6;12(3):562.

Pubblished papers are reported below:

Biomimetic Magnetite Nanoparticles as Targeted Drug Nanocarriers and Mediators of Hyperthermia in an Experimental Cancer Model

Francesca Oltolina [1,†,‡], **Ana Peigneux** [2,†], **Donato Colangelo** [1], **Nausicaa Clemente** [1], **Annarita D'Urso** [1], **Guido Valente** [3], **Guillermo R. Iglesias** [4], **Concepcion Jiménez-Lopez** [2,*] and **Maria Prat** [1,5,6,7,8,9,*]

1 Department of Health Sciences, Università del Piemonte Orientale A. Avogadro, Via Solaroli 17, 28100 Novara, Italy; francesca.oltolina@med.uniupo.it (F.O.); donato.colangelo@med.uniupo.it (D.C.); nausicaa.clemente@med.uniupo.it (N.C.); annarita.durso@uniupo.it (A.D.)

2 Department of Microbiology, University of Granada, Campus Fuentenueva, s/n, 18071 Granada, Spain; apn@ugr.es

3 Department of Translational Medicine, Università del Piemonte Orientale A. Avogadro, Via Solaroli 17, 28100 Novara, Italy; guido.valente@med.uniupo.it

4 Department of Applied Physic, University of Granada, Campus Fuentenueva, s/n, 18071 Granada, Spain; iglesias@ugr.es

5 Centro di Biotecnologie per la Ricerca Medica Applicata (BRMA), Via Solaroli 17, 28100 Novara, Italy

6 Consorzio Interuniversitario per Biotecnologie (CIB), Località Padriciano 99, 34149 Trieste, Italy

7 Consorzio Interuniversitario Nazionale per la Scienza e Tecnologia dei Materiali (INSTM), Via Giuseppe Giusti 9, 50121 Firenze, Italy

8 Consorzio Interuniversitario di Ricerca in Chimica dei Metalli nei Sistemi Biologici (CIRCMSB) Piazza Umberto I 1, 70121 Bari, Italy

9 Centro Interdipartimentale di Medicina Rigenerativa (CIMeR), Via Montpellier, 1, 00133 Roma, Italy

* Correspondence: cjl@ugr.es (C.J.-L.); maria.prat@med.uniupo.it (M.P.)

† These authors contributed equally to this work.

‡ Present Address: Department of Microbiology, Facultad de Ciencias, Universidad de Granada, Campus Fuentenueva, s/n, 18071 Granada, Spain.

Simple Summary: The application of simultaneous and different strategies to treat cancer appears a promising therapeutic approach. Herein we proposed the application of chemotherapy combined with a magnetic nanocarrier delivery system to an in vitro and an in vivo experimental mammary carcinoma model. Drug-loaded biomimetic magnetic nanoparticle can be directed and concentrated on the tumor cells or site by the apposition of a magnet. Moreover, these nanoparticles can respond to an alternating magnetic field by developing hyperthermia around 43 °C, a temperature at which tumor cells, but not healthy cells, are particularly sensitive and thus induced to death. Indeed, when this nanoformulation is injected in vivo in the tumor site, and hyperthermia is generated, the combined chemo-thermal therapy mediated by these drug-loaded magnetic nanoparticles have a stronger therapeutic benefit compared to that carried out by the chemotherapeutic alone. These nanoformulation and strategy are thus promising tools for translational applications in cancer therapy.

Abstract: Biomimetic magnetic nanoparticles mediated by magnetosome proteins (BMNPs) are potential innovative tools for cancer therapy since, besides being multifunctional platforms, they can be manipulated by an external gradient magnetic field (GMF) and/or an alternating magnetic field (AMF), mediating targeting and hyperthermia, respectively. We evaluated the cytocompatibility/cytotoxicity of BMNPs and Doxorubicin (DOXO)-BMNPs in the presence/absence of GMF in 4T1 and MCF-7 cells as well as their cellular uptake. We analyzed the biocompatibility and in vivo distribution of BMNPs as well as the effect of DOXO-BMNPs in BALB/c mice bearing 4T1 induced mammary

carcinomas after applying GMF and AMF. Results: GMF enhanced the cell uptake of both BMNPs and DOXO-BMNPs and the cytotoxicity of DOXO-BMNPs. BMNPs were biocompatible when injected intravenously in BALB/c mice. The application of GMF on 4T1 tumors after each of the repeated (6×) iv administrations of DOXO-BMNPs enhanced tumor growth inhibition when compared to any other treatment, including that with soluble DOXO. Moreover, injection of DOXO-BMNPs in the tumor combined with application of an AMF resulted in a significant tumor weight reduction. These promising results show the suitability of BMNPs as magnetic nanocarriers for local targeted chemotherapy and as local agents for hyperthermia.

Keywords: magnetic nanoparticles; tumor targeting; cytotoxicity; doxorubicin; hyperthermia

---

1. Introduction

With its high burden on lives and being the second most common cause of morbidity and mortality in western countries, cancer represents a major public health problem. Although substantial advancements in therapy have been reached with surgery, chemotherapy, radiotherapy, and immunotherapy, there are still many drawbacks that require novel approaches [1,2]. Chemotherapy is the most common treatment for the majority of tumors, although its limited specificity toward cancer targets is responsible for important severe side effects [3–5]. The anthracycline Doxorubicin (DOXO) is one of the most effective chemotherapeutics used for treatment of solid tumors and, in particular, breast cancer. DOXO acts on target cells with different mechanisms. Its interaction with cells begins with passive diffusion through the cell membrane; within the cells, it generates reactive oxygen species (ROS), causing free radical formation and oxidative stress. It can enter the mitochondria, causing DNA damage and energetic stress, by activating the caspase cascade, leading to cell death by apoptosis and triggering autophagy as a consequence of cell energy depletion. Finally, it can translocate into the nucleus, where it intercalates between double-stranded DNA helices and inhibits the enzymes topoisomerases I and II, provoking lethal changes in chromatin structure and the generation of free radicals which, when combined with iron ions, induce oxidative damage to cellular membranes, DNA, and proteins [6–9]. However, DOXO treatments can induce severe cardiotoxicity due to DOXO accumulation in cardiac tissue [10], which then imposes a narrow therapeutic dose, thus limiting DOXO effectiveness [11]. DOXO efficiency is also compromised by the generation of resistance in cancer cells and by the reduction of drug activity due to physicochemical or physiological conditions in the tumor microenvironment, e.g., hypoxia, acidity, defective vasculature, and the presence of lymphatic vessels [12].

It is then clear that new approaches need to be taken to overcome these limitations, so that the effectiveness of DOXO treatments can be increased. One way to increase DOXO efficiency is to optimize selective drug delivery to the tumor site, which could be done by means of nanocarriers that allow external guidance and control. In this context, magnetic nanoparticles (MNPs) offer a series of advantages that make them attractive candidates for this goal. On one hand, as with all nanoparticles (NPs), they can carry high amounts of drugs and provide controlled release of the drug at the tumor site [13–15]. NPs allow both passive and active targeting of the tumor. Passive targeting is possible because of the nanometric size of the carrier, thus taking advantage of the enhanced permeability and retention of the microvasculature in the tumor mass [16–18]. Active targeting can be achieved both by functionalization of the nanoparticle with probes against tumor-associated markers [15,19,20] or/and, as in the case of MNPs, by the application of a gradient magnetic field (GMF), usually a linear variation in the static magnetic field, which can enhance NP accumulation within the tumor [5,21,22]. Moreover, MNPs can also serve as magnetic hyperthermia (MH) agents, able to induce a local intratumor temperature increase—around 43–46 °C, which is effective against tumor cells—when exposed to an alternating magnetic field (AMF) [15,23,24]. Furthermore, MH also promotes the release or activation

of therapeutic molecules coupled to the nanocarriers, thus locally increasing the concentration of the chemotherapeutic drug at the tumor site and prompting the effectiveness of the treatment [15,25–27].

For biomedical applications, other than obviously being cytocompatible, MNPs should comply with very specific requirements in order to display the advantages listed above, which are difficult to meet in the already commercialized inorganic ones mainly because of their small size [22].

Firstly, MNPs should be superparamagnetic, i.e., they should show zero magnetization in the absence of a magnetic field. In these conditions, MNPs display only weak reciprocal attractive magnetic interactions that keep them well dispersed, avoiding aggregation due to magnetic dipole particle interaction. Since their size is small (<100 nm), all MNPs behave as single magnetic domains and, thus, are randomly oriented in the absence of an external magnetic field. However, they rapidly rotate to align their magnetic moments to the external field once the external field is applied [22], thus promoting a net magnetization responsible for their guidance [28,29]. These NPs can also develop magnetic energy, which is then translated into heat if they are subjected to an efficient AMF. This behavior is governed by Neel and Brown's relaxation and depends on the frequency and intensity of the applied magnetic field [30,31]. Therefore, the size of the nanoparticle becomes an important parameter to control. An increase in the size of these MNPs would increase their magnetic moment per particle [32], thus increasing targeting efficiency and the heating power generated per particle unit mass in hyperthermia.

Secondly, the nanocarrier should expose functional groups that allow functionalization. Moreover, ideally, its isoelectric point (iep) is an important parameter which should facilitate stable interactions with loaded moieties at physiological pH while allowing their release at acidic pH conditions found in the tumor microenvironment [14,15]. These properties are shared by the so-called smart nanomaterials [24].

Functionalization may require the addition of a coating; this can be a disadvantage from many points of view: (i) it requires further manipulations, (ii) it can increase the size, (iii) it increases the overall cost of the synthetic procedure, and (iv) it may interfere with the magnetic response of the MNPs [33].

Therefore, the "bottle neck" for clinical use of MNPs is pending upon the production of a good nano-device that serves as a dual platform for drug delivery and hyperthermia. While their production by chemical means is challenging, many of these drawbacks affecting synthetic MNPs are overcome in biomimetic MNPs (BMNPs), for which production is mediated by magnetosome membrane-associated proteins, mimicking magnetosome production by magnetotactic bacteria [32].

In this context, MamC-mediated BMNPs have been recently proposed as cytocompatible, superparamagnetic NPs. In fact, they have demonstrated their potential as promising drug nanocarriers, even when embedded in liposomes [14,15,34], and as hyperthermia agents [15,23,35], which opens the possibility for combined therapy using the same nanoplatform. MamC modulates the nucleation and growth of the crystal by both template and ionotropic effects [15,36] and remains attached to the nanoparticles, forming a nanocomposite of 95 wt% magnetite + 5 wt% MamC. Such control of MamC on magnetite synthesis in vitro results in magnetic nanoparticles of different sizes and morphologies and thus magnetic properties, compared to those of chemically produced ones, and in nanoparticles with novel surface properties. In fact, these BMNPs display larger sizes (approximately 40 nm) compared to most commercial MNPs (≤30 nm) and show (i) a higher blocking temperature while being superparamagnetic at room temperature and (ii) high saturation magnetization, with these features indicating well-structured MNPs with large magnetic moments per particle, although MamC coating of BMNPs could faintly interfere with their magnetic properties [15]. On the other side, MamC protects BMNPs from oxidation and confers new surface properties to the BMNPs due to exposition of the functional groups of the protein. In fact, these BMNPs have an iep at pH 4.4, which allows electrostatic coupling to positively charged molecules such as DOXO at physiological pH and then drug release at acidic pH [14,15]. In addition, this release can be significantly favored under hyperthermia conditions triggered by AMF [15]. The presence of MamC, conferring a highly negative charge, contributes to

electrostatic repulsion within particles and thus to their colloidal stability, which, however, is somehow decreased upon loss of free functional groups after functionalization. Indeed, colloidal stability is one of the major problems of NPs in general. BMNPs are thus potentially useful tools for magnetic drug targeting combined with MH for local regional treatment in cancer.

In this study, we investigated the in vitro responses of BMNPs and DOXO-BMNPs to GMF and AMF by using magnetic field strengths and frequencies physiologically tolerable to find the best working conditions. Then, for the first time, we have described the in vivo distribution and biocompatibility of BMNPs after intravenous injection to ensure a possible safe use in vivo. Finally, the in vivo suitability of the use of DOXO-BMNPs for nano-targeted chemotherapy and MH elicitation in a mammary carcinoma experimental model was evaluated.

2. Results and Discussion

2.1. In Vitro Cytocompatibility of BMNPs in the Absence/Presence of a GMF

The cytocompatibility of any kind of NP is the first parameter to be ascertained before their eventual biomedical in vivo application [37]. BMNPs were fully characterized in previous studies. In particular, X-ray diffraction (XRD) was run to determine the mineralogy of the solid precipitated (>95% magnetite), and TEM and HRTEM were used to determine the mineralogy, the presence of multiple domains, and/or the presence of organic matter inside the crystal. From TEM micrographs, imageJ program was used to determine the size of the crystals, counting over 1000 crystals. The size of the crystallites was also confirmed by XRD. The ζ-potential, thermogravimetry analyses (TGA) and Fourier Transform Infrared spectrometry (FTIR) were used to determine the surface charge of the nanoparticles and to further evidence functionalization. The hydrodynamic radius and stability measurements were performed in order to determine aggregation and colloidal stability. BET specific surface areas was done for surface area determination. The magnetic properties were determined by means of hysteresis cycle, field coolong-zero field cooling (FC-ZFC) curves, and magnetic hyperthermia, i.e., Specific Power Absorption and Intrinsic Loss Power (SAR and ILP) values [14,15,38]. Although still not ideal, these BMNPs have improved colloidal stability compared to MNPs, even if they are larger (36 ± 12 nm) than the latter (<30 nm). After functionalization with DOXO, their size is only slightly increased (of about 4%) [39].

Moreover, BMNPs were already reported to be cytocompatible on many human cell lines originating from tumors of different origins [14,15,23]. Herein, we tested their cytocompatibility on two breast carcinoma cell lines, the mouse 4T1 and the human MCF-7, both in the absence and in the presence of a GMF. Since the production of reactive oxygen species (ROS) is indicative of cellular oxidative stress leading to cytotoxicity, we first analyzed the cytocompatibility of BMNPs by assessing the level of ROS potentially induced in the two mammary carcinoma cell lines.

Cells were incubated with increasing concentrations of BMNPs (up to 100 µg/mL) and subjected or not to GMF generated by the application of a neodymium magnet (1.8 kg pull) for 4 h. Under these conditions, no ROS production was detected in any cell line. ROS production was observed as a virtual green color (CellROX® Green Reagent) under confocal microscopy (Figure 1A,B) only in the positive controls where cells were treated with menadione (100 µM), a redox-active quinone that generates superoxides [40], which shows that oxidative stress could be induced in these cells.
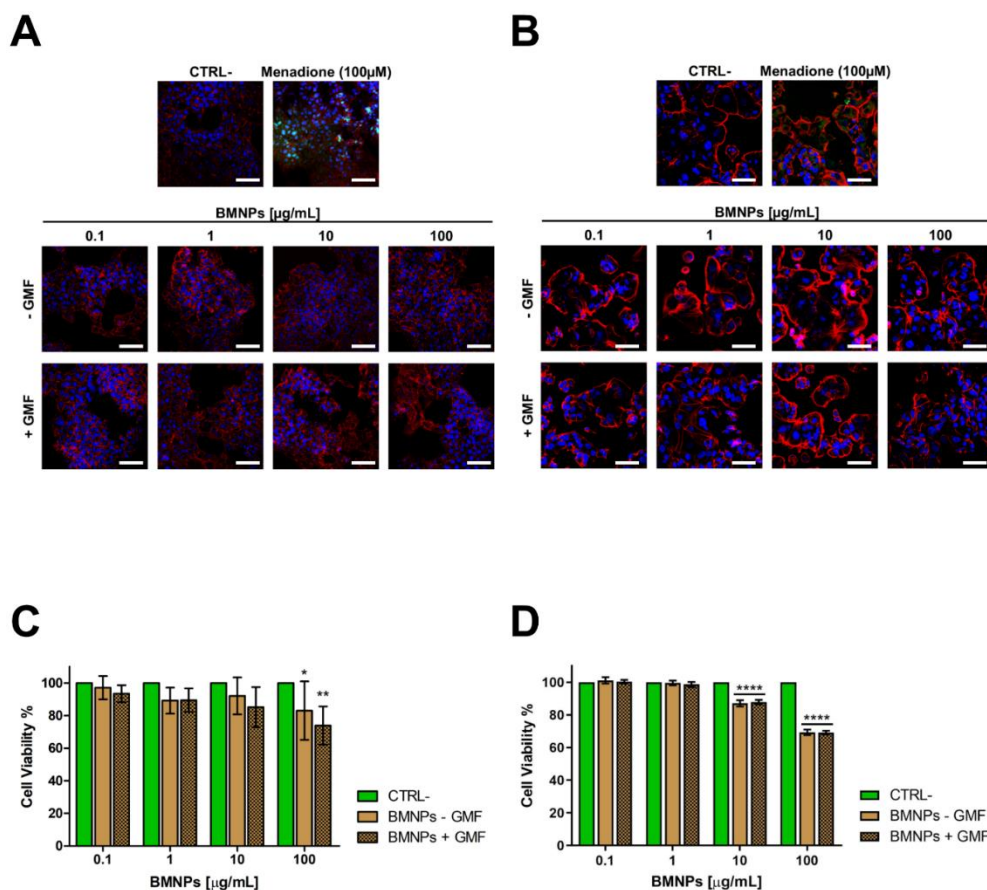
Figure 1. Cytocompatibility of biomimetic magnetic nanoparticles mediated by magnetosome proteins (BMNPs) on 4T1 (**A**,**C**) and MCF-7 (**B**,**D**) cells in the absence/presence of a gradient magnetic field: (**A**,**B**) Analysis of reactive oxygen species (ROS) production in the presence of different concentrations (0.1, 1, 10, and 100 μg/mL) of the BMNPs on 4T1 and on MCF-7 cells in the absence/presence of a gradient magnetic field by confocal microscopy. ROS production (green) was observed only in cells treated with menadione (100 μM), which was used as a positive control. Fixed and permeabilized cells were stained for actin with Tetramethylrhodamine B isothiocyanate (TRITC)-phalloidin (red) and for nuclei with TO-PRO3 (blue). Scale bar: 50 μm. (**C**,**D**) Cell viability assessed in an Methylthiazolyldiphenyl-tetrazolium (MTT) assay after incubation with the same different concentrations of BMNPs for 72 h in presence/absence of a gradient magnetic field (GMF). Differences between groups were assessed by 2-way ANOVA with Dunnett's multiple comparison test (**** $p < 0.0001$; ** $p < 0.001$; and * $p < 0.05$).

The ability of BMNPs to affect signaling pathways linked to cell survival, such as MAPK1/2, and Akt, was also investigated. In fact, the decrease in phosphorylation of these molecules has been linked to the cytotoxicity of some NPs [41,42]. For these experiments, 4T1 cells were incubated for 16 h with different BMNP concentrations up to 100 μg/mL and in the presence/absence of GMF. Protein expression and phosphorylation were analyzed by Western blot (Figure S1). As shown in Figure S1, no significant differences were observed in the levels of phosphorylated and not phosphorylated isoforms of these proteins in any condition tested with respect to untreated controls. The same results were observed for the expression of mTOR, for which expression and level of phosphorylation are under the control of Akt [43]. Taken together, these data show that the presence of BMNPs, either influenced or not by a magnetic field, has no biologic effect on the main signaling pathways controlling cell survival.

Finally, cytocompatibility of BMNPs was assessed by an MTT assay on cells treated with the BMNP concentrations listed above, both in the presence and in the absence of GMF. After the treatments

and regardless of the presence/absence GMF, cell viability was always higher than 80% for both cell lines (Figure 1C,D), in agreement with what was observed previously with other cells lines [14,15,23]. Altogether, these data confirm the high cytocompatibility of these BMNPs [44,45].

2.2. The Apposition of a GMF Enhances the Interaction of BMNPs with Cells

Showing the full cytocompatibility of BMNPs in the presence of a GMF, we evaluated whether the apposition of the GMF enhanced the interaction of BMNPs with cells. 4T1 and MCF-7 cells plated on coverslips were incubated for different times with 100 μg/mL BMNPs in the presence or absence of a magnet, were fixed, were washed, and were stained with Prussian blue. When a magnetic field was applied to cells, BMNPs were already clearly visible after 5 s of incubation the first time they were analyzed in both cases of 4T1 and MCF-7 cells, while in the absence of a magnetic field, BMNPs were detectable only and at a very low level after 1 min incubation (Figure 2A,C). In both cases, more BMNPs were detectable as the time of incubation increased, but there was always a significant difference between samples treated with the magnetic plate and not for the times assessed.
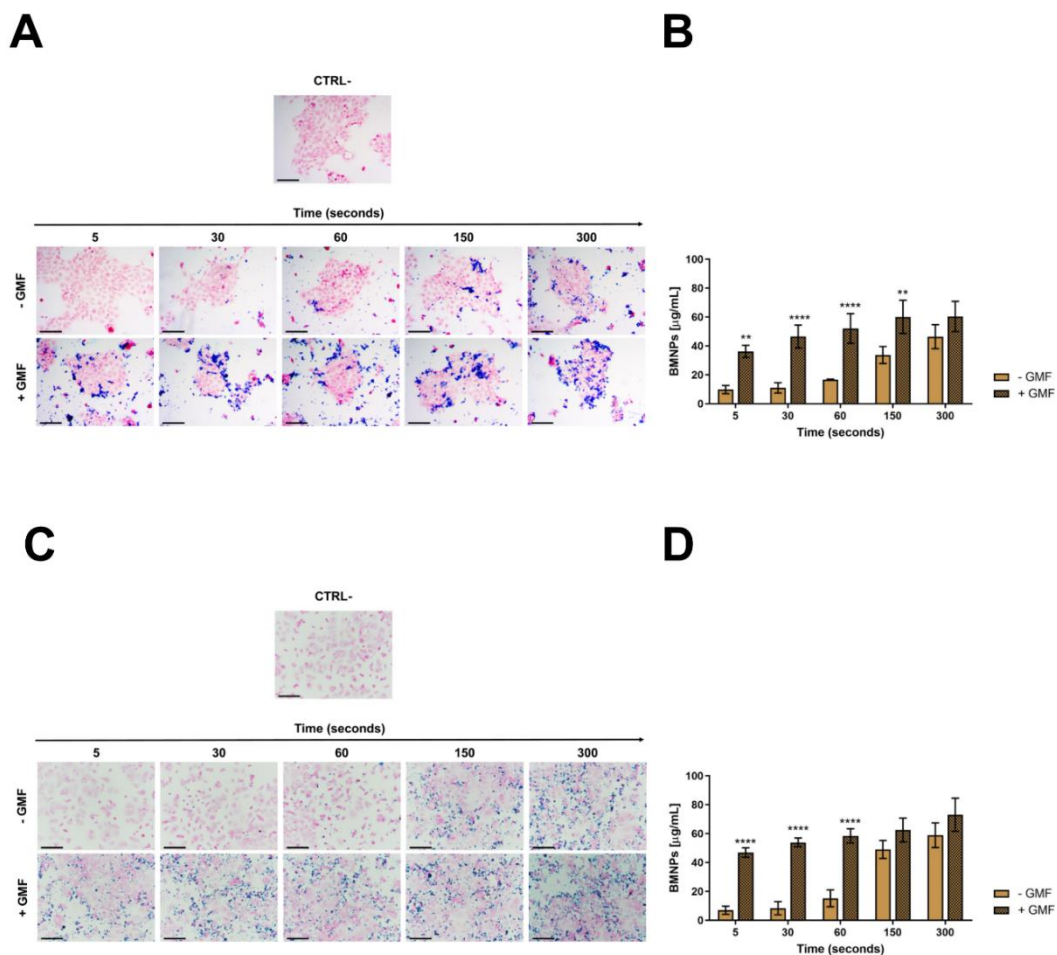

Figure 2. Interaction of BMNPs with 4T1 and MCF-7 cells in the presence/absence of a continuous gradient magnetic field: (**A**,**C**) Images showing BMNPs after Prussian blue staining and nuclear fast red counterstaining; scale bar: 50 μm. (**B**,**D**) Graphs showing the amount of iron associated with the types of cells as quantified with potassium thiocyanate: Cells were incubated with BMNPs (100 μg/mL) for different times (from 5 to 300 s) in the absence (−GMF) and presence (+GMF) of a gradient magnetic field. Untreated cells were used as a negative control. The results (expressed as mean ± SD) were obtained in three independent experiments made in triplicates. Differences between groups were assessed by 2-way ANOVA with Sidak's multiple comparison test. (**** $p < 0.0001$; ** $p < 0.001$).

In fact, the quantification of iron internalization in the cells also supports these differences (Figure 2B,D). In the absence of GMF, a very low concentration of iron was detected associated with the cells up to 1 min of incubation with BMNPs, and then, this concentration increased after 5 min up to 46 µg/mL for 4T1 cells and up to 59 µg/mL for MCF-7 cells. When the same experiments were performed in the presence of GMF, a significant amount of iron (36.2 µg/mL) was already found associated with 4T1 cells after 5 s of incubation, and this iron concentration increased in a time-dependent way until stabilization after 150 s, reaching a value of 60 µg/mL. An identical behavior was observed for MCF-7 cells in the presence of GMF. In this case, the iron concentration associated with the cells after 5 s of incubation with BMNP was 47 µg/mL, and after 150 s, it was 62.5 µg/mL. For longer periods of incubation, the amount of iron associated with cells increased also when GMF was absent, possibly because of the simple sedimentation of BMNPs on the cell surface. The lack of specific targeting for long periods of incubation under static conditions was already reported for apatite nanoparticles functionalized with a probe recognizing a tumor biomarker expressed at the surface of cancer cells [46–48]. It should be considered that these experiments were carried out in vitro in static conditions, while in vivo, GMF was applied in a dynamic situation in which BMNPs, which were circulating in the blood stream, were attracted and retained at the tumor site.

In this scenario, the advantage posed by the application of GMF to BMNP-cell interaction within the first minutes or, even, seconds after the treatment is worth noting and becomes crucial in increasing the effectivity of the treatment.

The interaction of BMNPs with cells was also analyzed at different time points by TEM that identified BMNPs through iron detection. In agreement with the data of optical microscopy after 30 s, only a few BMNPs were detected around the cell surface when cells were not subjected to the magnetic field. On the other hand, some BMNPs appeared to interact with the cell membrane and even to be internalized when a magnet was applied to the cells (Figure 3). The presence of iron in these samples was confirmed by microanalysis performed by energy dispersive X-ray (TEM-EDX) (Figure S2).
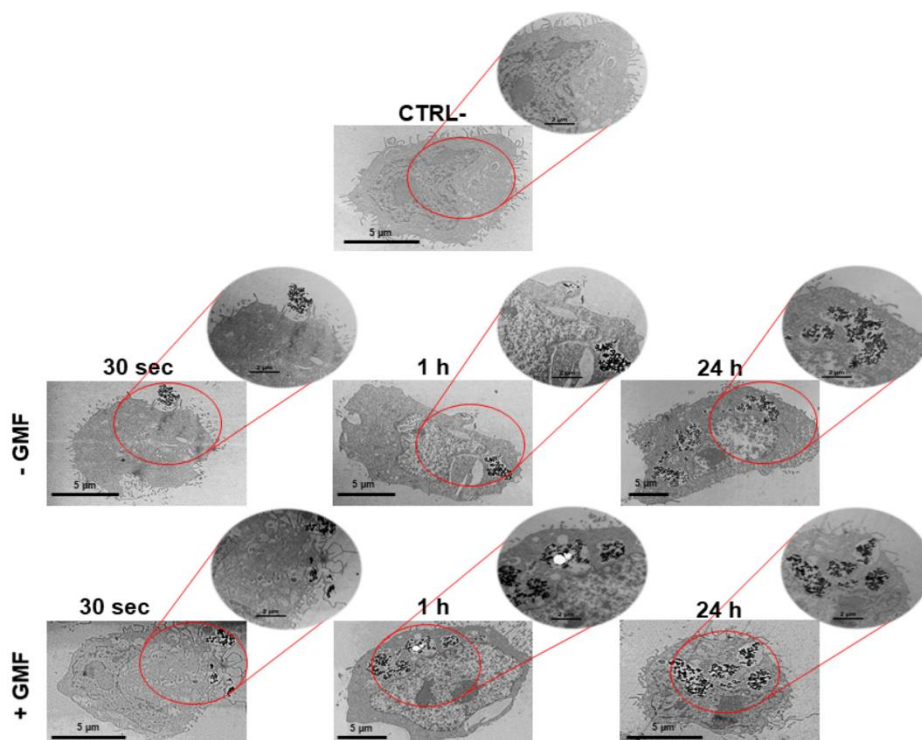

Figure 3. Interaction of BMNPs with 4T1 cells in the presence/absence of a continuous gradient magnetic field analyzed at TEM: Micrographs of the cells incubated with the 100 µg/mL of BMNPs for different periods of time. The micrographs are representative of alternate serial cuts of the cell pellets of each sample. Scale bar: 5 µm.

As expected, no significant differences between the two treatments were detected for the longer incubation times of 1 and 24 h. In both cases, BMNP internalization increased with time. Thus, the data obtained with TEM analysis are in accordance with those observed with Prussian blue staining and iron quantification. Altogether, these data show that BMNPs are highly responsive to a GMF in vitro, which allows an earlier and faster cellular interaction (Figure 2) and uptake (Figure 3). The faster internalization of BMNPs treated with a GMF is in good agreement with data reported by other authors in different cell lines, which also present enlarged endosomes where MNPs were accumulated in high amounts, without affecting cell viability [49,50]. Other researchers reported that, depending on the presence/absence of the magnet, a clear difference in the uptake of the MNPs was detected for at least 90 min [45]. Thus, our results show that the interaction and accumulation of BMNPs is reached earlier when cells are exposed to an external magnetic field as the magnetic force increases the sedimentation of BMNPs onto the cellular surface.

2.3. The Apposition of a GMF Enhances the Uptake of DOXO Coupled to BMNPs

Since BMNPs were planned as a drug delivery system, they were functionalized with DOXO and then incubated with 4T1 cells in the presence/absence of GMF. Their ability to deliver the drug to 4T1 cells was evaluated in experiments of confocal microscopy. DOXO, which was visualized in red by its intrinsic fluorescence, was already detectable in the cell nuclei after incubating functionalized BMNPs (100 ug/mL) in the presence of a magnet for 30 s, and the red signal increased over time (Figure 4).

By contrast, in the absence of the magnet, DOXO was observed within nuclei only after 30 min of incubation and, in any case, the signal was fainter. When soluble DOXO was incubated with cells, a strong red signal was detected but only after 30 min of incubation. The latter experiments are in line with others previously reported which showed that the cellular uptake of DOXO loaded on DOXO-BMNP nano-assemblies by cells was not as efficient as that of soluble DOXO [15,48]. This finding could probably be ascribed to the fact that soluble DOXO can easily diffuse through the plasma membrane, while DOXO associated with BMNPs either is internalized by a phagocytic pathway requiring a longer time or must first be released from the nanoparticles and then internalized. On the other side, the apposition of a magnet on DOXO functionalized BMNPs enhances cellular uptake of the drug when compared to freely diffusible soluble DOXO. Thus, the GMF favors quick concentration and accumulation of the drug in close contact with the cells and within the cells. Our results clearly show that DOXO adsorbed onto the BMNPs did not interfere with the applied magnetic field, in agreement with the data previously obtained by superconducting quantum interference device (SQUID) analysis [15].
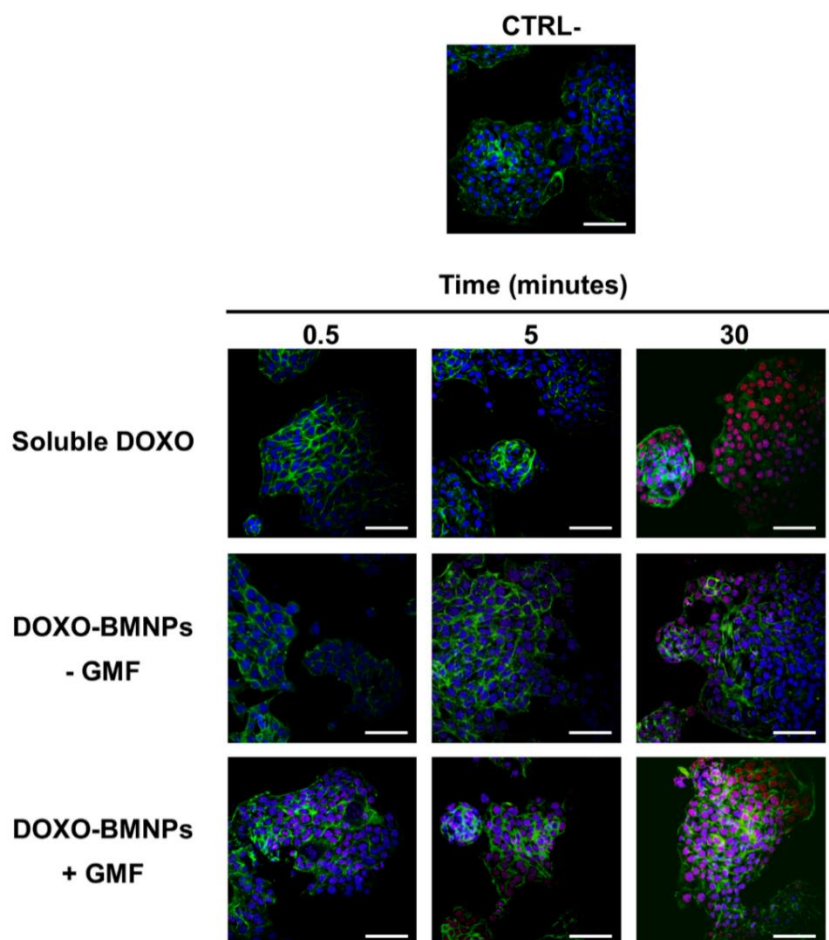
Figure 4. The apposition of a GMF enhances the cellular uptake of Doxorubicin (DOXO) coupled to BMNPs. 4T1 cells were incubated at 37 °C with DOXO-BMNPs for different times (0.5, 5, and 30 min) in the absence (−GMF) and presence (+GMF) of a gradient magnetic field. Soluble DOXO was used as a positive control. Cells were fixed, permeabilized, stained for cytoskeletal actin with fluorescein isothiocyanate (FITC)-phalloidin (green) and for nuclei with TO-PRO3 (blue) and visualized at confocal microscopy. DOXO was detectable for its intrinsic fluorescence in red. Scale bar: 50 μm.

2.4. The Apposition of a GMF Enhances the Cytotoxicity of DOXO-Coupled BMNPs

From the above experiments, it is clear that the application of a GMF enhances the interaction of BMNPs and its payload with cells when they are incubated for short times, but for longer periods BMNPs can interact even in the absence of GMF (Figures 2–4). Indeed, in preliminary experiments in which cytotoxicity of DOXO-BMNPs at different concentrations was evaluated in MTT assays carried out for 72 h, either in the presence or in the absence of a GMF, no differences could be appreciated between the two treatments. This suggests that relatively long incubations do not allow for perceiving the difference.

For this reason, to evaluate potential differences between the cytotoxicity in the samples treated with the magnetic field or not, a kind of pulse-chase MTT assay was carried out. 4T1 and MCF-7 cells incubated with DOXO-BMNPs (100 μg/mL) underwent GMF treatment or not for short times (from 5 to 300 s), and then, the medium and the BMNPs were withdrawn and incubation with fresh media at 37 °C was continued for further 72 h before reading the test. In the presence of the magnetic field at the time points of 5 and 30 s, DOXO-BMNPs exerted the same level of cytotoxicity exerted by soluble DOXO, while in the absence of the magnetic field, DOXO-BMNPs exerted lower toxicity (Figure 5A,B).
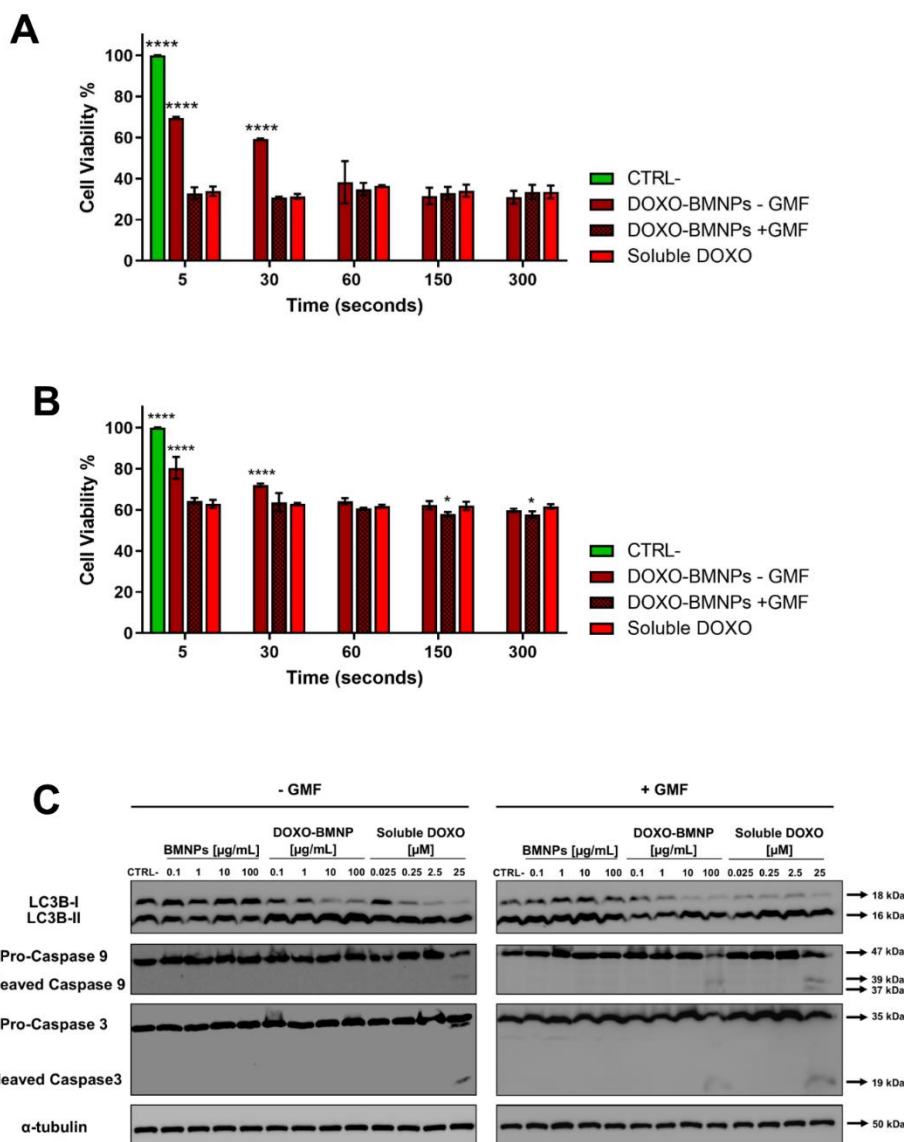
Figure 5. 4T1 (**A**) and MCF-7 (**B**) cells were incubated with drug-loaded BMNPs and treated with a GMF for different times, after which BMNPs and media were withdrawn and cells were replenished with fresh media and incubated for a further 72 h in an MTT assay. Soluble DOXO was used as a positive control. In all experiments, untreated cells receiving medium without nanoparticles were taken as the reference value (100%) of viable cells. Data are the average of 3 independent experiments performed in triplicates. Differences between groups were assessed by 2-way ANOVA with Dunnett's multiple comparison test (**** $p < 0.0001$). (**C**) Expression and state of activation of LC3b-I, caspase 3, and caspase 9. Extracts from 4T1 cells incubated for 16 h with different concentrations of BMNP ± DOXO in the absence/presence of a GMF were analyzed in Western blot. All blots shown are representative of three independent experiments. A Western blot representative of the bands of tubulin is shown, since in all experiments, similar patterns were observed.

This was observed for both cell lines, although MCF-7 showed a higher level of viability, possibly because these cells are more resistant to the effect of this drug [51]. It is expected that the application of the magnet in vivo at the tumor site could thus favor retention and accumulation of DOXO-BMNPs, which circulate in the bloodstream, promoting a higher toxicity against tumor cells [52,53]. Several scenarios could be envisaged regarding the interaction of DOXO-BMNPs with cells. Particles (or also some of them) could be uptaken by cells with their drug payload, or not internalized particles could release DOXO outside the cells and then the drug could be internalized. In any case, the application of

a magnetic field had a strong effect in terms of DOXO internalization and induced cytotoxicity. Indeed, without apposition of the GMF, the cytotoxic effect was delayed. Finally, these data suggest that DOXO is underestimated by confocal visualization, since its cytotoxic activity precedes in time its detection.

DOXO promotes cell death by various mechanisms, which are generally classified as caspase-independent and caspase-dependent; the former comprises autophagy, which is also called type II cell death [54]. Indeed, autophagy is an essential finely tuned housekeeping mechanism that enables cells to maintain homeostasis and normal functions by degrading and recycling injured organelles and misfolded proteins [55], and its dysregulation in both directions in cancer cells can lead to cell death and its modulation can thus represent a therapeutic strategy [56]. We thus evaluated whether DOXO-BMNPs in absence/presence of a GMF were able to activate an autophagic pathway with respect to not functionalized BMNPs and to soluble DOXO, for which the maximum level of cell death is already detectable after 16 h [57]. Figure 5C and Figure S3A,B show that the incubation of 4T1 cells with the two highest concentrations (10 and 100 µg/mL) of DOXO-BMNPs and with the corresponding doses of soluble DOXO induced activation of LC3b-I, which was nearly all cleaved to LC3b-II, as detected in Western blot analysis. This activation of autophagy is strictly dependent on the presence of DOXO, since neither nonfunctionalized BMNPs had an effect nor the apposition of a GMF enhanced the DOXO-induced cleavage of LC3b-I, a well-recognized autophagy biomarker [58]. It is thus concluded that DOXO, either soluble or coupled to BMNPs, exerts cytotoxicity, while the cytocompatibility of BMNPs is confirmed also with this parameter.

Apoptosis is another arm of the mechanisms contributing to efficient antitumor action for most anticancer drugs, including DOXO [59,60], and the activation of intracellular caspases is one of the main characteristics of the apoptotic cell death pathway. Two caspases, in particular caspase 9, which is involved in the first apoptotic events as a initiator, and caspase 3, which is an executer [61,62], were thus analyzed in Western blot prepared from lysates obtained from cells undergoing the same treatments as above. As shown in Figure 5C and Figure S3, only if cells were treated with DOXO-BMNPs and GMF were the two caspases activated to their cleaved forms. In the controls, soluble DOXO could induce caspase cleavage independently of the apposition of the magnetic field, while not functionalized BMNPs had no effect both in the presence and absence of a GMF.

2.5. In Vivo Biocompatibility and Nanoparticles Biodistribution

After showing that BMNPs were cytocompatible in different in vitro assays, we analyzed the in vivo biocompatibility as well as their distribution in different organs after systemic administration by tail vein injection. We chose the dose of 10 µg BMNPs/g mouse, corresponding to about 8 µg of Fe/g mouse, according to studies previously published on Fe_3O_4 MNPs [63,64]. All mice injected with BMNPs were found to be alive and in good shape for at least 60 days, the latest time point checked. Sections of brain, heart, lung, spleen, liver, and kidney prepared from animals 1, 7, and 60 days after BMNP injection do not show any morphological alterations compared to those from a control mouse (Figure S4). In the case of spleen, while the specimens from untreated control animals were positive for Prussian blue staining because of their endogenous iron deposits, such a staining was undetectable 1 day after BMNP injection, but it was resumed 1 week after, if not earlier. Moreover, BMNPs are not retained in the different organs, except for a low amount in the lungs and in the liver. Other authors also detected magnetic nanoparticles in spleen, liver, and lungs [65,66] after their intravenous administration due to the vascularized nature of these organs but without associated toxicity. Moreover, these organs are part of the reticuloendothelial system (RES), where many different nanoparticles of the BMNP size range accumulates because they are phagocytosed by macrophages through adsorption of opsonin [63,67]. On the other side, it is widely accepted that iron present in the injected MNPs can be recycled in ferritin proteins [68] or eliminated with the feces [69].

Altogether, these data confirm the full biocompatibility of BMNPs up to 10 µg/g mouse weight, in agreement with the in vitro data and the previously reported results [14,15]. In fact, Kim et al. [70]

demonstrated that doses of up to 100 mg/kg of MNPs, within the range of 50 nm, are not toxic after circulation for a month.

2.6. The Apposition of GMF Enhances the Antitumor Effect of DOXO-Coupled BMNPs

The antitumor efficacy of DOXO-BMNPs in combination with application of a GMF was studied in vivo in BALB/c mice bearing mammary carcinomas induced by intra fat pad mammary gland injection of 4T1 cells. This tumor model was chosen at the beginning of this study, since its growth and metastatic spread mimic very closely stage IV human breast cancer [71].

Mice bearing tumors of approximately 30 mm^3 were intravenously injected with BMNPs, DOXO-BMNPs, and soluble DOXO at the same corresponding amounts (2 mg/kg mouse) and with Phosphate Buffered Saline (PBS) as controls. Immediately after nanoparticle injection, in half of the mice, a GMF was applied on the tumor for 1 h. All treatments were repeated 5 more times at 3-day intervals and, each time, tumor sizes were evaluated and compared to the ones of control animals receiving only PBS or soluble DOXO. No differences between the groups receiving the different treatments were observed up to day 6 (Figure 6). At day 9, all treated animals displayed tumors with decreased sizes with respect to the controls receiving PBS.

From this moment on, significant differences emerged between the mice injected with DOXO versus those mice not receiving DOXO but injected with BMNPs ± GMF, with these differences being even more evident at the end of the experiment (day 18) when mice were euthanized for ethical reasons. The highest percentage of inhibition was observed in mice receiving the combined treatment of DOXO-BMNPs and apposition of GMF (52 ± 5%), versus animals receiving only DOXO-BMNPs (43 ± 3%) or soluble DOXO (38 ± 2%).

At the end of the experiment, tumors were excised and fixed and histologic sections were stained with Prussian blue to analyze and quantify the iron content. As expected, tumor sections from animals that were injected with BMNPs, both with the DOXO payload and without, and underwent GMF treatments displayed a higher level of the blue pigment revealing iron, which was quantified as being approximately double the amounts present in the tumors not treated with GMF. These values were similar in the two cases of BMNPs and DOXO-BMNPs (Figure 6B,C). This finding is in agreement with reports from other laboratories, which showed that the intravenously injected with synthetic MNPs accumulate from 2× to 8× within the target site when a GMF is applied there [72]. The presence of BMNPs in the tumors, even at low levels, in the absence of GMF treatment could be due to their passive accumulation related to the enhanced permeability and retention (EPR) effect. Indeed, for subcutaneous tumors with low vascularization, the EPR effect was reported to cause accumulation of about 1–15% of nanoparticles, relative to the injected dose, which was doubled upon apposition of the magnet doubled [72,73].

As a summary, our results confirm that DOXO-BMNPs maintain their ability to respond to a GMF also in vivo and can be directed to a specific organ/tumor for drug delivery or hyperthermia treatment (once arrived at the tumor site).

This targeted treatment potentially reduces the side effects of the drug on healthy cells in the rest of the body, thus favoring accumulation at the tumor site of the nanoparticles loaded with DOXO, which could exert its toxic effect. In this context, much work has been devoted to producing magnetically targeted chemotherapy treatments for tumors from different organs, including lung, prostate, brain, melanoma, breast, and liver, with the goal of achieving a high concentration of drugs in the affected area with a rapid response time and minimal side effects [74–76].
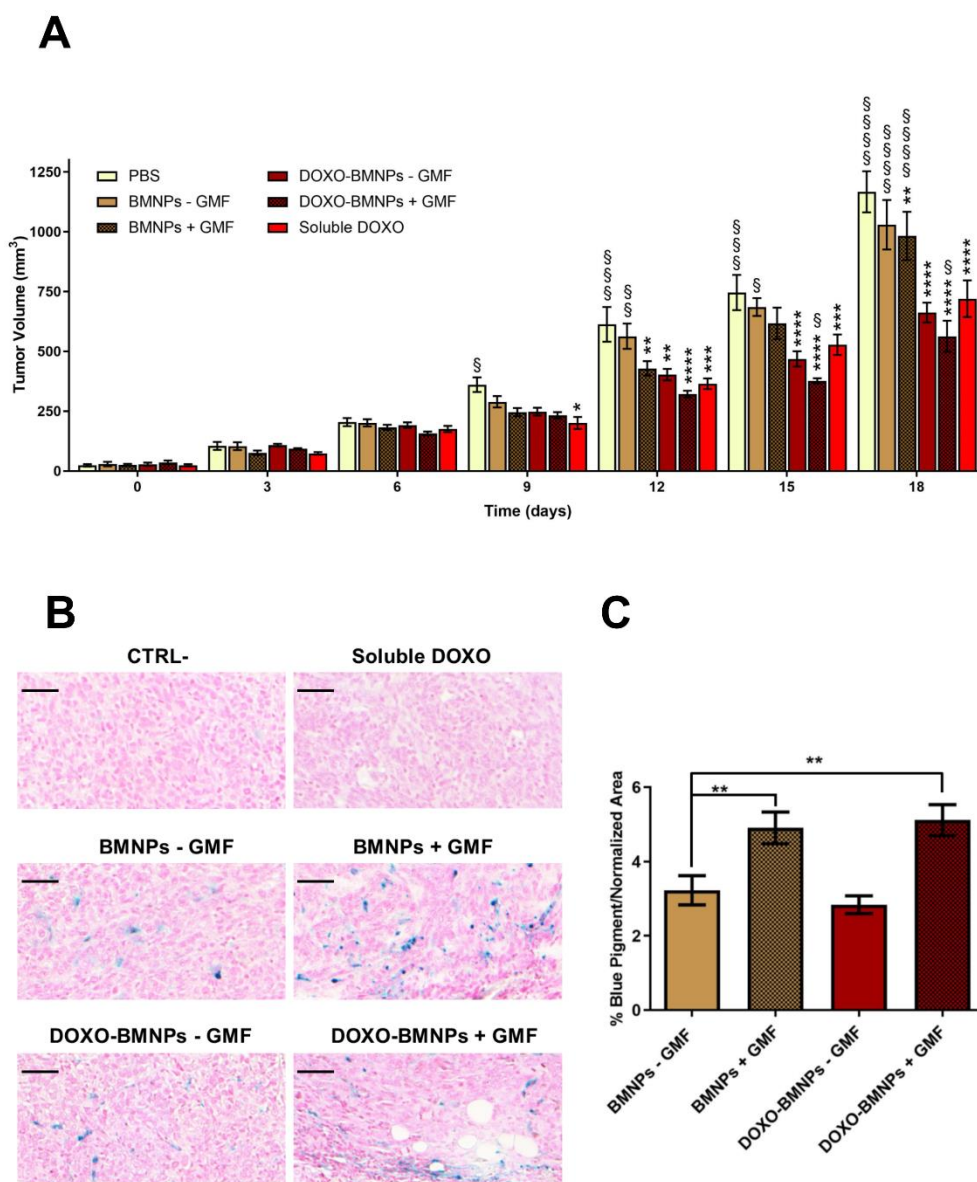
A

B

C

Figure 6. The apposition of GMF enhances the antitumor effect of DOXO-coupled BMNPs. (**A**) DOXO-BMNPs or BMNPs were injected intravenously in female BALB/c mice (*n* = 9) bearing tumors induced by 4T1, combined with GMF apposition or not. Each treatment was given 6 times, every 3 days starting from day 0, at a dose of 2 mg DOXO/kg mouse body weight or comparable amounts of BMNPs (15 μg BMNPs/g body weight). Controls included same amounts of soluble DOXO and PBS alone. Tumor sizes were measured every 3 days. The results are expressed as mean ± SD. Differences between groups were assessed by 2-way ANOVA with Dunnett's multiple comparison test (**** *p* < 0.0001; *** *p* = 0.0001; ** *p* = 0.001; and * *p* = 0.01; * indicates samples compared to PBS) (§§§§ *p* < 0.0001; §§§ *p* = 0.0001; §§ *p* = 0.001; and § *p* = 0.01; § indicates samples compared to soluble DOXO). (**B**) Presence of BMNPs, detected by Prussian blue staining, and (**C**) iron quantification in histologic sections of the tumors at the end of the experiment (d 18). Scale bar: 50 μm. The results are expressed as mean ± SD. Differences between groups were assessed by 1-way ANOVA with Dunnett's multiple comparison test (** *p* < 0.05).

2.7. In Vitro Cytotoxicity of BMNPs under the Influence of An AMF

Finally, a step forward is to use the same nanoplatform as nanocarrier and as a magnetic hyperthermia agent to enhance the cytotoxic effect of chemotherapy with hyperthermia. Indeed, it is well known that magnetic nanoparticles exposed to an AMF develop heat, thus selectively killing tumor

cells which are more sensitive than normal cells to high temperatures in the range of 43–46 °C [3,77]. Such a potential application was first tested in in vitro experiments. Briefly, 4T1 cells resuspended in Eppendorf tubes with different amounts of BMNPs were positioned under an AMF of 130 kHz and 18 kA m^{-1} for 20 min and cell viability was then analyzed in an MTT assay, which was read out 24 h after plating the cells. Cells were fully viable when incubated with 100 µg of BMNPs, both in the presence or absence of the AMF, and only by increasing BMNPs concentration was an effect of the applied AMF detected in a dose-dependent relationship (Figure S5). Indeed, when cells were incubated with 500 µg of BMNPs in the presence of the AMF, a temperature of about 45 °C was reached and cell viability was reduced to only 8.4%, while in the absence of the AMF, cell viability was still around 60% of the controls without BMNPs. It is thus clear from these data that the amount of BMNPs is critical to generate enough heating, which is then responsible for cell death [78].

2.8. AMF Enhances the in Vivo Antitumor Activity of DOXO-BMNPs

Since in vitro experiments showed that BMNPs could be used as hyperthermia agents, experiments were designed to demonstrate the effectiveness of the MH and the combination of this treatment with chemotherapy in vivo.

Mice bearing 4T1-induced tumors were injected once in situ with DOXO-BMNPs and DOXO-free BMNPs, and then half of the mice in each group were subjected to AMF. Controls included mice injected with the same doses of soluble DOXO (positive control) or PBS (negative control). When an AMF was applied in vivo, hyperthermia production was observed only in the mice injected with the NPs (Figure 7A, right vs left panel). Tumor temperature was found to reach 42–45 °C in the first 2–3 min, and this temperature was maintained throughout the treatment lasting 20 min.

At day 3 posttreatment, the best therapeutic effects were observed in mice treated either with soluble DOXO or with DOXO-BMNPs and were subjected to AMF (Figure 7B). In both cases, tumor volumes were significantly reduced, while in all the other cases, tumors increased their sizes, except for mice injected with DOXO-free BMNPs and subjected to AMF, where tumor volumes were stable.

At day 5 postinjection, the treatment with the strongest therapeutic benefit was DOXO-BMNPs + AMF. Mice from this specific group displayed tumor volumes virtually identical to those registered at day 3 posttreatment, while those from mice treated with soluble DOXO and BMNPs + AMF showed larger volumes compared to those measured at day 3 posttreatment, but still, these two treatments displayed better therapeutic effect compared to all the other treatments. A first conclusion from these experiments is that AMF-induced hyperthermia is a valid treatment to reduce tumor size. Regarding tumor weight, at day 5 posttreatment, this parameter was significantly reduced only in tumors from mice treated with DOXO-BMNPs + AMF (Figure 7C). Also, significantly higher necrosis of the cancer cells was observed in tumors from mice treated with NPs +AMF, irrespective of the presence or absence of DOXO based on results of Hematoxylin & Eosin staining of tumor tissue (Figure 7D). Indeed, in these cases, necrotic areas were around 45–46% of the tumor area, compared to those observed in all the other experimental conditions (20% of the tumor area). Combining the results of the two latter parameters, it is thus clear that DOXO-BMNPs together with hyperthermia have a strong antitumor efficacy.

In conclusion, DOXO coupled to BMNPs has a longer lasting and more efficient effect, possibly because, as a nano-assembly, it remains in the tumor site for longer periods, with the drug being slowly released following changes in the environmental pH values and also triggered by hyperthermia, as previously demonstrated by Peigneux et al. [15]. Therefore, higher DOXO doses are locally reached at the target site that, along with the local temperature increase triggered by application of the AMF, allow for better efficiency of the treatment. Although still not ideal, BMNPs have improved colloidal stability compared to MNPs, even if they are larger than the latter. Ways to improve colloidal stability that are presently investigated by our research group are embedding the BMNPs in liposomes [34], covering the BMNPs with protein corona from plasma [38], and/or mixing BMNPs and MNPs [39].
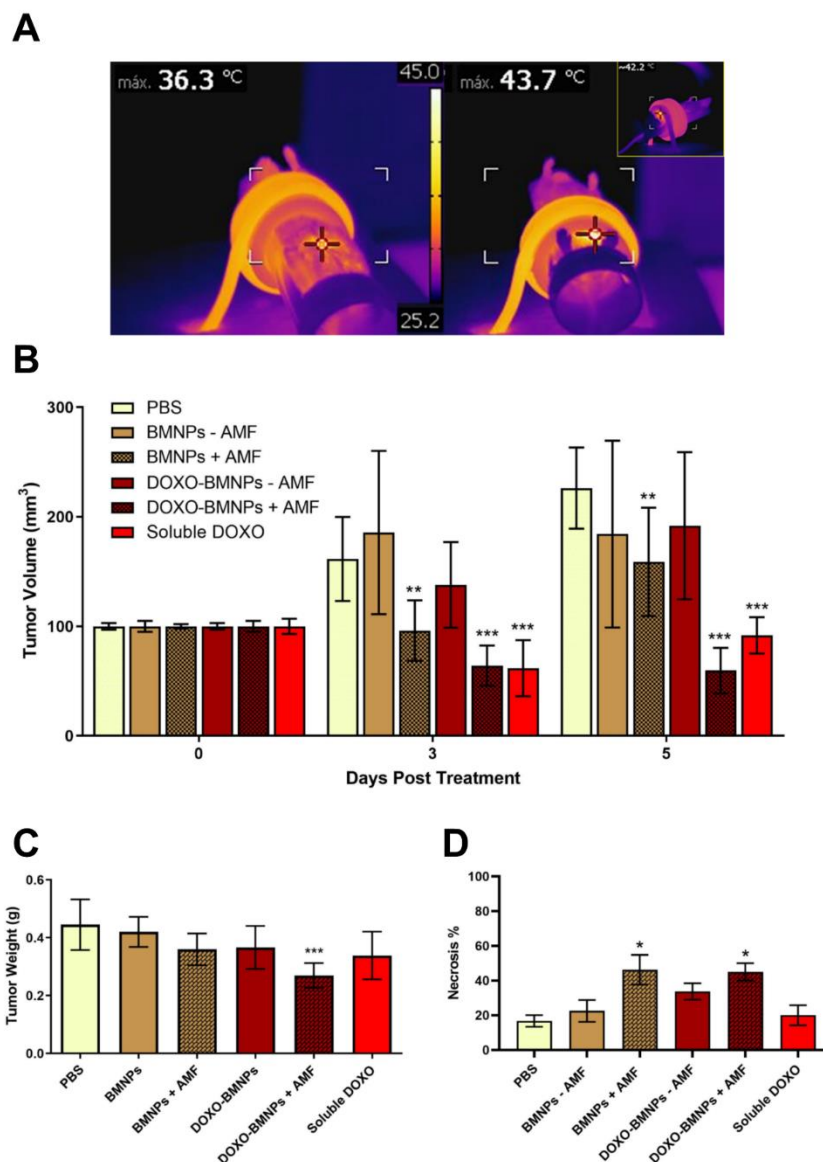
Figure 7. In vivo antitumor activity of BMNPs under the influence of an alternating magnetic field (AMF): (**A**) Images taken with a thermic camera of a representative mouse without (left) and with (right) injected BMNPs during AMF treatment. Note the different colors within the circle on the backside of the mouse. (**B**) Effect on the growth of 4T1 tumors (*n* = 8) in female BALB/c mice, analyzed 3 and 5 days after one single injection of DOXO-BMNPs or not functionalized BMNPs ± AMF: Each group received one intratumor injection of 3 mg BMNPs/mouse on the first day of the treatment (day 0). For the groups injected with soluble DOXO or DOXO-BMNPs, the dose of DOXO (either soluble or adsorbed on the BMNPs) was 80 μg/mouse. Differences between groups (all compared to PBS) were assessed by 2-way ANOVA with Dunnett's multiple comparison test (*** $p < 0.0001$; ** $p = 0.001$). Weight (**C**) and necrosis % (**D**) of tumors were measured at the end of the experiment (day 5), and all samples were compared to the PBS group. Differences between groups were assessed by ordinary one-way ANOVA with Dunnett's multiple comparison test (*** $p < 0.05$; * $p = 0.001$).

3. Materials and Methods

3.1. BMNP Synthesis

MamC protein was heterologous expressed in *E. coli* TOP10 competent (Life Technologies: Invitrogen, Grand Island, NY, USA), purified by affinity chromatography under denaturing conditions

(IMAC, GE Healthcare, Chicago, IL, USA), and refolded by serial dialysis steps as previously described by Valverde-Tercedor et al. [32]. Then, the biomimetic magnetic nanoparticles (BMNPs) were synthesized inside an anaerobic Coy chamber (96% N_2/4% H_2, Coy Laboratory Products, Grass Lake, MI, USA) at 25 °C and 1 atm total pressure following the protocol described by Peigneux et al. [15]. Briefly, 10 μg/mL of MamC protein was added to deoxygenated solutions of 2.78 mM $Fe(ClO_4)_2$, 5.56 mM $FeCl_3$, and 3.5 mM/3.5 mM $NaHCO_3$/Na_2CO_3 for the in vitro coprecipitation reaction. BMNPs were incubated for 30 days and then were washed three times with deoxygenated Milli-Q water, each time by concentrating BMNPs in the vial with a N42 neodymium magnet one (1.8 kg pull, Magnet Expert Ltd.; 10 mm diameter × 3 mm thickness) placed outside the vial, discarding the fluid, adding fresh water, shaking vigorously, and discarding the fluid again. BMNPs were kept in water inside the Coy chamber until further use. The concentration of BMNPs in suspension was calculated by weight difference taken in a precision scale between a given volume of a BMNP suspension and the same sample once all water was evaporated by using a thermoblock at 100 °C. This concentration was measured independently in, at least, five different samples from the same batch, and an average concentration value was taken.

3.2. Functionalization of the BMNPs Produced in Presence of MamC Protein

BMNPs were functionalized with doxorubicin (DOXO-BMNPs) following the same procedure carried out previously [15]. Briefly, 5 mg of BMNPs was mixed with 1 mg/mL of DOXO dissolved in water inside hermetic closed bottles to avoid magnetite oxidation. Mixtures were maintained at 25 °C in rotation on a wheel for 24 h. Then, the DOXO content was assessed by UV-Vis spectroscopy (λ = 490) with Nanodrop, indicative of the concentration of the molecule by comparison to a standard curve. The amount of adsorbed DOXO was calculated from the differences between the concentration of the molecule in the supernatant before and after adsorption on the BMNPs. The solid components were washed 5 times with 4-(2-Hydroxyethyl)piperazine-1-ethanesulfonic acid, N-(2-Hydroxyethyl)piperazine-N′-(2-ethanesulfonic acid) buffered saline solution (0.01 M HEPES and 0.15 M NaCl) until the absorbance was less than 0.02 units at 490 nm (equivalent to a negligible amount) using a magnet. Each washing was performed by concentrating BMNPs in the vial with the neodymium magnet placed outside the vial, discarding the fluid, adding fresh HEPES buffered saline solution, shaking vigorously, and discarding the fluid again. Then, the functionalized nanoparticles were resuspended in the same solution and kept at 4 °C until further use. The concentration of functionalized BMNPs was measured by iron quantification with potassium thiocyanate. Both BMNPs and functionalized BMNPs were dissolved in 37% HCl, mixed with 10% H_2O_2, and incubated for 20 min at room temperature. Samples were then stained with 1 mL of 1% potassium thiocyanate in Milli-Q water, and their absorbances were measured at 490 nm. The concentration of ferric ions in the samples was calculated referencing the obtained absorbances to a standard curve performed following the same protocol with known concentrations of BMNPs.

3.3. Cell Cultures

The 4T1 murine breast carcinoma cell line derived from BALB/c mice (ATCC® CRL-2539™) were maintained in Dulbecco's Modified Eagle Medium (DMEM) supplemented with 10% fetal calf serum (FCS), 50 U/mL penicillin, and 50 μg streptomycin (here referred as complete medium). Cells were sub-cultured twice a week, when they were at 80–90% confluence.

3.4. Interactions of BMNPs with Cells in the Absence/Presence of a GMF

3.4.1. Detection of Reactive Oxygen Species (ROS) Production

To measure the potential oxidative stress in living cells, as a consequence of the presence of the BMNPs, the CellROX® Green Reagent (ThermoFisher, Waltham, MA, USA) was used following the protocol recommended by the manufacturer. Briefly, cells (approximately 20 × 10³ 4T1/well) were

seeded on glass coverslips in 24-well plates. After exposure to different concentration of BMNPs (0.1, 1, 10, and 100 μg/mL) in the presence and absence of a gradient magnetic field for 4 h, the cells were washed with PBS and CellROX® Green Reagent was added to a final concentration of 5 μM in 300 μL of DMEM medium without serum. Then, the plate was incubated in the dark at 37 °C for 30 min. Menadione (100 μM) was used as a positive control [40]. After the incubation time, the coverslips were washed with PBS pH 7.2, fixed with 4% paraformaldehyde in PBS, washed again, and permeabilized with 0.1% Triton-X100 for 10 min. Finally, the coverslips were stained and mounted on specimen slides (Biosigma). The cytoskeletal actin was stained with TRITC-phalloidine (1/200, Sigma-Aldrich (St. Louis, MO, USA), excitation at 543 nm; emission at 560–620 nm), and the cell nuclei were stained with TO-PRO-3 (1/50, Life Technologies, excitation at 642 nm, emission at 650–750 nm). The CellROX® Green Reagent is only fluorescent in the oxidized state because of ROS production. Therefore, the emission of green fluorescence (at 485/520 nm) is stable and is produced after DNA binding, and therefore, its signal is mainly located in the nucleus. Fluorescence was detected using a Spectral Confocal Leica TCS SP2 AOBS microscope. The images were taken at 400× magnification. The ImageJ software was used for the analysis.

3.4.2. MTT Assay in the Absence/Presence of a GMF or an AMF

Cells (approximately 5×10^3 4T1/well) were incubated in 96-well plates for 24 h. Then, different concentrations of BMNPs (0.1, 1, 10, and 100 μg/mL) were added to plated cells in 100 μL of complete medium. These samples were incubated at 37 °C and 5% CO_2 in the absence or presence of a gradient magnetic field, using a magnetic plate below the 96-well plates, for 72 h. In another set of experiments, the cells were incubated with 100 μg/mL of BMNPs, DOXO-BMNPs, and a quantity of soluble DOXO normalized for the amount of drug adsorbed on BMNPs for shorter time points (5, 30, 60, 150, and 300 s), both in the presence and absence of the gradient magnetic field.

In the case of the alternating magnetic field treatment, approximately 95×10^4 4T1 cells were placed in a 0.5 mL tube. Then, suspensions of 100, 300, and 500 μg of BMNPs, resuspended in complete DMEM medium, were added and exposed or not to an alternating magnetic field (130 kHz and 18 kA m^{-1}) for 20 min. After this treatment, cells were counted by using trypan blue, seeded in 96-well plates (approximately 10×10^3 4T1/well), and incubated at 37 °C and 5% CO_2 for 24 h.

At the end of the incubation time of the different experiments, cell viability was evaluated by MTT colorimetric assay as described in Oltolina et al. [46]. Briefly, 20 μL of MTT solution (5 mg/mL in PBS solution) was added to each well. The plate was then incubated at 37 °C for 2 h, and then, supernatants were carefully aspirated. Afterwards, 100 μL of 0.2 N HCl in isopropanol was added to dissolve the formazan crystals formed, and the optical density was measured in a multiwell reader (2030 Multilabel Reader Victor TM X4, PerkinElmer, Waltham, MA, USA) at 570 nm. Viability of untreated cells was taken as 100% viability, and values obtained from cells undergoing the different treatments were referred to this value. Experiments were performed at least for 3 times using 3 replicates for each sample.

3.4.3. Prussian Blue Staining

Cells (approximately 20×10^3 4T1/well) were seeded on glass coverslips in 24-well plates, and after 24 h, 100-μg/mL BMNP suspensions were added. After the incubation at 37 °C for short (5 and 30 s) and longer periods of time (1, 2.5, and 5 min) in the absence and the presence of a GMF, coverslips were washed with fresh PBS pH 7.2 and fixed with paraformaldehyde (2 wt% in PBS). Then, Prussian blue solution (1:1 of 2% potassium ferrocyanide in H_2O and 2% HCl both in H_2O) was added to the coverslips. In that way, any ferric ion (+3) present in the samples combines with the ferrocyanide and results in the formation of bright blue pigments called Prussian blue or ferric ferrocyanide. After two other washes with fresh PBS, Nuclear Fast Red (Sigma-Aldrich) was added for staining cell nuclei. Finally, coverslips were washed with H_2O and mounted on slides by using one drop of Eukitt

quick-hardening mounting medium for each sample. The interaction of the stained BMNPs with cells was analyzed by optical microscopy at 100×. Experiments were performed at least 3 times.

3.4.4. Iron Quantification by Potassium Thiocyanate

Cells (approximately 22×10^4 4T1/well) were seeded in 6-well plates and, after 24 h incubation at 37 °C and 5% CO_2, 100-μg/mL BMNP suspensions in complete DMEM medium were added. After their incubation for 5, 30, 60, 150, and 300 s in the presence and absence of a GMF, the supernatant was removed, and cells were washed with fresh PBS, trypsinized, transferred to 0.5 mL tubes, and centrifuged at 1000 rpm for 5 min. Then, the cell pellets formed were dissolved in 37% HCl, mixed with 10% H_2O_2, and incubated for 20 min at room temperature. After the incubation time, the samples were reacted with 1 mL of 1% potassium thiocyanate in Milli-Q water, and their absorbance was measured at 490 nm. The concentration of ferric ions in the samples was calculated in reference to the absorbance obtained from a standard curve performed following the same protocol as that with the BMNPs alone. The endogenous iron of cells was subtracted from the treated samples normalized by the untreated control cells. Experiments were performed at least 3 times.

3.5. Internalization of BMNPs and DOXO in CELLs

3.5.1. Cellular Internalization by TEM

Cells (approximately 10×10^5 4T1/well) were incubated at 37 °C and 5% CO_2 for 24 h. Afterwards, 100 μg/mL of BMNPs were added and were incubated in the absence and presence a magnetic gradient field for 30 s and for 1 and 24 h. After these treatments, cells were washed three times with PBS prior to fixation with 2.5% glutaraldehyde and 2% paraformaldehyde in PBS for 1 h. Then, samples were washed again three times with sodium cacodylate buffer and embedded in Epon. Ultrathin sections (50–70 nm) were cut using a Reichert Ultracut S microtome (Leica Microsystems GmbH, Wetzlar, Germany), mounted on copper grids, and stained with lead citrate and uranyl acetate for transmission electron microscopy (TEM) analysis.

3.5.2. DOXO Internalization Analysis

Cells (approximately 20×10^3 4T1/well) were seeded on glass coverslips in 24-well plates and, after 24 h, 100 ug/mL of DOXO-BMNP suspensions or an amount of soluble DOXO (as a positive control) normalized for the one loaded on BMNPs was added. After incubation at 37 °C for different periods of time (30 s and 5 and 30 min) in the absence (−GMF) and the presence (+GMF) of a gradient magnetic field, coverslips were washed with fresh PBS pH 7.2 and fixed with paraformaldehyde (2 wt% in PBS). To minimize unspecific interactions and permeabilize cells, coverslips were washed with Tris-Buffered Saline (TBS) containing 5% Bovine Serum Albumin (BSA), 0.1% Triton X-100, and 5% goat serum and were then stained. In particular, cytoskeletal actin microfilaments were stained with FITC-phalloidin (Sigma-Aldrich, excitation at 488 nm; emission at 500–535 nm) and nuclei with TO-PRO-3 (1/70, Life Technologies; excitation at 633 nm; emission at 650–750 nm). DOXO was detected after excitation at 476 nm and emission at 575–630 nm. Fluorescence was detected using a Leica TCS SP2 AOBS Spectral Confocal Scanner microscope. Images were taken at 400× magnification. ImageJ software was used for analysis.

3.6. Western Blot Analysis

4T1 cells (approximately 22×10^4 4T1/well) were seeded in 6-well plates and, after 24 h incubation at 37 °C and 5% CO_2, were treated for 16 h with different concentrations of BMNPs, DOXO-BMNPs (0.1, 1, 10, and 100 μg/mL), and an amount of soluble DOXO normalized for the one adsorbed to BMNPs (0.025, 0.25, 2.5, and 25 μM) in the presence or absence of a gradient magnetic field. Cells were then washed twice in cold PBS and lysed in iced Radioimmunoprecipitation assay buffer (RIPA) buffer (20 mM Tris-HCl pH 7.5, 150 mM NaCl, 50 mM HEPES, 0.1% SDS, 1 mM Ethylene

glycol-bis(2-aminoethylether)-N,N,N′ (EGTA), 1% NP-40, 1% sodium deoxycholate, 2.5 mM sodium pyrophosphate, and 10% glycerol) supplemented with protease inhibitors cocktail (Sigma-Aldrich). Cell lysates were centrifuged at 13,000 rpm at 4 °C for 15 min. Clarified cell extracts (30 µg of protein) were denatured by heating for 5 min at 95 °C in reducing Laemmli buffer; proteins were separated in an appropriate concentration of sodium dodecyl sulfate-polyacrylamide gel electrophoresis (SDS-PAGE) and transferred onto polyvinylidene difluoride (PVDF) filters. Filters were blocked with 5% non-fat dry milk for 2 h, rinsed in water, and probed with different antibodies in Tris-buffered saline (TBS), pH 8.0, 5% BSA, overnight at 4 °C. The list of primary antibodies used is reported below (Table 1). After extensive washing, immunocomplexes were detected with appropriate horseradish peroxidase-conjugated secondary anti-IgG antibodies (diluted 1/5000), followed by enhanced chemiluminescence (ECL kit; Biorad), and were analyzed in a Versadoc instrument (Bio-Rad Laboratories S.r.l, Segrate, Milan, Italy). The Image Lab™ Software (Bio-Rad Laboratories Inc., Hercules, CA, USA) was used to perform densitometric analysis of the Western blots. Experiments were performed at least 4 times. The uncropped Western blot can be found at Figure S6.

Table 1. Antibody used for Western blot analysis.

Antigen	Species	Dilution	Expected Band (kDa)	Source	Cat. Number
LC3B	Rabbit Polyclonal	1/500	16–18	Sigma-Aldrich	L7543
Caspase 9	Mouse Monoclonal	1/1000	37–39–47	Cell Signaling Technology	9508
Caspase 3	Rabbit Polyclonal	1/1000	19–35	Cell Signaling Technology	9662
α-tubulin	Mouse Monoclonal	1/500	50	Millipore	05-829

3.7. Magnetic Hyperthermia Measurement in Vitro and Vivo

Both in vitro and in vivo experiments were carried out using a homemade AC current generator consisting of a resonant LC circuit set at 130 kHz and a magnetic field strength of 18 kA/m (HF~2.34×10^9 Am^{-1}s^{-1}). In any case, the product of field strength and frequency is within the safe limits of 4.85×10^8 Am^{-1}s^{-1} [79] or H-f $\leq 5 \times 10^9$ Am^{-1}s^{-1} proposed by Aktinson or later by Dutz and Hergt [80]. The magnetic field applicator consisted of a four-turn coil water-cooled copper pipe with 4-mm inside diameter. The temperature was monitored with a high-resolution infrared camera FLIR E60 with 320×240 pixel Infrared (IR) resolution and thermal sensitivity < 0.05 °C (FLIR Systems, Inc.) in real time. In all experiments, the temperature inside the coil was maintained at 37 °C. these values exceeded

3.8. In Vivo Test

3.8.1. Animals

All Balb/c female mice of about six weeks old used in this work were purchased from Charles River (Calco, Lecco, Italy) and housed under standard conditions in a pathogen-free environment. All procedures were approved (Ministero della Salute: #178/2019-PR) and carried out in accordance with the Animal Care and Use Committee of UPO, the European Community Directive for Care and Italian Laws on animal experimentation (Law by Decree 116/92).

3.8.2. In Vivo Magnetic Targeting and Antitumor Activity

Fifty-four female BALB/c mice were inoculated with 10^5 4T1 cells into the fat pad of mammary glands. When the tumors became palpable (10 days after cell inoculation), mice were divided into 6 different groups with comparable tumor volumes among the groups. The six groups of mice were intravenous injected and treated as follow: (i) PBS (negative control experiment), (ii–iii) BMNPs ± GMF, (iv–v) DOXO-BMNPs ± GMF, and (vi) soluble DOXO. Mice were injected 5 times with a dose of 2 mg/kg DOXO either soluble (positive control experiment) or as DOXO-BMNPs nano-assemblies (always maintaining the same DOXO concentration in any form) 3 days apart each time. In case of

BMNP-bearing treatments, after each injection, the neodymium magnet was immediately attached with 3MTM Vetbond^{TM} tissue adhesive on the tumor site and kept for 1 h. This neodymium magnet, with a magnetic anisotropy perpendicular to the plane and a saturation magnetization of 800 emu/cc, has an effect equivalent to the application of a local direct current GMF of the order of 100 Oe a few millimeters from the tumor surface.

Throughout the study, tumor volumes (measured with a caliper) were recorded every 3 days. Three days after the last injections (day 18), mice were euthanized, and then, tumors, hearts, livers, spleens, brains, lungs, and kidneys were collected for histologic analysis. Histologic sections of the tumors were prepared for hematoxylin-eosin and Prussian blue staining to analyze particle biodistribution. The % of blue Prussian staining and standard area from 5 randomly chosen areas from each of the 3 tumor sections (100 microns apart) for each of the 7 tumors ($n = 135$) were analyzed by using ImageJ software.

3.8.3. In Vivo Magnetic Hyperthermia and Antitumor Activity

Twenty-four female BALB/c mice were inoculated into the fat pads of two mammary glands with 10^5 4T1 cells each. Approximately 15 days after cell inoculation, when the tumor dimensions were approximately 100 mm^3, mice were divided into 6 different groups with comparable tumor volumes among the groups. The 6 groups were intratumor injected and treated as follow: (i) PBS (negative control experiment), (ii–iii) BMNPs ± AMF, (iv–v) DOXO-BMNPs ± AMF, and (vi) soluble DOXO (positive control experiment). Mice were injected only once at the beginning of treatment (day 0) with a dose of 3 mg BMNPs/mouse, equivalent to 80 μg DOXO for the soluble DOXO and DOXO-BMNP groups. Immediately after injection of the nanoparticles, some groups were exposed to an AMF (130 kHz and 18 kA m^{-1}) for 20 min. Throughout the study, tumor volumes were measured with a caliper every two days. Finally, five days posttreatment, mice were euthanized and their tumor weights recorded. Tumors were collected, fixed, embedded in paraffin, and processed for histologic analysis. Serial sections were stained with hematoxylin-eosin (Sigma Aldrich), and the percentage of necrosis was evaluated by a pathologist not informed of the sample identity.

3.9. Statistical Analysis

Data are expressed as mean ± standard error of at least 3 triplicates. Both for in vitro and in vivo test, statistical analyses were performed using a two-way ANOVA, with a Dunnet's multiple comparisons test for grouped analyses using GraphPad Prism version 8.4.2 for Windows, GraphPad Software (GraphPad Prism, San Diego, CA, USA). Statistical differences between the treatments were considered significant when p values were $p < 0.05$ (*), $p < 0.01$ (**), $p < 0.001$ (***), and $p < 0.0001$ (****). Only for the in vivo experiments related to the weight of the tumor and for the percentage of necrosis, statistical analyses were performed using a one-way ANOVA, with a Dunnet's multiple comparisons test for grouped analyses.

4. Conclusions

We performed preclinical studies aimed at validating biomimetic magnetic nanoparticles (BMNPs) as a drug (DOXO) delivery system, which can be manipulated externally by a gradient magnetic field (GMF) mediating tumor targeting or by an alternating magnetic field (AMF) developing hyperthermia in a mammary carcinoma model.

Results from the present study demonstrate that BMNPs are highly compatible both in vitro and in vivo. The apposition of a magnet (GMF) improves drug delivery and allows guidance of the nano-assembly to the tumor. In fact, our results show that GMF enhances the interaction of BMNPs with tumor cells and their toxicity if loaded with DOXO, both in vitro and in vivo. They also show that intravenously injected DOXO-BMNPs can be guided to the tumor mass by apposition of a magnet with a better therapeutic result than that produced by soluble DOXO.

Finally, our study shows that the combinatory chemothermal therapy mediated by BMNPs have a stronger therapeutic benefit compared to that carried out by soluble DOXO, possibly because BMNPs retain DOXO at the tumor site for longer periods and because the susceptibility of tumor cells to heat generated by hyperthermia can be simultaneously exploited by using the same BMNPs as a hyperthermia agent. These BMNPs are thus novel and promising nanocarriers for translational applications in cancer therapy.

Supplementary Materials: The following are available online at http://www.mdpi.com/2072-6694/12/9/2564/s1. Figure S1: Expression and state of phosphorylation of MAPK1/2, Akt, and mTOR, Figure S2: Microanalysis by energy dispersive X-ray (EDX) spectroscopy of 4T1 cells incubated with BMNPs, Figure S3: Densitometric analysis of the bands of activated LC3B-I, caspase 9, and caspase 3, Figure S4: Biodistribution profile of BMNPs after tail-vein injection in BALB/c mice, Figure S5: Cytocompatibility/cytotoxicity of different concentrations of BMNPs on 4T1 cells in the absence/presence of an alternating magnetic field (AMF) assessed as cell viability in an MTT assay. Figure S6: Uncropped Western blot.

Author Contributions: Conceptualization, M.P., C.J.-L., and G.R.I.; data curation, F.O. and A.P.; formal analysis, F.O. and D.C.; funding acquisition, M.P., C.J.-L., and G.R.I.; investigation, F.O., A.P., A.D., N.C., G.V., and G.R.I.; methodology, F.O., A.P., and G.R.I.; resources, M.P., D.C., G.R.I., and C.J.-L.; supervision, M.P. and C.J.-L.; validation, F.O., A.P., A.D., D.C., N.C., and G.V.; visualization, F.O. and A.P.; writing—original draft, F.O., A.P., and M.P.; writing—review and editing, F.O., A.P., M.P., G.R.I., D.C., and C.J.-L. All authors have read and agreed to the published version of the manuscript.

Conflicts of Interest: The authors declare no conflict of interest.

References

1. Fitzmaurice, C.; Akinyemiju, T.F.; Al Lami, F.H.; Alam, T.; Alizadeh-Navaei, R.; Allen, C.; Alsharif, U.; Alvis-Guzman, N.; Amini, E.; Anderson, B.O.; et al. Global, Regional, and National Cancer Incidence, Mortality, Years of Life Lost, Years Lived With Disability, and Disability-Adjusted Life-Years for 29 Cancer Groups, 1990 to 2016. *JAMA Oncol.* **2018**, *4*, 1553–1568. [CrossRef] [PubMed]

2. Siegel, R.L.; Miller, K.D.; Jemal, A. Cancer statistics, 2020. CA. *Cancer J. Clin.* **2020**, *70*, 7–30. [CrossRef] [PubMed]

3. Garanina, A.S.; Naumenko, V.A.; Nikitin, A.A.; Myrovali, E.; Petukhova, A.Y.; Klimyuk, S.V.; Nalench, Y.A.; Ilyasov, A.R.; Vodopyanov, S.S.; Erofeev, A.S.; et al. Temperature-controlled magnetic nanoparticles hyperthermia inhibits primary tumor growth and metastases dissemination. *Nanomed. Nanotechnol. Biol. Med.* **2020**, *25*. [CrossRef] [PubMed]

4. Dobson, J. Magnetic micro- and nano-particle-based targeting for drug and gene delivery. *Nanomedicine* **2006**, *1*, 31–37. [CrossRef]

5. Sun, C.; Lee, J.S.H.; Zhang, M. Magnetic nanoparticles in MR imaging and drug delivery. *Adv. Drug Deliv. Rev.* **2008**, *60*, 1252–1265. [CrossRef]

6. Tacar, O.; Sriamornsak, P.; Dass, C.R. Doxorubicin: An update on anticancer molecular action, toxicity and novel drug delivery systems. *J. Pharm. Pharmacol.* **2013**, *65*, 157–170. [CrossRef]

7. Moiseeva, A.A.; Artyushin, O.I.; Anikina, L.V.; Brel, V.K. Synthesis and antitumor activity of daunorubicin conjugates with of 3,4-methylendioxybenzaldehyde. *Bioorganic Med. Chem. Lett.* **2019**, *29*. [CrossRef]

8. Thorn, C.F.; Oshiro, C.; Marsh, S.; Hernandez-Boussard, T.; McLeod, H.; Klein, T.E.; Altman, R.B. Doxorubicin pathways:pharmacodynamics and adverse effects. *Pharm. Genom.* **2012**, *21*, 440–446. [CrossRef]

9. Taymaz-Nikerel, H.; Karabekmez, M.E.; Eraslan, S.; Kırdar, B. Doxorubicin induces an extensive transcriptional and metabolic rewiring in yeast cells. *Sci. Rep.* **2018**, *8*. [CrossRef]

10. Octavia, Y.; Tocchetti, C.G.; Gabrielson, K.L.; Janssens, S.; Crijns, H.J.; Moens, A.L. Doxorubicin-induced cardiomyopathy: From molecular mechanisms to therapeutic strategies. *J. Mol. Cell. Cardiol.* **2012**, *52*, 1213–1225. [CrossRef]

11. Humber, C.E.; Tierney, J.F.; Symonds, R.P.; Collingwood, M.; Kirwan, J.; Williams, C.; Green, J.A. Chemotherapy for advanced, recurrent or metastatic endometrial cancer: A systematic review of Cochrane collaboration. *Ann. Oncol.* **2007**, *18*, 409–420. [CrossRef] [PubMed]

12. Trédan, O.; Galmarini, C.M.; Patel, K.; Tannock, I.F. Drug resistance and the solid tumor microenvironment. *J. Natl. Cancer Inst.* **2007**, *99*, 1441–1454. [CrossRef] [PubMed]

13. Au, J.S.; Jang, S.H.; Zheng, J.; Chen, C.T.; Song, S.; Hu, L.; Wientjes, M.G. Determinants of drug delivery and transport to solid tumors. *J. Control. Release* **2001**, *74*, 31–46. [CrossRef]

14. García Rubia, G.; Peigneux, A.; Jabalera, Y.; Puerma, J.; Oltolina, F.; Elert, K.; Colangelo, D.; Gómez Morales, J.; Prat, M.; Jimenez-Lopez, C. PH-Dependent Adsorption Release of Doxorubicin on MamC-Biomimetic Magnetite Nanoparticles. *Langmuir* **2018**, *34*. [CrossRef]

15. Peigneux, A.; Oltolina, F.; Colangelo, D.; Iglesias, G.R.; Delgado, A.V.; Prat, M.; Jimenez-Lopez, C. Functionalized Biomimetic Magnetic Nanoparticles as Effective Nanocarriers for Targeted Chemotherapy. *Part. Part. Syst. Charact.* **2019**, *36*, 1–11. [CrossRef]

16. Duncan, R. The dawning era of polymer therapeutics. *Nat. Rev. Drug Discov.* **2003**, *2*, 347–360. [CrossRef]

17. Maeda, H. The enhanced permeability and retention (EPR) effect in tumor vasculature: The key role of tumor-selective macromolecular drug targeting. *Adv. Enzyme Regul.* **2001**, *41*, 189–207. [CrossRef]

18. Matsumura, Y.; Maeda, H. A New Concept for Macromolecular Therapeutics in Cancer Chemotherapy: Mechanism of Tumoritropic Accumulation of Proteins and the Antitumor Agent Smancs. *Cancer Res.* **1986**, *46*, 6387–6392.

19. Zhi, D.; Yang, T.; Yang, J.; Fu, S.; Zhang, S. Targeting strategies for superparamagnetic iron oxide nanoparticles in cancer therapy. *Acta Biomater.* **2020**, *102*, 13–34. [CrossRef]

20. Oltolina, F.; Colangelo, D.; Miletto, I.; Clemente, N.; Miola, M.; Verné, E.; Prat, M.; Follenzi, A. Tumor targeting by monoclonal antibody functionalized magnetic nanoparticles. *Nanomaterials* **2019**, *9*, 1575. [CrossRef]

21. Shubayev, V.I.; Pisanic, T.R.; Jin, S. Magnetic nanoparticles for theragnostics. *Adv. Drug Deliv. Rev.* **2009**, *61*, 467–477. [CrossRef] [PubMed]

22. Prozorov, T.; Bazylinski, D.A.; Mallapragada, S.K.; Prozorov, R. Novel magnetic nanomaterials inspired by magnetotactic bacteria: Topical review. *Mater. Sci. Eng. R Rep.* **2013**, *74*, 133–172. [CrossRef]

23. Jabalera, Y.; Sola-Leyva, A.; Peigneux, A.; Vurro, F.; Iglesias, G.R.; Vilchez-Garcia, J.; Pérez-Prieto, I.; Aguilar-Troyano, F.J.; López-Cara, L.C.; Carrasco-Jiménez, M.P.; et al. Biomimetic magnetic nanocarriers drive choline kinase alpha inhibitor inside cancer cells for combined chemo-hyperthermia therapy. *Pharmaceutics* **2019**, *11*, 408. [CrossRef] [PubMed]

24. Liu, D.; Yang, F.; Xiong, F.; Gu, N. The smart drug delivery system and its clinical potential. *Theranostics* **2016**, *6*, 1306–1323. [CrossRef]

25. Issels, R.D. Hyperthermia adds to chemotherapy. *Eur. J. Cancer* **2008**, *44*, 2546–2554. [CrossRef]

26. Mai, B.T.; Balakrishnan, P.B.; Barthel, M.J.; Piccardi, F.; Niculaes, D.; Marinaro, F.; Fernandes, S.; Curcio, A.; Kakwere, H.; Autret, G.; et al. Thermoresponsive Iron Oxide Nanocubes for an Effective Clinical Translation of Magnetic Hyperthermia and Heat-Mediated Chemotherapy. *ACS Appl. Mater. Interfaces* **2019**, *11*, 5727–5739. [CrossRef]

27. Iglesias, G.R.; Reyes-Ortega, F.; Fernandez, B.L.C.; Delgado, Á.V. Hyperthermia-Triggered Gemcitabine Release from Polymer-Coated Magnetite Nanoparticles. *Polymers* **2018**, *10*, 269. [CrossRef]

28. Williams, P.S.; Carpino, F.; Zborowski, M. Magnetic Nanoparticle Drug Carriers and Their Study by Quadrupole Magnetic Field-Flow Fractionation. *Mol Pharm.* **2009**, *6*, 1290–1306. [CrossRef]

29. Mody, V.V.; Cox, A.; Shah, S.; Singh, A.; Bevins, W.; Parihar, H. Magnetic nanoparticle drug delivery systems for targeting tumor. *Appl. Nanosci.* **2014**, *4*, 385–392. [CrossRef]

30. Torres, T.E.; Lima, E.; Calatayud, M.P.; Sanz, B.; Ibarra, A.; Fernández-Pacheco, R.; Mayoral, A.; Marquina, C.; Ibarra, M.R.; Goya, G.F. The relevance of Brownian relaxation as power absorption mechanism in Magnetic Hyperthermia. *Sci. Rep.* **2019**, *9*, 1–11. [CrossRef]

31. Hedayatnasab, Z.; Abnisa, F.; Daud, W.M.A.W. Review on magnetic nanoparticles for magnetic nanofluid hyperthermia application. *Mater. Des.* **2017**, *123*, 174–196. [CrossRef]

32. Valverde-Tercedor, C.; Montalbán-López, M.; Perez-Gonzalez, T.; Sanchez-Quesada, M.S.; Prozorov, T.; Pineda-Molina, E.; Fernandez-Vivas, M.A.; Rodriguez-Navarro, A.B.; Trubitsyn, D.; Bazylinski, D.A.; et al. Size control of in vitro synthesized magnetite crystals by the MamC protein of Magnetococcus marinus strain MC-1. *Appl. Microbiol. Biotechnol.* **2015**, *99*, 5109–5121. [CrossRef] [PubMed]

33. Maheshwari, R.; Raval, N.; Tekade, R.K. Surface Modification of Biomedically Essential Nanoparticles Employing Polymer Coating. *Methods Mol. Biol.* **2019**, *2000*, 191–201. [CrossRef] [PubMed]

34. Garcia-Pinel, B.; Jabalera, Y.; Ortiz, R.; Cabeza, L.; Jimenez-Lopez, C.; Melguizo, C.; Prados, J. Biomimetic magnetoliposomes as oxaliplatin nanocarriers: In vitro study for potential application in colon cancer. *Pharmaceutics* **2020**, *12*, 589. [CrossRef]

35. Reyes-Ortega, F.; Delgado, Á.V.; Schneider, E.K.; Fernández, B.L.C.; Iglesias, G.R. Magnetic nanoparticles coated with a thermosensitive polymer with hyperthermia properties. *Polymers* **2017**, *10*, 10. [CrossRef]

36. Ubago-Rodríguez, A.; Casares Atienza, S.; Fernández-Vivas, A.; Peigneux, A.; Jabalera, Y.; De La Cuesta-Rivero, M.; Jimenez-Lopez, C.; Azuaga Fortes, A.I. Structure-Function of MamC Loop and Its Effect on the in Vitro Precipitation of Biomimetic Magnetite Nanoparticles. *Cryst. Growth Des.* **2019**, *19*. [CrossRef]

37. Xia, T.; Kovochich, M.; Brant, J.; Hotze, M.; Sempf, J.; Oberley, T.; Sioutas, C.; Yeh, J.I.; Wiesner, M.R.; Nel, A.E. Comparison of the abilities of ambient and manufactured nanoparticles to induce cellular toxicity according to an oxidative stress paradigm. *Nano Lett.* **2006**, *6*, 1794–1807. [CrossRef]

38. Peigneux, A.; Glitscher, E.A.; Charbaji, R.; Weise, C.; Wedepohl, S.; Calderón, M.; Jimenez-Lopez, C.; Hedtrich, S. Protein corona formation and its influence on biomimetic magnetite nanoparticles. *J. Mater. Chem. B* **2020**, *8*, 4870–4882. [CrossRef]

39. Jabalera, Y.; Oltolina, F.; Peigneux, A.; Sola-Leyva, A.; Carrasco-Jiménez, M.P.; Prat, M.; Jimenez-Lopez, C.; Iglesias, G.R. Nanoformulation Design Including MamC-Mediated Biomimetic Nanoparticles Allows the Simultaneous Application of Targeted Drug Delivery and Magnetic Hyperthermia. *Polymers* **2020**, *12*, 1832. [CrossRef]

40. Loor, G.; Kondapalli, J.; Schriewer, J.M.; Chandel, N.S.; Vanden Hoek, T.L.; Schumacker, P.T. Menadione triggers cell death through ROS-dependent mechanisms involving PARP activation without requiring apoptosis. *Free Radic. Biol. Med.* **2010**, *49*, 1925–1936. [CrossRef]

41. Guo, C.; Yang, M.; Jing, L.; Wang, J.; Yu, Y.; Li, Y.; Duan, J.; Zhou, X.; Li, Y.; Sun, Z. Amorphous silica nanoparticles trigger vascular endothelial cell injury through apoptosis and autophagy via reactive oxygen species-mediated MAPK/Bcl-2 and PI3K/Akt/mTORsignaling. *Int. J. Nanomed.* **2016**, *11*, 5257–5276. [CrossRef] [PubMed]

42. Basu, S.; Harfouche, R.; Soni, S.; Chimote, G.; Mashelkar, R.A.; Sengupta, S. Nanoparticle-mediated targeting of MAPK signaling predisposes tumor to chemotherapy. *Proc. Natl. Acad. Sci. USA* **2009**, *106*, 7957–7961. [CrossRef] [PubMed]

43. Porta, C.; Paglino, C.; Mosca, A. Targeting PI3K/Akt/mTOR signaling in cancer. *Front. Oncol.* **2014**, *4*, 64. [CrossRef] [PubMed]

44. Alieva, I.B.; Kireev, I.; Garanina, A.S.; Alyabyeva, N.; Ruyter, A.; Strelkova, O.S.; Zhironkina, O.A.; Cherepaninets, V.D.; Majouga, A.G.; Davydov, V.A.; et al. Magnetocontrollability of Fe7C3@C superparamagnetic nanoparticles in living cells. *J. Nanobiotechnol.* **2016**, *14*. [CrossRef] [PubMed]

45. Prijic, S.; Scancar, J.; Romih, R.; Cemazar, M.; Bregar, V.B.; Znidarsic, A.; Sersa, G. Increased cellular uptake of biocompatible superparamagnetic iron oxide nanoparticles into malignant cells by an external magnetic field. *J. Membr. Biol.* **2010**, *236*, 167–179. [CrossRef] [PubMed]

46. Oltolina, F.; Gregoletto, L.; Colangelo, D.; Gómez-Morales, J.; Delgado-López, J.M.; Prat, M. Monoclonal Antibody-Targeted Fluorescein-5-isothiocyanate-Labeled Biomimetic Nanoapatites: A Promising Fluorescent Probe for Imaging Applications. *Langmuir* **2015**, *31*, 1766–1775. [CrossRef]

47. Remya, N.S.S.; Syama, S.; Gayathri, V.; Varma, H.K.K.; Mohanan, P.V. An in vitro study on the interaction of hydroxyapatite nanoparticles and bone marrow mesenchymal stem cells for assessing the toxicological behaviour. *Colloids Surf. B Biointerfaces* **2014**, *117*, 389–397. [CrossRef]

48. Shi, M.; Ho, K.; Keating, A.; Shoichet, M.S. Doxorubicin-Conjugated Immuno-Nanoparticles for Intracellular Anticancer Drug Delivery. *Adv. Funct. Mater.* **2009**, *19*, 1689–1696. [CrossRef]

49. Lu, Y.C.; Chang, F.Y.; Tu, S.J.; Chen, J.P.; Ma, Y.H. Cellular uptake of magnetite nanoparticles enhanced by NdFeB magnets in staggered arrangement. *J. Magn. Magn. Mater.* **2017**, *427*, 71–80. [CrossRef]

50. Garanina, A.; Kireev, I.; Zhironkina, O.; Strelkova, O.; Shakhov, A.; Alieva, I.; Davydov, V.; Murugesan, S.; Khabashesku, V.; Majouga, A.; et al. Long-term live cells observation of internalized fluorescent Fe@C nanoparticles in constant magnetic field. *J. Nanobiotechnol.* **2019**, *17*, 27. [CrossRef]

51. Mimnaugh, E.G.; Dusre, L.; Atwell, J.; Myers, C.E. Differential oxygen radical susceptibility of adriamycin-sensitive and -resistant MCF-7 human breast tumor cells. *Cancer Res.* **1989**, *49*, 8–15. [PubMed]

52. Ye, H.; Shen, Z.; Yu, L.; Wei, M.; Li, Y. Manipulating Nanoparticle Transport Within Blood Flow Through External Forces: An Exemplar of Mechanics in Nanomedicine. *Proc. Math. Phys. Eng. Sci.* **2018**, *474*, 20170845. [CrossRef] [PubMed]

53. Kong, S.D.; Zhang, W.; Lee, J.H.; Brammer, K.; Lal, R.; Karin, M.; Jin, S. Magnetically vectored nanocapsules for tumor penetration and remotely switchable on-demand drug release. *Nano Lett.* **2010**, *10*, 5088–5092. [CrossRef] [PubMed]

54. Cordani, M.; Somoza, Á. Targeting autophagy using metallic nanoparticles: A promising strategy for cancer treatment. *Cell. Mol. Life Sci.* **2019**, *76*, 1215–1242. [CrossRef] [PubMed]

55. Mathew, R.; Karantza-Wadsworth, V.; White, E. Role of autophagy in cancer. *Nat. Rev. Cancer* **2007**, *7*, 961–967. [CrossRef]

56. Yang, Z.J.; Chee, C.E.; Huang, S.; Sinicrope, F.A. Autophagy modulation for cancer therapy. *Cancer Biol. Ther.* **2011**, *11*, 169–176. [CrossRef]

57. Wei, L.; Surma, M.; Gough, G.; Shi, S.; Lambert-Cheatham, N.; Chang, J.; Shi, J. Dissecting the mechanisms of doxorubicin and oxidative stress-induced cytotoxity: The involvement of actin cytoskeleton and ROCK1. *PLoS ONE* **2015**, *10*, e0131763. [CrossRef]

58. Yoshii, S.R.; Mizushima, N. Monitoring and Measuring Autophagy. *Int. J. Mol. Sci.* **2017**, *18*, 1865. [CrossRef]

59. Johnstone, R.W.; Ruefli, A.A.; Lowe, S.W. Apoptosis: A link between cancer genetics and chemotherapy. *Cell* **2002**, *108*, 153–164. [CrossRef]

60. Hengartner, M.O. The biochemistry of apoptosis. *Nature* **2000**, *407*, 770–776. [CrossRef]

61. Parrish, A.B.; Freel, C.D.; Kornbluth, S. Cellular mechanisms controlling caspase activation and function. *Cold Spring Harb. Perspect. Biol.* **2013**, *5*. [CrossRef] [PubMed]

62. Taylor, R.C.; Cullen, S.P.; Martin, S.J. Apoptosis: Controlled demolition at the cellular level. *Nat. Rev. Mol. Cell Biol.* **2008**, *9*, 231–241. [CrossRef] [PubMed]

63. Jain, T.K.; Reddy, M.K.; Morales, M.A.; Leslie-Pelecky, D.L.; Labhasetwar, V. Biodistribution, Clearance, and Biocompatibility of Iron Oxide Magnetic Nanoparticles in Rats Tapan. *Mol. Pharm.* **2008**, *5*, 316–327. [CrossRef] [PubMed]

64. Borroni, E.; Miola, M.; Ferraris, S.; Ricci, G.; Žužek Rožman, K.; Kostevšek, N.; Catizone, A.; Rimondini, L.; Prat, M.; Verné, E.; et al. Tumor targeting by lentiviral vectors combined with magnetic nanoparticles in mice. *Acta Biomater.* **2017**. [CrossRef]

65. Tate, J.A.; Petryk, A.A.; Giustini, A.J.; Hoopes, P.J. In Vivo Biodistribution of Iron Oxide Nanoparticles: An Overview. In *Energy-based Treatment of Tissue and Assessment VI*; SPIE: Washington, DC, USA, 2011; Volume 7901, p. 790117.

66. Chaves, S.B.; Silva, L.P.; Lacava, Z.G.M.; Morais, P.C.; Azevedo, R.B. Interleukin-1 and interleukin-6 production in mice's lungs induced by 2, 3 meso-dimercaptosuccinic-coated magnetic nanoparticles. *J. Appl. Phys.* **2005**, *97*, 10Q915. [CrossRef]

67. Owens, D.E.; Peppas, N.A. Opsonization, biodistribution, and pharmacokinetics of polymeric nanoparticles. *Int. J. Pharm.* **2006**, *307*, 93–102. [CrossRef]

68. Lartigue, L.; Alloyeau, D.; Kolosnjaj-Tabi, J.; Javed, Y.; Guardia, P.; Riedinger, A.; Péchoux, C.; Pellegrino, T.; Wilhelm, C.; Gazeau, F. Biodegradation of iron oxide nanocubes: High-resolution in situ monitoring. *ACS Nano* **2013**, *7*, 3939–3952. [CrossRef]

69. Mejías, R.; Pérez-Yagüe, S.; Gutiérrez, L.; Cabrera, L.I.; Spada, R.; Acedo, P.; Serna, C.J.; Lázaro, F.J.; Villanueva, Á.; del Morales, M.P.; et al. Dimercaptosuccinic acid-coated magnetite nanoparticles for magnetically guided in vivo delivery of interferon gamma for cancer immunotherapy. *Biomaterials* **2011**, *32*, 2938–2952. [CrossRef]

70. Kim, J.S.; Yoon, T.J.; Yu, K.N.; Kim, B.G.; Park, S.J.; Kim, H.W.; Lee, K.H.; Park, S.B.; Lee, J.K.; Cho, M.H. Toxicity and tissue distribution of magnetic nanoparticles in mice. *Toxicol. Sci.* **2006**, *89*, 338–347. [CrossRef]

71. Aslakson, C.J.; Miller, F.R. Selective events in the metastatic process defined by analysis of the sequential dissemination of subpopulations of a mouse mammary tumor. *Cancer Res.* **1992**, *52*, 1399–1405.

72. Espinosa, A.; Reguera, J.; Curcio, A.; Muñoz-Noval, Á.; Kuttner, C.; Van de Walle, A.; Liz-Marzán, L.M.; Wilhelm, C. Janus Magnetic-Plasmonic Nanoparticles for Magnetically Guided and Thermally Activated Cancer Therapy. *Small* **2020**, *16*, 1904960. [CrossRef] [PubMed]

73. Kim, H.J.; Lee, S.-M.; Park, K.-H.; Mun, C.H.; Park, Y.-B.; Yoo, K.-H. Drug-loaded gold/iron/gold plasmonic nanoparticles for magnetic targeted chemo-photothermal treatment of rheumatoid arthritis. *Biomaterials* **2015**, *61*, 95–102. [CrossRef] [PubMed]

74. Alexiou, C.; Arnold, W.; Klein, R.J.; Parak, F.G.; Hulin, P.; Bergemann, C.; Erhardt, W.; Wagenpfeil, S.; Lubbe, A.S. Locoregional cancer treatment with magnetic drug targeting. *Cancer Res.* **2000**, *60*, 6641–6648. [PubMed]

75. Dürr, S.; Janko, C.; Lyer, S.; Tripal, P.; Schwarz, M.; Zaloga, J.; Tietze, R.; Alexiou, C. Magnetic nanoparticles for cancer therapy. *Nanotechnol. Rev.* **2013**, *2*, 395–409. [CrossRef]

76. Wu, M.; Huang, S. Magnetic nanoparticles in cancer diagnosis, drug delivery and treatment (Review). *Mol. Clin. Oncol.* **2017**, *7*, 738–746. [CrossRef] [PubMed]

77. Liu, X.; Zhang, Y.; Wang, Y.; Zhu, W.; Li, G.; Ma, X.; Zhang, Y.; Chen, S.; Tiwari, S.; Shi, K.; et al. Comprehensive understanding of magnetic hyperthermia for improving antitumor therapeutic efficacy. *Theranostics* **2020**, *10*, 3793–3815. [CrossRef]

78. Calatayud, M.P.; Soler, E.; Torres, T.E.; Campos-Gonzalez, E.; Junquera, C.; Ibarra, M.R.; Goya, G.F. Cell damage produced by magnetic fluid hyperthermia on microglial BV2 cells. *Sci. Rep.* **2017**, *7*, 1–16. [CrossRef]

79. Atkinson, W.J.; Brezovich, I.A.; Chakraborty, D.P. Usable Frequencies in Hyperthermia with Thermal Seeds. *IEEE Trans. Biomed. Eng.* **1984**, *BME-31*, 70–75. [CrossRef]

80. Dutz, S.; Hergt, R. Magnetic nanoparticle heating and heat transfer on a microscale: Basic principles, realities and physical limitations of hyperthermia for tumour therapy. *Int. J. Hyperth.* **2013**, *29*, 790–800. [CrossRef]

Article

Crystallization, Luminescence and Cytocompatibility of Hexagonal Calcium Doped Terbium Phosphate Hydrate Nanoparticles

Jaime Gómez-Morales [1,*], Raquel Fernández-Penas [1], Ismael Romero-Castillo [1], Cristóbal Verdugo-Escamilla [1], Duane Choquesillo-Lazarte [1], Annarita D'Urso [2], Maria Prat [2,3,4,5,*] and Jorge Fernando Fernández-Sánchez [6]

1 Laboratorio de Estudios Cristalográficos, IACT, CSIC-UGR, Avda. Las Palmeras, nº 4, 18100 Granada, Spain; raquel@lec.csic.es (R.F.-P.); ismaelrc92@gmail.com (I.R.-C.); cristobal.verdugo@csic.es (C.V.-E.); duane.choquesillo@csic.es (D.C.-L.)

2 Dipartimento di Scienze della Salute, Università del Piemonte Orientale, Via Solaroli, 17, 28100 Novara, Italy; annarita.durso@uniupo.it

3 Centro di Biotecnologie per la Ricerca Medica Applicata (BRMA), Via Solaroli 17, 28100 Novara, Italy

4 Consorzio Interuniversitario per Biotecnologie (CIB), Località Padriciano 99, 34149 Area di Ricerca, Italy

5 Consorzio Interuniversitario Nazionale per la Scienza e Tecnologia dei Materiali (INSTM), 28100 Novara, Italy

6 Department of Analytical Chemistry, Faculty of Sciences, University of Granada, Avda. Fuentenueva s/n, 18071 Granada, Spain; jffernan@ugr.es

* Correspondence: jaime@lec.csic.es (J.G.-M.); maria.prat@med.uniupo.it (M.P.); Tel.: +34-958-230000 (J.G.-M.); +39-0321-660662(M.P.)

Abstract: Luminescent lanthanide-containing biocompatible nanosystems represent promising candidates as nanoplatforms for bioimaging applications. Herein, citrate-functionalized calcium-doped terbium phosphate hydrate nanophosphors of the rhabdophane type were prepared at different synthesis times and different Ca^{2+}/Tb^{3+} ratios by a bioinspired crystallization method consisting of thermal decomplexing of Ca^{2+}/Tb^{3+}/citrate/phosphate/carbonate solutions. Nanoparticles were characterized by XRD, TEM, SEM, HR-TEM, FTIR, Raman, Thermogravimetry, inductively coupled plasma spectroscopy, thermoanalysis, dynamic light scattering, electrophoretic mobility, and fluorescence spectroscopy. They displayed ill-defined isometric morphologies with sizes ≤50 nm, hydration number n ~ 0.9, tailored Ca^{2+} content (0.42–8.11 wt%), and long luminescent lifetimes (800–2600 μs). Their relative luminescence intensities in solid state are neither affected by Ca^{2+}, citrate content, nor by maturation time for Ca^{2+} doping concentration in solution below 0.07 M Ca^{2+}. Only at this doping concentration does the maturation time strongly affect this property, decreasing it. In aqueous suspensions, neither pH nor ionic strength nor temperature affect their luminescence properties. All the nanoparticles displayed high cytocompatibility on two human carcinoma cell lines and cell viability correlated positively with the amount of doping Ca^{2+}. Thus, these nanocrystals represent promising new luminescent nanoprobes for potential biomedical applications and, if coupled with targeting and therapeutic moieties, they could be effective tools for theranostics.

Keywords: terbium phosphates; calcium doped; citrate; nanoparticles; luminescence; cytocompatibility

1. Introduction

Luminescent nanoparticles are excellent optical probes for uses in biological imaging since they provide the essential fluorescent contrast to analyze and study cells and tissues [1]. Different luminescent labeling agents, mainly organic dyes, and nanomaterials including semiconductor quantum dots, nanodiamonds, gold nanoparticles [2–4], several nanostructures labeled with organic dyes [5], and more recently calcium phosphate apatite nanoparticles (nAp) both labeled with organic dyes [6] or doped with luminescent lanthanides (Ln^{3+}) ions [7,8], have been proposed for these applications. The main limitation of organic dyes is photobleaching [5], while the use of quantum dots is controversial due

to their cytotoxicity [9]. In the last years lanthanide orthophosphates ($LnPO_4$, Ln^{3+} = Eu^{3+}, Tb^{3+}, Ce^{3+}, Y^{3+} ...) started to attract much attention because they combine the very low solubility and high thermal conductivity of the metal phosphates as host matrices with the favorable features of the luminescent lanthanide ions, such as sharp emission bands, Stokes shift of hundreds of nanometers, and luminescence lifetimes of the order of milliseconds. For all the above reasons they find applications as phosphors, catalysts, sensors and heat-resistant materials [10]. In addition, they exhibit low cytotoxicity, high photostability, and resistance to photobleaching, thus being good optical nanoprobes for bioimaging [11–13]. $LnPO_4 \cdot nH_2O$ (n = 0–2) presents five polymorphic modifications, among which the low temperature hydrated phase with hexagonal structure is known as raphdophane [14,15]. In respect to Ln^{3+}-doped nAp, the $LnPO_4 \cdot nH_2O$ system presents the main advantage that at low temperatures (<100 °C) raphdophane is usually the only precipitated phase from aqueous solutions [15]. In calcium phosphate solutions, in contrast, several poly-morphs can eventually appear including amorphous calcium phosphate (ACP), dicalcium phosphate dihydrate (DCPD, brushite), octacalcium phosphate (OCP), and Ap [16–18]. The synthetic methods to prepare $LnPO_4$ nanocrystals include hydrothermal crystalliza-tion [19–21], microwave heating [22], ultrasounds [23], oil bath [24], sol-gel combined with electrospinning [25], slow crystallization using surfactants [26], or the layer-by layer adsorption followed by the reaction and crystallization at room temperature [27].

Among lanthanides, Eu^{3+} and Tb^{3+} started to be used in various host structures using different excitation wavelength in the UV region, with main emission bands in the Visible spectral region. Concerning $LnPO_4$, the $TbPO_4 \cdot nH_2O$ raphdophane nanorods were excited in the UV region at either 270, 312, 350 or 370 nm, and in the visible region at 482 nm, result-ing in similar emission spectra, and yielding a characteristic green emission, due to $^5D_4$–$^7F_5$ transition at 546 nm emission of Tb^{3+} [28]. Doping with Eu^{3+} allows the preparation of Eu^{3+}: $TbPO_4$ of hexagonal form with improved energy transfer efficiency between Tb^{3+} and Eu^{3+} and non-cytotoxicity on HeLa cells [13]. Recently, our group used citrate (cit) to pre-pare new luminescent cit-coated Ca^{2+}:$EuPO_4 \cdot nH_2O$ (with n~1) by the method of thermal decomplexing of $M^{(2+/3+)}$/Ca^{2+}/cit/phosphate/carbonate solutions ($M^{(2+/3+)}$, metallic ions) [29]. The method was initially developed to precipitate monodisperse biomimetic apatites [30] and carbonated apatite nanocrystals, both undoped and doped with transition metals [31,32], and Eu^{3+} [8]. In this method citrate ions played an active role in the nucle-ation and growth steps, and remained adsorbed on the nanoparticles surface [33], a feature presented in bone apatite nanocrystals [34]. The new luminescent cit-Ca^{2+}:$EuPO_4 \cdot H_2O$ nanomaterials proved to be fully cytocompatible against GTL-16 human carcinoma cells and showed an improved cytocompatibility as the Ca^{2+} content increased when contacted with the more sensitive m17.ASC murine mesenchymal stem cells, thus proving to be suitable for bioimaging and cell labeling.

The aim of the present work is to employ the same bioinspired route to prepare cit-Ca^{2+}:$TbPO_4 \cdot nH_2O$ nanocrystals with tuned luminescence and high cytocompatibility, in the assumption that the presence of Ca^{2+} in the structure and citrate adsorbed on these luminescent solids must be beneficial from the point of view of the cytocompatibility required in bioimaging.

2. Materials and Methods

2.1. Materials and Precipitation Method

For the experiments the following reagents were purchased from Sigma-Aldrich (St Louis, MO, USA): Terbium (III) chloride anhydrous ($TbCl_3$, 99.9% pure, trace metals), sodium citrate tribasic dihydrate (Na_3(cit)$\cdot 2H_2O$, where cit = citrate = $C_6H_5O_7$, ACS reagent, ≥99.0% pure), calcium chloride dihydrate ($CaCl_2 \cdot 2H_2O$, Bioxtra, ≥99.0% pure), and sodium phosphate dibasic (Na_2HPO_4, ACS reagent, ≥99.0% pure). Sodium carbonate monohydrate ($Na_2CO_3 \cdot H_2O$, ACS reagent, 99.5% pure) and hydrochloric acid (HCl, ACS reagent, 37 wt % in H_2O) were provided by Merck (Darmstadt, Germany) and Panreac

(Barcelona, Spain), respectively. Solutions were prepared with ultrapure deionized water (0.22 µS, 25 °C, Milli-Q, Millipore, Burlington, MA, USA).

The synthesis of nanocrystals was carried out by the already established method of thermal decomplexing of $M^{(2+/3+)}/Ca^{2+}/cit/phosphate/carbonate$ solutions [29], using Tb^{3+} as lanthanide ion (y = 0.09, 0.07, 0.05 and 0.03 M) and increasing concentrations of doping Ca^{2+} in the solution (x = 0.01 M, 0.03, 0.05, and 0.07 M) to set $x + y$ = 0.1 M. The experiments lasted 4 h, 24 h, and 96 h. Some of them were matured for 7 days. The precipitates were subjected to washing by centrifugation with ultrapure water (6 cycles, 9000 rpm, 9 min each) and freeze-dried overnight at -50 °C under vacuum (3 mbar).

2.2. Physico-Chemical Characterization of Solid Nanoparticles

As-prepared powders were analyzed by different techniques, as it is described below:

X-ray powder diffraction (XRD) patterns were recorded using a diffractometer PANAlytical MPD (PANAlytical, Almelo, The Netherlands) with a Bragg-Brentano parafocusing geometry and Cu Kα radiation. Data processing of most matured samples was carried out with software TOPAS 6.0 (Coelho Software, Brisbane, Australia) [35]. The contribution of the isotropic peak broadening due to domain size was modeled using the "CS_L" TOPAS macro based on the Scherrer approximation, and considering the instrumental contribution from a measurement of LaB$_6$ standard (NIST SRM 660c).

TEM observations were performed with a TEM Libra 120 Plus (EELS) instrument at 80 kV (Carl Zeiss, Jena, Germany). Prior to observation samples were dispersed in absolute ethanol ($\geq$99.8% v/v) and deposited on copper microgrids coated with FORMVAR carbon film. HRTEM analysis were done with a TITAN G2 60-300 FEI Instrument (FEI, Hillsboro, OR, USA) operating at 300 kV, equipped with EDX Super X detector to perform microanalysis, and STEM type HAADF.

Fourier transform infrared spectra (FTIR) were recorded in transmittance mode within the wavelength range from 4000 cm^{-1} to 400 cm^{-1} using a Perkin-Elmer Spectrum One FTIR spectrometer (Perkin Elmer, Shelton, WA, USA). Pellets with ~1 wt% sample in anhydrous KBr were prepared and pressed with a hydraulic pump at 10 tons. Pure KBr pellets were used to record the background. Raman spectra were recorded with a LabRAM HR spectrometer (Jobin–Yvon, Horiba, Tokyo, Japan). The excitation line was provided by a diode laser emitting at a wavelength of 532 nm while a Peltier cooled charge–couple device (CCD) (1064 $\times$ 256 pixels) was used as a detector.

Crystal size distribution (CSD) and electrophoretic mobility (ζ-potential) were analyzed with a Zetasizer Nano ZS analyzer (Malvern Instruments Ltd., Malvern, UK) in aqueous suspensions (~0.5 mg/mL, 25 °C) contained in disposable polystyrene cuvettes. For ζ-potential versus pH measurements the MPT-2 autotitrator (Malvern Instruments Ltd., Malvern, UK) was employed to adjust the pH of the suspensions. Diluted HCl and NaOH solutions (0.25 and 0.1 M, respectively) were used as titration agents without any additional electrolyte.

Elemental analysis of Tb was carried out by inductively coupled plasma mass spectroscopy (ICP MS) using a Perkin Elmer NexION 300D ICP Mass spectrometer (Perkin Elmer). Ca and P were analyzed with Perkin Elmer ICP-OES OPTIMA 8300 spectrometer (Perkin Elmer); C and H were determined by thermoanalysis using Thermo Scientific™ FLASH 2000 CHNS/O Analyzer of Thermo Fisher Scientific (Waltham, MA, USA). TGA analyses were performed with a thermogravimetric analyzer TGA-50H model (Shimadzu, Tokyo, Japan). Samples were weighted in a platinum crucible and heated from room temperature (~28 °C) to 950 °C under 50 mL/min air flow with a heating rate of 20 °C/min.

2.3. Luminescence Spectroscopy

Excitation and emission spectra of both powder and aqueous suspension mg/mL samples, the latter being at ~0.5 mg/mL, were recorded using a Cary Eclipse Varian Fluorescence Spectrophotometer (Varian Australia, Mulgrave, Australia) using λ_{exc} = 375 nm, λ_{em} = 545 nm, 0.120 µs delay time (td) and 5 ms gate time (t$_g$); photomultiplier voltage

of 470 V and slit width$_{exc/em}$ 5/5 nm for powder samples and photomultiplier voltage of 800 V and slit width$_{exc/em}$ 10/10 nm for aqueous suspension particles. The excitation and emission spectra were recorded within the range 250–500 nm and 500–750 nm, respectively. Lifetime (τ) measurements were also recorded by a Cary Eclipse Varian Fluorescence Spectrophotometer (Varian Australia, Mulgrave, Australia) using $\lambda_{exc/em}$ = 375/475 nm, 100 μs delay time (t$_d$), 0.010 ms gate time (t$_g$), photomultiplier voltage of 600 V, slit width$_{exc/em}$ 10/10 nm and 100 cycles.

For solid sample analysis, a Cary Eclipse Solid Sample Holder (https://www.agilent.com/en/product/molecular-spectroscopy/fluorescence-spectroscopy/fluorescence-accessories/cary-eclipse-solid-sample-holder) was used to allow the measuring at the optimum angle and to minimize the effect of the thickness.

Concerning the dispersity of the measurements, they are not shown in the figures due to their lower value. In all the case the RSD (relative standard deviation) were lower than 2% (*n* = 3).

2.4. Cytocompatibility Tests

Nanocrystal cytocompatibility was tested on two cell lines: GTL-16 (a human gastric carcinoma cell line) and A549 (a human lung adenocarcinoma cell line). Then, 24 h after seeding cells (12,000 GTL-16 and 5000 A549 cells/well in 96-well plates), different concentrations of the differentially doped (*x* = 0.01, 0.03, 0.05, 0.07 M Ca^{2+}) nanoparticles, ranging from 0.1 to 100 mg/mL, were added in 100 mL of fresh medium. Hydrogen peroxide (1 mM) was used as control of toxicity. After 72 h incubation, cell viability was evaluated by the 3-(4,5-Dimethylthiazol-2-yl)-2,5-diphenyltetrazolium bromide) (MTT, Sigma) colorimetric assay. Briefly, 20 mL of MTT solution (5 mg/mL in a PBS solution) were added to each well and the plate was incubated at 37 °C for 3 h. After the removal of the solution, 125 mL of isopropanol, 0.2 M HCl was added to dissolve formazan crystals. One hundred mL were then removed carefully, and the optical density was measured in a multiwell reader (2030 Multilabel Reader Victor TM X4, Perkin Elmer) at 570 nm. Viability of parallel cultures of untreated cells was taken as 100% viability, and values obtained from cells undergoing the different treatments were referred to this value. Experiments were performed 3 times using 3 replicates for each sample. Data were statistically analyzed and are expressed as mean ± standard deviation. Statistical analyses were performed using a one-way ANOVA with Bonferroni's post-hoc test for grouped analyses using GraphPad Prism version 4.03 for Windows, GraphPad Software (GraphPad Prism, San Diego, CA, USA). Differences at *p* < 0.05 were considered to be statistically significant.

3. Results

3.1. Structural, Physicochemical, Morphological Characteristics, and Colloidal Stability of Solid Nanoparticles

The XRD patterns of the solids precipitated for increasing concentration of Ca^{2+} (*x*, from 0.01 M to 0.07 M) and increasing maturation times (from 4 to 96 h) are reported in Figure 1. In particular, the patterns showing the distinguishing reflections of the hexagonal (raphdophane) phase identified as TbPO$_4$·nH$_2$O, space group P3$_1$21 (PDF 20 1244) are displayed in panels a–d. At *x* = 0.01 M Ca^{2+} this is the only crystalline phase identified. The main reflections of this phase are located at 2θ 14.85° (100), 20.43° (101), 25.91° (110), 30.02° (200), 32.10° (102), 38.72° (112), 42.70° (003), 48.10° (301), 49.63° (212), 53.2° (203), and 54.5° (302). Other minor reflections (non-indexed) appear beyond 2θ 55°. These latter peaks are not shown in the PDF 20-1244 card, but are similar to those appearing in the PDF 20-1044 card corresponding to the raphdophane structure in the EuPO$_4$·H$_2$O. In addition, small differences in 2θ positions are found between the two patterns because some peak assignments in PDF file 20 1244 are affected with errors ≥ 0.2°. When x ≥ 0.03 M Ca^{2+} (Figure 1b–d), however, an additional phase started to crystallize. The reflections of this phase at ~27° and 32.8° are assigned to CaCO$_3$ vaterite (PDF 33-0268), possibly doped with terbium. The presence of vaterite is more evident at *x* = 0.05 and 0.07 M Ca^{2+}. Thus, this

compound becomes stable in calcium-rich medium due to the presence of residual $CO_3{}^{2-}$ in the crystallizing solutions. Nevertheless, its presence does not represent a problem concerning biomedical uses since this polymorph of $CaCO_3$ is biocompatible [36]. At 0.07 M Ca^{2+} we found a slightly different phase evolution with time. At 4 h, the bulging of the baseline is characteristic of an amorphous phase, probably of terbium phosphate, whereas at 24 h the reflections of the raphdophane phase started to emerge from the bulging baseline. In none of the experiments have we detected the presence of any calcium phosphate phase.
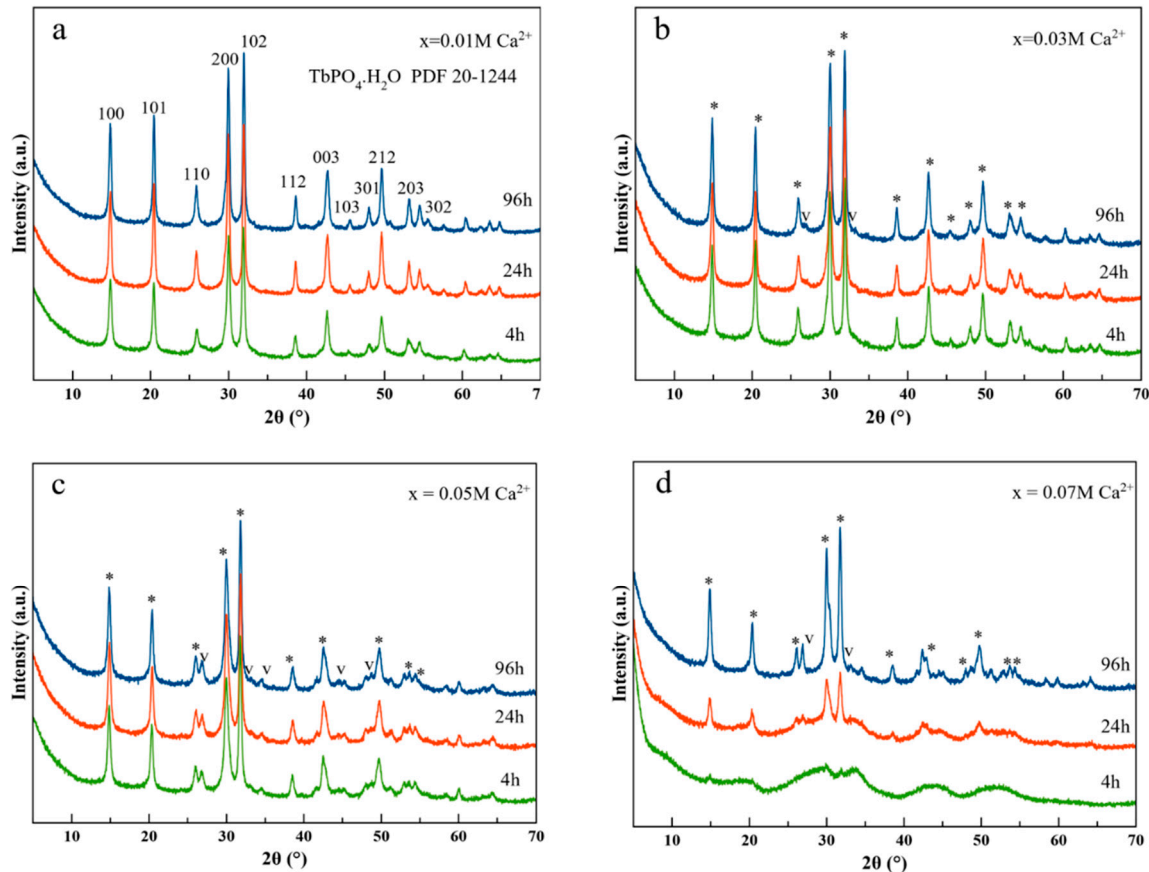
Figure 1. Evolution of XRD patterns with maturation time (4 h, green; 24 h, red; 96 h, blue) of samples precipitated from Ca^{2+}/Tb^{3+}/cit/phosphate/carbonate solutions in presence of increasing concentrations of Ca^{2+}: (**a**) x = 0.01 M Ca^{2+}; (**b**) x = 0.03 M Ca^{2+}; (**c**) x = 0.05 M Ca^{2+}, and (**d**) x = 0.07 M Ca^{2+}. * hexagonal phase $TbPO_4 \cdot nH_2O$ PDF 20-1244.

The microstructural study of 96 h samples was performed by analysis of the full XRD pattern, excluding the reflections of vaterite (Figure 2). Results show isometric crystalline domains whose average Scherrer diameters were 37.6 ± 0.2 nm for the less Ca^{2+}-doped sample (Figure 2a), 28.6 ± 0.2 nm for x = 0.03 M Ca^{2+} (Figure 2b), 24.9 ± 0.2 for x = 0.05 (Figure 2c), and 30.2 ± 0.1 for x = 0.07 M Ca^{2+} (Figure 2d), respectively.

TEM observations of these precipitates show nanocrystals with ill-defined shapes and aspect ratios close to 1 (Figure 3a–c). In contrast to what has been reported for cit-Ca^{2+}:$EuPO_4 \cdot H_2O$ nanoparticles, no appreciable dependence of their morphology with Ca^{2+} doping was found [29].
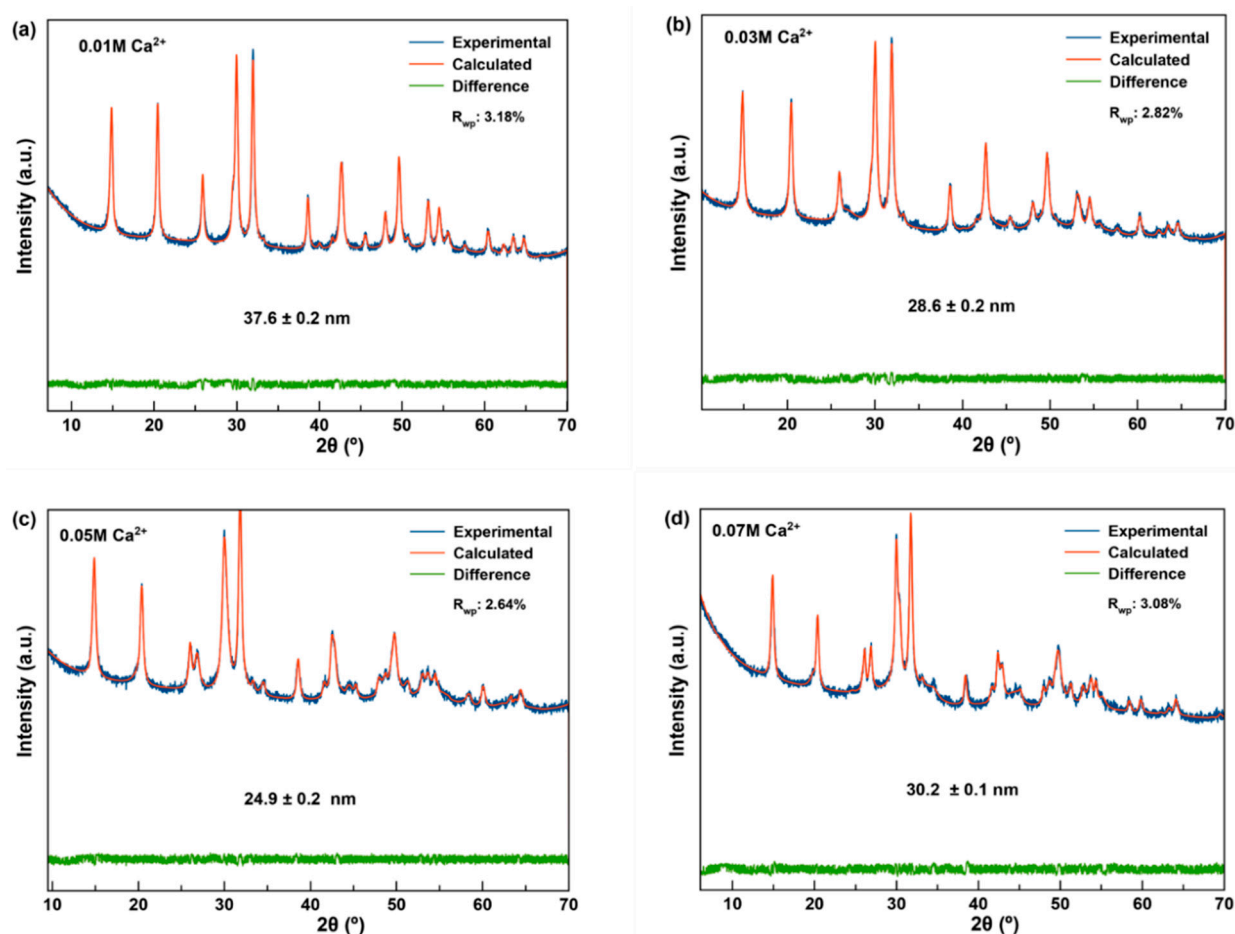
Figure 2. Crystalline domain sizes of Ca^{2+}:$TbPO_4 \cdot nH_2O$ nanoparticles prepared with, (**a**) *x* = 0.01 M; (**b**) *x* = 0.03 M; (**c**) *x* = 0.05 M and (**d**) *x* = 0.07 M Ca^{2+} for 96 h, calculated by analysis of the full XRD pattern using TOPAS 6.0. The two XRD vaterite reflections are excluded. R_{wp}, weighted profile R-factor as described in Young [37].

The sizes deduced on the basis of either TEM (29 ± 5, 28 ± 3, 33 ± 6, Figure 3a–c) or SEM (*x* = 0.07 M Ca^{2+}, L = 55 ± 20 nm, not shown) images are equivalent to those measured from XRD data. The indexed SAED patterns (insets) show the crystallographic planes of the hexagonal phase, i.e., (100), (110) in Figure 3a, or (100), (102), (200) in Figure 3c. The sample obtained for *x* = 0.01 Ca^{2+} was studied in more details, as shown in Figure 3d–i. Figure 3d displays the image in high angle annular dark field (HAADF) in Scanning Transmission Electron Microscopy (STEM). The elemental mappings composition of the nanoparticles (Figure 3e,f,h,i) show a homogeneous distribution of Tb, Ca, P, and O. HRTEM images of this sample (Figure 3g) reveal lattice fringes, basically monodomains, whose d-spacing of 2.78 Å corresponds to plane (102), also shown in the fast Fourier transform FFT images of this sample (Figure 3d, inset).

FTIR and Raman spectroscopy were employed to reveal the spectroscopic features of the Ca^{2+}-doped samples (see Figure 4 for the stacking of spectra of precipitates prepared at different Ca^{2+} doping concentrations, and Supplementary Figures S1 and S2 for the stackings as a function of maturation time).
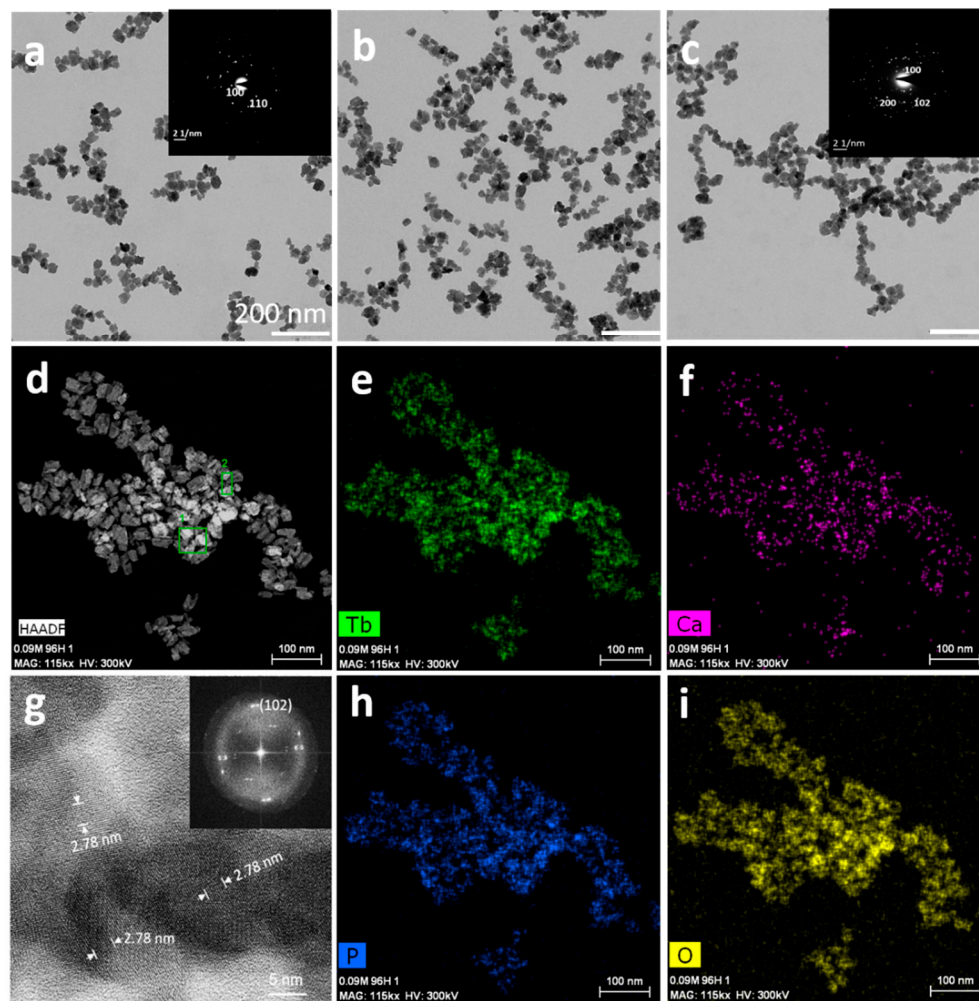
Figure 3. (**a–c**) TEM micrographs of cit-Ca^{2+}:$TbPO_4 \cdot H_2O$ nanorods prepared with different Ca^{2+} doping concentrations at 96 h: (**a**) x = 0.01 M; (**b**) x = 0.03 M; (**c**) x = 0.05 M. Insets display SAED patterns of the nanoparticles. (**d**) HAADF-STEM micrograph of sample x = 0.01 M Ca^{2+}. (**e,f,h,i**) EDX element mapping analysis of Tb, Ca, P, and O in nanoparticles of image (**d**). (**g**) HR-TEM image showing lattice fringes and d-spacing of 2.78 Å corresponding to plane (102) of nanocrystals of sample x = 0.01 M Ca^{2+}. Inset in (**g**) shows the corresponding Fourier transform (FFT) image displaying the (102) plane.
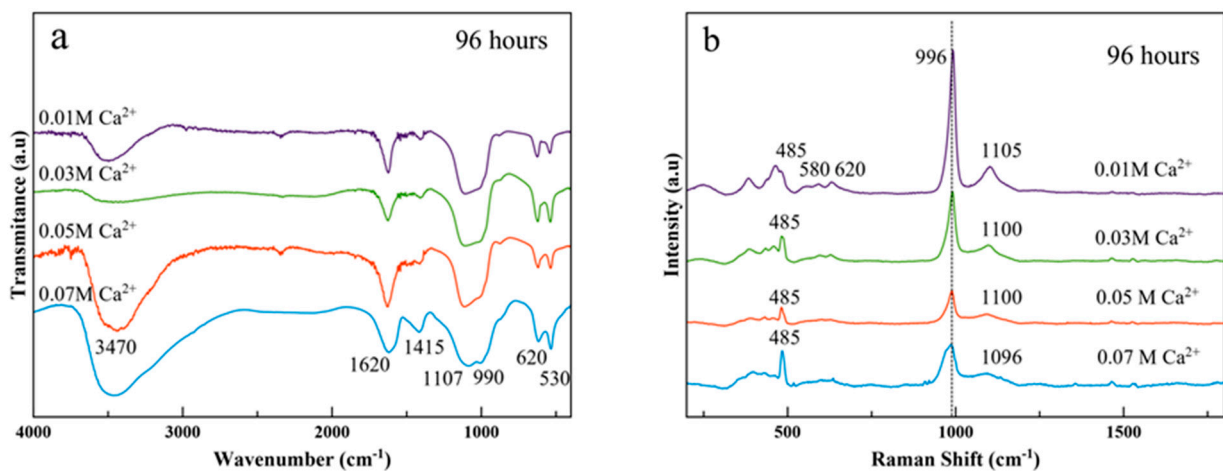
Figure 4. (**a**) FTIR and (**b**) Raman spectra of samples precipitated at 96 h using Ca^{2+}-doping concentrations x = 0.01 M (purple), x = 0.03 M (green), x = 0.05 M (red), x = 0.07 M (light blue).

FTIR spectra of Ca^{2+}-doped samples (Figure 4a) show basically the same spectroscopic features upon calcium doping, especially for x = 0.01, 0.03, and 0.05 M Ca^{2+}. These are a broadband between 3600–3700 cm^{-1} and 2600 cm^{-1} corresponding to the O–H stretching of associated water, a main broad band at 1000–1100 cm^{-1}, which corresponds to the antisymmetric stretching mode of PO_4^{3-} groups (ν_3PO_4) and two intense bands at ~620 and 535 cm^{-1} ascribed to the bending mode of the same PO_4^{3-} groups (ν_4PO4). The broader signals around 1590–1620 cm^{-1} and 1405–1430 cm^{-1} are assignable to the antisymmetric and symmetric stretching frequencies of carboxylate ($-COO^-$) groups of the adsorbed citrate [29]. No appreciable differences in peak assignments in the FTIR profiles were found after 4 h of maturation at any of the Ca^{2+} doping concentrations used (Supplementary Figure S1a–d).

In parallel, Raman characterization (Figure 4b) show the most intense band at 996 cm^{-1} (ν_1), which can be assigned to the P–O symmetric stretching mode of PO_4 group in raphdophane-type orthophosphates, while that at ~1100 cm^{-1} is attributed to the antisymmetric stretching (ν_3PO_4). The intensity of both bands decreases upon Ca^{2+} doping. The region comprised between 300 and 700 cm^{-1} corresponds to the deformation modes of the PO_4 tetrahedron. The most intense band in this region is at 485 cm^{-1} and is assigned to the symmetric vibrations, while those at ~570 and 620 cm^{-1} can be ascribed to the asymmetric vibrations (ν_4) [38,39]. The presence of vaterite in the spectra for x = 0.05 and 0.07 M Ca^{2+}, with bands at 1080–1090 cm^{-1} ν_1CO_3 and 740–750 cm^{-1} ν_4CO_3 [40] is hidden by the most intense bands of the phosphate groups. Clear differences were detected when plotting Raman spectra at increasing maturation times (Supplementary Figure S2). First, an increase in the intensity of the antisymmetric stretching mode ν_3PO_4 at ~1100 cm^{-1}, and particularly in the less Ca^{2+}-doped sample (Supplementary Figure S2a) is observed. Second, the highest Ca^{2+}-doped sample shows the ν_1PO_4 mode shifted from 970 cm^{-1} to 990 cm^{-1} (Supplementary Figure S2d), and the appearance of bands around 745 cm^{-1} and 1080 cm^{-1} (related to the vaterite phase). Also, the peaks at 845 cm^{-1} and 1460 cm^{-1} in samples at 4 and 24 h, in vibrational zones of citrate groups [41].

Thermogravimetric analyses (Supplementary Figure S3) revealed a behavior very close to the ones reported for lanthanide phosphate materials of raphdophane structure [29,42–45] but with some peculiarities reflecting the presence of citrates and carbonates in samples prepared at x = 0.05 and 0.07 M Ca^{2+}. The first weight loss, recorded between T_{amb} and 120–140 °C of about 2 wt%, is attributed to the residual adsorbed water, while the second one between 140 °C and about 600 °C, of 5–5.5 wt%, corresponds to the release of structural water, and this is the main weight loss. The third weight loss above 600 °C is associated with the decomposition of citrate molecules in samples prepared with x = 0.01 and 0.03 M Ca^{2+}, and with decomposition of citrate and of $CaCO_3$ in CO_2 and CaO, when x = 0.05 and 0.07 M Ca^{2+}. Specific losses are observed in these two samples. For x = 0.05 M Ca^{2+} the loss of CO_2 is around 0.6 wt% and for x = 0.07 M Ca^{2+} is of 2.2 wt%.

Quantitative analyses of Ca, P, Tb, C, and H of as-prepared samples are reported in Table 1. This table also shows the percent weights of structural H_2O determined by TGA and thus, the hydration number (n) of the raphdophane phase. Percent weights of $CaCO_3$ and citrate were determined by combining TGA data with mass balances. The data reveal increased percentages of dopant Ca from 0.42 wt% to 8.11 wt% in the structure of $TbPO_4.nH_2O$ as the percentage of Tb decreases, according to the increase of Ca^{2+}/Tb^{3+} ratio in the precursor solutions.

In these samples, the percentages of adsorbed citrate were around 1.1–1.2 wt% but in the highest Ca^{2+}-doped sample that percentage rose to 4 wt%. This higher amount of citrate is likely due to the higher percentage of $CaCO_3$, which can be also coated with citrate. Table 1 also shows that structural H_2O ranges between 5.0 and 6.3 wt% rendering hydration numbers around 0.9.

Table 1. Quantitative analyses of Ca, P, Tb, C, H, and estimated percent weights of structural citrate, H_2O, $CaCO_3$ and hydration number n of the samples prepared with Ca^{2+} doping concentration x ranging from 0.01 to 0.07 M, at 96 h.

x [Ca^{2+}] mol/L	Ca (wt%)	P (wt%)	Tb (wt%)	C (wt%)	H (wt%)	Cit (wt%)	H_2O str (wt%)	$CaCO_3$ (wt%)	n
0.01	0.42	10.5	61.4	0.46	0.72	1.21	5.0	0	0.88
0.03	2.91	10.9	39.8	0.42	0.74	1.10	5.44	0.2	0.86
0.05	6.76, 6.09 *	12.0	27.5	0.52	0.75	1.12	6.68	0.76	0.93
0.07	10.32, 8.11 *	11.45	16.9	1.72	1.04	3.96	6.33	1.75	0.95

* wt% of dopant Ca in the $TbPO_4 \cdot nH_2O$ structure.

The analysis of CSD and ζ-potential versus pH of aqueous suspensions of the nanoparticles is also relevant to assess their potential as luminescent probes in nanomedicine applications. The tendency of the colloid to disperse or aggregate in simulated physiological conditions in the blood (pH around 7.4) or in the tumor microenvironment (pH around 5–6) are related to the size and surface charge of the nanoparticles [16,46]. In addition, these features have an impact on the formation of the protein corona around the nanoparticles [47]. In this study, the CSD of cit-Ca^{2+}:$TbPO_4 \cdot nH_2O$ nanoparticles was plotted as cumulative volume-based distribution because they visually show the percentiles of the distribution D_{10}, D_{50} and D_{90} (Figure 5 and Supplementary Figure S4), widely employed to characterize crystal populations in pharmaceutical industry. These percentiles characterize the percentage of cumulative volume undersize distribution (percentage of the population smaller than the indicated size). Thus, D_{10} is a percentile closer to the size of the individual particles while D_{50}, the median of the population, is here somewhat influenced by particle aggregation. D_{90} is entirely influenced by the aggregation of nanocrystals. The percentiles for samples prepared with x = 0.01, 0.03, 0.05, and 0.07 M Ca^{2+} for 96 h were D_{10} 21, 51, 57, and 45 nm, respectively, and D_{50} 37, 531, 122, and 94 nm, respectively (Figure 5b).

In these samples, the evolution of cumulative CSD versus time (at 4 h, 24 h and 96 h, Figure S4a–d) does not follow a general trend, thus reflecting a difference in Ca composition as well as the presence of a secondary phase (vaterite) at high doping concentrations and its influence in the aggregation.

These differences are also reflected in the profile of the ζ-potential versus pH curves (Figure 5c–f). While samples obtained with x = 0.01 and 0.03 M Ca^{2+} displayed similar curves, with ζ-potential values −17.3 and −17.4 mV at pH 7, and −14.0 and −10.5 mV at pH 5 (Figure 5c,d), the curves of sample obtained with x = 0.05 M Ca^{2+} (Figure 5e) and x = 0.07 M Ca^{2+} (Figure 5f) show a different profile. The minimum ζ-potential values were found at pH 6.0 (−11.5 mV) and pH 8.0 (−15.9 mV) respectively. ζ-potentials were 0 beyond pH 6.0 in the first case, and below pH 8.0 in the second one.

3.2. Luminescence Properties of Cit-Ca^{2+}:$TbPO_4 \cdot nH_2O$ Nanoparticles

3.2.1. Luminescence in Solid-State

It is well-known that some lanthanides, especially europium (III) and terbium (III), form highly fluorescent chelates with many different organic ligands. The sensitized fluorescence results from the ligand absorbing light, the energy of which is then transferred to the chelated metal ion. In fact, Tb(III) emits the energy as narrow-banded, line-type fluorescence with a long Stokes shift (over 250 nm) and an exceptionally long fluorescence decay time (up to 1 ms) [48]. Because of the long fluorescence decay time (over 10 times longer than the average background fluorescence) of Tb(III), a delay time (t_d) and a gate time (t_g) can be used during the measuring, remarkably reducing the background fluorescence.
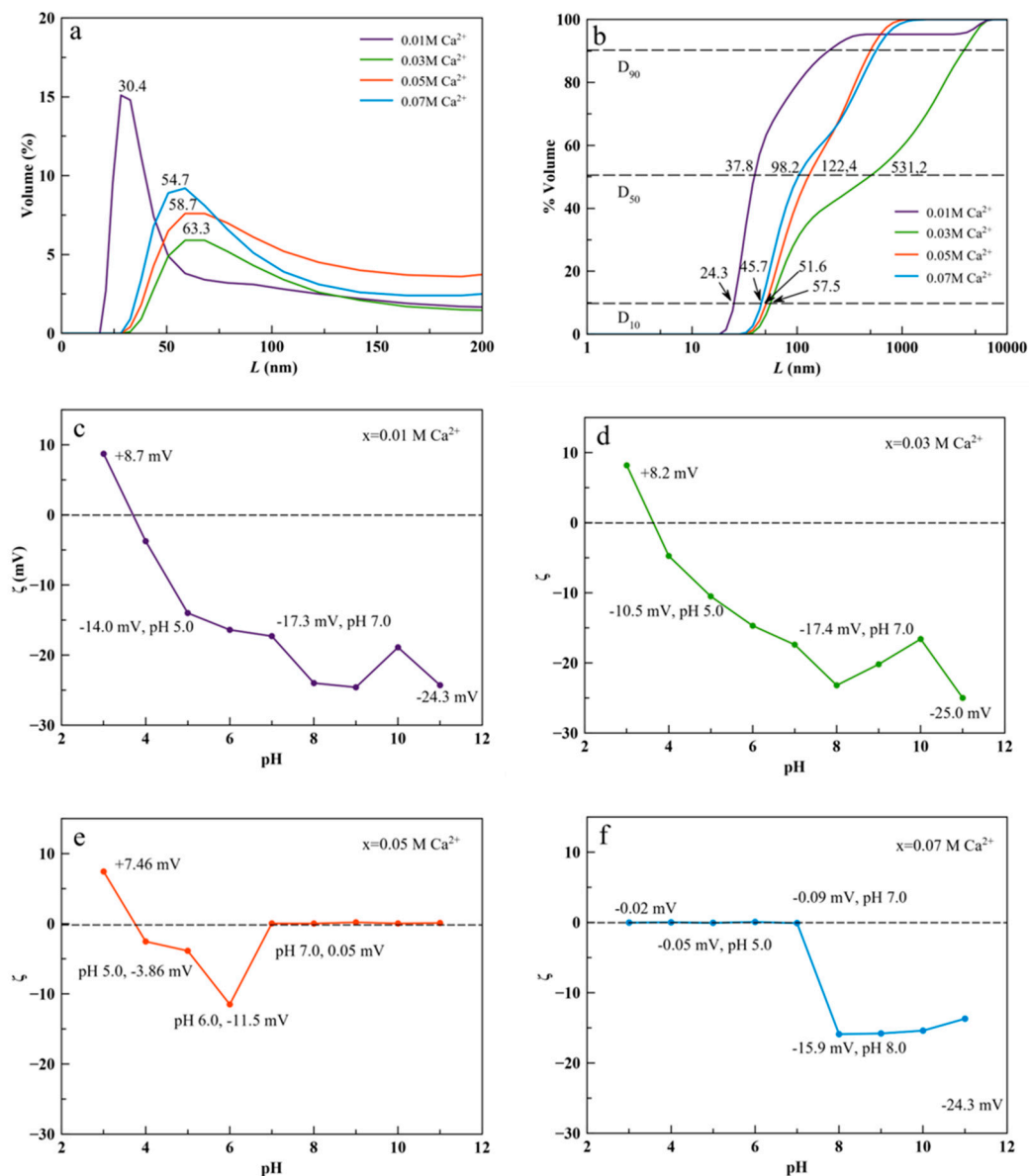
Figure 5. (**a**) Volume-based CSD and (**b**) cumulative volume-based CSD of cit-Ca^{2+}:$TbPO_4 \cdot nH_2O$ nanocrystals prepared with Ca^{2+} doping concentrations x = 0.01 (purple), 0.03 (green), 0.05 (red) and 0.07 M (light blue) for 96 h, measured in aqueous suspensions (pHs 8.4, 8.9, 8.3, and 7.80, respectively). (**c–f**) ζ-potential versus pH of aqueous suspensions of cit-Ca^{2+}:$TbPO_4 \cdot nH_2O$ nanocrystals.

The luminescence properties of solid cit-Ca^{2+}:$TbPO_4 \cdot nH_2O$ samples are shown in Supplementary Materials (Figures S5 and S6). They are the same as those depicted in Figure 6 which correspond to x = 0.01 M Ca^{2+}; neither the maturation time nor the Ca^{2+} doping concentrations affect the excitation and emission wavelengths. This finding is expected because the electronic transitions of f orbitals are not affected by crystal's field.

The observed excitation wavelengths for the powder were 230, 284, 300, 320, 340, 350, 368 and 375 nm. The broad bands between 200 and 300 nm, centered at 230 nm, correspond to charge transfer (called charge transfer band, CTB), which occurs by electron delocalization from the filled 2p shell of O^{2-} to the partially filled 4f shell of Tb^{3+}. Also, this band can partially be attributed to the charge transfer transition X^{5+}–O^{2-} [49,50]. The rest of the less intensive excitation wavelengths correspond to the $^7F_6 \rightarrow {}^5I_8$ and $^5F_{4,5} \rightarrow {}^5H_4$, $^7F_6 \rightarrow {}^5H_{5,6}$, $^7F_6 \rightarrow {}^5H_7$, $^7F_6 \rightarrow {}^5L_{7,8}$ and $^7F_6 \rightarrow {}^5L_{7,8}$, $^7F_6 \rightarrow {}^5L_9, {}^5D_2, {}^5G_5$, $^7F_6 \rightarrow {}^5L_{10}$, and $^7F_6 \rightarrow {}^5G_6, {}^5D_3$ transitions [51].
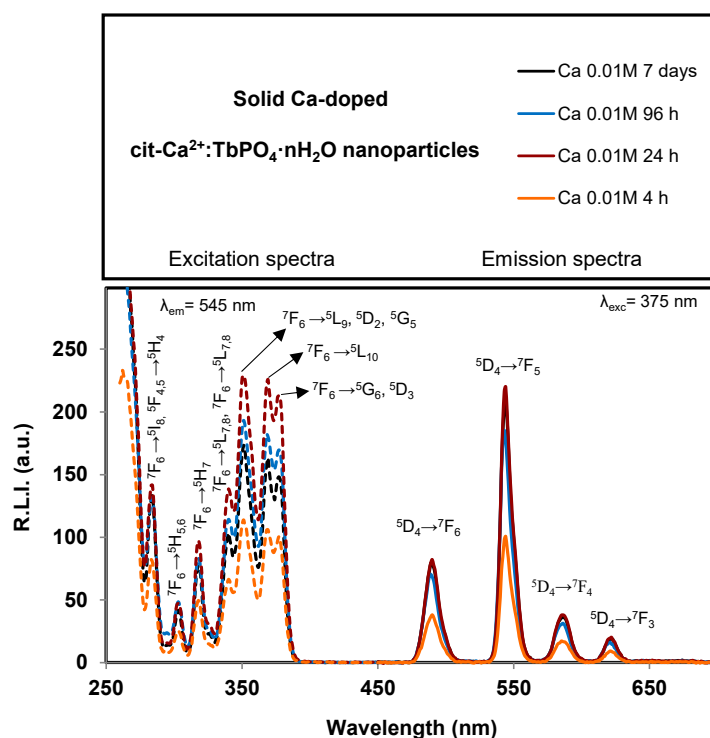
Figure 6. Excitation (dashed lines) and emission (solid lines) uncorrected spectra of solid cit-Ca^{2+}:$TbPO_4 \cdot nH_2O$ samples prepared with $x = 0.01$ M Ca^{2+} at maturation times of 4 h, 24 h, 96 h and 7 days.

SM (see Supplementary Figure S5) shows the emission spectra of the cit-Ca^{2+}:$TbPO_4 \cdot nH_2O$ with $x = 0.01$ M and 96 h of maturation time using 230 and 375 nm excitation wavelengths. It is possible to conclude that the emission spectra are the same; only the emission intensity is affected. In order to increase the biological applicability of the system, 375 nm (which is closer to the visible range) was selected as excitation wavelength.

Concerning the emission wavelengths, they are centered at 490, 545, 586 and 620 nm which correspond to the Tb^{3+} $^5D_4 \rightarrow {}^7F_6$, $^5D_4 \rightarrow {}^7F_5$, $^5D_4 \rightarrow {}^7F_4$ and $^5D_4 \rightarrow {}^7F_3$ transitions, respectively [52]. The emission wavelength corresponding to the hypersensitive transition without inversion centre ($^5D_4 \rightarrow {}^7F_5$, 545 nm for Tb^{3+}) produces the highest relative luminescence intensity (R.L.I.). Therefore, the optimum excitation and emission wavelengths of solid cit-Ca^{2+}:$TbPO_4 \cdot nH_2O$ samples were 375 nm and 545 nm, respectively.

Supplementary Figures S7 and S8 show the effect of maturation time (t) at different doping Ca^{2+} concentrations (*x*) on the relative luminescence intensity (R.L.I.).

The R.L.I. of samples prepared with $x = 0.01$, 0.03 and 0.05 M Ca^{2+} is not affected by the maturation time (Supplementary Figure S7). It can be due to the slowing down of the crystal growth caused by the adsorption of citrate up to 2 h maturation [29]. In contrast, for $x = 0.07$ M Ca^{2+} doping concentration, the R.L.I is highly affected; at shorter times (4 and 24 h) the signal is high, but it decreases drastically in the sample prepared at 96 h. As it was previously commented for this concentration, at shorter times (4 and 24 h) the material is amorphous without an ordered structure and with a high amount of Tb^{3+} adsorbed on its surface, showing high luminescence. However, at 96 h it is crystalline, exhibiting an improved internal ordering in which Tb^{3+} is buried in the structure of the nanoparticles, resulting in a decrease on the luminescence. It was previously reported that amorphous materials provide much more luminescence emission than crystalline ones [29]. On the other hand, this sample contains a higher proportion of citrate (~4 wt%) providing a less emissive material than at other Ca^{2+}-doped concentrations.

Analyzing the variation of the R.L.I at a fixed maturation time versus *x* it is also possible to observe that the main differences are found for $x = 0.07$ M (Supplementary

Figure S8). It can be explained for the same reasons commented before that, at shorter maturation times, the sample has an amorphous nature and at the higher one it is crystalline, and the amount of citrate is higher, providing a less luminescent material.

Concerning the luminescence lifetime (τ), Supplementary Figures S9–S11 show the luminescence decay curves and the variation of the luminescence lifetime versus both maturation time and Ca^{2+} doped concentrations, respectively. For each case, the decay profile was analyzed as a single exponential component (R.L.I. = $A\cdot e\hat{}(-t/\tau)$ + C). It is possible to conclude that the maturation time at a given Ca^{2+} doped concentration does not affect the lifetime (Supplementary Figure S10). However, the luminesce lifetime for a given maturation time is increased by increasing the x. It might be due to the presence of progressive amounts of vaterite.

3.2.2. Luminescence of the Nanoparticles in Aqueous Suspension

The luminescence properties of cit-Ca^{2+}:$TbPO_4 \cdot nH_2O$ dispersed in aqueous media are similar to those depicted in Figure 7, which corresponds to x = 0.01 M Ca^{2+}, 96 h maturation time, pH 7.4, and 25 °C. It is also possible to observe that the excitation and emission wavelength of the material dispersed in water is practically the same than those in powder as well as the luminescence lifetime is not affected by dispersing the sample in an aqueous media. On the other hand, it is possible to conclude that the material has the same luminescence properties (R.L.I. and lifetime) at any physiological pH, so variation of the pH in real biological samples does not affect the luminescence properties of the particles.

The effect of ionic strength was evaluated by suspending the particles in 0, 25, 50, 75 and 100 mM NaCl solutions (Figure S12). It is possible to deduce that neither the R.L.I. nor the luminescence lifetime is significantly affected by the ionic strength, which is also important for the final applications of these nanoparticles.

The temperature may also theoretically affect the luminescence by quenching of the excited states, i.e., for increasing T the molecular motion and collisions increase, and hence the luminescence emission decreases by increasing encounters probabilities. [53] Figure S13 shows the experimental results. To sum up, increasing from 25 to 40 °C does not affect considerably the luminescence emission of all the tested materials in suspension. The change in fluorescence intensity is normally 1% per degree Celsius [53] and the decreases for these materials were 0.2, 0.4, 2.6, and 0.6% per degree Celsius, for 0.01 M, 0.03 M, 0.05 M and 0.07 M Ca^{2+} doping concentration, respectively. This is very important in view of medical and biomedical imaging (~37.4 °C) while the rest of the experiments were performed at room temperature (25 °C).

3.3. *Cytocompatibility of Cit-Ca^{2+}:$TbPO_4 \cdot nH_2O$ Nanoparticles*

The cytocompatibility of cit-$TbPO_4 \cdot nH_2O$ samples doped with different concentrations of Ca^{2+} was tested in a MTT assay on the GTL-16 human carcinoma cells and the A549 human lung adenocarcinoma cells, after incubation at concentrations ranging from 0.1 to 100 μg/mL. GTL-16 cells were chosen because this is the reference standard cell line used in the lab for this type of experiments. In particular, the fact that these tumor cells express a high level of receptors for a growth factor has made this cell line a good model for studying tumor cell ligand-mediated targeting by nanoparticles, possibly loaded by a drug [6,16]. A549 cells were chosen since they are easily available cells in many laboratories.

No toxicity was observed on both cell lines at any nanoparticle concentration (Figure 8), since in all cases a cell viability higher than 85% was observed, largely above the cut-off of 70% indicated by ISO 10993–5:2009 [54]. The presence of the doping Ca^{2+} appears to increase the biocompatibility of the nanocrystals in a dose-dependent manner. On the other side, both cell types were sensitive to the toxic activity of hydrogen peroxide, which reduced their viability to less than 50%. This in vitro assay thus shows the good cytocompatibility of the cit-Ca^{2+}:$TbPO_4 \cdot nH_2O$ nanoparticles.

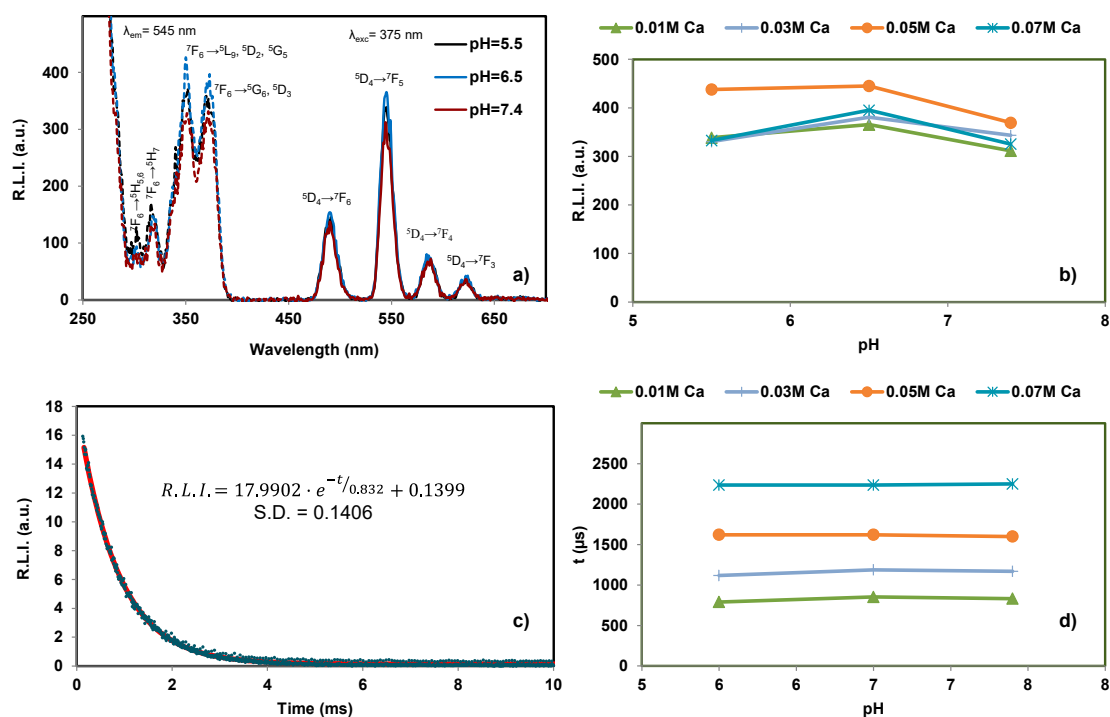**Figure 7.** Luminescence properties of cit-Ca^{2+}:TbPO$_4$·nH$_2$O dispersed in aqueous media with x = 0.01 M Ca^{2+}, 96 h maturation time and 25 °C versus pH; (**a**) Excitation (dashed line) and emission (solid line) spectra; (**b**) Variation of R.L.I. versus pH; (**c**) Luminescence decay curve; and (**d**) Variation of luminescence lifetime with the pH.
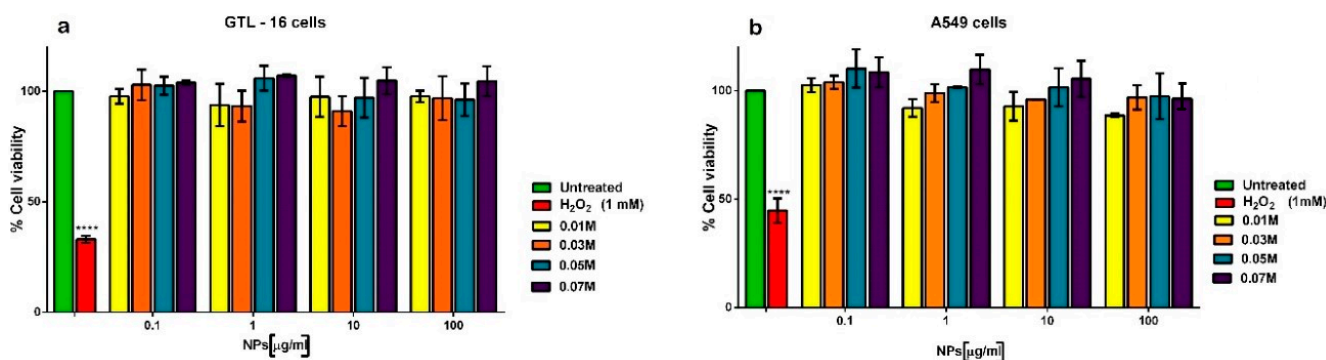

Figure 8. Viability of GTL-16 cells (**a**) and of A549 cells (**b**) incubated with cit-Ca^{2+}:TbPO$_4$·nH$_2$O particles prepared with different Ca^{2+}-doping concentration for three days. Viability was assessed in MTT assays. Data represent means ± SD of three independent experiments performed in triplicate and statistical analyses were carried on using One-way ANOVA, with Bonferroni comparison test. For statistical analysis all data were compared to untreated samples and only samples treated with H$_2$O$_2$ displayed statistically significant difference (**** p = 0.0005).

4. Discussion

The above results confirm the herein reported bioinspired crystallization route succeeded in preparing cit-Ca^{2+}:TbPO$_4$·nH$_2$O nanocrystals of the hexagonal rhabdophane phase, with n~0.9 and tailored Ca^{2+}content between 0.42 wt% and 8.11 wt%. The nanocrystals displayed isometric ill-defined morphologies, and adsorbed citrate on their surfaces, a chemical feature exhibited by bone nAps [34]. As Ca^{2+} increases the risk of appearance of a secondary phase of CaCO$_3$ (vaterite) must be considered. However, this trouble can be properly assumed since vaterite is biocompatible. In addition, the percent weight of citrate increases, particularly in the sample prepared with x = 0.07 M. As citrate molecules were not removed after different cycles of washing, they should be adsorbed not only to Ca^{2+}:TbPO$_4$·H$_2$O but also to the CaCO$_3$ surface. As hypothesized, these features have an

impact on the cytocompatibility of the cit-Ca^{2+}:$TbPO_4 \cdot H_2O$. In fact, all samples displayed a high cytocompatibility when tested on two human carcinoma cell lines and cell viability appears to positively correlate with the amount of doping Ca^{2+} in the nanocrystals, in line with what was reported for cit-Ca^{2+}:$EuPO_4 \cdot nH_2O$ nanocrystals [29].

Also important are the average sizes of the nanocrystals. The average sizes measured in TEM or SEM micrographs were equivalent to those of their crystal domains, indicating they are basically monodomains, with no appreciable dependence of their morphology (isometric) with Ca^{2+} doping. This finding contrasts with what was reported for cit-Ca^{2+}:$EuPO_4 \cdot H_2O$ nanoparticles [29]. Those nanoparticles showed elongated (anisometric) morphologies and their aspect ratio decreased with Ca^{2+} doping. It is worth highlighting that percentiles D_{10} of the CSD are close to these average sizes deduced from electron microscopy images. This finding indicates that aggregation is very low and D_{10} could define the nanoparticle size in the context of the whole population, particularly in the less Ca^{2+} doped sample. D_{50}, instead, doubles the D_{10} percentile or is even 10 times higher in sample $x = 0.03M$ Ca^{2+}, suggesting a higher contribution of particle aggregation below the median size.

Concerning the ζ-potential versus pH of nanoparticle suspensions, those samples prepared at $x = 0.01$ and 0.03 M Ca^{2+} show a high and negative ζ-potential above pH 4, therefore they display great stability both at pH~7.4 simulating physiological pH, and at pHs~5–6, simulating the environment of cancer cells. The CSD of the sample prepared at $x = 0.01$ M Ca^{2+} correlates well with the ζ-potential versus pH measurements of this sample, and reflects the role of surface charge on the stability of the nanoparticles and their aggregation behavior. However, there is a lack of correlation between the CSD and the ζ-potential values for the 0.03 M Ca^{2+}sample, indicating that other effects besides the nanoparticles surface charge can be involved in particle aggregation. Also, the other samples present a negative ζ-potential, but these are less negative, indicating poorer stability of the suspensions at the pHs of interest for biological applications. In the latter samples, the curves reflect the presence of vaterite, and also the increasing amount of citrate, which correlate with a relatively higher cytocompatibility. Thus, when $x = 0.05$ M Ca^{2+} the ζ -potential value close to zero indicates a high amount of surface Ca^{2+} that compensate the negative charge due to citrate at basic pH. When $x = 0.07$ M Ca^{2+} (Figure 5f) the ζ-potential values at basic pHs are again negative. This finding is due to the higher percentage of citrate negatively charged respect to positively charged surface Ca^{2+} coating both Ca^{2+}:$TbPO_4 \cdot nH_2O$ and $CaCO_3$ particles. It was reported that the mode of adsorption of citrate on a substrate depends on the pH of the solution. Citrate molecules absorb on monodentate or bidentate configuration (i.e., on nanoapatites [55]) displaying the third carboxylate group upward toward the solution. This arrangement gives rise to a negative net surface charge that is reflected in a negative ζ -potential. While preventing aggregation, the negative ζ -potentials of nanocrystal could interfere with their interaction with the cell surface, which is also negatively charged, and their eventual uptake by cell endocytosis. This behavior, however, is not the only possibility, since some negatively charged nanoparticles, such as Fluorescein-5-isothiocyanate-labelled hydroxypatite nanoparticles [6] and magnetic nanoparticles [56], were reported to be internalized by cells.

To discuss how the nanocrystals herein described were formed, one must consider both the influence of their tridimensional crystal structure and the presence of additives in the precursor solution. Indeed, the growth morphology of a nanocrystal results from the interplay between the growth rates of its outermost crystallographic planes and the growth-inhibiting/promoting effect of the additives. The raphdophane structure of the $LnPO_4 \cdot nH_2O$ is described as chains formed by lanthanide with eight-fold coordination alternating with tetrahedral orthophosphate ions. These chains are extended along with the c-axis, each one linked to four neighboring chains, thus forming open channels which are filled with between 0.5 to 2 H_2O molecules per formula unit, stabilizing the structure [15,20,57]. Consequently, $LnPO_4 \cdot nH_2O$ show the general trend to grow along [001] direction forming nanowires.

The second influence we must consider is the effect of citrate, which is a known growth inhibitor. Citrate adsorbs on specific outermost planes of incipiently formed nanocrystals slowing down its growth along the [001] direction, and leading to the formation of nanocrystals with lower aspect ratios than those formed in additive-free solutions. As we obtain basically the same crystal morphology irrespective of the amount of Ca^{2+} doping the cit-Ca+:$TbPO_4 \cdot nH_2O$ structure, we conclude that Ca^{2+} has limited inhibiting/promoting effect on the growth of these nanocrystals, against that of citrate, in contrast to what found in cit-Ca^{2+}:$EuPO_4 \cdot nH_2O$ [29]. On the other side, as already discussed above, the addition of this metal ion had a positive effect on the cytocompatibility of the nanoparticles, in line with the previous report relative to cit-Ca^{2+}:$EuPO_4 \cdot nH_2O$ [29]. Moreover, at the highest doping dose, Ca^{2+} enhances the adsorption of citrate, an ion contributing to biomimetic properties of apatites [34].

Finally, the luminescence study of these nanoparticles in solid phase indicate that R.L.I. is affected by neither the maturation time nor the Ca^{2+} content when x is lower than 0.07 M Ca^{2+}, as occurred on cit- Ca^{2+}:$EuPO_4 \cdot nH_2O$, while the R.L.I. at x = 0.07 M Ca^{2+} is high at short maturation time (due to the amorphous nature of the samples) and low at high maturation time (due to the crystalline nature of the sample and also due the higher citrate amount coating the raphdophane and vaterite nanoparticles). Concerning the luminescence properties in aqueous dispersion, neither pH nor ionic strength nor temperature affect their luminescence properties at physiological range.

According to all the above considerations the optimal conditions to synthesize cytocompatible cit-Ca^{2+}:$TbPO_4 \cdot nH_2O$ nanocrystals free of vaterite or with negligible amount of this phase, with enough and exploitable luminescent properties (R.L.I and luminescent lifetimes) and higher stability of their aqueous suspensions at the pH range of biological interest (5–7.4), are when using Ca^{2+} doping concentration x = 0.01 M and x = 0.03 M, at any of the maturation times from 4 to 96 h.

Summing up, all the above properties are positive relative to the applications of these nanoparticles as luminescent labeling agents and highlight the potential of the thermal decomplexing synthetic method to prepare this kind of nanophosphors.

5. Conclusions

Cit-Ca^{2+}:$TbPO_4 \cdot nH_2O$ nanocrystals of the hexagonal rhabdophane phase, with n ~ 0.9 and tailored Ca^{2+} content between 0.42 and 8.11 wt% were successfully obtained by thermal decomplexing of Ca^{2+}/Tb^{3+}/citrate/phosphate/carbonate solutions. These nanocrystals of about 29–37 nm are mainly monodomains and display basically isometric ill-defined morphologies, with Ca^{2+} having limited inhibiting/promoting effect on the growth of these nanoparticles, but enhancing the amount of citrate adsorbed on the surface in dose-depending manner. All the nanoparticles displayed high cytocompatibility on two human carcinoma cell lines and cell viability correlated positively with the amount of doping Ca^{2+}.

Luminescence properties of the nanocrystals reveal that luminescent lifetimes increase (between ~800 and ~2600 μs) by increasing the Ca^{2+} doping concentration. Their relative luminescence intensities in solid state (around 200 units) are affected by neither Ca^{2+}, nor citrate content, nor maturation time for Ca^{2+} doping concentrations below 0.07 M Ca^{2+}. Only at this doping concentration the maturation time strongly affects R.L.I, decreasing it. At low maturation times (4 h, 24 h) it is high (around 650 units). However, at 96 h, it strongly decreases up to ~40. This finding was related to the amorphous nature of the precipitates obtained at 4 and 24 h, whereas at 96 h, the precipitates were crystalline. In addition, this sample also contains vaterite and a higher percent weight of citrate than the samples obtained with lower doping concentrations of Ca^{2+}, and therefore it presents a lower percent weight of emissive material. In aqueous suspensions, neither pH nor ionic strength nor the temperature affect their luminescence properties.

According to all the above considerations, the optimal conditions to synthesize cytocompatible cit-Ca^{2+}:$TbPO_4 \cdot nH_2O$ nanocrystals free of vaterite or with negligible amount of this phase, with enough and exploitable luminescent properties (R.L.I and luminescent

lifetimes) and higher stability of their aqueous suspensions at the pH range of biological interest (5–7.4), are when using Ca^{2+} doping concentration x = 0.01 M and x = 0.03 M, at any of the maturation times from 4 to 96 h.

Summing up, the above properties are encouraging relative to the potential bioimaging applications of the nanocrystals. They can thus represent promising new luminescent nanoprobes for such applications and, if coupled with targeting and therapeutic moieties, they could be effective tools for theranostics.

Supplementary Materials: The following are available online at https://www.mdpi.com/2079 -4991/11/2/322/s1, Figure S1: Evolution of FTIR spectra with time of samples prepared with different Ca^{2+} doping concentrations x = 0.01 to 0.07 M, Figure S2: Evolution of Raman spectra with time of samples prepared with different Ca^{2+} doping concentrations x = 0.01 to 0.07 M, Figure S3: TGA analyses of precipitates obtained at 96 h from solutions with Ca^{2+} doping concentrations ranging from (a) x = 0.01 to (d) x= 0.07 M, Figure S4: Cumulative volume oversize distribution of the cit-Ca^{2+}:TbPO$_4$.nH$_2$O nanocrystals prepared with Ca^{2+} doping concentrations x = 0.01, 0.03, 0.05 and 0.07 M at 4, 24 and 96 h, Figure S5: Excitation (dashed lines) and emission (solid lines) uncorrected spectra of solid cit-Ca^{2+}:TbPO$_4$·nH$_2$O samples prepared with x = 0.01 M Ca^{2+} at maturation times of 96 h using t$_d$ = 120 μs, t$_d$ = 5 ms and (a) λexc/em = 230/545 nm, slit width exc/em = 2.5/2.5 nm, detector voltage 545 V; b) λexc/em = 375/545 nm, slit width exc/em = 5/5 nm, detector voltage 470 v, Figure S6: Excitation (dashed lines) and emission (solid lines) uncorrected spectra of solid cit-Ca^{2+}:TbPO$_4$·nH$_2$O samples prepared with different Ca^{2+} doped concentration at maturation times of 4 h, 24 h, 96 h and 7 days, Figure S7: Variation of the R.L.I. of the solid cit-Ca^{2+}:TbPO$_4$·nH$_2$O samples at the maximum excitation and emission wavelengths at several Ca^{2+} concentrations when the maturation time is changed. Figure S8: Variation of the R.L.I. of the solid cit-Ca^{2+}:TbPO$_4$·nH$_2$O samples at the maximum excitation and emission wavelengths at several maturation time when the Ca^{2+} concentration is changed. Figure S9: Luminescence decay curve of different solid cit-Ca^{2+}:TbPO$_4$·nH$_2$O samples at maturation times of 96 h, t$_d$ = 100 μs, t$_g$ = 0.01 ms, λ$_{exc/em}$ = 375/545 nm, slit-widths$_{exc/em}$ = 10/10 nm, and detector voltage = 600 V. Circles correspond to experimental data (100 cycles) and lines to the fitting equation. Figure S10: Variation of the luminescence lifetime of the solid cit-Ca^{2+}:TbPO$_4$·nH$_2$O nanoparticles prepared at several Ca^{2+} concentrations when the maturation time is changed. Figure S11: Variation of the luminescence lifetime of the solid cit-Ca^{2+}:TbPO$_4$·nH$_2$O samples at several maturation times when the Ca^{2+} concentration is changed. Figure S12: Effect of the ionic strength over the (a) R.L.I. and (b) luminescence lifetime of the cit-Ca^{2+}:TbPO$_4$·nH$_2$O samples at 96 h maturation time dispersed in aqueous media at several Ca^{2+} concentrations is changed. Figure S13. Effect of the temperature over the (a) R.L.I. and (b) luminescence lifetime of the cit-Ca^{2+}:TbPO$_4$·nH$_2$O samples at 96h maturation time dispersed in aqueous media at several Ca^{2+} concentrations.

Author Contributions: Conceptualization, J.G.-M., D.C.-L., and M.P.; Investigation, J.G.-M., J.F.F.-S., M.P., I.R.-C., R.F.-P., A.D., and C.V.-E.; methodology, R.F.-P., A.D., J.F.F.-S., and C.V.-E; Supervision, J.G.-M.; writing—original draft preparation, J.G.-M. and M.P.; writing—review and editing, J.G.-M., M.P., and J.F.F.-S.; funding acquisition, J.G.-M., D.C.-L. and M.P. All authors have read and agreed to the published version of the manuscript.

Conflicts of Interest: The authors declare no conflict of interest.

References

1. Sreenivasan, V.K.A.; Zvyagin, A.V.; Goldys, E.M. Luminescent nanoparticles and their applications in the life sciences. *J. Phys. Condens. Matter* **2013**, *25*, 194101. [CrossRef] [PubMed]
2. Li, J.; Zhu, J.-J. Quantum dots for fluorescent biosensing and bio-imaging applications. *Analyst* **2013**, *138*, 2506. [CrossRef] [PubMed]
3. Fu, C.-C.; Lee, H.-Y.; Chen, K.; Lim, T.-S.; Wu, H.-Y.; Lin, P.-K.; Wei, P.K.; Tsao, P.H.; Chang, H.-C.; Fann, W. Characterization and application of single fluorescent nanodiamonds as cellular biomarkers. *Proc. Natl. Acad. Sci. USA* **2007**, *104*, 727–732. [CrossRef]
4. Yeh, Y.-C.; Creran, B.; Rotello, V.M. Gold nanoparticles: Preparation, properties, and applications in bionanotechnology. *Nanoscale* **2012**, *4*, 1871–1880. [CrossRef]
5. Wang, F.; Tan, W.B.; Zhang, Y.; Fan, X.P.; Wang, M.Q. Luminescent nanomaterials for biological labelling. *Nanotechnology* **2006**, *17*, R1–R13. [CrossRef]
6. Oltolina, F.; Gregoletto, L.; Colangelo, D.; Gómez-Morales, J.; Delgado-López, J.M.; Prat, M. Monoclonal antibody-targeted fluorescein-5-isothiocyanate-labeled biomimetic nanoapatites: A promising fluorescent probe for imaging applications. *Langmuir* **2015**, *31*, 1766–1775. [CrossRef] [PubMed]
7. Neacsu, I.A.; Stoica, A.E.; Vasile, B.S.; Andronescu, E. Luminescent hydroxyapatite doped with rare earth elements for biomedical applications. *Nanomaterials* **2019**, *9*, 239. [CrossRef]
8. Gómez-Morales, J.; Verdugo-Escamilla, C.; Fernández-Penas, R.; Parra-Milla, C.M.; Drouet, C.; Maube-Bosc, F.; Oltolina, F.; Prat, M.; Fernández-Sánchez, J.F. Luminescent biomimetic citrate-coated europium-doped carbonated apatite nanoparticles for use in bioimaging: Physico-chemistry and cytocompatibility. *RSC Adv.* **2018**, *8*, 2385–2397. [CrossRef]
9. Derfus, A.M.; Chan, W.C.W.; Bhatia, S.N. Probing the cytotoxicity of semiconductor quantum dots. *Nano Lett.* **2004**, *4*, 11–18. [CrossRef]
10. Fang, Y.-P.; Xu, A.-W.; Song, R.-Q.; Zhang, H.-X.; You, L.-P.; Yu, J.C.; Liu, H.-Q. Systematic synthesis and characterization of single-crystal lanthanide orthophosphate nanowires. *JACS* **2003**, *125*, 16025–16034. [CrossRef]
11. Luo, Q.; Shen, S.; Lu, G.; Xiao, X.; Mao, D.; Wang, Y. Synthesis of cubic ordered mesoporous YPO4:Ln^{3+} *and* their photoluminescence properties. *J. Mater. Chem.* **2009**, *19*, 8079–8085. [CrossRef]
12. Zhang, F.; Wong, S.S. Ambient large-scale template-mediated synthesis of high-aspect ratio single-crystalline, chemically doped rare-earth phosphate nanowires for bioimaging. *ACS Nano* **2010**, *4*, 99–112. [CrossRef] [PubMed]
13. Di, W.; Li, J.; Shirahata, N.; Sakka, Y.; Willingere, M.-G.; Pinna, N. Photoluminescence, cytotoxicity and in vitro imaging of hexagonal terbium phosphate nanoparticles doped with europium. *Nanoscale* **2011**, *3*, 1263–1269. [CrossRef]
14. Ito, H.; Fujishiro, Y.; Sato, T.; Okuwaki, A. Preparation of lanthanide orthophosphates by homogeneous precipitation under hydrothermal conditions using lanthanide-EDTA chelates. *Br. Ceram. Trans.* **1995**, *94*, 146–150.
15. Zollfrank, C.; Scheel, H.; Brungs, S.; Greil, P. Europium(III) orthophosphates: Synthesis, characterization, and optical properties. *Cryst. Growth Des.* **2008**, *8*, 766–770. [CrossRef]
16. Iafisco, M.; Delgado-López, J.M.; Varoni, E.M.; Tampieri, A.; Rimondini, L.; Gómez-Morales, J.; Prat, M. Cell surface receptor targeted biomimetic apatite nanocrystals for cancer therapy. *Small* **2013**, *9*, 3834–3844. [CrossRef]
17. Iafisco, M.; Marchetti, M.; Gómez-Morales, J.; Hernández-Hernández, M.A.; García-Ruiz, J.M.; Roveri, N. Silica gel template for calcium phosphates crystallization. *Cryst. Growth Des.* **2009**, *9*, 4912–4921. [CrossRef]
18. Ramírez-Rodríguez, G.B.; Delgado López, J.M.; Gómez-Morales, J. Evolution of calcium phosphate precipitation in hanging drop vapor diffusion by in situ Raman microspectroscopy. *CrystEngComm* **2013**, *15*, 2206–2212. [CrossRef]
19. Bu, W.; Zhang, L.; Hua, Z.; Chen, H.; Shi, J. Synthesis and characterization of uniform spindle-shaped microarchitectures self-assembled from aligned single-crystalline nanowires of lanthanum phosphates. *Cryst. Growth Des.* **2007**, *7*, 2305–2309. [CrossRef]
20. Fang, Y.-P.; Xu, A.-W.; Dong, W.-F. Highly improved green photoluminescence from CePO4:Tb/LaPO4 core/shell nanowires. *Small* **2005**, *1*, 967–971. [CrossRef]
21. Nuñez, N.O.; Liviano, S.R.; Ocaña, M.J. Citrate mediated synthesis of uniform monazite LnPO4 (Ln = La, Ce) and Ln:LaPO4 (Ln = Eu, Ce, Ce + Tb) spheres and their photoluminescence. *Colloid Interface Sci.* **2010**, *349*, 484–491. [CrossRef]
22. Patra, C.R.; Bhattacharya, R.; Patra, S.; Basu, S.; Mukherjee, P.; Mukhopadhyay, D. Inorganic phosphate nanorods are a novel fluorescent label in cell biology. *J. Nanobiotechnol.* **2006**, *4*, 11. [CrossRef]
23. Yu, C.; Yu, M.; Li, C.; Liu, X.; Yang, J.; Yang, P.; Lin, J. Facile sonochemical synthesis and photoluminescent properties of lanthanide orthophosphate nanoparticles. *J. Solid State Chem.* **2009**, *182*, 339–342. [CrossRef]
24. Wang, X.; Gao, M. A facile route for preparing rhabdophane rare earth phosphate nanorods. *J. Mater. Chem.* **2006**, *16*, 1360–1365. [CrossRef]
25. Hou, Z.; Wang, L.; Lian, H.; Chai, R.; Zhang, C.; Cheng, Z.; Lin, J. Preparation and luminescence properties of Ce^{3+} and/or Tb^{3+} doped LaPO4 nanofibers and microbelts by electrospinning. *J. Solid State Chem.* **2009**, *182*, 698–708. [CrossRef]
26. Xing, Y.; Li, M.; Davis, S.A.; Mann, S. Synthesis and characterization of cerium phosphate nanowires in microemulsion reaction media. *J. Phys. Chem. B* **2006**, *110*, 1111–1113. [CrossRef]
27. Liu, X.; Wang, Q.; Gao, Z.; Sun, J.; Shen, J. Fabrication of lanthanide phosphate nanocrystals with well-controlled morphologies by layer-by-layer adsorption and reaction method at room temperature. *Cryst. Growth Des.* **2009**, *9*, 3707–3713. [CrossRef]

28. Huong Tran, T.; Anh Tran, K.; Khuyen Hoang, T.; Hien Pham, T.; Minh Le, Q. Fabrication and properties of terbium phosphate nanorods. *Adv. Nat. Sci. Nanosci. Nanotechnol.* **2012**, *3*, 015010. [CrossRef]

29. Gómez-Morales, J.; Verdugo-Escamilla, C.; Fernández-Penas, R.; Parra-Milla, C.M.; Drouet, C.; Iafisco, M.; Oltolina, F.; Prat, M.; Fernández-Sánchez, J.F. Bioinspired crystallization, sensitized luminescence and cytocompatibility of citrate-functionalized Ca-substituted europium phosphate monohydrate nanophosphors. *J. Colloid Interface Sci.* **2019**, *538*, 174–186. [CrossRef]

30. López-Macipe, A.; Gómez-Morales, J.; Rodríguez-Clemente, R. Nanosized hydroxyapatite precipitation from homogeneous calcium/citrate/phosphate solutions using microwave and conventional heating. *Adv. Mater.* **1998**, *10*, 49–53. [CrossRef]

31. Delgado-López, J.M.; Iafisco, M.; Rodríguez, I.; Prat, M.; Gómez-Morales, J.; Tampieri, A. Crystallization of bioinspired citrate-functionalized nanoapatites with tailored carbonate content. *Acta Biomater.* **2012**, *8*, 3491–3499. [CrossRef]

32. Martínez-Casado, F.J.; Iafisco, M.; Delgado-López, J.M.; Martínez-Benito, C.; Ruiz-Pérez, C.; Colangelo, D.; Oltolina, F.; Prat, M.; Gómez-Morales, J. Bioinspired citrate–apatite nanocrystals doped with divalent transition metal ions. *Cryst. Growth Des.* **2016**, *1*, 145–153. [CrossRef]

33. Delgado-López, J.M.; Frison, R.; Cervellino, A.; Gómez-Morales, J.; Guagliardi, A.; Masciocchi, N. Crystal size, morphology, and growth mechanism in bio-inspired apatite nanocrystals. *Adv. Funct. Mater.* **2014**, *24*, 1090–1099. [CrossRef]

34. Hu, Y.Y.; Rawal, A.; Schmidt-Rohr, K. Strongly bound citrate stabilizes the apatite nanocrystals in bone. *Proc. Natl. Acad. Sci. USA* **2010**, *107*, 22425–22429. [CrossRef]

35. Coelho, A.A. TOPAS and TOPAS-Academic: An optimization program integrating computer algebra and crystallographic objects written in C++. *J. Appl. Cryst.* **2018**, *51*, 210–218. [CrossRef]

36. Combes, C.; Bareille, R.; Rey, C. Calcium carbonate–calcium phosphate mixed cement compositions for bone reconstruction. *J. Biomed. Mater. Res. Part A* **2006**, *79*, 318–328. [CrossRef]

37. Young, R.A. Introduction to the Rietveld method. In *The Rietveld Method*; Young, R.A., Ed.; Oxford University Press: Oxford, UK, 1993; pp. 1–38.

38. Clavier, N.; del Mesbah, A.; Szenknect, S.; Dacheux, N. Monazite, rhabdophane, xenotime & churchite: Vibrational spectroscopy of gadolinium phosphate polymorphs. *Spectrochim. Acta Part A Mol. Biomol. Spectrosc.* **2018**, *205*, 85–94. [CrossRef]

39. Assaaoudi, H.; Ennaciri, A.; Rulmont, A. Vibrational spectra of hydrated rare earth orthophosphates. *Vibrat. Spectr.* **2001**, *2*, 81–90. [CrossRef]

40. Donnelly, F.C.; Purcell-Milton, F.; Framont, V.; Cleary, O.; Dunne, P.W.; Gun'k, Y.K. Synthesis of $CaCO_3$ nano- and micro-particles by dry ice carbonation. *Chem. Commun.* **2017**, *53*, 6657–6660. [CrossRef] [PubMed]

41. Tada, H.; Bronkema, J.L.; Bell, A. Application of in situ surface-enhanced Raman spectroscopy (SERS) to the study of citrate oxidation on silica-supported silver nanoparticles. *Catal. Lett.* **2004**, *92*, 93–99. [CrossRef]

42. Lucas, S.; Champion, E.; Bernache-Assollant, D.; Leroy, G. Rare earth phosphate powders $RePO_4 \cdot nH_2O$ (Re = La, Ce or Y) II. Thermal behavior. *J. Solid State Chem.* **2004**, *177*, 312–1320. [CrossRef]

43. Cho, J.; Kim, C.H. Solid-state phase transformation mechanism from hexagonal $GdPO_4$:Eu^{3+} nanorods to monoclinic nanoparticles. *RSC Adv.* **2014**, *4*, 31385–31392. [CrossRef]

44. Kijkowska, R. Thermal decomposition of lanthanide orthophosphates synthesized through crystallisation from phosphoric acid solution. *Thermochim. Acta* **2003**, *404*, 81–88. [CrossRef]

45. Colomer, M.T.; Delgado, I.; Ortiz, A.L.; Fariñas, J.C. Microwave-assisted hydrothermal synthesis of single-crystal nanorods of rhabdophane-type Sr-doped $LaPO_4 \cdot nH_2O$. *J. Am. Ceram. Soc.* **2014**, *97*, 750–758. [CrossRef]

46. Jabalera, Y.; Oltolina, F.; Prat, M.; Jimenez-Lopez, C.; Fernández-Sánchez, J.F.; Choquesillo-Lazarte, D.; Gómez-Morales, J. Eu-Doped Citrate-Coated Carbonated Apatite Luminescent Nanoprobes for Drug Delivery. *Nanomaterials* **2020**, *10*, 199. [CrossRef]

47. Lundqvist, V.; Stigler, J.; Elia, G.; Lynch, I.; Cedervall, T.; Dawson, K.A. Nanoparticle size and surface properties determine the protein corona with possible implications for biological impacts. *Proc. Natl. Acad. Sci. USA* **2008**, *105*, 14265–14270. [CrossRef]

48. Hemmilä, I.; Dakubu, S.; Mukkala, V.-M.; Siitari, H.; Lövgren, T. Europium as a label in time-resolved immunofluorometric assays. *Anal. Biochem.* **1984**, *137*, 335. [CrossRef]

49. Siqueira, K.P.F.; Lima, P.P.; Ferreira, R.A.S.; Carlos, L.D.; Bittar, E.M.; Matinaga, F.M.; Paniago, R.; Krambrock, K.; Moreira, R.L.; Dias, A.J. Influence of the Matrix on the Red Emission in Europium Self-Activated Orthoceramics. *Phys. Chem. C* **2015**, *119*, 17825. [CrossRef]

50. Siqueira, K.P.F.; Lima, P.P.; Ferreira, R.A.S.; Carlos, L.D.; Bittar, E.M.; Granado, E.; González, J.C.; Abelenda, A.; Moreira, R.L.; Dias, A. Lanthanide Orthoantimonate Light Emitters: Structural, Vibrational, and Optical Properties. *Chem. Mater.* **2014**, *26*, 6351. [CrossRef]

51. Medina-Velazquez, D.Y.; Caldiño, U.; Morales-Ramirez, A.; Reyes-Miranda, J.; López, R.E.; Escudero, R.; Ruiz-Guerrero, R.; Morales Perez, M.F. Synthesis of luminescent terbium-thenoyltriflouroacetone MOF nanorods for green laser application. *Opt. Mater.* **2019**, *87*, 3–10. [CrossRef]

52. Richardson, F.S. Terbium(III) and europium(III) ions as luminescent probes and stains for biomolecular systems. *Chem. Rev.* **1982**, *82*, 541. [CrossRef]

53. Guilbault, G.G. *General Aspects of Luminescence Spectroscopy, Practical Fluorescence*; Guilbault, G.G., Ed.; Marcel Dekker: New York, NY, USA, 1990.

54. *ISO 10993-5 Biological Evaluation of Medical Devices Part 5: Tests for In Vitro Cytotoxicity*; International Standard Organization: Geneva, Switzerland, 2009.

55. López-Macipe, A.; Gómez-Morales, J.; Rodriguez-Clemente, R. The role of pH in the adsorption of citrate ions on hydroxyapatite. *J. Colloid Interface Sci.* **1998**, *200*, 114–120. [CrossRef]

56. Borroni, E.; Miola, M.; Ferraris, S.; Ricci, G.; Žužek Rožman, K.; Kostevšek, N.; Catizone, A.; Rimondini, L.; Prat, M.; Verné, E.; et al. Tumor targeting by lentiviral vectors combined with magnetic nanoparticles in mice. *Acta Biomater.* **2017**, *59*, 303–316. [CrossRef] [PubMed]

57. Mooney, C.L. X-ray diffraction study of cerium phosphate and related crystals. I. Hexagonal modification. *Acta Cryst.* **1950**, *3*, 337–340. [CrossRef]

Biomimetic Citrate-Coated Luminescent Apatite Nanoplatforms for Diclofenac Delivery in Inflammatory Environments

Sandra Maria Cano Plá [1,†], **Annarita D'Urso** [2,†], **Jorge Fernando Fernández-Sánchez** [3], **Donato Colangelo** [2], **Duane Choquesillo-Lazarte** [1], **Riccardo Ferracini** [4,5], **Michela Bosetti** [6], **Maria Prat** [2,7,8,9,*] and **Jaime Gómez-Morales** [1,*]

[1] Laboratorio de Estudios Cristalográficos, IACT, CSIC-UGR, Avda. Las Palmeras, n° 4, E-18100 Armilla, Granada, Spain; sandra@lec.csic.es (S.M.C.P.); duane.choquesillo@csic.es (D.C.-L.)

[2] Dipartimento di Scienze della Salute, Università del Piemonte Orientale, "A. Avogadro" Via Solaroli, 17, 28100 Novara, Italy; annarita.durso@med.uniupo.it (A.D.); donato.colangelo@med.uniupo.it (D.C.)

[3] Department of Analytical Chemistry, Faculty of Sciences, University of Granada, Avda. Fuentenueva s/n, 18071 Granada, Spain; jffernan@ugr.es

[4] Dipartimento di Scienze Chirurgiche e Diagnostiche Integrate, Università di Genova, Viale Benedetto XV 6, 16132 Genova, Italy; ferracini@edu.unige.it

[5] Ospedale Koelliker, Corso Galileo Ferraris, 247/255, 10134 Torino, Italy

[6] Dipartimento di Scienze del Farmaco, Università del Piemonte Orientale "A. Avogadro", Via Bovio 4, 28100 Novara, Italy; michela.bosetti@uniupo.it

[7] Centro di Biotecnologie per la Ricerca Medica Applicata (BRMA), Via Solaroli 17, 28100 Novara, Italy

[8] Consorzio Interuniversitario per Biotecnologie (CIB), Località Padriciano 99, 34149 Area di Ricerca, Trieste, Italy

[9] Consorzio Interuniversitario Nazionale per la Scienza e Tecnologia dei Materiali (INSTM), Via Giuseppe Giusti, 9, 50121 Firenze, Italy

* Correspondence: maria.prat@med.uniupo.it (M.P.); jaime@lec.csic.es (J.G.-M.); Tel.: +39-0321660662 (M.P.); +34-958525020 (J.G.-M.)

† These authors equally contributed to this work.

Abstract: Luminescent nanoparticles are innovative tools for medicine, allowing the imaging of cells and tissues, and, at the same time, carrying and releasing different types of molecules. We explored and compared the loading/release ability of diclofenac (COX-2 antagonist), in both undoped- and luminescent Terbium^{3+} (Tb^{3+})-doped citrate-coated carbonated apatite nanoparticles at different temperatures (25, 37, 40 °C) and pHs (7.4, 5.2). The cytocompatibility was evaluated on two osteosarcoma cell lines and primary human osteoblasts. Biological effects of diclofenac-loaded-nanoparticles were monitored in an in vitro osteoblast's cytokine–induced inflammation model by evaluating COX-2 mRNA expression and production of PGE$_2$. Adsorption isotherms fitted the multilayer Langmuir-Freundlich model. The maximum adsorbed amounts at 37 °C were higher than at 25 °C, and particularly when using the Tb^{3+}-doped particles. Diclofenac-release efficiencies were higher at pH 5.2, a condition simulating a local inflammation. The luminescence properties of diclofenac-loaded Tb^{3+}-doped particles were affected by pH, being the relative luminescence intensity higher at pH 5.2 and the luminescence lifetime higher at pH 7.4, but not influenced either by the temperature or by the diclofenac-loaded amount. Both undoped and Tb^{3+}-doped nanoparticles were cytocompatible. In addition, diclofenac release increased COX-2 expression and decreased PGE$_2$ production in an in vitro inflammation model. These findings evidence the potential of these nanoparticles for osteo-localized delivery of anti-inflammatory drugs and the possibility to localize the inflammation, characterized by a decrease in pH, by changes in luminescence.

Keywords: inflammation treatment; diclofenac-loaded nanoparticles; apatite; Tb^{3+}-doped apatite; luminescence; cytocompatibility

1. Introduction

Nanotechnology is finding increasing applications in medicine; in particular nanoparticles (NPs) can be used as vehicles to transport and deliver different classes of biologically active molecules (so-called nanocarriers), including chemotherapeutics, antibiotics, anti-inflammatory drugs, hormones, fluorophores, targeting agents [1–7], depending on the pathology considered, acting both in diagnosis and therapy. Their main advantage is linked to their nanoscale dimensions, enabling them to carry high amounts of molecules to chosen body sites, in the meantime protecting the drugs from rapid degradation or clearance. This allows to reduce the dose of the administered drugs, lowering or eliminating their unwanted systemic side effects. From the other side, also the nature/composition of the nanocarrier can vary depending on the diseases to be treated. Today bone tissue pathologies, such as osteoporosis, osteoarthritis and rheumatoid arthritis represent important health problems with considerable socio-economic burden, linked to the general population aging [8,9]. These musculo-skeletal disorders are characterized by a clinical condition of inflammation. In osteoporosis osteocatabolic processes prevail during bone remodelling, leading to a decrease of trabecular mass density, increasing the risk of bone fracture with concurrent inflammatory reaction [10]. In osteoarthritis the articular cartilages are consumed exposing the bones in the joint to mechanical stresses, with the development of a painful inflammatory reaction [11], while rheumatoid arthritis is an autoimmune disease characterized by chronic inflammation of synovial tissues, joints and cartilage leading to function loss and joint destruction [12]. For all these pathologies the available therapeutic strategies are still unsatisfactory, namely because of the associated side effects.

In this context, apatite (Ap) NPs, which consist of calcium phosphate and closely mimic bone apatite nanocrystals both from chemical and structural points of view, are particularly suited for therapeutic and diagnostic applications. Bone nanoapatite is nonstoichiometric calcium- (and OH-) deficient in respect to the mineral hydroxyapatite [HA, $Ca_{10}(PO_4)_6(OH)_2$], it incorporates substituting ions such as CO_3^{2-}, Mg^{2+}, Na^+ and other minor elements in its crystal structure [13], and contains citrate molecules strongly adsorbed on its surface [14]. Synthetic apatite-based materials including injectable calcium phosphates, or natural and synthetic polymer-apatite composites, are being used for bone repair applications exploiting their well-known properties of biodegradability, bioactivity and osteoinductivity, besides the capability of improving bone mechanical properties [15–18]. The apatite surfaces can be modified (charged to improve the interactions with living cells, particularly the osteoblasts) [19]. In addition, Ap NPs have already been shown to be valuable nanocarriers for different types of molecules [20], including nucleic acids [21], proteins [22], antibiotics [3], chemotherapeutics [23,24], fluorophores [25], and luminescent moieties [26,27]. Among their advantageous properties are high biocompatibility, good biodegradability, high loading capacity with the ability to bind moieties through both surface calcium and phosphate groups by isothermal adsorption. Moreover, because of their good stability at physiological pH with partial solubility at acidic pH they behave as smart complexes sensitive to local stimuli, e.g., binding drugs at physiological pH and releasing them at acidic pH [28], as the one found in inflamed or tumor tissues. Synthetic Ap NPs with CO_3^{2-} substitutions and covered by a certain amount of citrate, makes them even more biomimetic to bone apatite in terms of chemical composition and reactivity [14,29]. Lanthanide elements such as Eu^{3+} and Tb^{3+} have been recently employed to prepare luminescent apatite-based nanomaterials for drug release and bioimaging applications [30,31]. They exhibit different fluorescence emission colors (red and green, respectively), long luminescence lifetimes, and good resistance to photobleaching. In addition to these features, Tb^{3+} was found to have bactericidal activity [32], and to promote adhesion and osteogenic differentiation of mesenchymal stem cells [33,34].

Sodium diclofenac (DF) is a non-steroidal anti-inflammatory drug (NSAID) with analgesic, anti-inflammatory and anti-pyretic activities, exerting its activity by

competitively blocking cyclooxygenases-2 (COX-2) enzymatic activity responsible for the synthesis of inflammatory mediators, e.g., prostaglandin E$_2$ (PGE$_2$) [35,36]. As all the NSAIDs, DF has adverse systemic side effects, such as gastrointestinal ulceration and bleeding, hepato-renal dysfunction, disorders in the cardiovascular and central nervous systems, and skin reactions [37,38]. Local delivery of this drug via Ap NPs would offer a method of bypassing inconveniences. In addition, the use of Tb^{3+}-doped Ap NPs would allow their localization by luminescence emission. Thus, our aim is to explore the loading/release behavior, luminescence properties, and *in vitro* biological effects of these NPs in normal physiological conditions and in a condition simulating inflammation.

In particular, herein we produced biomimetic citrate-coated CO$_3$-Ap (cAp) and citrate-coated Tb^{3+}-doped CO$_3$-Ap (cAp-Tb) NPs. Next, we studied the adsorption and release of DF at physiological pH 7.4 (25 and 37 °C), and release at pHs 7.4 and 5.2 simulating local inflammation, as well as the luminescent properties of DF-loaded cAp-Tb NPs at pHs 7.4 and 5.2, and at 25, 37 and 40 °C. Then, we tested their cytocompatibility on different cell lines of bone origin, as well as on human primary osteoblasts (hOB) and osteoblasts differentiated *in vitro* from adipose-derived mesenchymal stem cells (differentiated hOB). Finally, we analysed the anti-inflammatory activity of DF-loaded cAp NPs on osteoblasts treated with a mixture of inflammatory cytokines (IL-1β, TNF-α, IFN-γ) by evaluating COX-2 activity and cellular production of PGE$_2$.

2. Materials and Methods

2.1. Reagents

Diclofenac sodium salt (2-[(2,6-Dichlorophenyl)amino]benzeneacetic acid sodium salt, MW = 318.13), calcium chloride dihydrate (CaCl$_2$·2H$_2$O, Bioxtra, ≥99.0% pure, MW = 147.01), terbium (III) chloride anhydrous (TbCl$_3$, 99.9% pure, trace metals, MW = 265.28), sodium citrate tribasic dihydrate (Na$_3$(cit)·2H$_2$O, cit = citrate = C$_6$H$_5$O$_7$, ACS reagent, ≥99,0% pure; MW = 294.1), and sodium phosphate dibasic (Na$_2$HPO$_4$, ACS reagent, ≥99.0% pure, MW = 141.96) were provided by Sigma-Aldrich (St. Louis, MO, USA), while sodium carbonate monohydrate (Na$_2$CO$_3$·H$_2$O, ACS reagent, 99.5% pure, MW = 124) and hydrochloric acid (HCl, ACS reagent, 37 wt % in H$_2$O, MW = 36.46) were supplied by Merck (Darmstadt, Germany) and Panreac (Barcelona, Spain), respectively. The solutions were prepared with Milli-Q water (deionized 0.22 μS, 25 °C, Millipore, Burlington, MA, USA).

2.2. Preparation of cAp and cAp-Tb Nanoparticles

Nanoparticles of cAp were prepared by the method of thermal decomplexing of Ca^{2+}/cit/phosphate/carbonate solutions [29]. A solution of composition 0.06 M Na$_2$HPO$_4$ + 0.1 M Na$_2$CO$_3$ (50 mL) was mixed with a solution of composition 0.1 M CaCl$_2$ + 0.2 M Na$_3$(cit) (50 mL) at 4 °C in a Pyrex glass bottle, and the pH adjusted to 8.5 with diluted HCl. The bottle was immediately introduced in a water bath at 80 °C and then in an oven at the same temperature for 96 h. For the preparation of cAp-Tb nanoparticles the second solution was composed of 0.010 M Tb^{3+} + 0.09 M CaCl$_2$ + 0.2 M Na$_3$(cit). This experiment lasted 4 h. Both precipitates were washed 4 consecutive times by centrifugation (9000 rpm, 30 min each) using Milli-Q water and dried in an oven with circulating forced air at 37.5 °C for 4 days.

2.3. Characterization of the Nanoparticles

The nanoparticles were characterized by X-ray diffraction (XRD) using a Bruker D8 Advance Vario Serie II (Bruker AXS, (Bruker GmbH, Karlsruhe, Germany) using CuKα radiation (1.5406 Å). Fourier Transform Infrared Spectrum (FTIR) was recorded with a Perkin-Elmer Spectrum One FTIR (Perkin Elmer, Shelton, WA, USA) in the wavenumber range from 4000 cm^{-1} a 400 cm^{-1}. Plates were prepared with a concentration of ~ 1 wt% in anhydrous KBr (MW = 119) and then pressed with a hydraulic pump to 10 tons. Raman

spectrum were recorded with a LabRAMHR spectrometer (Jobin-Yvon, Horiba, Tokyo, Japan) provided of a laser diode that emits at a wavelength of 532 nm. Transmission electron microscopy images (TEM) were taken with a Libra 120 Plus TEM instrument (EELS) at 80 kV (Carl Zeiss, Jena, Germany). Prior observation, the samples were dispersed in absolute ethanol (≥ 99.8% *v/v*) and deposited on copper microgrids coated with film of FORMVAR carbon. The particle size distribution (PSD) and ζ-potential were analysed by dynamic light scattering (DLS) with a Zetasizer Nano ZS analyser (Malvern Instruments Ltd., Malvern, UK) in aqueous suspensions (~0.5 mg/mL, room temperature) contained in polystyrene vials. For measurements of ζ-potential versus pH, suspensions of the nanoparticles were prepared at pHs from 4 to 9 using the MPT2 autotitrator with dilute HCl and NaOH (MW 39.997) solutions (0.25 and 0.1 M, respectively). Elemental analysis of Tb^{3+} was carried out by inductively coupled plasma mass spectroscopy (ICP-MS) using a Perkin Elmer NexION 300D ICP Mass spectrometer (Perkin Elmer, Beaconsfield, UK). C and H were determined by thermoanalysis using Thermo Scientific™ FLASH 2000 CHNS/O Analyzer of Thermo Fisher Scientific (Waltham, MA, USA).

2.4. Adsorption Kinetics

For adsorption kinetic studies we prepared 7 eppendorf tubes containing 2 mg of adsorbent (cAp and cAp-Tb) in 1 mL of phosphate buffered saline (PBS) solution containing DF at the maximum solubility (0.45 mg/mL). The PBS buffer (pH = 7.4) was prepared with the following composition: 137 mM NaCl (MW = 58,44), 2,7 mM KCl (MW = 74.55), 10 mM Na_2HPO_4 and 1.8 mM KH_2PO_4 (MW = 136.08). The tubes were left in the dark each one for a different time: 1 h, 2 h, 4 h, 8 h, 15 h, 24h and 48 h. At the end of the experiment, the solid was decanted by centrifugation at 10,000 rpm for 5 min. The absorbance of the residual solution was then measured with an UV-Vis (Agilent Technologies Cary Series UV-Vis, Agilent Technologies, Madrid, Spain) Spectrophotometer at λ = 280 nm [39] and the amount of DF adsorbed per unit mass of adsorbent as a function of time determined. The DF concentration C_{DF} was determined from the calibration straight line whose equation is the following:

$$Abs = 32.267 C_{DF} + 0.02 \tag{1}$$

2.5. Adsorption Isotherms

Experiments were carried out in several Eppendorf tubes containing 2 mg of adsorbent (cAp and cAp-Tb) in 1 mL of PBS solution with varying concentrations of DF (0.05, 0.1, 0.15, 0.20, 0.25, 0.30, 0.35, 0.40 and 0.45 mg/mL). The trials were carried out in triplicate under continuous stirring at 25 and 37 °C for 24 h (time higher than that necessary to reach the adsorption equilibrium according to adsorption kinetics). At the end, samples were centrifuged at 10,000 rpm for 5 min, and then filtered. The equilibrium concentration (C_{eq}, mg/mL) of DF in the supernatants were analysed by UV-Vis applying Equation (1). The adsorbed amount of DF per unit mass of adsorbent (Q_{ads}, mg/mg) was then calculated by difference between the initial (C_0) and equilibrium (C_{eq}) concentrations, divided by the mass (mg) of adsorbent, for a 1 mL total volume. The plot of Q_{ads} versus C_e is the adsorption isotherm.

2.6. Release Experiments

Release experiments at a function of time (1 h to 7 days) were performed at 25 and 37 °C under agitation using PBS (pH 7.4) and citrate/NaOH (pH = 5.2) buffers solutions. Each Eppendorf tube contained 2 mg of nanoparticles (DF-cAp and DF-cAp-Tb) with maximum adsorbed DF amount (Q_{max}) immersed in 1 mL buffer solution. At each programmed time, the suspensions were centrifuged at 10,000 rpm for 5 min, filtered, and

the C_{DF} in the supernatant analysed by UV-Vis. All assays were performed in triplicate and in the dark since the DF is photosensitive.

2.7. Luminescence Studies of cAp-Tb-DF Samples

Measurements were carried out at 25, 37, and 40 °C, at pHs 5.2 and 7.4 (adjusted with diluted HCl and NaOH), using a 0.5 mg/mL suspension of cAp-Tb sample. The nanoparticles were loaded in 0.0, 0.1, 0.3 and 0.4 mg/mL DF solution for 24 h, as in the adsorption experiments. The excitation and emission wavelengths used were $\lambda_{exc} = 350$ nm and $\lambda_{em} = 545$ nm. The instrumental parameters for the spectral characterization of the particles in aqueous suspensions were: $t_d = 120$ μs, $t_g = 5$ ms, slitswidth$_{exc/em} = 20/20$ nm and detector voltage 750 v. The instrumental parameters for the lifetime characterization were: $t_d = 120$ μs, $t_g = 0.01$ ms, slitswidth$_{exc/em} = 20/20$ nm and detector voltage 900 V.

2.8. Cells

The two human osteosarcoma cell lines MG-63 (CRL-1427) and U-2 OS (HTB-96TM), which were obtained from ATTC, were grown in Dulbecco modified Eagle's medium (DMEM) (Sigma-Aldrich, Milan, Italy) supplemented with 10% foetal bovine serum (FBS), antibiotic solution (streptomycin 100 μg/mL and penicillin 100 U/mL, Sigma-Aldrich) and 2 mM L-glutamine (complete medium) in a humidified atmosphere containing 5% CO_2 at 37 °C. Human primary osteoblasts (hOB) at passages from 2 to 7 obtained from explants of human trabecular bone fragments from knee joints taken at surgery (kindly provided by the Orthopedic Institute, Major Hospital Charity, Novara, Italy) were cultured in Iscove's modified Dulbecco's medium supplemented as above (complete Ob medium), as described previously [40]. Mesenchymal Stem Cells (MSCs) were obtained from the stromal vascular fraction of lipoaspirates, after enzymatic digestion with Collagenase NB4 (SERVA Electrophoresis, GmbH, Heidelberg, Germany) and elimination of blood cells, isolated and characterized as described by Roato [41]. MSCs were induced to osteogenesis by 2 week treatment with (complete Ob medium containing 50 mg/mL ascorbic acid (MW 176.12), 10 mM β-glicerophosphate (MW 216.04), and 10 nM dexamethasone (MW 392.5) (all from Sigma-Aldrich), which were changed every 3 days [42]. The osteogenic differentiation was evaluated by staining with an alkaline phosphatase detection kit (Millipore, Merk Millipore, Milano, Italy) according to the manufacturer's protocol (see Supplementary data). These cells were named differentiated hOB. All patients were free of systemic disease or treatment. The samples represent surgical discharge materials, and therefore their use does not need ethics committee approval. All patients were informed about the scientific use of the materials removed and gave their consent.

2.9. Cytocompatibility Tests

MG-63 and U-2OS cells (5000 cells/wells in 96-well plates) were seeded and 24 h after different concentrations (ranging from 0.1 to 100 μg/mL) of the differentially DF uploaded nanoparticles, either Tb-doped or undoped, were added in 100 μL of fresh medium. Hydrogen peroxide (1 μM) was used as control of toxicity. After 72 h incubation, cell viability was evaluated by the 3-(4,5-Dimethylthiazol-2-yl)-2,5-diphenyltetrazolium bromide) (MTT, Sigma) colorimetric assay, and the optical density was measured in a multiwell reader (2030 Multilabel Reader Victor TM X4, Perkin Elmer, Beaconsfield, UK) at 570 nm, as described [23]. In the case of hOB and differentiated hOB (15,000 cells/wells in 96-well plates) the assay was continued for 7 days, with careful medium changes every 3–4 days. Viability of parallel cultures of untreated cells was used as 100% viability, and values obtained from cells undergoing the different treatments were referred to this value. Experiments were performed 3 times using 3 replicates for each sample.

2.10. Inflammatory Cytokine Treatment

hOS, both induced and not, were seeded at a concentration of 15,000 cells/microwell and when 95% confluent (after about 3–4 days) recombinant human IL-1β, human TNF-α and human IFN-γ (ImmunoTools GmbH, Friesoythe, Germany) were added in complete culture medium at final concentrations of 1, 10, 100 ng/mL, respectively (cytokine mix), following a published protocol with some modifications [43]. The following day medium was changed with all cytokine concentrations reduced to 1:4 and after a further day the medium with the same cytokine concentration was changed and 50 µg/mL of UV-sterilized Tb-doped NPs functionalized with DF or not and comparable amounts of soluble DF were added. Medium was then changed on day 3, maintaining the same concentrations of cytokines and of the different NPs and controls. Some experiments lasted 1 or 5 days.

2.11. Quantitative Real-Time PCR (qPCR)

hOS (500,000/6 cm diameter plate) were seeded and when confluent they were treated for induction of inflammation by the addition of the cytokines mixture. After 24 h cAp-Tb uploaded with DF or not were added at a concentration of 50 µg/mL. In this case, 16 h later, total cell RNAs were extracted with Trizol (Invitrogen Life Technologies, Monza, Italy). After RNA purification and treatment with DNAse I (Fermentas, St. Leon-Rot, Germany), 1 µg was retrotranscribed in cDNA with the RevertAid™ H Minus First Strand cDNA Synthesis Kit (Fermentas) using oligo(dT) primers. Gene assays were performed in triplicate for each treatment in a 20 µL reaction volume containing 1 µL of RT products, 10 µL Sso-Fast EVA Green SMX (Bio-Rad, Hercules, CA, USA), 500 nM each forward and reverse primers (COX-2, Fw: TATCACAGGCTTCCATTGACC; Rev: TTTCTACCAGAAGGGCAGGAT) [44]. Gene expression was normalized on the housekeeping gene ribosomal 18S rRNA (Fw: 5′-GTGGAGCGATTTGTCTGGTT-3′; Rev: 5′-ACGCTGAGCCAGTCAGTGTA-3′). Automated CFX96 real-time thermocycler (Bio-Rad) was used and the reaction conditions were 95 °C for 1 min, followed by 45 cycles at 98 °C for 5 s and anneal/extend step for 5 s at 60 °C, with data collection. At the end of these cycles, a melting curve (65 °C to 95 °C, with plate read every 0.5 °C) was performed to assess the specificity of the amplification product by single peak melting temperature verification. Results were analysed with Bio-Rad CFX Manager. Calculations and statistical analyses were performed using GraphPad Prism version 5.00 for Windows (GraphPad Software, San Diego, CA, USA).

2.12. PGE2 Production

PGE2 produced by cells and released in the culture medium was evaluated in an ELISA Kit (Cayman kit, Vinci-Biochem, Vinci, Italy), according to the manufacturer's protocol. This is a competitive-binding assay, which was performed on 1/5 diluted samples in triplicates and was repeated twice. Optical absorbance was read at 405 nm.

2.13. Statistical Analysis

Data were statistically analysed and are expressed as mean ± standard deviation. Statistical analyses were performed using a one-way ANOVA with Bonferroni's post test for grouped analyses using GraphPad Prism version 5.04 for Windows, GraphPad Software (GraphPad Prism, San Diego, CA, USA). Differences at $p < 0.05$ were considered to be statistically significant.

3. Results

3.1. Characterization of the NPs

Precipitation experiments yielded cAp and cAp-Tb NPs with needle-like morphologies, elongated along the *c*-axis, of 40 ± 10 nm and 30 ± 8 nm, respectively (Figure 1). XRD patterns (see Supplementary Material, Figure S1) show the diffraction peaks at 2θ = 25.87° (002), 31.77°, 32.19° and 32.90° (planes (211), (112) and (300)), respectively, at 33.9°

(202) and 39.81° (310)) and minor reflections within the range 38°–55°, characteristics of the apatite phase (PDF 01-1008) [29].
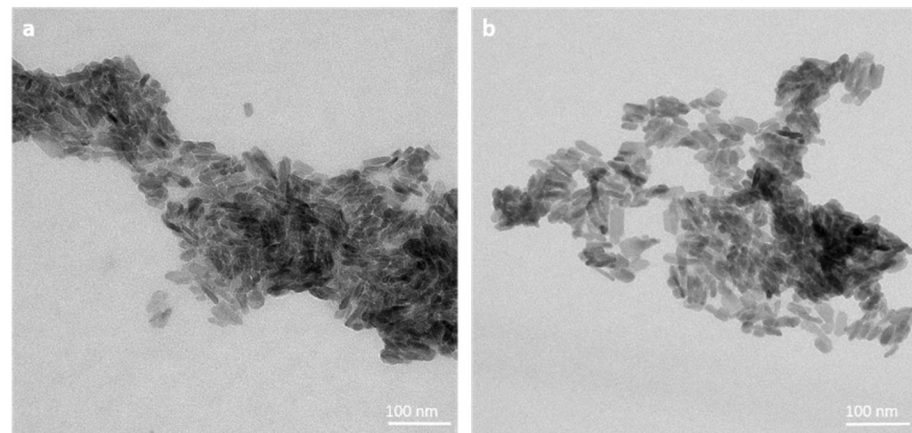

Figure 1. TEM micrographs of cAp (a) and cAp-Tb NPs (b) prepared by thermal decomplexing method [27,29].

FTIR spectra (Figure S2a) display the main band at 1000–1100 cm⁻¹ (asymmetric stretching $\upsilon_3 PO_4$), the shoulder at ~965 cm⁻¹ (symmetric stretching $\upsilon_1 PO_4$), and the less intense bands at ~608 and 568 cm⁻¹ (bending mode $\upsilon_4\ PO_4$). The presence of carbonate (CO_3^{2-}) is attested by the small band at 873 cm⁻¹ ($\upsilon_2\ CO_3$) and $\upsilon_3 CO_3$ mode, with bands ~1417 cm⁻¹ and 1468 cm⁻¹. The band at ~1590 cm⁻¹ observed in both samples, is ascribed to the antisymmetric stretching frequencies of the carboxylate groups of the citrate, indicating the citrate molecules are adsorbed on the apatite surface, as previously reported [27]. On the other hand, the complementary characterization by Raman (Figure S2b) reveals the main band at 960 cm⁻¹ which corresponds to the antisymmetric vibration mode of phosphate groups ($\upsilon_1 PO_4$) of the apatite phase [45]. The elemental composition of the new cAp-Tb sample revealed by ICP-MS and thermoanalysis yields 30.78 wt% Ca, 14.44 wt% P, 0.69 wt% Tb, 2.23 wt% C, and 0.53 wt% H.

The measurements of DLS of the dispersed nanoparticles in aqueous media are shown in Figure S3, which displays the plots as a) PSD in volume and b) cumulative volume oversize distribution. The last one shows D_{10} percentiles for cAp and cAp-Tb of 55 and 75 nm, respectively, which are close to the individual particle size observed by TEM. The D_{50} percentiles (75 and 276 nm) are affected by aggregation, especially in the cAp-Tb sample. The D_{90} are highly affected by aggregation.

3.2. Adsorption Isotherms

The evolution of the adsorbed amount of DF per unit mass of adsorbent (Q_{ads}) with the time on both substrates (Figure S4) draws different profiles but reveals that adsorption equilibrium is reached after about 15 h. Thus, the adsorption experiments for the elaboration of the isotherms were performed at 24 h, to assure that all points were determined after reaching the equilibrium.

Figure 2 shows the adsorption isotherms (Q_{ads} vs. C_{eq}) of DF on cAp at 25 °C (a) and 37 °C (c), and on cAp-Tb at 25 °C (e) and 37 °C (g). Adsorption data were fitted to different adsorption models: Langmuir [44-48], Freundlich [49] and Langmuir-Freundlich [30,50,51]. The Langmuir model considers a monolayer of adsorbate and the surface of the adsorbent energetically homogeneous. The linearized equation is described as:

$$1/Q\_eq = 1/Q\_max + 1/(Q\_max\ K\_L\ C\_eq) \tag{2}$$

being Q_max the maximum adsorbed amount per unit mass of adsorbent (mg/mg) and K_L the Langmuir affinity constant (L/mg). The Freundlich model considers an

energetically heterogeneous surface and multilayer adsorption. The linearized equation is:

$$\log Q\_eq = \log K\_F + 1/n \ \log C\_eq \tag{3}$$

where the Freundlich constant K_F and $1/n$ are related to the adsorption capacity of the substrate and the intensity of the adsorption, respectively. The third model, Langmuir-Freundlich, is more versatile, and simulate both behaviours. The linearized equation is the following:
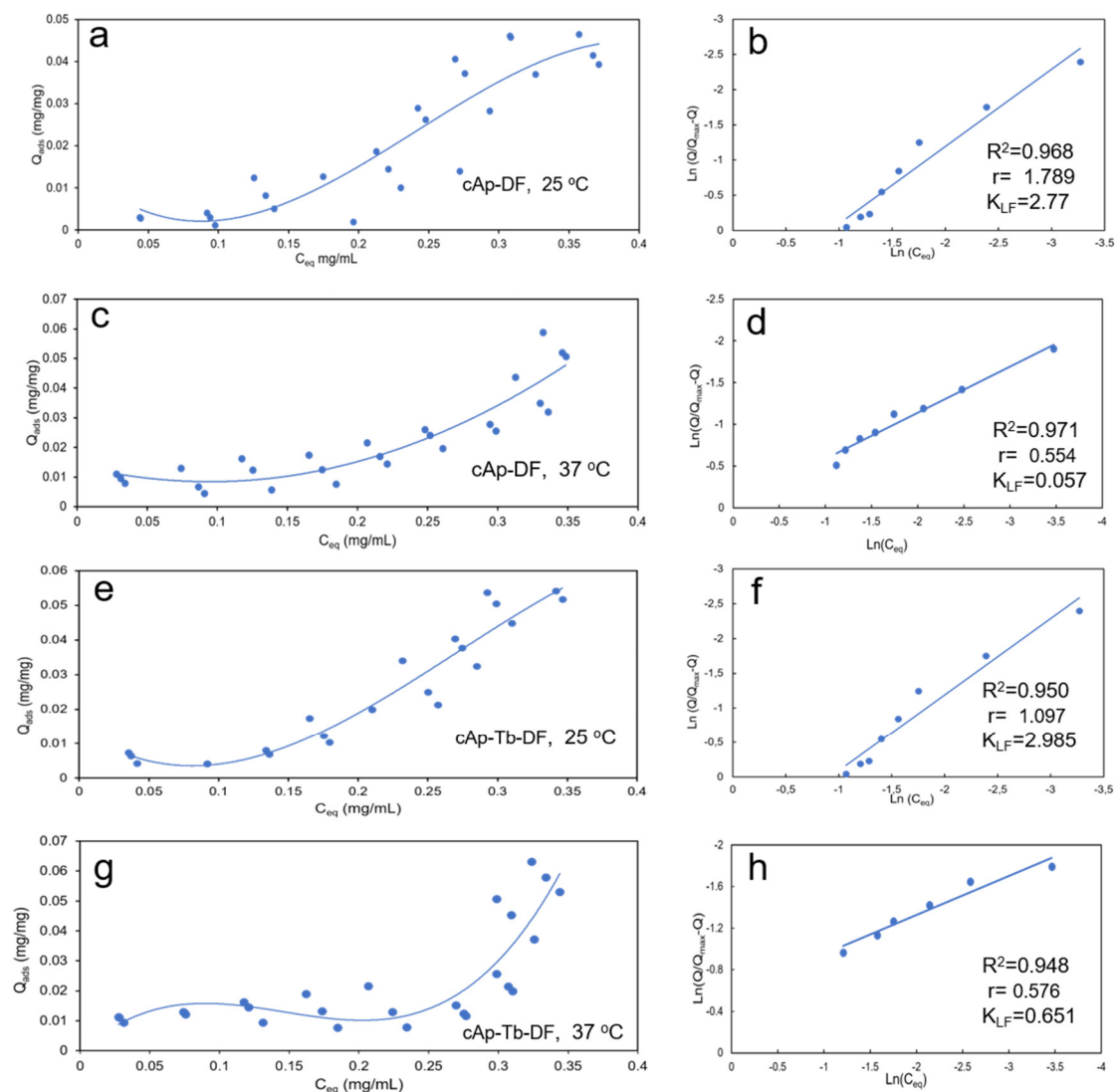
$$\ln(Q/(Q\_(max) - Q)) = r\ln K\_LF + r\ln C\_eq \tag{4}$$

Figure 2. Adsorption isotherms of DF in (**a**) cAp at 25 °C, (**c**) cAp at 37 °C, (**e**) cAp-Tb at 25 °C, and (**g**) cAp-Tb at 37 °C. Fitting of adsorption data to the Langmuir-Freundlich model (**b**) cAp at 25 °C, (**d**) cAp at 37 °C, (**f**) cAp-Tb at 25 °C, and (**h**) cAp-Tb at 37 °C.

In equation 4 K_{LF} is the Langmuir-Freundlich constant and r the cooperativity coeficient, with $r > 1$ indicating a positive cooperativity or $r < 1$ negative cooperativity [50].

Only the Langmuir-Freundlich model fitted reasonably the adsorption data (Figures 2b,d,f,h), with regression coefficients (R^2) higher than 0.97 and 0.95 for cAp and cAp-Tb experiments, respectively, whereas the other two models yielded $R^2 < 0.7$. This indicates

that DF adsorbs in multilayers with a limited number of layers. The K_{LF}, r and Q_{max} values obtained by this model are shown in Table 1.

Table 1. Regression coefficients and parameters K_{LF}, r and Q_{max} determined from Langmuir-Freundlich model.

Substrate, *T* (°C)	R²	K_{LF}	*r*	Q_{max} (mg/mg)	Adsorption Type
cAp, 25 °C	0.9679	2.77	1.794	0.04648	Cooperative, high affinity
cAp, 37 °C	0.9709	0.05	0.5536	0.05067	Non-cooperative, low affinity
cAp-Tb, 25 °C	0.9503	2.98	1.0973	0.05411	Cooperative, high affinity
cAp-Tb, 37 °C	0.9482	0.65	0.3751	0.06306	Non-cooperative, low affinity

We can appreciate that at 25 °C the K_{LF} values for cAp and cAp-Tb are higher than at 37 °C, revealing the higher affinity of DF molecules for the adsorbent at this temperature. In addition, the *r* values at 25 °C are higher than 1, while at 37 °C are lower, indicating the process is cooperative at 25 °C and non-cooperative at 37 °C. However, Q_{max} is always higher in the cAp-Tb substrate irrespective of the temperature.

3.3. ζ-Potential versus pH of Unloaded and DF-Loaded cAp and cAp-Tb NPs Suspensions

The measurements of ζ-potential of both type of unloaded NPs (blue lines in Figure 3) reveal a decrease to more negative values with increasing the pH, especially for the sample cAp-Tb, with values of −19 mV (pH 7) and of −16 mV (pH 5). This indicates that NPs tend to be dispersed in aqueous media at physiological and acidic pHs, which is a desirable feature in view of their applications in nanomedicine.
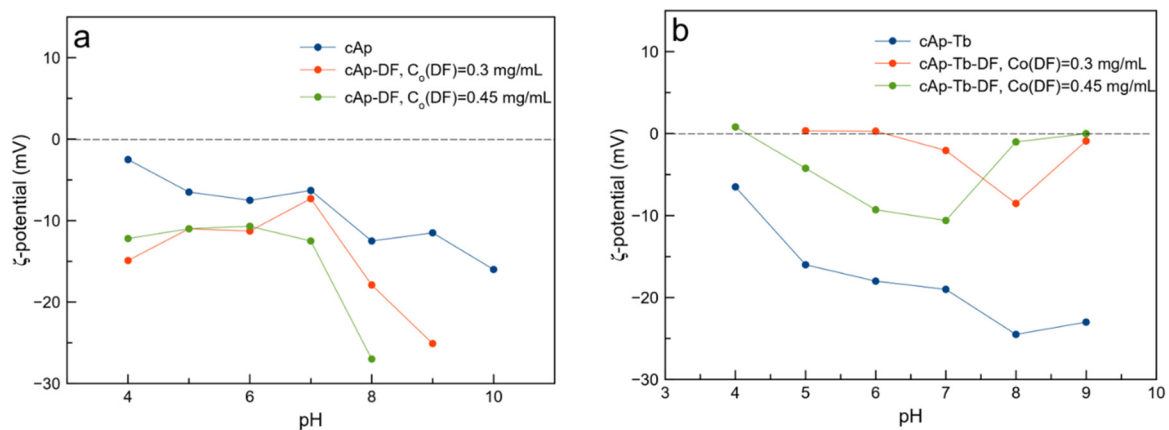
Figure 3. Plots ζ-potential versus pH: (**a**) cAp (blue), cAp-DF loaded in solutions of DF 0.3 mg/mL (red) (Q_{ads} = 0.02304 mg/mg) and cAp-DF loaded in solutions of DF 0.45 mg/mL (green) (Q_{ads} =0.04246 mg/mg). (**b**) cAp-Tb (blue), cAp-Tb-DF loaded in solutions of DF 0.3 mg/mL (red) (Q_{ads} =0.02680 mg/mg) and cAp-Tb-DF loaded in solutions of DF 0.45 mg/mL (green) (Q_{ads} =0.04435 mg/mg).

However, when loading the nanoparticles with DF in solutions of concentrations 0.3 and 0.45 mg/mL, we found a different behaviour depending on the type of adsorbent. Thus, when loading cAp, the ζ-potential of cAp-DF nanoassemblies decreases (more negative), especially when their payload is higher. The behaviour is the opposite when loading cAp-Tb nanoparticles, being the ζ-potential of the cAp-Tb-DF nanoassemblies higher (less negative), especially when they were loaded in the solution with the lower DF concentration at pH ≤ 7. This finding reveals a higher tendency of the cAp-Tb-DF nanoassemblies to aggregate. Nevertheless, for the cAp-Tb-DF sample (C_o = 0.45mg/mL

DF, Q_{ads} = 0.04435 mg/mg), the ζ-potentials are still negative being -4.2 mV at pHs 5 and -10.6 mV at pH 7.

3.4. Release Profiles and Release Efficiency

Figure 4 shows the DF release profiles (C_{des} vs. time) at pH 7.4 (a,b) and 5.2 (c,d) by comparing the effect of the temperature (25 and 37 °C) for both types of nanoparticles. It is observed that at pH 7.4 the released DF mass per mL of buffer solution at 37 °C is slightly higher than at 25 °C, and always higher for cAp than from cAp-Tb. At pH 5.2 the released amount from cAp-DF at 37 °C even increases within the time interval of the experiment (Figure 4c). It is worth mentioning the peculiar release profile of the cAp-Tb substrate at 37 °C, which shows a burst during the first 10 h, and then stabilizing with time.
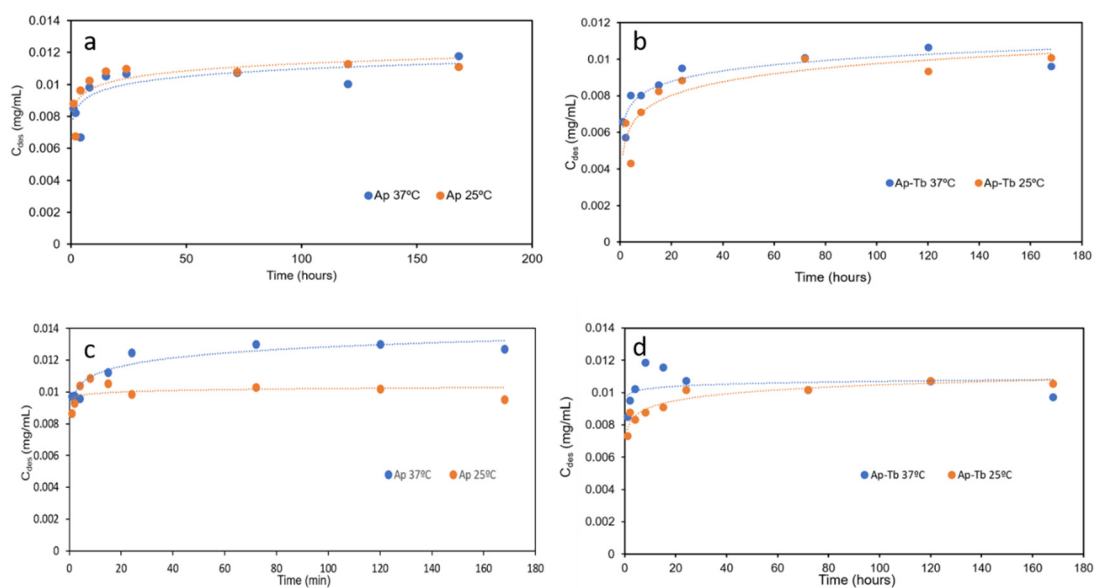
Figure 4. Release profiles of DF from (**a**) cAp-DF at 25 and 37 °C, pH 7.4; (**b**) cAp-Tb-DF at 25 and 37 °C, pH 7.4; (**c**) cAp-DF at 25 and 37 °C, pH 5.2, and (**d**) cAp-Tb-DF at 25 and 37 °C, pH 5.2.

When comparing the effect of pH (7.4 and 5.2) on the release of DF a higher release was observed at pH 5.2 (citrate buffer) than at pH 7.4 (PBS buffer), at both temperatures, with the only exception for cAp at 25 °C after the first 10 h of the experiment, when the delivery trend versus pH is the opposite (Figure 5a–d). This pH-responsive drug release behaviour is very useful concerning DF delivery in pathological environments.

The release efficiency Dr [30,50] defined as the percentage of drug released at a given time (t) respect to maximum amount of drug adsorbed (Equation (5)),

$$Dr\ (\%wt) = Q_{(t)}/Q_{(max)}\ \times 100 \qquad (5)$$

revealed that considering the larger times of the experiment, Dr and $Q_{D,max}$ for cAp-DF are in general larger than for cAp-Tb-DF at both pHs (see Table 2). This trend is just the opposite to that found in the adsorption experiments, in which the maximum adsorption corresponded to cAp-Tb.
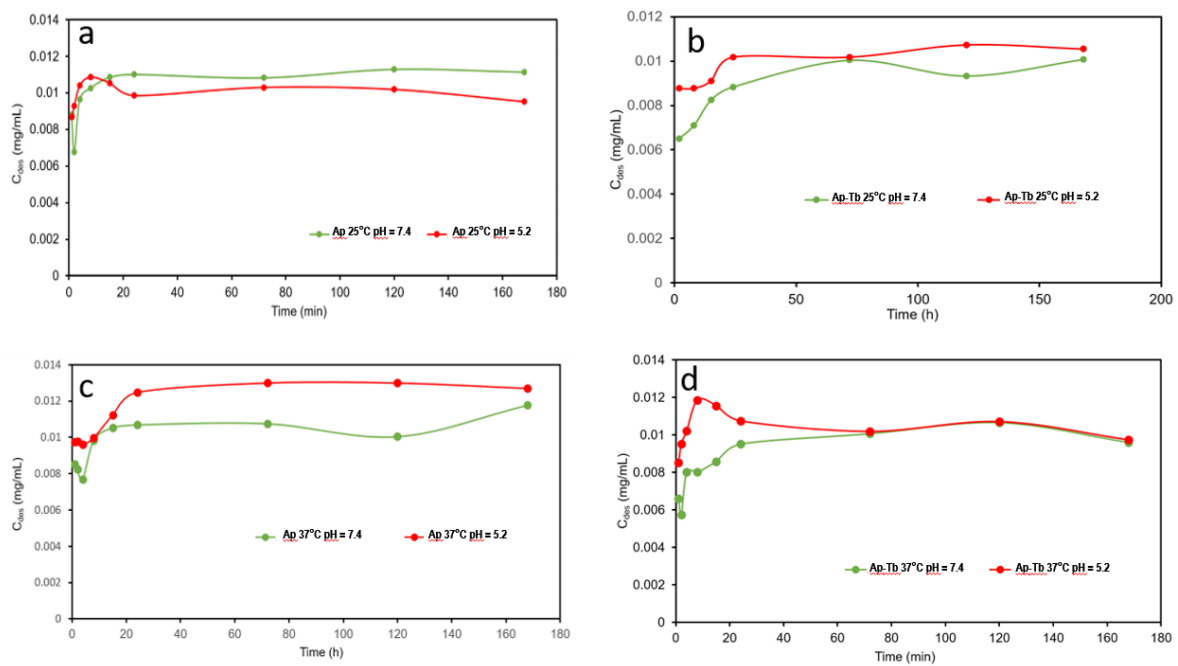
Figure 5. Release kinetics of DF from cAp-DF at 25 °C (**a**) and 37 °C (**c**) and from cAp-Tb-DF at 25 °C (**b**) and at 37 °C (**d**) at pH 7.4 (green line) and 5.2 (red line).

Table 2. Maximum released amount of DF per unit mass of adsorbent ($Q_{D,max}$, mg/mg) and *Dr* at pHs 7.4 and 5.2 for cAp-DF and cAp-Tb-DF nanoassemblies.

Parameter	cAp-DF, 25 °C, pH = 7.4	cAp-DF, 37 °C, pH = 7.4	cAp-Tb-DF, 25 °C, pH = 7.4	cAp-Tb-DF, 37 °C, pH = 7.4	cAp-DF, 25 °C, pH = 5.2	cAp-DF, 37 °C, pH = 5.2	cAp-Tb-DF, 25 °C, pH = 5.2	cAp-Tb DF, 37 °C, pH = 5.2
Q_{Dmax} (mg/mg)	0.01128	0.01177	0.01007	0.01066	0.01048	0.01300	0.01073	0.01185
Dr (%wt)	24.26	23.24	18.55	16.90	23.33	25.66	19.84	18.79

3.5. Luminescence Properties of Unloaded and DF-Loaded cAp and cAp-Tb NPs Suspensions

It is well-known that Tb^{3+}- luminescent chelates shows narrow-banded, line-type fluorescence with long Stokes shifts and high luminescence decay times [52]. This luminescent emission can be used for sensitized fluorescence detection of chelates [53], the development of FRET analytical methods [54], as well as for the incorporation of luminescent properties to materials in order to develop new imaging applications [29,34]. In this work, Tb^{3+} was incorporated to provide the nanocarrier with a luminescence signal which can be measured to determine where the particles are located.

Figure 6 shows the excitation and emission spectra of NPs dispersed in aqueous media at pH 5.2 at 37 °C which are similar to those obtained for 25 and 40 °C as well as for pH 7.4 at these three temperatures (see Supplementary Material Figures S5–S9).
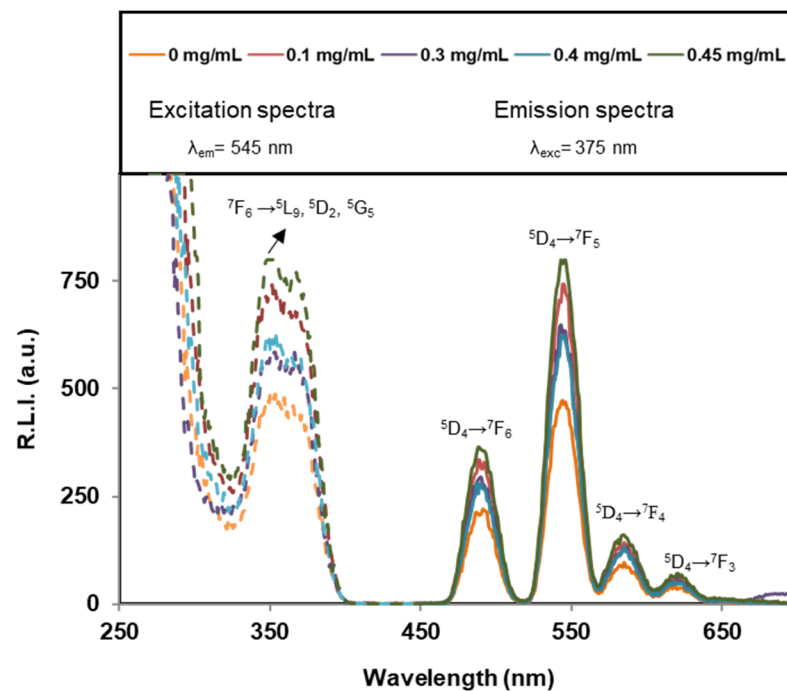
Figure 6. Excitation (dashed lines) and emission (solid lines) uncorrected spectra of cAp-Tb-DF samples containing different DF adsorbed amounts, dispersed in a pH 5.2 aqueous suspension at 0.5 mg/mL and 37 °C. The instrumental conditions were t_d = 120 μs, t_g = 5 ms, slitwidth$_{exc/em}$ = 20 nm / 20 nm and detector voltage 750 V.

Concerning the excitation wavelength (λ_{exc}), these particles can be excited at the Charge Tranfer Band, CTB [55], (centred at 230 nm approximately) obtaining the same emission spectra as that obtained by exciting at 350 nm [34]. In order to increase the biological applicability of the system, 350 nm (corresponding to the Tb^{3+} $^7F_6 \rightarrow ^5L_9, ^5D_2, ^5G_5$ transition [56] was selected as excitation wavelength.

Concerning the emission wavelengths (λ_{em}), they are centred at 491, 545, 586 and 623 nm, corresponding to the Tb^{3+} $^5D_4 \rightarrow ^7F_6$, $^5D_4 \rightarrow ^7F_5$, $^5D_4 \rightarrow ^7F_4$ and $^5D_4 \rightarrow ^7F_3$ transitions, respectively [57]. The emission wavelength which produces the highest relative luminescence intensity (R.L.I.) corresponds to the hypersensitive transition without inversion centre ($^5D_4 \rightarrow ^7F_5$, 545 nm for Tb^{3+}) Therefore, the optimum λ_{exc} and λ_{em} of solid particles were 350 and 545 nm, respectively.

Figure 7 shows the effect of DF concentration. It is possible to conclude that the adsorption of DF on the particles does not affect significantly the Tb^{3+} luminescence emission. Therefore, this signal cannot be used to determine if DF is released or not.
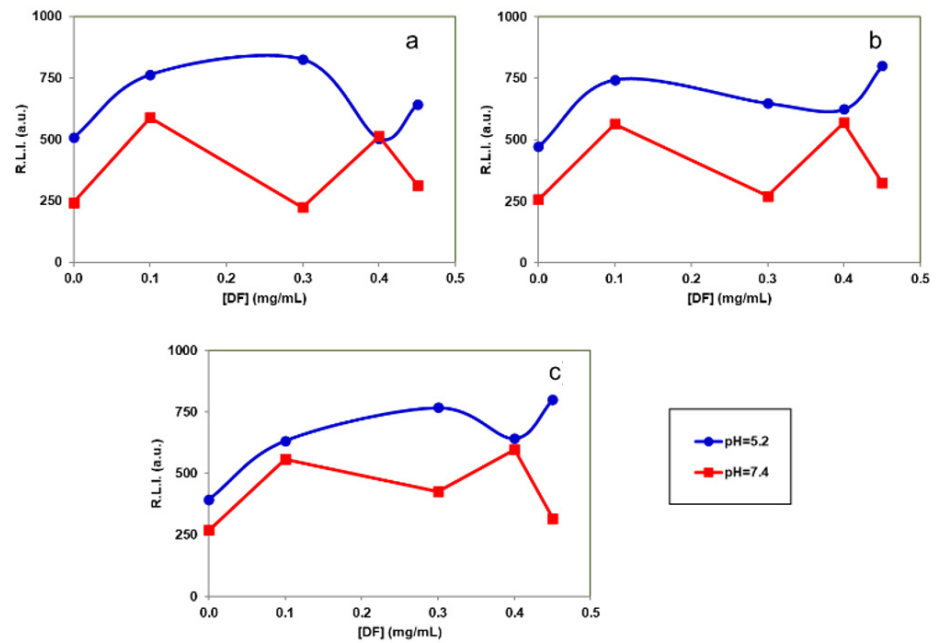
Figure 7. Effect of the DF concentration on the R.L.I. of the particles suspended in aqueous suspension at different pHs and temperatures: (**a**) T = 25 °C, (**b**) T = 37 °C and (**c**) T = 40 °C. Excitation (dashed lines) and emission (solid lines) uncorrected spectra of samples containing different DF concentrations dispersed in a pH 5.2 aqueous suspension at 0.5 mg/mL and 37 °C. The instrumental conditions were $\lambda_{exc/em}$ = 350/545 nm, t_d = 120 µs, t_g = 5 ms, slitwidth$_{exc/em}$ = 20/20 nm and detector voltage 750 V.

Figure 8 shows the effect of pH and temperature. We can observe that, at all tested DF concentrations, the signals at pH 5.2 are higher than those obtained at pH 7.4. Thus, the luminescence emission of these particles could be used to determine pH changes, which are related to inflammatory processes. In addition, it is possible to conclude that the luminescence signal is not affected between 25 and 40 °C demonstrating that it can be used for biological applications, since the luminescence is not affected by local increases of temperature due to inflammatory processes.
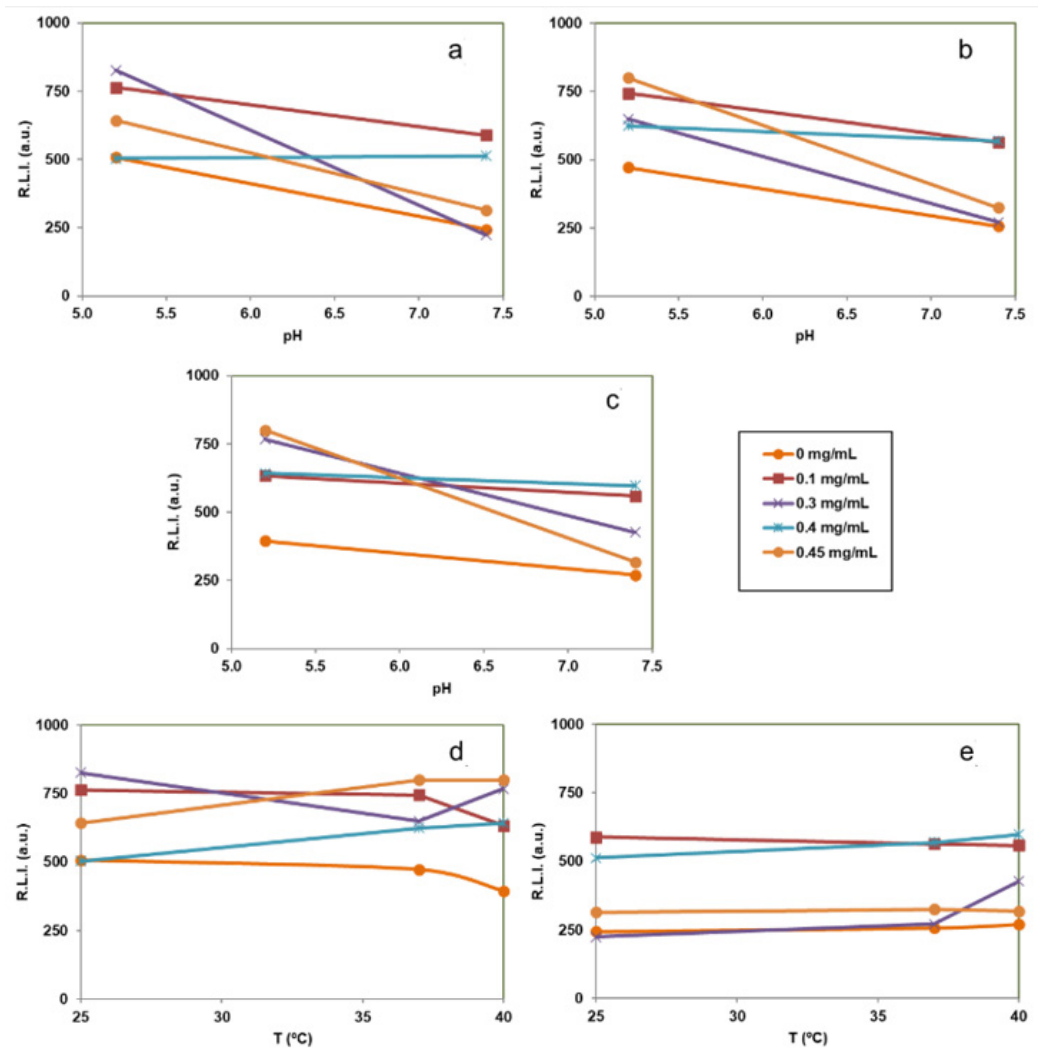
Figure 8. Effect of the pH and the temperature on the R.L.I. of the cAp-Tb-DF with different amounts of DF adsorbed suspended in aqueous media at different pHs and temperatures [(**a**) 25 °C, (**b**) 37 °C and (**c**) 40 °C, (**d**) pH 5.2 and (**e**) pH 7.4]. In all measurements the concentration of the suspended particles was 0.5 mg/mL and the instrumental conditions were $\lambda_{exc/em}$ = 350/545 nm, t$_d$ = 120 μs, t$_g$ = 5 ms, slitwidth$_{exc/em}$ = 20/20 nm and detector voltage 750 V.

Figures S10–S15 in Supplementary Materials show the luminescence decay curves. For each case, the decay profile was analysed as a single exponential component (Equation 6)

$$R.L.I. = e^{\left(-\frac{t}{\tau}\right)} + C \tag{6}$$

Figure 9 shows the variation of the luminescence lifetime (τ) versus DF concentration, pH and temperature. It is shown that only pH is affecting the lifetime; larger lifetimes are obtained at pH 7.4 than at pH 5.2 while different DF concentrations and temperatures do not affect the luminescence lifetimes.
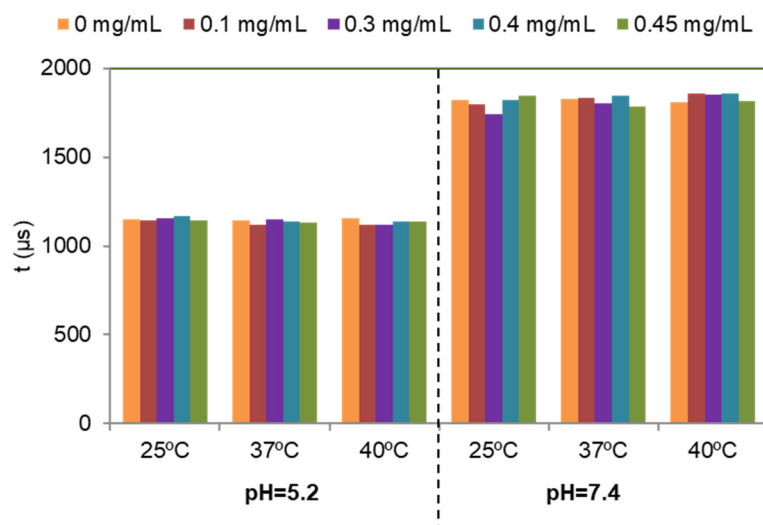
Figure 9. Effect of DF concentration, pH and temperature on the luminescence lifetime of the particles suspended in aqueous suspension. In all the cases the concentration of the suspended particles was 0.5 mg/mL and the instrumental conditions were $\lambda_{exc/em}$ = 350/545 nm, t_d = 120 μs, t_g = 0.01 ms, slitwidth$_{exc/em}$ = 20/20 nm and detector voltage 900 V.

3.6. Cytocompatibility of the Different Nanoparticles

The cytocompatibility of cAp NPs, doped with Tb or not, and uploaded with different concentrations of DF was first assessed on two human osteosarcoma cell lines (MG-63 and U2OS) in MTT assays performed after 3 days of incubation with NPs (Figures 10 and S16). No significant toxicity was observed in any condition; only when cells were incubated with the highest NPs concentration of 100 μg/mL cell viability was decreased, but it was always higher than 80%, which are values above the cut off of 70% indicated by ISO 10993-5:2009 [58]. cAp NPs cytocompatibility was tested also on primary human osteoblasts (hOB) and on differentiated hOBs, which stained positive for alkaline phosphatase (Figure S17), a typical marker of bone differentiation. In view of the fact that experiments of inflammation would last longer than 3 days, and that 100 μg/mL reduced somehow the viability of the osteosarcoma cell lines, MTT assays were carried out also after 1 week of incubation with NPs and lower doses of NPs, ranging from 50 to 0.5 μg/mL were assessed. Similar data were obtained at the two end-points evidencing no significant reduction in cell viability and results were in line with those obtained with the two osteosarcoma cell lines. In particular Figure 11 shows the results obtained with Tb-doped NPs. All the cells were sensitive to the addition of 1 μM hydrogen peroxide, since their viability was reduced to about 30–50%. Thus, these data show the good cytocompatibility of the different nanoparticles that will be used in this study.
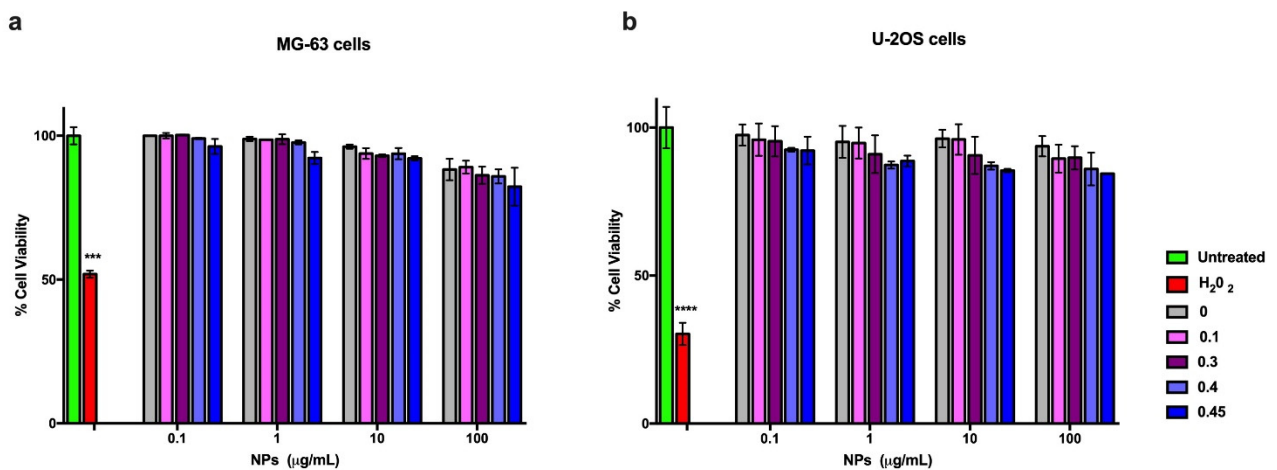
Figure 10. Viability of MG-63 cells (**a**) and of U-2OS cells (**b**) incubated with cAp-DF particles loaded with different DF concentration, ranging from 0.1 to 0.45 mg/mg NP, for three days. Viability was assessed in MTT assays. Data represent means ± sd of three independent experiments performed in triplicate and statistical analyses were carried on using One-way ANOVA, with Bonferroni comparison test. For statistical analysis all data were compared to untreated samples and only samples treated with 1μM H_2O_2 displayed statistically significant difference (*** $p < 0.001$, **** $p < 0.0005$).
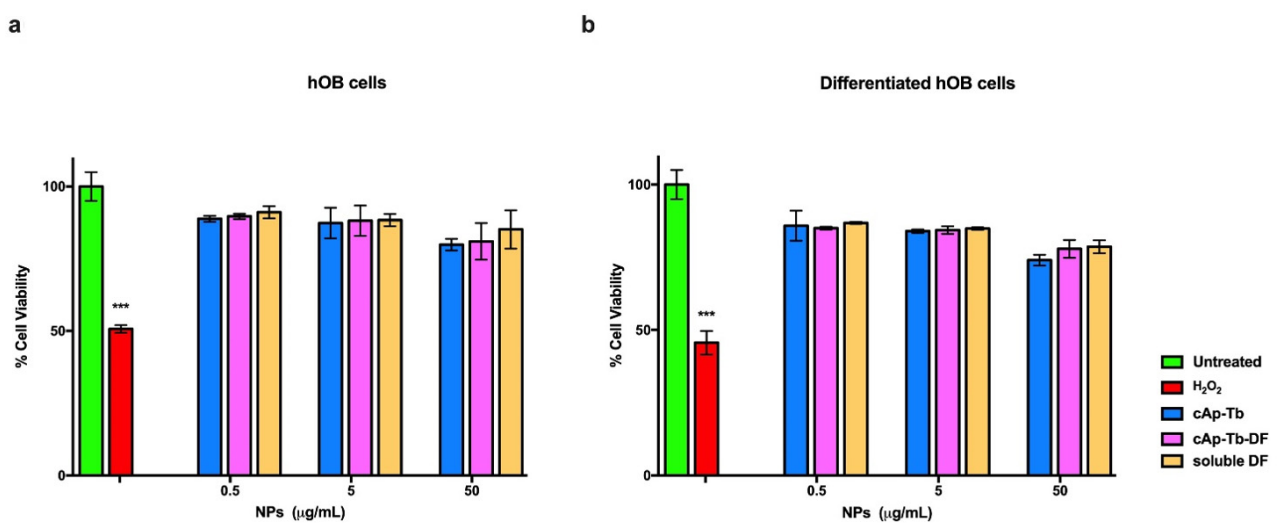
Figure 11. Viability of human primary osteoblasts hOB (**a**) and of hOB differentiated from mesenchymal stem cells (**b**) incubated with different concentrations of cAp-Tb particles loaded with DF (50 μg/mL) and unloaded, and comparable soluble DF amounts for seven days. Viability was assessed in MTT assays. Data represent means ± sd of three independent experiments performed in triplicate and statistical analyses were carried on using One-way ANOVA, with Bonferroni comparison test. For statistical analysis all data were compared to untreated samples and only samples treated with 1μM H_2O_2 displayed statistically significant difference (*** $p < 0.001$).

3.7. Effect of DF-Loaded Nanoparticles on the Osteoblasts Treated for Inflammation: COX-2 Expression

To assess the expression of COX-2 mRNA we performed semiquantitative RT-PCR. Differentiated hOB cells showed a low basal expression of the enzyme that was significantly increased after the stimulation with inflammation cytokines for 16 h, as determined by the calculation of relative expression ($2^{-\Delta\Delta Ct}$; Figure 12). The exposure to cAp-Tb induced a slightly significant increase of COX-2 expression, indicating a minimal interference of these NP on cell metabolism. On the other hand, the challenge of hOB cells with soluble DF, a potent competitive antagonist of COX-2, did not alter the induction of COX-

2 expression evoked by inflammatory stimuli. This observation was also confirmed in the cells treated with cAP-Tb-DF 50 μg/mL. Soluble DF 2.5 μg/mL concentration was chosen to pair the amount released from cAP-Tb-DF at 50 μg/mL, as described above. These data were related to prostaglandin-E_2 release in order to show any possible interaction on COX-2 mRNA expression levels.
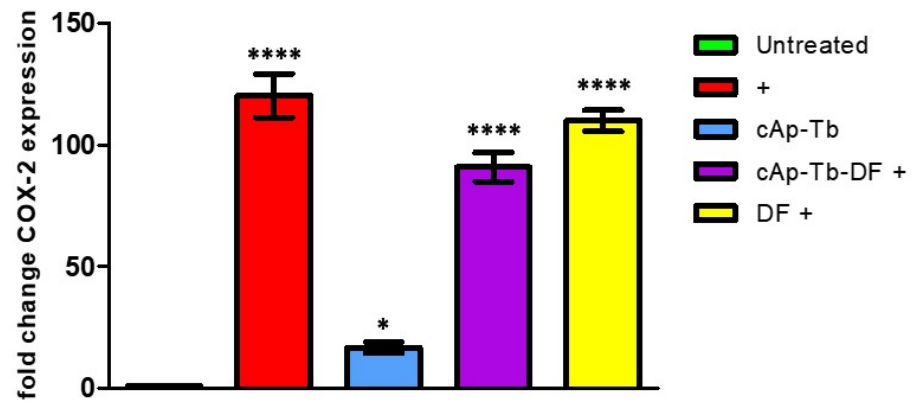
Figure 12. Effect of inflammation stimuli, cAP-Tb and soluble DF or cAp-Tb-DF, on COX-2 mRNA levels were assayed on hOB differentiated from mesenchymal stem cells. Cells were incubated for 24 h in presence or absence of the inflammatory stimuli. Data were calculated by comparing the fold increase vs. the untreated control and significance is shown on the figure. Bonferroni comparison post-test analysis of each treatment was calculated vs. the inflammation stimuli effects (marked as +). Data indicated that DF and cAp-Tb-DF did not significantly modify the expression pattern induced by inflammation. Data represent means ± SD of four independent experiments (* $p < 0.01$, **** $p < 0.0005$).

3.8. DF-Loaded Nanoparticles Inhibit the Release of PGE₂ from Osteoblasts Treated for Inflammation

The concentration of PGE_2 in the culture medium was measured on days 1 and 5 using a PGE metabolite assay kit, which converts all major PGE_2 metabolites in a single stable derivative, thus making more reliable the evaluation of PGE_2 production. The amount of 50 μg/mL NPs was chosen for these experiments, since 100 μg/mL decreased cell viability, although not significantly. This amount was the best compromise for loading a significant amount of DF, and in the meantime it was fully cytocompatible. PGE_2 was constitutively released from hOB induced from mesenchymal stem cells at a measurable level (Figure 13: 50 ± 10 pg/mL), which was increased 9 fold (450 ± 64 pg/mL) 1 day after the inflammation treatment. The addition of cAp-Tb-DF to osteoblasts treated for inflammantion reduced the amount of the released PGE_2 to about 4% (25 ± 5 pg/mL) of the amount released upon the inflammatory treatment, at levels even below the amount of the basally produced PGE_2. cAp-Tb NPs did not show a significant inhibitory effect (435 ± 35 pg/mL), while soluble DF at comparable concentrations reduced PGE_2 release at about the same levels observed for DF loaded on NPs (16 ± 4 pg/mL). Thus, DF treatment reduced of >95% the amount of PGE_2 released 1 day after the inflammatory treatment.

When the levels of the released PGE_2 were measured after 5 day treatments, similar results were observed, although all the values were increased. In this case the amount of constitutively released PGE_2 was 135 ± 15 pg/mL, which was increased about 5 times by the inflammatory treatment (680 ± 35 pg/mL), reaching even higher levels than those observed after 1 day. Coincubation with cAp-Tb-DF, as well as with soluble DF, resulted in a significant inhibition of cytokine-induced PGE_2 production (110 ± 12 and 87 ± 25, respectively), with a reduction around 85%.
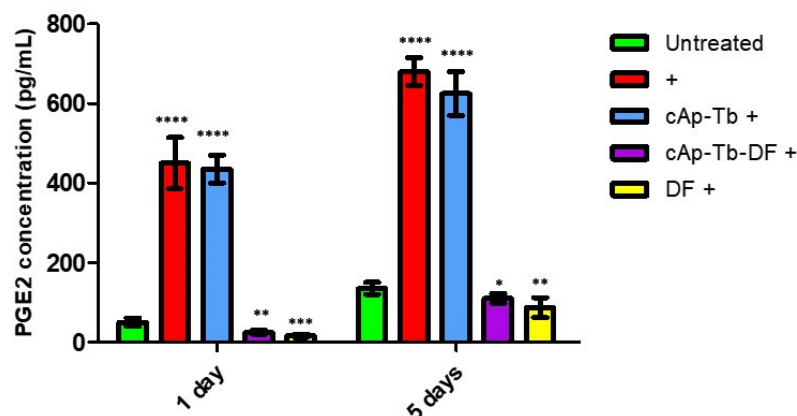
Figure 13. Effect of cAp-Tb-DF NPs on PGE2 released from differentiated hOBs treated with inflammatory cytokine mixture (IL-1β, TNF-α, IFN-γ; +). After 2 days, the different cAp (50 µg/mL) or DF (at comparable amount) were added and cells were incubated for further 1 day or 5 days. (see MM section for details). Data represent means ± sd of three independent experiments performed in triplicate and statistical analyses were carried on using One-way ANOVA, with Bonferroni comparison test. For statistical analysis all data were compared to control untreated samples and the effect of DF was determined vs. the inflammatory treatment. Statistical significance (* $p < 0.01$, ** $p < 0.005$, *** $p < 0.001$, **** $p < 0.0005$).

4. Discussion

cAp NPs are efficient tools for delivering biologically active molecules that might find applications in theranostics, especially in the field of oncology [59,60]. Herein we have prepared cAp and cAp-Tb nanoparticles and investigated their loading/release ability of DF, a potent non-steroidal antiinflammatory drug, using both nanocarriers in different conditions, and we have analyzed their cytocompatibility as well as their biological activities in an in vitro human osteoblast inflammation model. Indeed, today bone tissue pathologies, such as osteoporosis, osteoarthritis, rheumatoid arthritis represent important health problems with considerable socio-economic burden, linked to the general population aging [8,9] and are all characterized by a clinical condition of inflammation.

As a result of the study, we have determined that cAp and cAp-Tb NPs -DF adsorption isotherms follow the Langmuir-Freundlich model at the two temperatures analysed of 25 °C and 37 °C. Our data indicates that the adsorption is heterogeneous and takes place in multilayers, with a finite thickness. The K_{LF} constants at 25 °C are higher than at 37 °C, for both NPs, thus showing a higher affinity of the DF molecules for the adsorbent at room temperature. Moreover, at 25 °C the adsorption is cooperative ($r > 1$) indicating that the binding of one molecule facilitates the adsorption of the next one, and that two or more molecules can even be adsorbed together. On the contrary, at 37 °C the adsorption is non-cooperative, indicating that the adsorption of one molecule is not facilitated by the adsorption of the previous one. The maximum adsorbed amounts Q_{max}, however, are greater at 37 °C, although they do not exceed the 0.063 mg/mg adsorbed on cAp-Tb for an initial DF concentration in the solution of 0.45 mg/mL. The influence of the temperature on the adsorption processes, in general, is well documented [51]. Adsorption is an exothermic phenomenon, and thus an increase in temperature leads to a decrease in the adsorption capacity, which results in a lower K_{LF}, but, at the same time, it favours the solvate-solvate interaction so that the outermost layers attract a greater number of molecules.

Adsorption is influenced also by the pH, especially when the adsorbents are ionic salts, since it determines their surface speciation, i.e., the concentration of cationic, anionic and neutral surface species (in apatite the species $> Ca^{\delta+}$ and $> PO_x^{\delta-}$) and, therefore, the net surface charge and the value and sign of the ζ-potential of NP colloidal suspensions. In this work the adsorption experiments were carried out on NPs coated with citrate at pH

7.4. At this pH, the ζ-potentials of cAp and cAp-Tb nanoparticle suspensions are ~ −5 mV and ~20 mV, respectively (Figure 3), indicating that in both cases the surface is negatively charged. The net negative charge is due to the citrate, which is a tricarboxylic acid, whose pKs are $pK_1 = 3.128$, $pK_2 = 4.761$, and $pK_3 = 6.396$. At pH 7.4, citrate would be electrostatically adsorbed on the apatite surface with one or two carboxylates (-COO$^-$), leaving the third deprotonated carboxylate exposed towards the solution [48]. In cAp-Tb, some of the surface species would be >Tb$^{\delta+}$ atoms, which would mediate a slightly stronger electrostatic adsorption of citrate, resulting in more negatively charged nanoparticle (more negative ζ-potential). After adsorbing DF at pH 7.4 (25 °C), either at 0.3 mg/mL (Q_{ads} = 0.02304 mg/mg), or at 0.45 mg/mL (Q_{ads} = 0.04246 mg/mg) concentrations, both cAp suspensions are stable (ζ-potential very different from 0), although in different pH intervals, as shown in the graphs of ζ-potential versus pH (Figure 3a).In the first case, this is in the range $7 < pH \leq 9$ and to a lesser extent in the interval $4 < pH < 7$, while in the second it is in the interval $6 < pH \leq 8$ and to a lesser extent in $4 < pH \leq 6$. Comparing the ζ-potential at pH 7, before and after the adsorption of DF, the values went from −5.0 mV, to −6.9 mV in the first case and to −12.5 mV in the second one. A possible explanation is that the adsorption of Na$^+$ and H$^+$ on the freely exposed -COO$^-$ groups of citrates, which partially neutralizes the negative charge, is followed by the adsorption of DF molecules through the dichloro phenyl ring, leaving the acetate group of the second phenyl exposed toward the solution, whose number would increase for cAp-DF loaded at 0.45 mg/mL (Q_{ads}= 0.04246 mg/mg). The multilayer could be produced by π-π interaction between aromatic rings of different DF molecules. In the case of cAp-Tb-DF loaded with the 0.3 mg/mL DF solution (Figure 3b, Q_{ads} = 0.02680 mg/mg), the suspension is quite stable in the range $6 < pH \leq 8$, and unstable at pHs lower and higher than these, since the ζ-potential is around 0. The suspension of cAp-Tb-DF particles loaded with the 0.45 mg/mL solution (Q_{ads} = 0.04435 mg/mg) shows a slight stability in the range $5 \leq pH \leq 7$, and instability at lower and higher pHs, with ζ-potential values close to 0 (Figure 3b). Comparing at pH 7, the values went from −19.0 mV for the unloaded particles to −10.6 mV and −2.05, for the DF-loaded ones, respectively. The presence of >Tb$^{\delta+}$ atoms on the surface of cAp-Tb nanoparticles influenced both citrate and DF binding differently to what observed for the cAp nanoparticles. Thus, DF showed almost similar affinity for the citrate-coated nanoparticles (similar K_{LF} value), but a lower r value, and outermost DF layers were less negatively charged.

Concerning the release trials, a slightly higher amount of drug was found to be released at acidic pH and at 37 °C. This can be explained on the following basis. Since the medium is acidic (pH = 5.2) and DF is a weak acid (pKa = 3.99), its non-ionized form is still abundant and this favours the release of the molecules from the outermost layers in this medium, which would be more loosely linked.

Comparing the results of this work with those of the adsorption of a chemotherapeutic drug (doxorubicin) on cAp previously performed [50], we observed that at 37 °C the K_{LF} values for DF (K_{LF}cAp = 0.0572 and K_{LF} cAp-Tb = 0.651) are lower than for doxorubicin (K_{LF}cAp = 8). This indicates that doxorubicin is more strongly attracted to apatite than DF, since the molecule is positively charged and interacts electrostatically with the free carboxylates of the citrate molecules.

Other studies of DF adsorption have been reported in the literature. In particular, DF was adsorbed on activated carbon at pH 4 at 80 °C, and in this case the adsorption followed the Langmuir model [61], and on bentonite at neutral pH and temperatures from 10 to 77 °C [62]. Nanocarriers of different composition have also been studied for the delivery of DF for biomedical applications, such as polysaccharides [63], poly(ε-caprolactone) micelles [64,65], magnetic NPs [66]. Concerning the adsorption of DF on any form of apatite as adsorbent, it was recently reported the adsorption on amino hydroxyapatite/chitosan/glutaraldehyde hybrids composites at pH 6 [67], and the release of DF from injectable CaP-loaded systems to treat inflammation [68], but these authors did not study the adsorption isotherms, nor used luminescent apatites, therefore we cannot compare

our results. In line with what we reported here (see beyond), in all these cases the compositions showed an anti-inflammatory activity on inflammation in vitro and in vivo experimental models.

In this work, Tb^{3+} was incorporated to provide the nanocarrier with a luminescence signal which can be measured to determine where the particles are located for imaging applications [29,55]. The excitation and emission spectra of NPs dispersed in aqueous media at pH 5.2 or pH 7.4 and at different temperatures (25, 37 and 40 °C) were similar. In view of possible biological applications of the system the optimum λ_{exc} and λ_{em} of solid particles suggested are 350 nm and 545 nm, respectively. The luminescence results of the cAp-Tb-DF conjugated nanoparticles show that R.L.I. is higher at pH 5.2 than at pH 7.4, and the luminescence lifetime higher at pH 7.4 than at 5.2, and that neither the concentration of DF nor the temperature affect the R.L.I. and the luminescence lifetime significantly. Thus, this signal cannot be used to determine if DF is released or not. On the other side, the luminescence emission of these particles could be used to determine pH-changes, which are associated to the inflammatory processes. These NPs could be used in the context of inflammation, where local increases of temperature are observed, also because luminescence emission of these NPs does not change between 25 and 40 °C.

When tested on cells, all NPs displayed high cytocompatibility on two human osteosarcoma cell lines after 3 day incubation. These NPs were cytocompabible after 7 days of incubation also on human osteoblasts, both primary, which were obtained from explants of human trabecular bone fragments, and differentiated with an appropriate protocol from human mesenchymal stem cells. These data are in line with previous ones, reporting the properties of other lanthanide-doped nanocrystals [27,69]. The absence of toxicity after long incubation time allowed us to do experiments lasting up to 5 days to assess the effects of the DF loaded on Tb-doped NPs. NPs loaded with the highest amounts of DF (0.45 mg/mg NP) released enough soluble DF (0.046 mg/mg NP) to promote an anti-inflammatory effect in osteoblasts. We adopted a model where a cytokine mixture induced a significant inflammatory response in these cells monitored by the quantification of the cellular release of PGE_2, an important inflammatory mediator produced after COX-2 enzyme activation [70]. To confirm that these nanoparticles do not interfere with the transcription of this enzyme, we performed quantitative real time PCR for determining COX-2 mRNA levels. Our data show that these nanocarriers do not influence cell metabolism at a transcription level. These data were also confirmed by the high levels of COX-2 mRNA expression observed after the treatment with DF-loaded cAP-Tb or soluble DF in the inflammation cell model which were comparable to the levels observed for the inflammation stimuli treatment. Thus, the significant reduction in the $PG2_2$ release that we observed after the treatment of the inflamed cells with DF loaded cAp-Tb could be attributed specifically to the ability of cAp-Tb to release DF.

These results show the potential of cAp nanoparticles as nanocarriers for loading and controlled release of DF, and of cAp-Tb nanoparticles as luminescent nanoprobes with diagnostic, as well as therapeutic (theranostic) applications in pathological conditions.

5. Conclusions

We have studied the loading/release ability of DF on biomimetic cAp and cAp-Tb. The adsorption of the drug in both apatites has shown that, both at 25 °C and at 37 °C, follows the Langmuir-Freundlich model, giving rise to the formation of multilayers. The K_{LF} constants at 25 °C (K_{LF} cAp = 2.77 and K_{LF} cAp-Tb = 2.98) are greater than at 37 °C (K_{LF} cAp = 0.0572, and K_{LF} cAp-Tb = 0.651), reflecting a higher affinity for the molecules by the nanoparticles at 25 °C, and in particular towards cAp-Tb. Furthermore, in both cases the adsorption is cooperative.

The release of DF from the nanoparticles is favoured when it occurs at an acidic pH (5.2) and at a temperature of 37 °C, releasing 2% more of the drug than in a neutral medium. This data is relevant since the aim of this study is to be able to use biomimetic nanoparticles loaded with DF in pathological conditions, in bone trauma and fractures, in

which prolonged inflammatory processes occur with a local increase in temperature and a decrease in the pH of the medium. The luminescence results of the cAp-Tb-DF conjugated nanoparticles show that R.L.I. is higher at pH 5.2 than at pH 7.4, and the luminescence lifetime higher at pH 7.4 than at 5.2, and that neither the concentration of DF nor the temperature affect the R.L.I. and the luminescence lifetime significantly. Luminescence emission of these particles could have biological applications in inflammation, since it can detect pH-changes, not being affected by the raise of temperature, being both conditions associated with the inflammatory process. Concerning cell behaviour, all the nanocarriers studied showed no reduction in osteoblasts cell vitality and in an in vitro model of osteoblasts cytokine–induced inflammation, they affected COX-2 expression and decreased the cellular production of prostaglandin E_2. These results show the potential of cAp nanoparticles as nanocarriers for loading and controlled release of DF, and of cAp-Tb nanoparticles as luminescent nanoprobes with diagnostic, as well as therapeutic (theranostic) applications in pathological conditions.

Supplementary Materials: The following figures are available online at www.mdpi.com/article/10.3390/nano12030562/s1. Figure S1: X-ray diffraction patterns of cAp and cAp-Tb prepared by thermal decomplexing method, Figure S2: (a) FTIR and (b) Raman spectra of cAp and cAp-Tb prepared by thermal decomplexing method, Figure S3: (a) PSD in volume and (b) cumulative oversize PSD of cAp and cAp-Tb. Figure S4: Evolution of the adsorbed amount of DF with time on cAp (a) and cAp-Tb (b). Figure S5: Excitation (dashed lines) and emission (solid lines) uncorrected spectra of samples containing different DF concentrations dispersed in a pH = 5.2 aqueous suspension at 0.5 mg/mL and 25 °C. Figure S6: Excitation (dashed lines) and emission (solid lines) uncorrected spectra of samples containing different DF concentrations dispersed in a pH = 5.2 aqueous suspension at 0.5 mg/mL and 40 °C. Figure S7: Excitation (dashed lines) and emission (solid lines) uncorrected spectra of samples containing different DF concentrations dispersed in a pH = 7.4 aqueous suspension at 0.5 mg/mL and 25 °C. Figure S8: Excitation (dashed lines) and emission (solid lines) uncorrected spectra of samples containing different DF concentrations dispersed in a pH = 7.4 aqueous suspension at 0.5 mg/mL and 37 °C. Figure S9: Excitation (dashed lines) and emission (solid lines) uncorrected spectra of samples containing different DF concentrations dispersed in a pH = 7.4 aqueous suspension at 0.5 mg/mL and 40 °C. Figure S10: Luminescence decay curves at different DF concentrations of 0.5 mg/mL suspended particles at 25 °C and pH 5.2. $\lambda_{exc/em}$ = 350/545 nm, t_d = 120 μs, t_g = 0.01 ms, slitwidth$_{exc/em}$ = 20/20 nm and detector voltage 900v. Figure S11: Luminescence decay curves at different DF concentrations of 0.5 mg/mL suspended particles at 37 °C and pH 5.2. $\lambda_{exc/em}$ = 350/545 nm, t_d = 120μs, t_g = 0.01 ms, slitwidth$_{exc/em}$ = 20/20 nm and detector voltage 900 v. Figure S12: Luminescence decay curves at different DF concentrations of 0.5 mg/mL suspended particles at 40 °C and pH 5.2. $\lambda_{exc/em}$ = 350/545 nm, t_d = 120 μs, t_g = 0.01 ms, slitwidth$_{exc/em}$ = 20/20 nm and detector voltage 900 v. Figure S13: Luminescence decay curves at different DF concentrations of 0.5 mg/mL suspended particles at 25 °C and pH 7.4. $\lambda_{exc/em}$ = 350/545 nm, t_d = 120 μs, t_g = 0.01 ms, slitwidth$_{exc/em}$ = 20/20 nm and detector voltage 900 v. Figure S14: Luminescence decay curves at different DF concentrations of 0.5 mg/mL suspended particles at 37 °C and pH 7.4. $\lambda_{exc/em}$ = 350/545 nm, t_d = 120 μs, t_g = 0.01 ms, slitwidth$_{exc/em}$ = 20/20 nm and detector voltage 900 v. Figure S15: Luminescence decay curves at different DF concentrations of 0.5 mg/mL suspended particles at 40 °C and pH 7.4. $\lambda_{exc/em}$ = 350/545 nm, t_d = 120 μs, t_g = 0.01 ms, slitwidth$_{exc/em}$ = 20/20 nm and detector voltage 900 v. Figure S11: Luminescence decay curves at different DF concentrations of 0.5 mg/mL suspended particles at 37 °C and pH 5.2. $\lambda_{exc/em}$ = 350/545 nm, t_d = 120 μs, t_g = 0.01 ms, slitwidth$_{exc/em}$ = 20/20 nm and detector voltage 900 v. Figure S12: Luminescence decay curves at different DF concentrations of 0.5 mg/mL suspended particles at 40 °C and pH 5.2. $\lambda_{exc/em}$ = 350/545 nm, t_d = 120 μs, t_g = 0.01 ms, slitwidth$_{exc/em}$ = 20/20 nm and detector voltage 900 v. Figure S13: Luminescence decay curves at different DF concentrations of 0.5 mg/mL suspended particles at 25 °C and pH 7.4. $\lambda_{exc/em}$ = 350/545 nm, t_d = 120 μs, t_g = 0.01 ms, slitwidth$_{exc/em}$ = 20/20 nm and detector voltage 900 v. Figure S14: Luminescence decay curves at different DF concentrations of 0.5 mg/mL suspended particles at 37 °C and pH 7.4. $\lambda_{exc/em}$ = 350/545 nm, t_d = 120 μs, t_g = 0.01 ms, slitwidth$_{exc/em}$ = 20/20 nm and detector voltage 900 v. Figure S15: Luminescence decay curves at different DF concentrations of 0.5 mg/mL suspended particles at 40 °C and pH 7.4. $\lambda_{exc/em}$ = 350/545 nm, t_d = 120 μs, t_g = 0.01 ms, slitwidth$_{exc/em}$ = 20/20 nm and detector voltage 900 v. Figure S16: Viability of MG-63 cells (a) and of U-2OS cells (b) incubated with cApTb-DF particles loaded with different DF concentration, ranging from 0.1 to 0.45 mg/mg NP, for three days. Figure S17: Osteoblasts differentiated from human mesenchymal stem cells express alkaline phosphatase.

Data Availability Statement: Not applicable.

Conflicts of Interest: The authors declare no conflict of interest.

References

1. Etter, E.L.; Mei, K.-C.; Nguyen, J. Delivering More for Less: Nanosized, Minimal-Carrier and Pharmacoactive Drug Delivery Systems. *Adv. Drug Deliv. Rev.* **2021**, *179*, 113994. https://doi.org/10.1016/j.addr.2021.113994.
2. Dutta, B.; Barick, K.C.; Hassan, P.A. Recent Advances in Active Targeting of Nanomaterials for Anticancer Drug Delivery. *Adv. Colloid Interface Sci.* **2021**, *296*, 102509. https://doi.org/10.1016/j.cis.2021.102509.
3. Subramaniam, S.; Joyce, P.; Thomas, N.; Prestidge, C.A. Bioinspired Drug Delivery Strategies for Repurposing Conventional Antibiotics against Intracellular Infections. *Adv. Drug Deliv. Rev.* **2021**, *177*, 113948. https://doi.org/10.1016/j.addr.2021.113948.
4. Jelinkova, P.; Mazumdar, A.; Sur, V.P.; Kociova, S.; Dolezelikova, K.; Jimenez, A.M.J.; Koudelkova, Z.; Mishra, P.K.; Smerkova, K.; Heger, Z.; et al. Nanoparticle-Drug Conjugates Treating Bacterial Infections. *J. Control. Release* **2019**, *307*, 166–185. https://doi.org/10.1016/j.jconrel.2019.06.013.
5. Macedo, L.D.O.; Barbosa, E.J.; Löbenberg, R.; Bou-Chacra, N.A. Anti-Inflammatory Drug Nanocrystals: State of Art and Regulatory Perspective. *Eur. J. Pharm. Sci.* **2021**, *158*, 105654. https://doi.org/10.1016/j.ejps.2020.105654.
6. Wong, C.Y.; Al-Salami, H.; Dass, C.R. Potential of Insulin Nanoparticle Formulations for Oral Delivery and Diabetes Treatment. *J. Control. Release* **2017**, *264*, 247–275. https://doi.org/10.1016/j.jconrel.2017.09.003.
7. Ozawa, T.; Yoshimura, H.; Kim, S.B. Advances in Fluorescence and Bioluminescence Imaging. *Anal. Chem.* **2013**, *85*, 590–609. https://doi.org/10.1021/ac3031724.
8. Clynes, M.A.; Harvey, N.C.; Curtis, E.M.; Fuggle, N.R.; Dennison, E.M.; Cooper, C. The Epidemiology of Osteoporosis. *Br. Med. Bull.* **2020**, *133*, 105–117. https://doi.org/10.1093/bmb/ldaa005.
9. Salari, N.; Ghasemi, H.; Mohammadi, L.; Behzadi, M.H.; Rabieenia, E.; Shohaimi, S.; Mohammadi, M. The Global Prevalence of Osteoporosis in the World: A Comprehensive Systematic Review and Meta-Analysis. *J. Orthop. Surg. Res.* **2021**, *16*, 609. https://doi.org/10.1186/s13018-021-02772-0.
10. Curtis, E.M.; Moon, R.J.; Dennison, E.M.; Harvey, N.C.; Cooper, C. Recent Advances in the Pathogenesis and Treatment of Osteoporosis. *Clin. Med.* **2016**, *16*, 360–364. https://doi.org/10.7861/clinmedicine.16-4-360.
11. Grässel, S.; Zaucke, F.; Madry, H. Osteoarthritis: Novel Molecular Mechanisms Increase Our Understanding of the Disease Pathology. *J. Clin. Med.* **2021**, *10*, 1938. https://doi.org/10.3390/jcm10091938.
12. Ain, Q.; Zeeshan, M.; Khan, S.; Ali, H. Biomimetic Hydroxyapatite as Potential Polymeric Nanocarrier for the Treatment of Rheumatoid Arthritis. *J. Biomed. Mater. Res. Part A* **2019**, *107*, 2595–2600. https://doi.org/10.1002/jbm.a.36765.
13. Gomez-Morales, J.; Iafisco, M.; Delgado-López, J.M.; Sarda, S.; Drouet, C. Progress on the preparation of nanocrystalline apatites and surface characterization: Overview of fundamental and applied aspects. *Prog. Cryst. Growth Charact. Mater.* **2013**, *59*, 1–46.
14. Hu, Y.Y.; Rawal, A.; Schmidt-Rohr, K. Strongly bound citrate stabilizes the apatite nanocrystals in bone. *Proc. Natl. Acad. Sci. USA* **2010**, *107*, 22425–224259.
15. Low, K.L.; Tan, S.H.; Zein, S.H.S.; Roether, J.A.; Mouriño, V.; Boccaccini, A.R. Calcium Phosphate-Based Composites as Injectable Bone Substitute Materials: A Review. *J. Biomed. Mater. Res. Part B Appl. Biomater.* **2010**, *94B*, 273–286. https://doi.org/10.1002/jbm.b.31619.
16. Ding, Z.Z.; Fan, Z.H.; Huang, X.W.; Bai, S.M.; Song, D.W.; Lu, Q.; Kaplan, D.L. Bioactive Natural Protein–Hydroxyapatite Nanocarriers for Optimizing Osteogenic Differentiation of Mesenchymal Stem Cells. *J. Mater. Chem. B* **2016**, *4*, 3555–3561. https://doi.org/10.1039/C6TB00509H.
17. Gera, S.; Sampathi, S.; Dodoala, S. Role of Nanoparticles in Drug Delivery and Regenerative Therapy for Bone Diseases. *Curr. Drug Deliv.* **2017**, *14*, 904–916. https://doi.org/10.2174/1567201813666161230142123.
18. Pietrzykowska, E.; Romelczyk-Baishya, B.; Chodara, A.; Koltsov, I.; Smogór, H.; Mizeracki, J.; Pakieła, Z.; Łojkowski, W. Microstructure and Mechanical Properties of Inverse Nanocomposite Made from Polylactide and Hydroxyapatite Nanoparticles. *Materials* **2022**, *15*, 184.
19. Bystrova, A.; Dekhtyar, Y.D.; Popov, A.; Coutinho, J.; Bystrov, V. Modified hydroxyapatite structure and properties: Modeling and synchrotron data analysis of modified hydroxyapatite structure. *Ferroelectrics* **2015**, *475*, 135–147.

20. Munir, M.U.; Salman, S.; Javed, I.; Bukhari, S.N.A.; Ahmad, N.; Shad, N.A.; Aziz, F. Nano-Hydroxyapatite as a Delivery System: Overview and Advancements. *Artif. Cells Nanomed. Biotechnol.* **2021**, *49*, 717–727. https://doi.org/10.1080/21691401.2021.2016785.

21. Tram Do, T.N.; Lee, W.-H.; Loo, C.-Y.; Zavgorodniy, A.V.; Rohanizadeh, R. Hydroxyapatite Nanoparticles as Vectors for Gene Delivery. *Ther. Deliv.* **2012**, *3*, 623–632. https://doi.org/10.4155/tde.12.39.

22. Zhang, Y.; Zhang, L.; Ban, Q.; Li, J.; Li, C.-H.; Guan, Y.-Q. Preparation and Characterization of Hydroxyapatite Nanoparticles Carrying Insulin and Gallic Acid for Insulin Oral Delivery. *Nanomed. Nanotechnol. Biol. Med.* **2018**, *14*, 353–364. https://doi.org/10.1016/j.nano.2017.11.012.

23. Iafisco, M.; Delgado-Lopez, J.M.; Varoni, E.M.; Tampieri, A.; Rimondini, L.; Gomez-Morales, J.; Prat, M. Cell Surface Receptor Targeted Biomimetic Apatite Nanocrystals for Cancer Therapy. *Small* **2013**, *9*, 3834–3844. https://doi.org/10.1002/smll.201202843.

24. Khalifehzadeh, R.; Arami, H. Biodegradable Calcium Phosphate Nanoparticles for Cancer Therapy. *Adv. Colloid Interface Sci.* **2020**, *279*, 102157. https://doi.org/10.1016/j.cis.2020.102157.

25. Oltolina, F.; Gregoletto, L.; Colangelo, D.; Gómez-Morales, J.; Delgado-López, J.M.; Prat, M. Monoclonal Antibody-Targeted Fluorescein-5-Isothiocyanate-Labeled Biomimetic Nanoapatites: A Promising Fluorescent Probe for Imaging Applications. *Langmuir* **2015**, *31*, 1766–1775. https://doi.org/10.1021/la503747s.

26. Chen, M.-H.; Yoshioka, T.; Ikoma, T.; Hanagata, N.; Lin, F.-H.; Tanaka, J. Photoluminescence and Doping Mechanism of Theranostic Eu $^{3+}$ /Fe $^{3+}$ Dual-Doped Hydroxyapatite Nanoparticles. *Sci. Technol. Adv. Mater.* **2014**, *15*, 055005. https://doi.org/10.1088/1468-6996/15/5/055005.

27. Gómez-Morales, J.; Fernández-Penas, R.; Romero-Castillo, I.; Verdugo-Escamilla, C.; Choquesillo-Lazarte, D.; D'Urso, A.; Prat, M.; Fernández-Sánchez, J.F. Crystallization, Luminescence and Cytocompatibility of Hexagonal Calcium Doped Terbium Phosphate Hydrate Nanoparticles. *Nanomaterials* **2021**, *11*, 322. https://doi.org/10.3390/nano11020322.

28. Haque, S.T.; Islam, R.A.; Gan, S.H.; Chowdhury, E.H. Characterization and Evaluation of Bone-Derived Nanoparticles as a Novel pH-Responsive Carrier for Delivery of Doxorubicin into Breast Cancer Cells. *Int. J. Mol. Sci.* **2020**, *21*, 6721. https://doi.org/10.3390/ijms21186721.

29. Delgado-López, J.M.; Iafisco, M.; Rodríguez, I.; Tampieri, A.; Prat, M.; Gómez-Morales, J. Crystallization of Bioinspired Citrate-Functionalized Nanoapatite with Tailored Carbonate Content. *Acta Biomater.* **2012**, *8*, 3491–3499. https://doi.org/10.1016/j.actbio.2012.04.046.

30. Jabalera, Y.; Oltolina, F.; Prat, M.; Jimenez-Lopez, C.; Fernández-Sánchez, J.F.; Choquesillo-Lazarte, D.; Gómez-Morales, J. Eu-doped citrate-coated carbonated apatite luminescent nanoprobes for drug delivery. *Nanomaterials* **2020**, *10*, 199.

31. Shang, H.-B.; Chen, F.; Wu, J.; Qi, C.; Lu, B.-Q.; Chen, X.; Zhu, Y.-J. Multifunctional biodegradable terbium-doped calcium phosphate nanoparticles: Facile preparation, pH-sensitive drug release and in vitro bioimaging. *RSC Adv.* **2014**, *4*, 53122–53129.

32. Wang, Y.; Lu, Y.; Zhang, J.; Hu, X.; Yang, Z.; Guo, Y.; Wang, Y. A synergistic antibacterial effect between terbium ions and reduced graphene oxide in a poly(vinyl alcohol)–alginate hydrogel for treating infected chronic wounds. *J. Mater. Chem. B* **2019**, *7*, 538–547.

33. Liu, D.D.; Ge, K.; Jin, Y.; Sun, J.; Wang, S.X.; Yang, M.S.; Zhang, J.C. Terbium promotes adhesion and osteogenic differentiation of mesenchymal stem cells via activation of the Smad-dependent TGF-β/BMP signaling pathway. *J. Biol. Inorg. Chem.* **2014**, *19*, 879–891.

34. Romero-Castillo, I.; López-Ruiz, E.; Fernández-Sánchez, J.F.; Marchal, J.A.; Gómez-Morales, J. Self-Assembled Type I Collagen-Apatite Fibers with Varying Mineralization Extent and Luminescent Terbium Promote Osteogenic Differentiation of Mesenchymal Stem Cells. *Macromol. Biosci.* **2021**, *21*, 2000319.

35. Gan, T.J. Diclofenac: An Update on Its Mechanism of Action and Safety Profile. *Curr. Med. Res. Opin.* **2010**, *26*, 1715–1731. https://doi.org/10.1185/03007995.2010.486301.

36. Rojas, A.; Chen, D.; Ganesh, T.; Varvel, N.H.; Dingledine, R. The COX-2/Prostanoid Signaling Cascades in Seizure Disorders. *Expert Opin. Ther. Targets* **2019**, *23*, 1–13. https://doi.org/10.1080/14728222.2019.1554056.

37. Rainsford, K.D. Profile and Mechanisms of Gastrointestinal and Other Side Effects of Nonsteroidal Anti-Inflammatory Drugs (NSAIDs). *Am. J. Med.* **1999**, *107*, 27–35. https://doi.org/10.1016/S0002-9343(99)00365-4.

38. Kołodziejska, J.; Kołodziejczyk, M. Diclofenac in the Treatment of Pain in Patients with Rheumatic Diseases. *Reumatol. / Rheumatol.* **2018**, *56*, 174–183. https://doi.org/10.5114/reum.2018.76816.

39. Gouda, A.A.; Kotb El-Sayed, M.I.; Amin, A.S.; el Sheikh, R. Spectrophotometric and Spectrofluorometric Methods for the Determination of Non-Steroidal Anti-Inflammatory Drugs: A Review. *Arab. J. Chem.* **2013**, *6*, 145–163. https://doi.org/10.1016/j.arabjc.2010.12.006.

40. Bosetti, M.; Leigheb, M.; Brooks, R.A.; Boccafoschi, F.; Cannas, M.F. Regulation of Osteoblast and Osteoclast Functions by FGF-6. *J. Cell. Physiol.* **2010**, *225*, 466–471. https://doi.org/10.1002/jcp.22225.

41. Roato, I.; Belisario, D.C.; Compagno, M.; Verderio, L.; Sighinolfi, A.; Mussano, F.; Genova, T.; Veneziano, F.; Pertici, G.; Perale, G.; et al. Adipose-Derived Stromal Vascular Fraction/Xenohybrid Bone Scaffold: An Alternative Source for Bone Regeneration. *Stem Cells Int.* **2018**, *2018*, 4126379. https://doi.org/10.1155/2018/4126379.

42. Zamperone, A.; Pietronave, S.; Merlin, S.; Colangelo, D.; Ranaldo, G.; Medico, E.; di Scipio, F.; Berta, G.N.; Follenzi, A.; Prat, M. Isolation and Characterization of a Spontaneously Immortalized Multipotent Mesenchymal Cell Line Derived from Mouse Subcutaneous Adipose Tissue. *Stem Cells Dev.* **2013**, *22*, 2873–2884. https://doi.org/10.1089/scd.2012.0718.

43. Sidney, L.E.; Heathman, T.R.; Britchford, E.R.; Abed, A.; Rahman, C.V.; Buttery, L.D. Investigation of localized delivery of diclofenac sodium from poly(D,L-lactic acid-co-glycolic acid)/poly(ethylene glycol) scaffolds using an in vitro osteoblast inflammation model. *Tissue Eng. Part A* **2015**, *21*, 362–373. https://doi.org/10.1089/ten.TEA.2014.0100.

44. Fornai, M.; Blandizzi, C.; Colucci, R.; Antonioli, L.; Bernardini, N.; Segnani, C.; Baragatti, B.; Barogi, S.; Berti, P.; Spisni, R.; et al. Role of Cyclooxygenases 1 and 2 in the Modulation of Neuromuscular Functions in the Distal Colon of Humans and Mice. *Gut* **2005**, *54*, 608–616. https://doi.org/10.1136/gut.2004.053322.

45. Ramírez-Rodríguez, G.B.; Delgado-López, J.M.; Gómez-Morales, J. Evolution of Calcium Phosphate Precipitation in Hanging Drop Vapor Diffusion by in Situ Raman Microspectroscopy. *CrystEngComm* **2013**, *15*, 2206. https://doi.org/10.1039/c2ce26556g.

46. Langmuir, I. The Adsorption of Gases on Plane Surfaces of Glass, Mica and Platinum. *J. Am. Chem. Soc.* **1918**, *40*, 1361–1403. https://doi.org/10.1021/ja02242a004.

47. Adamson, A.W. *Physical Chemistry of Surfaces*; Wiley: New York, NY, USA, 1997.

48. López-Macipe, A.; Gómez-Morales, J.; Rodríguez-Clemente, R. The Role of pH in the Adsorption of Citrate Ions on Hydroxyapatite. *J. Colloid Interface Sci.* **1998**, *200*, 114–120. https://doi.org/10.1006/jcis.1997.5343.

49. Reed, B.E.; Matsumoto, M.R. Modeling Cadmium Adsorption by Activated Carbon Using the Langmuir and Freundlich Isotherm Expressions. *Sep. Sci. Technol.* **1993**, *28*, 2179–2195. https://doi.org/10.1080/01496399308016742.

50. Rodríguez-Ruiz, I.; Delgado-López, J.M.; Durán-Olivencia, M.A.; Iafisco, M.; Tampieri, A.; Colangelo, D.; Prat, M.; Gómez-Morales, J. pH-Responsive Delivery of Doxorubicin from Citrate–Apatite Nanocrystals with Tailored Carbonate Content. *Langmuir* **2013**, *29*, 8213–8221. https://doi.org/10.1021/la4008334.

51. Azizian, S.; Eris, S. Adsorption Isotherms and Kinetics. In *Interface Science and Technology*; Academic Press: London, UK, 2021; Volume 33, pp. 445–509. https://doi.org/10.1016/B978-0-12-818805-7.00011-4.

52. Hemmilä, I.; Dakubu, S.; Mukkala, V.-M.; Siitari, H.; Lövgren, T. Europium as a Label in Time-Resolved Immunofluorometric Assays. *Anal. Biochem.* **1984**, *137*, 335–343. https://doi.org/10.1016/0003-2697(84)90095-2.

53. Lakowicz, J.R. *Principles of Fluorescence Spectroscopy*; Springer: Boston, MA, USA, 2006. https://doi.org/10.1007/978-0-387-46312-4.

54. Kaur, A.; Dhakal, S. Recent Applications of FRET-Based Multiplexed Techniques. *TrAC Trends Anal. Chem.* **2020**, *123*, 115777. https://doi.org/10.1016/j.trac.2019.115777.

55. Hänninen, P.; Härmä, H. (Eds.) *Lanthanide Luminescence Photophysical, Analytical and Biological Aspects*; Springer: Berlin/Heidelberg, 2011. https://doi.org/10.1007/978-3-642-21023-5.

56. Medina-Velazquez, D.Y.; Caldiño, U.; Morales-Ramirez, A.; Reyes-Miranda, J.; Lopez, R.E.; Escudero, R.; Ruiz-Guerrero, R.; Morales Perez, M.F. Synthesis of Luminescent Terbium-Thenoyltriflouroacetone MOF Nanorods for Green Laser Application. *Opt. Mater.* **2019**, *87*, 3–10. https://doi.org/10.1016/j.optmat.2018.08.021.

57. Richardson, F.S. Terbium(III) and Europium(III) Ions as Luminescent Probes and Stains for Biomolecular Systems. *Chem. Rev.* **1982**, *82*, 541–552. https://doi.org/10.1021/cr00051a004.

58. International Standard Organization. *ISO 10993-5 Biological Evaluation of Medical Devices Part 5: Tests for In Vitro Cytotoxicity*; International Standard Organization: Geneve, Switzerland, 2009.

59. Fenton, O.S.; Olafson, K.N.; Pillai, P.S.; Mitchell, M.J.; Langer, R. Advances in Biomaterials for Drug Delivery. *Adv. Mat.* **2018**, *30*, e1705328. https://doi.org/10.1002/adma.201705328.

60. Van der Meel, R.; Sulheim, E.; Shi, Y.; Kiessling, F.; Mulder, W.J.M.; Lammers, T. Smart cancer nanomedicine. *Nat. Nanotechnol.* **2019**, *14*, 1007–1017.

61. Larous, S.; Meniai, A.-H. Adsorption of Diclofenac from Aqueous Solution Using Activated Carbon Prepared from Olive Stones. *Int. J. Hydrog. Energy* **2016**, *41*, 10380–10390. https://doi.org/10.1016/j.ijhydene.2016.01.096.

62. Abbas, A.M.B.; Muhseen, R.J. Adsorption of Diclofenac Sodium and Ibuprofen by Bentonite Polyureaformaldehyde Thermodynamics and Kinetics Study. *Iraqi J. Chem. Pet. Eng.* **2018**, *19*, 29–43.

63. Cohen, Y.; Rutenberg, R.; Cohen, G.; Veltman, B.; Gvirtz, R.; Fallik, E.; Danino, D.; Eltzov, E.; Poverenov, E. Aminated Polysaccharide-Based Nanoassemblies as Stable Biocompatible Vehicles Enabling Crossing of Biological Barriers: An Effective Transdermal Delivery of Diclofenac Medicine. *ACS Appl. Bio Mater.* **2020**, *3*, 2209–2217. https://doi.org/10.1021/acsabm.0c00048.

64. Arias, J.L.; López-Viota, M.; Sáez-Fernández, E.; Ruiz, M.A. Formulation and Physicochemical Characterization of Poly(ε-Caprolactone) Nanoparticles Loaded with Ftorafur and Diclofenac Sodium. *Colloids Surf. B Biointerfaces* **2010**, *75*, 204–208. https://doi.org/10.1016/j.colsurfb.2009.08.032.

65. Al-Lawati, H.; Vakili, M.R.; Lavasanifar, A.; Ahmed, S.; Jamali, F. Reduced Heart Exposure of Diclofenac by Its Polymeric Micellar Formulation Normalizes CYP-Mediated Metabolism of Arachidonic Acid Imbalance in an Adjuvant Arthritis Rat Model: Implications in Reduced Cardiovascular Side Effects of Diclofenac by Nanodrug Delivery. *Mol. Pharm.* **2020**, *17*, 1377–1386. https://doi.org/10.1021/acs.molpharmaceut.0c00069.

66. Agotegaray, M.; Palma, S.; Lassalle, V. Novel Chitosan Coated Magnetic Nanocarriers for the Targeted Diclofenac Delivery. *J. Nanosci. Nanotechnol.* **2014**, *14*, 3343–3347. https://doi.org/10.1166/jnn.2014.8256.

67. Pereira, M.B.B.; França, D.B.; Araújo, R.C.; Silva Filho, E.C.; Rigaud, B.; Fonseca, M.G.; Jaber, M. Amino Hydroxyapatite/Chitosan Hybrids Reticulated with Glutaraldehyde at Different PpH Values and Their Use for Diclofenac Removal. *Carbohydr. Polym.* **2020**, *236*, 116036. https://doi.org/10.1016/j.carbpol.2020.116036.

68. Fasolino, I.; Soriente, A.; Ambrosio, L.; Grazia Raucci, M. Osteogenic and Anti-Inflammatory Behavior of Injectable Calcium Phosphate Loaded with Therapeutic Drugs. *Nanomaterials* **2020**, *10*, 1743. https://doi.org/10.3390/nano10091743.

69. Gómez-Morales, J.; Verdugo-Escamilla, C.; Fernández-Penas, R.; Parra-Milla, C.M.; Drouet, C.; Iafisco, M.; Oltolina, F.; Prat, M.; Fernández-Sánchez, J.F. Bioinspired Crystallization, Sensitized Luminescence and Cytocompatibility of Citrate-Functionalized Ca-Substituted Europium Phosphate Monohydrate Nanophosphors. *J. Colloid Interface Sci.* **2019**, *538*, 174–186. https://doi.org/10.1016/j.jcis.2018.11.083.

70. Hughes, F.J.; Buttery, L.D.K.; Hukkanen, M.V.J.; O'Donnell, A.; Maclouf, J.; Polak, J.M. Cytokine-Induced Prostaglandin E2 Synthesis and Cyclooxygenase-2 Activity Are Regulated Both by a Nitric Oxide-Dependent and -Independent Mechanism in Rat Osteoblasts in Vitro. *J. Biol. Chem.* **1999**, *274*, 1776–1782. https://doi.org/10.1074/jbc.274.3.1776.

Ringrazio anche i ragazzi del laboratorio d'istologia del piano di sotto, che sono stati sempre gentili con me, disponibili a un confronto scientifico in modo da risolvere i miei mille dubbi. Infine, un immenso grazie va a tutto il Dipartimento di Scienze della Salute a partire dalla portineria di Palazzo Bellini, ai tecnici, agli informatici, alle segretarie, ai professori, ai post-doc, ai dottorandi di altri laboratori. Tutti in qualche modo mi hanno sempre aiutato, dato delle indicazioni, suggerimenti oppure semplicemente hanno alleggerito la mia permanenza qui con una chiacchierata davanti alle macchinette del caffè facendomi sentire quasi a casa; pertanto, è doveroso ringraziare tutti.

Un grazie speciale va ai miei i genitori, Laura e Giuseppe, che cosa farei senza di loro …… i miei maestri di vita, la mia ricchezza. Se oggi sono quella che sono lo devo semplicemente a loro, ai loro insegnamenti, so bene che tutti i miei traguardi sono il frutto dei loro mille sacrifici e questo non potrò mai dimenticarlo. Oggi desidero ringraziarli per essere i genitori meravigliosi che sono, sempre al mio fianco a supportarmi in tutte le mie decisioni, ad incoraggiarmi ad andare avanti, a dirmi che non è la distanza un problema anche se ad essere onesta i loro volti dicono tutt'altro quando giunge il momento dell'odiosa partenza, ma come sempre il mio bene al primo posto. Grazie di cuore per essere quello che siete!

Inoltre, desidero ringraziare mio fratello Luigi insieme alla mia sorella adottiva Paola per esserci sempre …lì pronti ad appoggiarmi nelle mie scelte, ma nello stesso tempo a "badare" ai nostri genitori. Grazie!

Un grandissimo grazie va al mio amico, al mio compagno, al mio amore Paolo! Grazie per essere la persona stupenda che sei, lì sempre a supportarmi, ad ascoltarmi, a ripetermi che posso farcela, a strapparmi un sorriso con un bacio o una battuta anche in questo periodo così difficile per te. Non potevo desiderare un uomo migliore al mio fianco, con te ho concluso questo importante capitolo della mia vita, ma spero che insieme ne scriveremo tanti altri ancora più belli. Grazie di tutto amore mio!

Voglio ringraziare anche tutte le persone che hanno sempre creduto in me, come alcuni miei parenti, amici, i miei nonni. Purtroppo, alcuni si sono addormentati come la mia adorata nonna Gerardina, ma sono sicura che ovunque sia adesso sta facendo come sempre il tifo per la sua Annarita, perciò grazie.

Alla fine di questi lunghi ringraziamenti, desidero ricordare, ringraziare una persona speciale per me, mia cugina Lucia….. ormai sono trascorsi diversi anni da quando lei ci ha lasciato, ma lei continua a vivere nel mio cuore come viva è quella promessa che gli feci tempo fa e sinceramente all'epoca non credevo di riuscire a mantenere, ma lei credeva in me e per questo sono andata avanti. Ho effettuato il mio lavoro in laboratorio con dedizione non dimenticando mai chi avessi a casa, come mi ricordava spesso Lucia quando insieme leggevamo degli articoli scientifici e mi faceva notare che dietro quei dati c'è la speranza di tante persone. Il suo ricordo in questi anni è stato sempre il mio faro che mi ha indicato la strada portandomi fino a qui e non facendomi mai mollare nemmeno nei momenti difficili. Pertanto, non posso non dedicare tutto questo lavoro di tesi a lei, a quella piccola grande guerriera che ha combattuto fino alla fine credendo che un giorno grazie alla ricerca le cose potessero cambiare e lei potesse riprendere a respirare, a vivere la sua vita. Purtroppo, per lei le cose non sono cambiate, come non sono cambiate per il sig. Sebastiano che oggi voleva essere qui, ma questo non significa che le cose non cambieranno in futuro, perciò continuo a confidare nella buona ricerca scientifica portando con me il ricordo di queste persone. Grazie di tutto Lucia!

Annarita

"Niente nella vita va temuto, dev'essere solamente compreso. Ora è tempo di comprendere di più, così possiamo temere di meno."

Marie Curie